

Faculty of Engineering

Department of Mechanical, Materials and Manufacturing Engineering

Investigation of Friction Stir Welding of Aluminium Alloy and Aluminium Matrix Composites

Thesis submitted to the University of Nottingham
for the degree of Doctor of Philosophy

by

Omar Saad Salih Al-Jumaili

November 2018

Abstract

Friction stir welding (FSW) is an upgraded version of the conventional friction welding process, and it is considered the latest development and the most important one during the past two decades in the welding of metals. The dependence of FSW on friction and plastic work as a heat source precludes the melting in the workpiece and leads to avoiding many of the difficulties arising from the change in the state of the material, such as defects, distortion and residual stresses, which often happen in conventional welding processes. FSW gained significant attention as a solid-state welding process of aluminium alloys, but now there is a need to extend its application to advanced materials such as metal matrix composites (MMCs). However, the process has always represented a challenge owing to the complexity of microstructural development and the associated number of process parameters to take into consideration.

This thesis investigates the feasibility of welding two new advanced aluminium matrix composites (AMCs), AA 6092/SiC/17.5p-T6 and AA 6061B/SiC/20p-T1 by FSW for the first time. Also, aluminium alloy AA6082-T6 has been investigated as base-line material to specify the benefit, drawback, and FSW window. Experiment analyses were conducted to evaluate the influence of FSW parameters, including tool rotation and traverse speeds on the quality of weldments.

Weld joints were characterised in terms of thermal history, metallurgical behaviour, mechanical properties, and residual stresses. The metallurgical characterisations have been done by optical, scanning electron microscopy (SEM), electron backscattered diffraction (EBSD), transmission electron microscopy (TEM), and energy dispersive X-ray spectroscopy (EDS). Microhardness, tensile, and low-cycle fatigue (LCF) test with the axial total strain-amplitude control mode $R = \varepsilon_{min}/\varepsilon_{max} = -1$ were used for evaluating the mechanical properties.

The results showed that the generated peak temperature in the welding joints is affected more significantly by the rotating tool speed, while the exposure time and subsequent cooling rate are controlled by tool traverse speed. The microstructure of nugget zone (NZ) exhibits an elliptical shape with a substantial grain refinement resulted from continuous dynamic recrystallisation (CDR) process with an increase in the fraction of high angle grain boundaries (HAGBs). The evolved grain size was greatly influenced by weld pitch as the ratio between tool traverse speed to tool rotation speed, which is a key parameter to control the amount of heat input, exposure time and cooling rate. In addition, in the case of AMCs more homogeneous distribution of reinforcement particles (SiC) coupled with particle refinement were formed in the NZ.

The cross-weld microhardness profile revealed a significant difference in microhardness among the base metals, heat affected zone (HAZ), thermo-mechanically affected zone (TMAZ), and NZ in the case of AA 6082 and AMC (AA 6092/SiC/17.5p), as they depend on the strengthening precipitate. Meanwhile, the hardness profile of AMC (AA 6061B/SiC/20p) FSW joints showed that there is no difference in the measured hardness between the welding zone and base materials because the welded joints are exposed to thermal history similar to the initial heat treatment condition of the base metal, T1, cooled from an elevated temperature shaping process and naturally aged.

The tensile strength of AA6082, and AMC (AA 6092/SiC/17.5p) cross-weld FSW specimens was found to be lower than their base metals with a joint efficiency (the ratio of the tensile strength of joint to the tensile strength of base metal) of about 71 and 75 %, respectively. While for SAMC (AA 6061B/SiC/20p) FSW joints it is reached 108 % of that of the base metal. The low-cycle fatigue results indicate that the fatigue life of the cross-weld joints varies with grain size in the NZ, and it is always lower than that of the base metal. A significant improvement in fatigue life is found to be related to the finer equiaxed

grains dominated by HAGBs in the NZ, as well as, to less gradient in the grain size of the cross-weld.

Residual stresses are significant concerns associated with the welding process, as it can combine with applied stresses, which may lead to the reduction of structural properties. The result of residual stress measurement by neutron diffraction techniques exhibited a typical ‘‘M’’ profile, which indicates that compressive and tensile residual stress existed in the base metal and welding zone, respectively. This has not only provided an improved understanding of residual stresses in FSW joints but also has contributed to the validation of 3D fully coupled thermo-mechanical finite element (FE) model, which has been developed based on Coupled Eulerian-Lagrangian (CEL) technique. The model is also used to predict the thermal history and material flow in the FSW of aluminium alloy AA6082. The numerical results showed a good agreement with the experimental results.

List of publications

1- Omar S. Salih, Hengan Ou, W. Sun and Graham McCartney, 2015. A review of friction stir welding of aluminium matrix composites. Materials & Design, 86, 61-71.

2- Omar S. Salih, Hengan Ou, Xingguo Wei and W. Sun, 2019. Microstructure and mechanical properties of friction stir welded AA6092/SiC metal matrix composite. Materials Science and Engineering: A, 742, 78-88.

3- Omar S. Salih, Hengan Ou and W. Sun. Effect of FSW parameters on the metallurgical behaviour and mechanical properties of AA6082-T6. (To be submitted).

4- Omar S. Salih, Hengan Ou and W. Sun. Fully coupled thermomechanical finite element analysis of friction stir welding of AA6082-T6. (In preparation).

5- Omar S. Salih, Hengan Ou and W. Sun. Comparative study on the effect of FSW parameters on the aluminium alloy and aluminium matrix composites. (In preparation).

Acknowledgements

I would like to thank my supervisors, Associate Prof. Hengan Ou and Prof. Wei Sun for their guidance, support, expertise and their patience during this work. It is my pleasure to have an opportunity to work with them. I would like also to thank my internal assessors, Prof. Graham McCartney for the feedback during my progression assessments and Prof. Adib Becker.

I would like to express my gratitude to the Iraqi Ministry of Higher Education and Scientific Research (IMHESR), Middle Technical University for the research scholarship. This work was also supported by the Engineering and Physical Science Research Council (EPSRC) of UK (EP/L02084X/1 - EP/L022494/1) and the University of Nottingham, and International Research Staff Exchange Scheme (IRSES, MatProFuture project, 318,968) within the 7th European Community Framework Programme (FP7).

I would like to especially thank the staff members of Nanoscale and Microscale Research Centre (NMRC), particularly Dr Nigel Neate, Mr Martin Roe, Dr Christopher Parmenter, Dr Elisabeth Steer, and Dr Karen Alvey for their support and providing access to instrumentation through my experimental work. I would like to extend my thanks to the technicians in the L3 workshop and Wolfson laboratory.

I also acknowledge the support of TWI Technology Centre (Yorkshire), and the Science and Technology Facilities Council (STFC) ISIS Neutron and Muon (Oxford) for this research, especially Dr Xingguo Wei., and Dr Joe Kelleher.

It is a great pleasure to thank my former and present colleagues in the Structural Integrity and Dynamics (SID) group who were always helpful and provided a comfortable research environment.

I would like to express my love and gratitude to my parents, my sister, and my brothers for their support. Finally, I owe sincere and earnest thankfulness to Ruqaya, my wife, and Farah and Sarah my daughters. I cannot find words to express how grateful I am for their love and support. Words fail me.

ABBREVIATIONS

2D	Two-Dimensional
3D	Three-Dimensional
ALE	Arbitrary Lagrangian-Eulerian
Al-Mg-Si	Aluminum-Magnesium-Silicon
AMCs	Aluminium Matrix Composites
AS	Advancing Side
AWS	American Welding Society
BM	Base Metal
BSE	Backscattered Electron
CAGR	Compound Annual Growth Rate
CCD	Coupled Charge Device
CDR	Continuous Dynamic Recrystallisation
CEL	Coupled Eulerian-Lagrangian
CFD	Computational Fluid Dynamics
DIC	Digital Image Correlation
DR	Dynamic Recovery
EBSD	Electron-Backscattered Diffraction
EBW	Electron Beam Welding
EDM	Electrical Discharge Machine
EDS	Energy Dispersive X-ray Spectroscopy
El	Elongation
EVF	Eulerian Volume Fraction
F	Axial Force
FE	Finite Element
FEG	Field Emission Gun
fs	Shear force
FSP	Friction Stir Processing
FSW	Friction Stir Welding
FSZ	Friction Stir Zone
ft	Tensile force
GNDs	Geometrically Necessary Dislocations
GTAW	Gas Tungsten Arc Welding
HAGBs	High-Angle Grain Boundaries
HAZ	Heat Affected Zone
HCF	High Cycle Fatigue
Ir	Infrared Reading
J-C	Johnson-Cook
LAGBs	Low-Angle Grain Boundaries
LBW	Laser Beam Welding
LCF	Low Cycle Fatigue
LD	Longitudinal Direction

LMIS	Liquid Metal Ion Source
MMCs	Metal Matrix Composites
ND	Normal Direction
Nf	Number of Cycle to failure
NZ	Nugget Zone
PAW	Plasma Arc Welding
PD	Pin Diameter
PS	Plastic Slip
Pt	Platinum
PWHT	Post Weld Heat Treatment
R	Shoulder Radius
RP	Reference point
RS	Retreating Side
SAED	Selected Area Electron Diffraction
SAMC	Sandwich Aluminium Matrix Composite
SD	Shoulder Diameter
SD	Slip Direction
SEM	Scanning Electron Microscopy
SFE	Stacking Fault Energy
SHPB	Split Hopkinson Pressure Bar
SP	Slip Plane
SR	Static Recovery
SRC	Static Recrystallisation
SS	Slip System
SSSS	Super-Saturated Solid Solution
t	Plate Thickness
T	Temperature
TC	Thermocouple
TD	Transverse Direction
TEM	Transmission Electron Microscopy
TIG	Tungsten Inert Gas
TMAZ	Thermo-Mechanically Affected Zone
TOF	Time-of-Flight
TWI	The Welding Institute
TZ	Transition Zones
UTS	Ultimate Tensile Strength
V	Traverse Speed
WD	Welding Direction
WP	Weld Pitch
YS	Yield Stress
Z	Zenner-Hollomon parameter

NOMENCLATURES

$\dot{\varepsilon}_o$	Reference strain rate
D^A	Area-weighted mean size
D^N	Arithmetical mean size
T_m	Melting temperature
T_o	Reference temperature
d_o	Strain-free lattice spacing
q_o	Net Power
$\dot{\varepsilon}$	Strain rate
σ_o	Mises flow stress
τ_R	Critical resolved shear stress
θ	Lattice rotation
E	Young's modulus
P	Pressure
Q	Activation energy
d	Lattice parameter spacing
v	Poisson's ratio
ε	Equivalent plastic strain
μ	Friction Coefficient
ω	Rotation Speed

Table of contents

Chapter 1 Introduction 1

1.1 Background and motivation 1

1.2 Research challenges 3

1.3 Aims and objectives 4

1.4 Thesis contributions 5

1.5 Thesis structure 6

Chapter 2 Literature review 8

2.1 Introduction 8

2.2 Friction stir welding (FSW) 9

2.3 FSW tool design 10

2.3.1 FSW tool types 11

2.3.2 Shapes and dimensions of FSW tool shoulder 11

2.3.3 Shapes and dimensions of FSW tool pin 13

2.4 Metal matrix composites (MMCs) 14

2.5 Weldability of aluminium alloys and AMCs 15

2.6 Macrostructure and microstructure of FSW joints in AMCs 18

2.6.1 Macrostructure of AMC joints 19

2.6.2 Microstructure of AMC joints 23

2.7 Mechanical properties of FSW joints in AMCs 25

2.7.1 Microhardness of AMC joints 25

2.7.2 Tensile strength of AMC joints 27

2.7.2.1 Effect of tool design 29

2.7.2.2 Effect of welding parameters 30

2.7.2.3 Effect of other factors 33

2.7.3 Fatigue strength of AMC joints 34

2.8 Tool wear in FSW of AMCs 36
2.9 FSW of aluminium alloy AA 6082 41
2.10 Conclusions and future challenges 43

Chapter 3 Materials and experimental work 46

3.1 Introduction 46
3.2 Materials 46
3.3 Friction stir welding 49
3.3.1 Friction stir welding fixture 49
3.3.2 Friction stir welding tool design and machine setup 49
3.3.3 Design of friction stir welding experiments 51
3.3.4 Measuring welding temperature and thermal history 55
3.4 Metallurgical inspection 59
3.4.1 Optical microscope and Scanning Electron Microscopy (SEM) 59
3.4.2 Electron Backscattered Diffraction (EBSD) 59
3.4.3 Transmission Electron Microscope (TEM) 60
3.5 Mechanical testing 63
3.5.1 Hardness testing 63
3.5.2 Tensile testing 63
3.5.3 Low cycle fatigue (LCF) testing 66
3.6 Residual stress measurement 68
3.6.1 Overview of instrument 68
3.6.2 Samples 70
3.6.3 Measurement set-up 71
3.6.4 Data analysis of neutron measurements 73
3.7 Summary 74

Chapter 4 Thermal history and metallurgical characterisations of AA 6082, AMC, and SAMC FSW joints 75

4.1 Introduction 75
4.2 Aluminium alloy AA 6082-T6 76
4.2.1 Welding temperature and thermal history 76
4.2.2 Metallurgical characterisations of the as-received AA 6082 78
4.2.3 Metallurgical characterisations of AA 6082 FSW joints 83
4.2.3.1 Macrostructure and surface morphologies of the weldment 83
4.2.3.2 Microstructure evolution in AA 6082 FSW joints 87
4.2.3.3 Grain texture in AA 6082 FSW joints 94
4.2.3.4 Strengthening precipitate in AA 6082 FSW joints 96
4.3 Aluminium matrix composite AA 6092/SiC/17.5p-T6 98
4.3.1 Welding temperature and thermal history 98
4.3.2 Metallurgical characterisations of the as-received AMC 103
4.3.3 Metallurgical characterisations of AMC FSW joints 105
4.3.3.1 Macrostructure and surface morphologies of the weldment and FSW tool 105
4.3.3.2 Microstructure evolution in AMC FSW joints 110
4.4 Sandwich aluminium matrix composite AA 6061B/SiC/20p-T1 115
4.4.1 Welding temperature and thermal history 115
4.4.2 Metallurgical characterisations of the as-received SAMC 118
4.4.3 Metallurgical characterisations of SAMC FSW joints 120
4.4.3.1 Macrostructure and surface morphologies of the weldment 120
4.4.3.2 Microstructure evolution in SAMC FSW joints 125
4.5 Analysis and discussion of results 129
4.5.1 Effect of FSW parameters on the heat input and thermal cycle 131
4.5.2 Effect of thermal history on the metallurgical characteristics of FSW joints 135
4.5.2.1 Influence of FSW parameters on the macrostructural characterisation 135
4.5.2.2 Influence of FSW parameters on the microstructural characterisations 137

4.5.2.3 Influence of thermal history on the strengthening precipitate 142
4.6 Summary 143
Chapter 5 Mechanical characterisations and residual stresses of AA 6082, AMC, and SAMC FSW joints 145
5.1 Introduction 145
5.2 Microhardness distribution 146
5.2.1 Microhardness distribution in AA 6082 FSW joints 146
5.2.2 Microhardness distribution in AMC FSW joints 148
5.2.3 Microhardness distribution in SAMC FSW joints 150
5.3 Monotonic tensile properties 151
5.3.1 Tensile properties of AA 6082 FSW joints 151
5.3.2 Tensile properties of AMC FSW joints 154
5.3.3 Tensile properties of SAMC FSW joints 156
5.4 Low cycle fatigue properties of FSW joints 157
5.4.1 Fatigue life of FSW joints 159
5.4.2 Cyclic deformation response and hysteresis loop of the base materials and FSW joints 163
5.4.3 Cyclic stress-strain curves 172
5.5 Residual stresses 175
5.6 Analysis and discussion of results 179
5.6.1 Hardness profile of friction stir welded joints 182
5.6.2 Tensile property of FSW joints 184
5.6.3 Microstructure evolution induced fatigue life of FSW joints 190
5.7 Summary 194
Chapter 6 Finite element simulation of friction stir welding 196
6.1 Overview 196

6.2 Introduction 197
6.3 Finite element (FE) modelling 202
6.3.1 FE analysis 202
6.3.2 Geometrical definition 202
6.3.3 Material properties 204
6.3.4 Contact interaction and boundary conditions 206
6.3.5 Meshing and element type 209
6.4 Results and discussion 210
6.4.1 Temperature distribution 210
6.4.2 Material flow 214
6.4.3 Residual stresses 218
6.5 Summary 220

Chapter 7 Conclusions and future works 222

7.1 Introduction 222
7.2 Conclusions 222
7.2.1 Thermal history and metallurgical characterisations 222
7.2.2 Mechanical characterisation and residual stresses 224
7.2.3 Finite element simulation 226
7.3 Future works 227

References 229

Appendices 250

A. Thermal histories of AA 6082 FSW joints 250
B. Cyclic deformation response of AA 6082 and FSW joints 255
C. Cyclic deformation response of AMC and FSW joints 259
D. Cyclic deformation response of SAMC and FSW joints 263

Table of figures

Figure 2-1 Schematic drawing of FSW 10

Figure 2-2 Types of FSW tool; (a) Fixed, (b) Adjustable, and (c) Self-reacting [23] 11

Figure 2-3 Shoulder shapes and features [23] 12

Figure 2-4 (a) Tool shoulder and pin (probe) diameters versus plate thickness, and (b) Relation between tool shoulder and pin diameters [23] 12

Figure 2-5 Pin shapes and features [23] 13

Figure 2-6 Global demand for MMCs [29] 14

Figure 2-7 Reinforcement types; (a) Fibres, (b) Whiskers, and (c) Particles [19] 15

Figure 2-8 Trapped porosity [34] 16

Figure 2-9 Centre-line cracks in AA 6082 plate /4043 filler metal TIG weld [34] 17

Figure 2-10 Optical micrograph of a fusion weld by LBW on AA 6061/Al_2O_3/20p [37] 18

Figure 2-11 Optical micrograph of a fusion weld by LBW on AA 2124/SiC/20w [37] 18

Figure 2-12 Cross-sectional macrostructure of FSW AA 2009/SiC/17p joint [38] 19

Figure 2-13 Nugget zone shape; (a) Basin, and (b) Elliptical [15] 20

Figure 2-14 Optical micrographs of onion ring in FSW AA 6061/Al_2O_3/20p [44] 21

Figure 2-15 Partial appearances of onion ring in cross-section of AA 6063/B_4C/10.5p welded by FSW [47] 21

Figure 2-16 Tunnel defect in cross-section morphology of an AA 6061/AlN/10p joint welded in 1,200 rpm and 85 mm/min [50] 22

Figure 2-17 Reorientation of reinforcement in FSW AA 2124/SiC/20w [37] 24

Figure 2-18 Microhardness profile across the weld region of AA 6061/SiC/10p at different heat input [51] 26

Figure 2-19 Microhardness profile across the weld region of AA 2124/SiC/25p [45] 27

Figure 2-20 Hysteresis loops at different strain amplitudes for AA 6061/Al_2O_3/20p; (a) FSW joints, and (b) Base metal [44] 34

Figure 2-21 Fatigue failures in the FSW AA 6061/Al_2O_3/22p; (a) stirred FSW zone, and (b) Out of the FSW zone [54] 35

Figure 2-22 (a) through (d) Wear features of FSW tool pin at different weld distance (in meters) and constant tool rotation speed of 1000 rpm at different traverse speeds: a. 1, b. 3, c. 6, and d. 9 mm/s, (e) Wear rate versus weld length at different traverse speed, and (f) Wear rate versus weld speed [72] .. 38
Figure 2-23 Pin tool wear as a per cent of initial tool shape projections versus weld traverse distance for different tool rotation and traverse speeds [74] 39
Figure 3-1 Friction stir welding fixture 49
Figure 3-2 Geometry of FSW tool (dimensions in mm) 51
Figure 3-3 Effect of tilt angle and rotation direction on flash formations at a tool rotation speed of 1500 rpm and tool traverse speed of 75mm/min; (A) 0° tilt angle with clockwise rotation, and (B) 2° tilt angle with anticlockwise rotation 51
Figure 3-4 Conventional milling machine 53
Figure 3-5 Bespoke friction stir welding machine 54
Figure 3-6 (a) Illustration of friction stir welds and the positions of the thermocouples attached on the samples and the extraction of cross-weld testing sample locations are highlighted, and (b) The extraction of longitudinal tensile sample locations is highlighted (all dimensions in mm) 56
Figure 3-7 Photograph of the experimental setup and thermocouples locations 57
Figure 3-8 Infrared camera 58
Figure 3-9 Temperature gradients through FSW joint measured by thermocouples and infrared camera 58
Figure 3-10 SEM micrographs showing the stage of TEM samples preparation by FIB machine; (a) Platinum coating, (b through f) Sample extraction steeps, (g and h) Sample thinning 62
Figure 3-11 Tensile sample (all dimensions in mm) 64
Figure 3-12 Tensile with an extensometer 64
Figure 3-13 Tensile with DIC system 65
Figure 3-14 DIC tensile sample 65
Figure 3-15 LCF sample (all dimensions in mm) 67
Figure 3-16 Fatigue machine and anti-buckling 67
Figure 3-17 Low cycle fatigue buckling sample 67
Figure 3-18 ENGIN-X 69

Figure 3-19 (a) Plan view of the ENGIN instrument. The arrows marked ‘Q’ indicate the directions in which strain is measured by the two detectors, and (b) Schematic view of the ENGIN instrument [107] 70
Figure 3-20 Schematic drawing FSW sample measured by neutron diffraction the grey shaded area and red dot show the positions of measurement 71
Figure 3-21 (a) Sample position of ENGIN-X measurement, (b) Sample position to measure longitudinal strain, and (c) Sample position to measure traverse strain 72
Figure 4-1 Effect of FSW parameter on the peak temperature of AA 6082 FSW joints 76
Figure 4-2 Effect of FSW parameters on thermal history in the NZ of AA 6082 FSW joints 77
Figure 4-3 Thermal cycles on the RS and AS of W1, W5, W16, and W20 AA 6082 FSW joints 78
Figure 4-4 Microstructure characterisation of AA 6082; (a) EBSD map, (b) Grain size distribution, and (c) Misorientation angle 79
Figure 4-5 Pole figures of the as-received AA 6082 80
Figure 4-6 (a-d) TEM bright field micrographs in the as-received AA 6082, and (e-f) Related selected area electron diffraction (SAED) 82
Figure 4-7 EDS spectrum related to the TEM 83
Figure 4-8 Surface morphology and exit hole profile of AA 6082 FSW joints under different welding parameters (AS on the right) 84
Figure 4-9 Cross-weld macrostructure of AA 6082 FSW joints under different welding parameters (AS on the right) 85
Figure 4-10 Typical cross weld section macrostructure of AA 6082 FSW joint welded at 1100 rpm - 20 mm/min (W6) 86
Figure 4-11 Transition zone of the W1 joint cross-section; (a) AS, and (b) RS 88
Figure 4-12 EBSD maps obtained in the centre of NZ of AA 6082 under different FSW conditions. In the maps, HAGBs and LAGBs are depicted by black and red colour, respectively 90
Figure 4-13 Grain size distribution in the NZ of AA 6082 under different welding conditions 91
Figure 4-14 Effect of welding temperature on the grain size 92
Figure 4-15 Misorientation angle distribution in the NZ of AA 6082 under different welding conditions ... 93

Figure 4-16 Pole figures generated from EBSD maps of AA 6082 FSW joints; (a) {111} pole of the NZ, showing the variation in texture with welding parameters, and (b) {100} pole of the NZ for 1800 rpm tool rotation speed, showing the variation in texture with tool traverse speed 95
Figure 4-17 (a-c) TEM bright field micrographs in the HAZ, and (d) Selected area electron diffraction (SAED) 97
Figure 4-18 TEM bright field micrographs in NZ; (a and b) round precipitate, (c) Coarse precipitate B, and (d) Fine precipitate B 98
Figure 4-19 Effect of FSW parameters on the peak generated temperature in the NZ of AMC 99
Figure 4-20 Effect of FSW parameters on thermal history in the NZ of AMC 100
Figure 4-21 Thermal histories of AMC joints welded at a tool rotation speed of 1500 rpm and different tool traverse speed; (a) 25, (b) 50, and (c) 100 mm/min 101
Figure 4-22 Thermal histories of AMC joints welded at a tool rotation speed of 1800 rpm and different tool traverse speed; (a) 25, (b) 50, and (c) 100 mm/min 102
Figure 4-23 Thermal histories of AMC joints welded at a tool rotation speed of 2100 rpm and different tool traverse speed; (a) 25, (b) 50, and (c) 100 mm/min 103
Figure 4-24 Microstructure characterisation of AMC; (a) SEM image, (b) EBSD map, (c) Grain size distribution, (d) Misorientation angle, and (e) EBSD legend 105
Figure 4-25 Surface morphologies of AMC FSW joints under different welding parameters (AS on the right) 106
Figure 4-26 Cross-weld macrostructure of AMC FSW joints under different welding parameters (AS on the right) 107
Figure 4-27 EDS map and spectrum of AMC joint welded at 2100 rpm and 50 mm/min (W8) 107
Figure 4-28 Surface morphology of FSW tool; (a) Before welding, and (b) After welding 108
Figure 4-29 Typical cross-weld of AMC joint W5 (AS on the right) 109
Figure 4-30 (a) Typical onion ring microstructures in AMC FSW joint at the centre of NZ for W3 welds, and (b) Higher magnification from the indicated region in (a) 110
Figure 4-31 SiC distribution in the NZ of AMC joints under different welding conditions 111
Figure 4-32 Gradient in the grain size of the AMC cross-weld sample (W1) 112
Figure 4-33 EBSD images of grain morphology and the distribution of HAGBs (black line), and LAGBs (red line) under different welding conditions 113

Figure 4-34 Grain size distribution in the NZ of AMC joints under different welding conditions 114
Figure 4-35 Misorientation angle in the NZ of AMC joints under different welding conditions 114
Figure 4-36 Effect of FSW parameters on the peak temperature in the NZ of SAMC 115
Figure 4-37 Thermal histories of SAMC joints welded at a tool rotation speed of 1500 rpm and different tool traverse speed; (a) 25, (b) 50, and (c) 100 mm/min 116
Figure 4-38 Thermal histories of SAMC joints welded at a tool rotation speed of 1800 rpm and different tool traverse speed; (a) 25, (b) 50, and (c) 100 mm/min 117
Figure 4-39 Thermal histories of SAMC joints welded at a tool rotation speed of 2100 rpm and different tool traverse speed; (a) 25, (b) 50, and (c) 100 mm/min 118
Figure 4-40 Optical and SEM microstructure observed at the cross-section of SAMC 119
Figure 4-41 Microstructure characterisation of SAMC; (a) EBSD map, (b) Grain size distribution, and (c) Misorientation angle 120
Figure 4-42 Surface morphologies of SAMC FSW joints under different welding parameters (AS on the right) 121
Figure 4-43 Cross-weld macrostructure of SAMC FSW joints under different welding parameters (AS on the right) 122
Figure 4-44 EDS map and spectrum of SAMC joint welded at 1800 rpm and 50 mm/min (W5) 122
Figure 4-45 Typical onion ring microstructures of SAMC in the centre of NZ for W5 welds; (a) SEM, (b) Higher magnification from the indicated region in (a), and (c) Related EBSD map 124
Figure 4-46 SiC distribution in the NZ of SAMC joints under different welding conditions 125
Figure 4-47 EBSD images of grain morphology and the distribution of HAGBs (black line), and LAGBs (red line) under different welding conditions 127
Figure 4-48 Grain size distribution in the NZ of SAMC joints under different welding conditions 128
Figure 4-49 Misorientation angle in the NZ of SAMC joints under different welding conditions 128
Figure 4-50 Friction stir zone on the AS of the W6 SAMC FSW joint 129
Figure 4-51 Interaction diagram linking the experimental parameters with the physical parameters and joint characterisations, which are influence the weld quality 130
Figure 4-52 Relationship between peak temperatures and weld pitch at constant traverse and rotation speeds for different materials; (a) AA 6082, (b) AMC, and (c) SAMC 134

Figure 4-53 Relationship between peak temperatures and grain size for investigated materials; (a) AA 6082, (b) AMC, and (c) SAMC. [TTS: tool traverse speed] 139
Figure 4-54 Schematic variation of temperature and strain in the NZ of friction stir process [112] 140
Figure 4-55 Continuous dynamic recrystallisation. As deformation progresses, the serrated HAGBs (thick lines) become closer, although the subgrain size remains approximately constant [136] 142
Figure 5-1 Cross-weld microhardness profile of AA 6082 FSW joints with the measured temperature and microstructure at different tool rotation speed; (a) 800 rpm, and (b) 1800 rpm 148
Figure 5-2 Cross-weld microhardness profiles of AMC at a traverse speed of; (a) 25 mm/min, (b) 100 mm/min 149
Figure 5-3 Cross-weld microhardness profiles of SAMC at a traverse speed of; (a) 25 mm/min, (b) 100 mm/min 151
Figure 5-4 (a-d) Engineering stress-strain curves of AA 6082 FSW joints at various tool rotation speed; (a) 800, (b) 1100, (c) 1500, and (d)1800 rpm, respectively, including BM and weld line (W12-WL) ... 153
Figure 5-5 Bar graph compare among UTS, YS, and fracture elongations of AA 6082 BM, weld line (WL), and FSW joints 153
Figure 5-6 Tensile properties of AMC including BM, cross-weld under different welding conditions (w1-W9), and longitudinal weld (WL3); (a) Stress-strain curves, (b) Bar graphs representing strength and elongation, and (c and d) Fracture locations and DIC images of typical samples 155
Figure 5-7 Tensile properties of SAMC including the as-received BM, BM without aluminium layers, and cross-weld under different welding conditions (W1-W9); (a) Stress-strain curves, (b) Bar graphs representing strength and elongation 157
Figure 5-8 Total strain amplitude versus fatigue life of AA 6082 for BM and FSW joints 159
Figure 5-9 Total strain amplitude versus fatigue life of AMC for BM and FSW joints 160
Figure 5-10 Total strain amplitude versus fatigue life of SAMC for BM and FSW joints 160
Figure 5-11 Cyclic stress response under different strain amplitudes of the as-received AA 6082 and typical FSW joint (W7/1100 rpm – 40 mm/min) 164
Figure 5-12 Cyclic stress response under different strain amplitudes of the as-received AMC and typical FSW joint (W1/1500 rpm – 25 mm/min) 165
Figure 5-13 Cyclic stress response under different strain amplitudes of the as-received SAMC and typical FSW joint (W8/2100 rpm – 50 mm/min) 165

Figure 5-14 Hysteresis loops of the as-received AA 6082 and typical FSW joint (W7) at different strain amplitudes; (a) 0.35%, (b) 0.5%, and (c) 0.7% 169
Figure 5-15 Hysteresis loops of the as-received AMC and typical FSW joint (W1) at different strain amplitudes; (a) 0.3%, (b) 0.4%, and (c) 0.5% 170
Figure 5-16 Hysteresis loops of the as-received SAMC and typical FSW joint (W8) at different strain amplitudes; (a) 0.2%, (b) 0.3%, and (c) 0.5% 171
Figure 5-17 Typical saturated hysteresis loops at different total strain amplitude for AMC FSW joint fabricated at 1800 rpm and 100 mm/min (W6) joints 173
Figure 5-18 Comparison of cyclic and monotonic stress-strain curves for AA 6082; (a) As-received BM, and (c-d) FSW joints at 1100, 1500, and 1800 rpm, respectively 174
Figure 5-19 Comparison of cyclic and monotonic stress-strain curves for AMC; (a) As-received BM, and (c-d) FSW joints at 1500, 1800, and 2100 rpm, respectively 174
Figure 5-20 Comparison of cyclic and monotonic stress-strain curves for SAMC; (a) As-received BM, and (c-d) FSW joints at 1500, 1800, and 2100 rpm, respectively 175
Figure 5-21 The longitudinal (left) and transverse (right) residual stress measured at the mid-length position of FSW joint as a function of distance from the weld line for; (a) AA 6082, (b) AMC, and (c) SAMC (Retreating side on the left) 178
Figure 5-22 (a) Gradient in the grain size of cross-weld sample (W1), (b) Schematic illustration of the gradient in the grain size, (c) Slip due to the tensile component, (d) Slip due to the shear component, and (e) Effect of stored GNDs on the final deformation 181
Figure 5-23 Tensile strength of FSW joints versus mean grain size in the nugget zone; (a) AA 6082, (b) AMC, and (c) SAMC 186
Figure 5-24 Fatigue life of FSW joints versus mean grain size in the nugget zone; (a) AA 6082, (b) AMC, and (c) SAMC 193
Figure 6-1 FSW geometry definition; (a) Eulerian domain (plate), and (b) FSW tool profile 203
Figure 6-2 Velocity boundary conditions in the plunge steep 208
Figure 6-3 Velocity boundary conditions in the welding steep 208
Figure 6-4 Mesh of Eulerian domain and FSW tool 209

Figure 6-5 Typical cross-weld temperature distributions of W5 FSW joint at different time (sec) during plunge step; (a) 0, (b) 0.25, (c) 1, (d) 1.5, (e) 1.8, and weld steep (f), 9.4 (AS on the right, Temperature in °K) 211
Figure 6-6 Cross-weld thermal history of W5; (a) Experimentally measured temperature, (b) Comparison between experimental and FE model solution 213
Figure 6-7 Cross-weld thermal history of W10; (a) Experimentally measured temperature, (b) Comparison between experimental and FE model solution 213
Figure 6-8 Cross-weld equivalent plastic strain distributions of W5 FSW joint at plunge step at a different time (sec); (a) 0.25, (b) 1, (c) 1.5, and welding steeps (d) 9.4 (AS on the right) 215
Figure 6-9 Longitudinal weld cross section of W5 FSW joint 215
Figure 6-10 Plastic strain distribution during the welding step 216
Figure 6-11 Comparison between the experimental an FE formed void, (a) W5, and (b) W10 217
Figure 6-12 Surface morphology of W5 FSW joint 218
Figure 6-13 Residual stresses of W5 FSW joint as functions of position relative to the weld centreline; (a) Longitudinal, and (b) Transverse 220

Chapter 1 Introduction

1.1 Background and motivation

Lightweight and high-performance materials are of vital importance to such as automotive, marine and aerospace industries. These industries have a set goal of reducing the weight of their components so that better fuel economy and increased payload capacity can be achieved, and greenhouse gases emission policies can be met [1]. One way to achieve weight reduction with keeping the design to maximum performance is through the using of advanced lighter materials [2]. Aluminium alloys have relied primarily instead of the heavy alloys on these industries. In the last few years, the development of advanced materials in particular metal matrix composites (MMCs), has opened the door to even lighter structures. MMCs possess a wide range of properties, and these have led to introducing it gradually as an alternative to high strength aluminium alloys in aero-engines and aerospace structures in particular components, such as the Space Shuttle Orbiter, the Hubble Space Telescope, and communications satellites [3-6]. The industry will continue its push for lighter materials, particularly MMCs, which require advanced welding technique such as friction stir welding (FSW).

FSW process is a relatively new solid-state welding technique invented by The Welding Institute (TWI) in the early 90's. In this process, the joint takes place in the solid phase below the melting point of the materials to be joined. Thus, all the problems related to the solidification of molten material are avoided. Since its invention, the FSW process has attracted worldwide interest [7]. This process was first used to weld the super lightweight external tank for the Space Shuttle at NASA [8]. Currently, this process is considered a mature process for joining all aluminium alloys, many of which are considered difficult or non-weldable by using conventional fusion welding processes [9, 10]. The

automotive, transport and aerospace industries are currently the main users of this welding process, and some examples are presented in Table 1-1 [1, 11, 12]. Furthermore, it is used to join structural components of the Falcon IX rockets, Delta IV, and Atlas V, as well as, the Orion Crew Exploration Vehicle [2]. The global FSW market is projected to reach USD 885.55 million by 2024 from USD 510.8 million in 2016, exhibiting a compound annual growth rate (CAGR) of 7.12 % during 2016-2024 [13].

Therefore, there is a need to extend the current focus of the FSW process to MMCs, because the size of MMCs components is severely limited by difficulties encountered in joining these materials using conventional fusion processes. Efficient joints regarding strength cannot be achieved by fusion based welding methods due to the reaction between reinforcements and matrices leading to the formation of undesirable phase, which leaves a depleted strength region along the joint line [6, 14]. With respect to welding processes, it has been proven by several studies that more efficient joints with much-reduced porosity, cracking, distortion, and reinforcement dissolution can be achieved when FSW is adopted.

Table 1-1 Examples of the welded components by FSW in different industries [2, 15-17]

Industry	Examples
Automotive	Brake rotors Space frame Cradles in chassis or engine Fuel tank Truck body
Marine	Sailing boats Landing platforms Panels for decks
Railway	High-speed trains Container bodies
Aerospace	Fuselage and wings Fuel tanks Rocket Military aircraft

1.2 Research challenges

Aluminium matrix composites (AMCs) have emerged as a class of MMCs which offer a number of potential benefits for advanced applications, due to their tailored mechanical, physical, and thermal properties that include low density, high thermal conductivity, low coefficient of thermal expansion, high specific stiffness, good dimensional stability, and excellent strength to weight ratio [18, 19]. The properties of AMCs reflect their status as prime materials for use in the aerospace structures. However, weldability is the primary barrier to their widely spread in the aerospace industry. Several challenges remain in using FSW to join AMCs even with considerable progress having been made in recent years.

Currently, there are a minimal amount of the existing data in term of tensile strength and fatigue life of AMCs FSW joints, and even less information about the optimum process parameters. This can be related to the mechanical microstructural complexity of the process and the relatively large number of process parameters (traverse and rotation speeds, tool design, and applied force) that could influence the properties of joints. Also, it appears from the literature that there is a lack of detailed understanding on the effect FSW parameters, such as tool rotation and traverse speeds on the thermal history, microstructure evolution, residual stresses and its impacts on the structural properties of FSW joints, in particular, tensile and low cycle fatigue behaviour.

Furthermore, until today, there has been no work carried out to investigate the applicability of FSW to weld AMC (AA 6092/SiC/17.5p-T6) and Sandwich aluminium matrix composite (SAMC) (AA 6061B/SiC/20p-T1). These materials are attractive for many industries such as aerospace and automotive. The welding of these materials is technically challenging due to the existence of hard reinforcement particles (SiC) and low ductility, which leads to reducing the flowability of softened material during the welding

process and consequently effect on the joint soundness. Therefore, there is a clear need to examine the feasibility of FSW to join AMCs.

1.3 Aims and objectives

The aim of this work is to establish a fundamental understanding of microstructural changes and mechanical properties of the FSW components, with a particular focus on the 6xxx series as aluminium alloy and composite aluminium. This primary research aim is supported by achieving the following research objectives:

- Improved understanding of the effect of FSW parameters on the thermal history and microstructural changes.
- Determination of the main microstructural factors that control the local mechanical properties.
- Development of interactive relations between the quality of weldments and the FSW parameters, i.e., tool rotation and traverse speeds.
- Assessment of the feasibility of joining AMCs using FSW process.
- Clarify the residual stress state in friction stir butt welds Al and AMCs as a function of varying process parameters.
- Detailed finite element (FE) simulation to predict the welding temperature, residual stresses and materials flow in the FSW of aluminium alloy.

The microstructural investigations in this project were performed using optical, Scanning Electron Microscopy (SEM), Electron-backscattered diffraction (EBSD), and Transmission Electron Microscopy (TEM). Microhardness, tensile and low cycle fatigue (LCF) testing was used to characterise the structural properties of FSW joints. The obtained results are elucidated in the light of the interaction between the welding parameters and based on the existing theoretical background. Finally, simulation of the FSW process was carried out using the ABAQUS software.

1.4 Thesis contributions

The ultimate goal of this thesis is to extend the usability of Al and AMCs to aerospace structures, an outcome which can only be achieved by solving the problem of weldability, specifying the suitable welding windows, and improving the quality of weldments. The contribution of this thesis can be summarised as follows:

- For the first time, FSW has been used to weld two new materials namely AMC (AA 6092/SiC/17.5p-T6) and SAMC (AA 6061B/SiC/20p-T1). Also, aluminium alloy AA 6082-T6 has been investigated.
- A parametric study for each material with a goal to cover a wider range of FSW parameters, i.e. tool rotation and traverse speeds, has been done followed by a comprehensive joints characterisation in term of the evolved microstructures and mechanical properties.
- Identification of the defect formation in FSW joints, its relationship with FSW parameters and its effect on tensile strength.
- This thesis serves as a starting point to improve the understanding of the interrelationship between the process parameters and mechanical properties of FSW joints. This is accomplished by looking into the basic physics of how the experimental parameters influence the physical mechanisms. Knowledge of these interrelations is required to develop process maps that could be used to predict optimised weld conditions to produce high weld quality.
- Advancement of tool surface heat treatment which prevents and/or mitigates the wear of FSW tool.
- Develop finite element based model which can predict the amount of heat input, material flow and residual stresses based on the process parameters and material properties.

- This work is undertaken as a first step in providing essential information that will assist the manufacturing industry to make sound decisions concerning selecting FSW parameters for weldable structural alloys.

1.5 Thesis structure

This thesis is presented in seven chapters with the main content of each chapter summarised as follows:

Chapter 1 gives a general background and motivation of the need for lightweight materials and FSW process followed by some examples of industrial applications. Also, particular attention paid to the research challenges of FSW of Al-alloy and AMCs, the aims and objectives of the research, and the contribution of this work.

Chapter 2 provides a detailed review of the current state-of-the-art of the FSW process in order to summarise the current understanding of the subject and highlight areas where further research is needed.

Chapter 3 presents a detailed description of the experimental techniques utilised in this project, including the candidate material and its properties, FSW setup, welding temperature measurements, microstructural characterisation, mechanical testing, and residual stresses measurements.

Chapter 4 presents a parametric study to examine the effects of FSW parameters on the thermal histories and metallurgical characterisations of Al alloy and AMCs with a detailed discussion of the microstructural development in the various welds.

Chapter 5 studies the mechanical characterisations and residual stresses of Al alloy and AMCs; the obtained results are analysed based on the obtained microstructural results in Chapter 4.

Chapter 6 presents the FE simulation of FSW of aluminium alloy. Also, this chapter provides a comparison between the results obtained from FE simulation and corresponding experimental measurements for validation.

Chapter 7 is the last chapter which summarises the conclusions of this work and outlines possible recommendations for future studies.

Chapter 2 Literature review

2.1 Introduction

Aluminium alloy and advanced materials like aluminium matrix composites (AMCs) have attracted considerable attention due to their appealing mechanical properties and a clear potential for transportation and aerospace applications. They are thus viewed as an ideal candidate as a new generation of lightweight and high strength materials. However, the implementation of AMCs is restricted, and it is not widely used in the aviation industry, in part because of the difficulties that are related to the welding of these metals by conventional welding processes. FSW is a relatively new solid-state joining technology process, which makes the process promising for joining AMCs and produce more efficient joints with much-reduced defects and reinforcement dissolution. However, FSW of AMCs has yet to be fully implemented to mainstream high-value manufacturing industries due to a number of challenges, all of which are directly related to FSW process parameters and the nature of the base materials.

This chapter aims to provide a detailed review of the current state-of-the-art of FSW of aluminium alloy and AMCs, and it is structured as follows: firstly gives a description on the FSW process, tool design, metal matrix composites (MMCs), and the weldability of aluminium alloys and AMCs in Sections 2.2 to 2.5. This is followed by a detailed evaluation of a number of critical issues in FSW of AMCs focusing on the macrostructure and microstructure, mechanical properties of AMC joints, as well as tool wear in Sections 2.6 to 2.8. Section 2.9 reviewed the work that has been done in FSW of aluminium alloy AA 6082. Finally, conclusions are drawn with a particular view on future challenges and research directions.

2.2 Friction stir welding (FSW)

The invention of the FSW process in 1991 was made by The Welding Institute (TWI) in the United Kingdom as a solid-state joining process for joining aluminium alloys [20]. The peak welding temperature can be limited to 80% of the melting temperature of the base metal. Therefore, this process can be considered a hot working process. As FSW has been widely used to join aluminium alloys, it may be developed as a viable route to join AMCs especially for high strength non-weldable series (AA 2xxx, AA6 xxx, and AA 7xxx), which are susceptible to solidification cracking in the weld zone and liquation cracking in the heat affected zone (HAZ) [21]. Dissimilar joints of AMCs or with different metals can be manufactured by using FSW without concerns for composition compatibility, which is an essential consideration in fusion welding to avoid solidification cracking [15].

FSW is an ideal process for producing low cost and high-performance joints. The practical approach of FSW is to use a non-consumable rotating tool consisting of two parts including a shoulder and a pin. During FSW the pin is inserted into the faying surface of the plates and then moved horizontally in the direction of the joint line as shown in Figure 2-1. The surface of the tool has dual actions for heat generation and mechanical sweeping of softened metal. The heat input through the frictional action between the tool and workpiece leads to softening of the area around the pin. Meanwhile, the softened materials are swept in the form of severe plastic deformation from the advancing side (AS) to the retreating side (RS) to form a solid-state joint. The advancing and retreating sides of the plates to be joined are defined by the direction of tool rotation (clockwise or anti-clockwise) and the traverse movement of the tool. Plate side is defined as advancing if the tool movement is in the same direction of the tool rotation, whilst it is retreating if the tool moves in the opposite direction (see Figure 2-1). Different types of joints like butt, lap, and T-joints can be welded successfully by FSW [15, 22, 23].

Moreover, FSW is considered as a green and environmentally friendly welding technology because of low energy consumption, no gas emission, and no need for consumable material such as electrodes, filler metals, and shielding gases (normally present in fusion welding processes). A survey carried out by the American Welding Society (AWS) in 2002 showed that $34.4 billion per year is spent on arc welding including the use of consumables, repair, and energy consumption in the USA. The adoption of FSW has increased rapidly, and 10% of joining processes have reportedly been replaced by FSW [24].

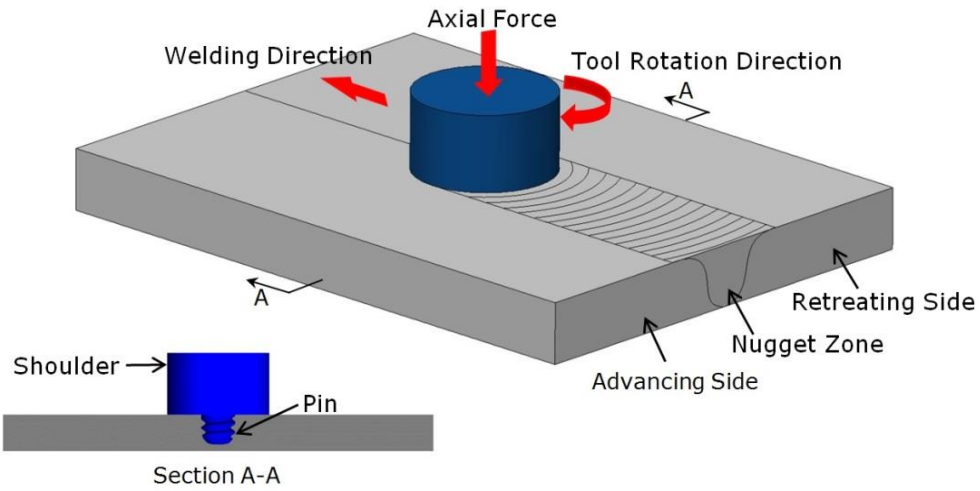


Figure 2-1 Schematic drawing of FSW

2.3 FSW tool design

Each part of the FSW tool (shoulder and pin) has a particular function. The rate of heat generation, the flow of plasticised metal, and rotational and linear motion are experienced by tool geometry. The use of a proper FSW tool design is the crucial factor in ensuring a high-quality welding joint. Three main criteria should be considered when designing FSW tools which are tool types, shoulder shapes and dimensions, and pin shapes and dimensions [23, 25-27].

2.3.1 FSW tool types

FSW tools can be classified into three types, fixed, adjustable, and self-reacting (bobbin) tool as shown in Figure 2-2. The first one is used for constant base metals thickness, while the second one is used for a range of thickness and both of them can work with a tilt angle. On the other hand, the self-reacting tool is used for different thickness without needing for the backing plate and cannot work with tilt angle [23].

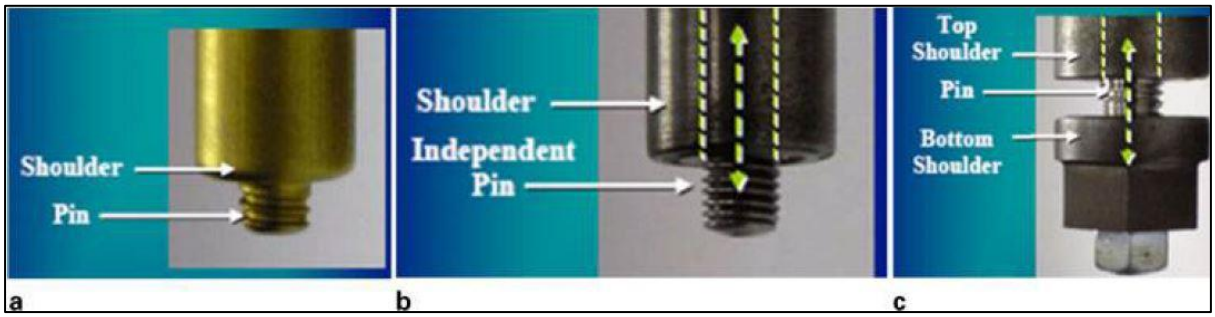


Figure 2-2 Types of FSW tool; (a) Fixed, (b) Adjustable, and (c) Self-reacting [23]

2.3.2 Shapes and dimensions of FSW tool shoulder

Heat generation, forging action to consolidate welding, and heat concentration in the NZ are the main purposes of tool shoulders. The net power (q_o) during the welding process can be calculated based on the equation ($q_0 = 4/3\ \pi^2 \mu\ P\ \omega\ R^3$), where ($\mu$): friction coefficient, (P): pressure (MPa), (ω): rotation speed (rev/min), and (R): shoulder radius (mm). According to Zhang et al. [23] and Fuller, C.B. [25] tool shoulders consists of three parts; outer surface, end surface, and end surface features as shown in Figure 2-3. Firstly, the outer surface of shoulder is either cylindrical or conical, which does not affect significantly on the weld quality due to the shallow plunge depth (1-5% of plate thickness). Secondly, flat, convex, and 6-10°concave is the main shoulder end. Metal flash and removal from the welding zone during FSW are the main limitations of flat and convex shoulders respectively. While concave shoulders with 6-10° angle are leading to trapping the flow of stirring metal under the end of the shoulder effectively. Finally, the end surface of the shoulder can have features such as scroll, grooves, and circles to increase the mixing

process and the amount of deformed materials. Shoulder diameter (SD) can be calculated based on the equation $(SD = 2.2\,t + 7.3)$, where t: plate thickness or from Figure 2-4 (a) [23].

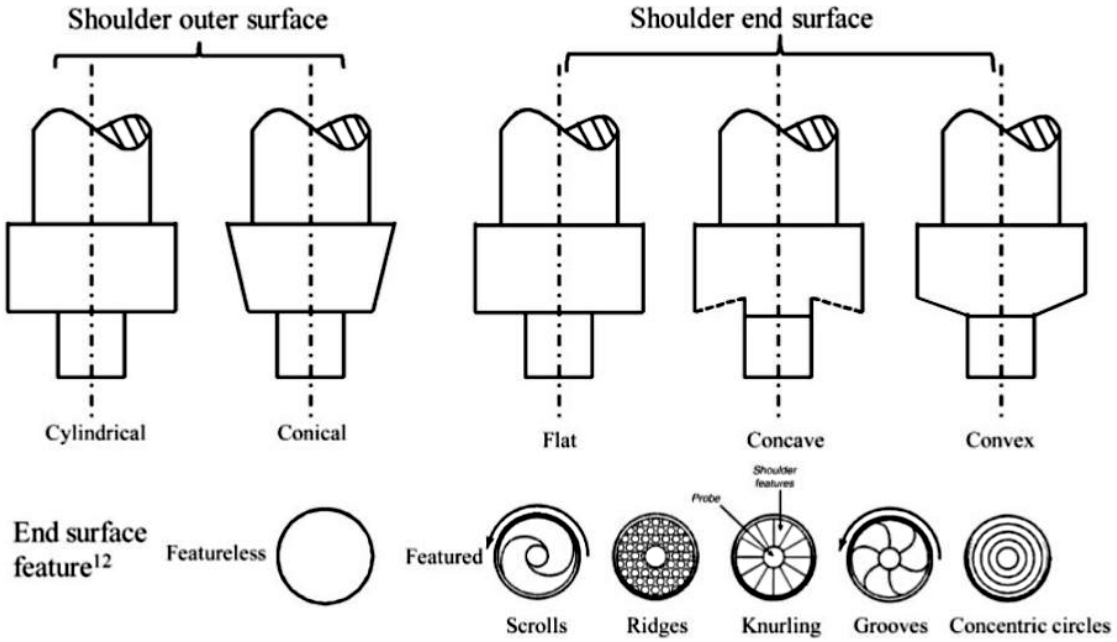


Figure 2-3 Shoulder shapes and features [23]

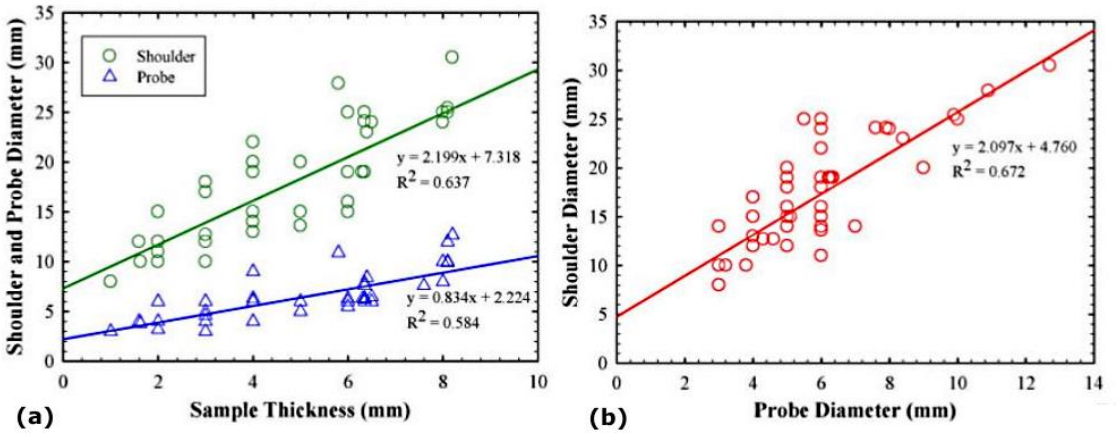


Figure 2-4 (a) Tool shoulder and pin (probe) diameters versus plate thickness, and (b) Relation between tool shoulder and pin diameters [23]

2.3.3 Shapes and dimensions of FSW tool pin

The shape of tool pin influences the flows of plasticised materials and disruption of the faying surfaces. It is designed to shear the material facing the tool and move it behind the tool. Figure 2-5 shows the shape of the pin and their major features. Dome or flat is the main shape of pin end. Domed shape is used to reduce the plunging force (stress concentration), tool wear, and improve the quality of the joints. Best results are achieved when the dome radius is 75% of the pin diameter. The thickness of plate influences the shape of the pin, i.e. the cylindrical probe is used for up to 12 mm plate thickness. In contrast, a tapered pin is used for thicker materials, which needs more plastic deformation. The pin diameter (PD) can be calculated from equation ($PD = 0.8\,t\, + 2.2$), where (t): plate thickness or from Figure 2-4 (a) [23, 25, 27, 28].

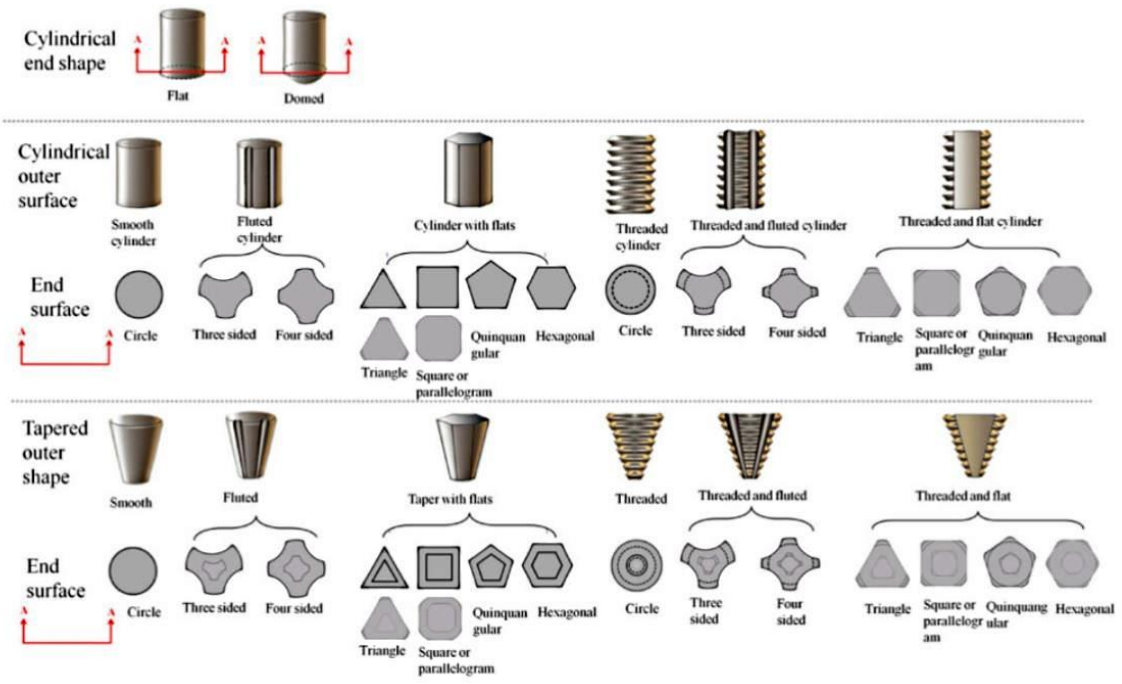


Figure 2-5 Pin shapes and features [23]

2.4 Metal matrix composites (MMCs)

In recent years, MMCs have attracted considerable attention for critical applications in industrial sectors such as spacecraft structures, deck panels, and automotive and railway brake discs. The global demand for MMCs is expected to increase from about 5,496 tons to nearly 8,000 tons in the period from 2012 to 2019, and it is continuously rising as shown in Figure 2-6 [29].

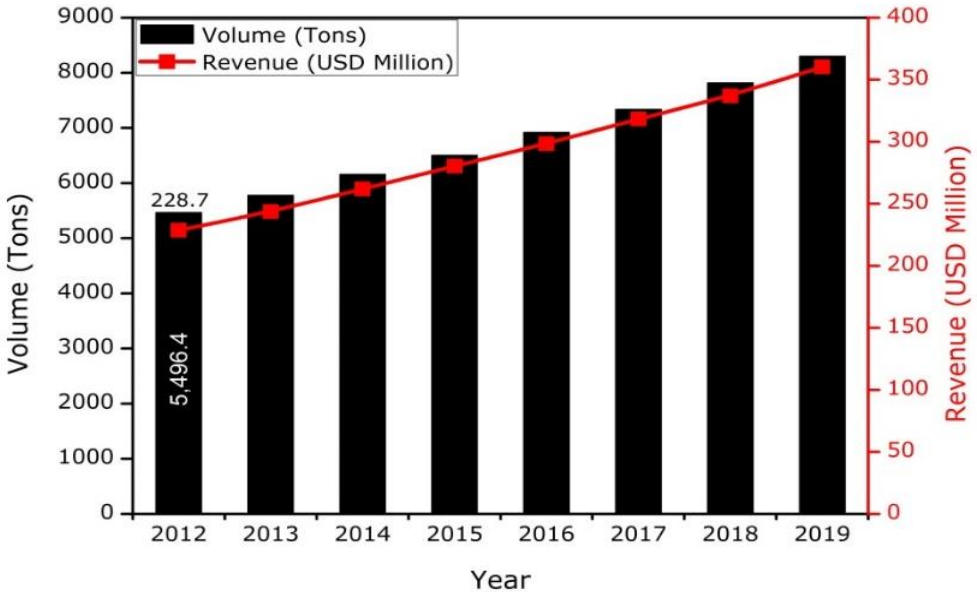


Figure 2-6 Global demand for MMCs [29]

Light metals like aluminium, magnesium, and titanium alloys are considered as ideal base matrices to produce MMCs reinforced by carbide, nitride, boride, and oxide in the form of particles, whiskers, and fibres [30] as shown in Figure 2-7 [19]. MMCs can possess unique properties including good thermal conductivity, low coefficient of thermal expansion, low specific density, high specific stiffness, good dimensional stability, and excellent strength to weight ratio depending on the type of reinforcements used [6, 31, 32]. As a result of these desirable properties, MMCs have been used to withstand excessive space environmental condition of substantial changes in temperature. For example, the

International Space Station is exposed to varying temperatures from +125°C to -125 °C as it orbits around the earth [33].

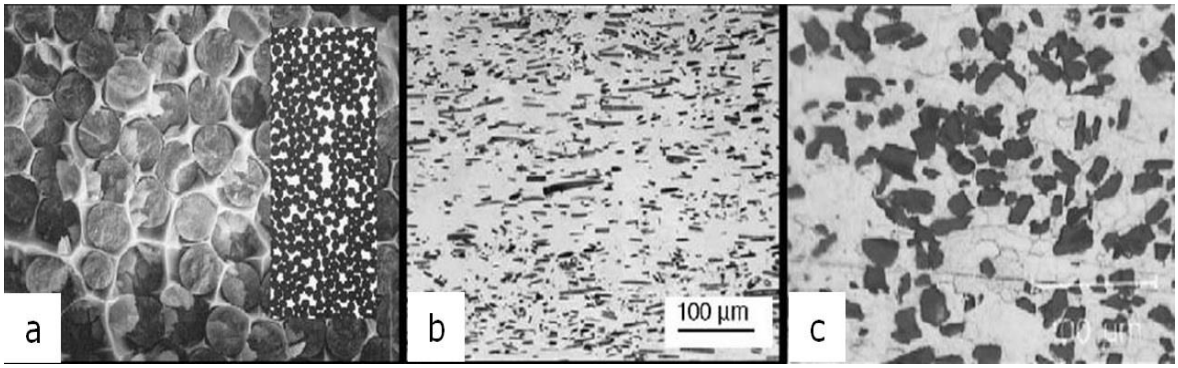


Figure 2-7 Reinforcement types; (a) Fibres, (b) Whiskers, and (c) Particles [19]

As a versatile material, AMCs may be selected as an alternative to high strength aluminium alloys in aerospace structures like fins, wings, and fuselage. In 2001 NASA used composite aluminium Al-Li 2195 rather than aluminium alloy Al 2219 for the external fuel tank of space shuttles leading to a reduction of weight by 3,400 kg. This saving in weight increases the cargo capacity of space shuttles and enables it to transport more than one components in a single flight to the International Space Station [2]. Also, the use of B/Al in truss and frame of aeroplanes saved 45% weight from an all-aluminium design. Another application of AMCs is a 3.6 m antenna for Hubble Space Telescope manufactured from Gr/Al (P100/6061 Al). It offers high stiffness, superb electrical conductivity, and low coefficient of thermal expansion [33]. Also, AMCs have found a wide range of applications in the military sector such as armour, due to the combined static strength and high ballistic performance [15].

2.5 Weldability of aluminium alloys and AMCs

The strength of pure aluminium is inadequate for structural applications. Therefore, to eliminate this limitation it is alloyed with other metals like copper, manganese, magnesium, zinc, and silicon. Different mechanical properties can be achieved by controlling the amount of alloying elements and heat treatments. Aluminium and its alloys are considered

as formable and ductile due to their face-centred cubic crystal structure. It is available in wrought and cast forms. The former can be produced by rolling (hot or cold), extrusion, and forging, while the latter can be made from sand casting, lost wax casting, permanent steel mould casting, and die-casting. Wrought aluminium is classified into two types depending on the main alloying elements. Non-heat treatable weldable aluminium alloys including AA 1xxx, AA 3xxx, and AA 5xxx series are strengthened by cold working, whereas AA 2xxx, AA 6xxx and AA 7xxx series are heat treatable non-weldable alloys can be strengthened by precipitation hardening [34, 35].

In general, welding of aluminium and its alloys needs more attention, especially for the non-weldable ones. Problems may occur including the loss of strength and defect formation when fusion welding processes are used. Trapped porosity may also appear in the cross section of coalescence, due to the dissolution of shielding gases (oxygen, nitrogen and hydrogen) or moisture in the electrode and flux in molten metal as shown in Figure 2-8. Furthermore, lack of fusion occurs in part due to the high melting temperature up to 2060 °C of stable aluminium oxide on the surface. Centre-line or solidification cracking is also a serious problem in fusion welding of aluminium alloys as shown in Figure 2-9. This failure occurs as a result of stresses induced by a metal contraction in cooling due to the difference between the solidification temperatures of pure metal and alloying elements. The variations in the heating and cooling cycle in the HAZ normally result in lowered the strength of joint in non-weldable alloy [34, 36].

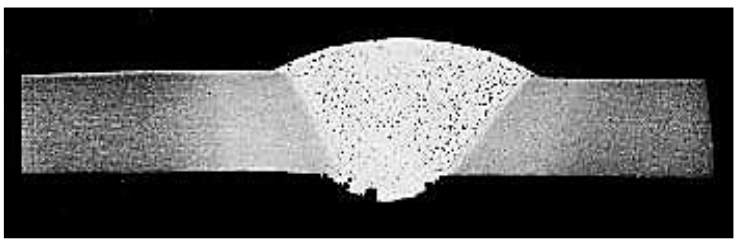


Figure 2-8 Trapped porosity [34]



Figure 2-9 Centre-line cracks in AA 6082 plate /4043 filler metal TIG weld [34]

In addition to the aforementioned problems accompanied by welding of aluminium and its alloys, other difficulties come into view when AMCs are welded by fusion welding processes including. (a) Incomplete mixing between filler and base metal (BM). (b) Formation of the excess eutectic. (c) The presence of large size porosity of more than 100 µm in the fusion zone, and (d) Reaction between molten metals and reinforcements resulting in undesirable phases such as Al_4C_3 [15]. A study was reported by Storjohann et al. [37] to compare three types of fusion welding (GTA, LBW, and EBW) with heat inputs of 165, 108, and 5.9 J/mm, respectively, with solid state welding (FSW) to fabricate similar AMC joints for AA 6061/Al_2O_3/20p (20% Volume of Al_2O_3 particles) and AA 2124/SiC/20w (20% Volume of SiC whiskers). They found that in all fusion welding processes Al_2O_3 particles completely dissolved in molten aluminium leading to the reduction in the strength of joints as shown in Figure 2-10. In the case of SiC whiskers, the formation of Al_4C_3 and precipitation of rich Si phase occurred as a result of the fast reaction between the reinforcement and molten metal as shown in Figure 2-11. In contrast, good joint was achieved by FSW and there was no significant change in reinforcement volume fraction for both AMC joints. Therefore, the findings of this study gave a clear indication of the suitability of FSW to weld different types of AMCs.

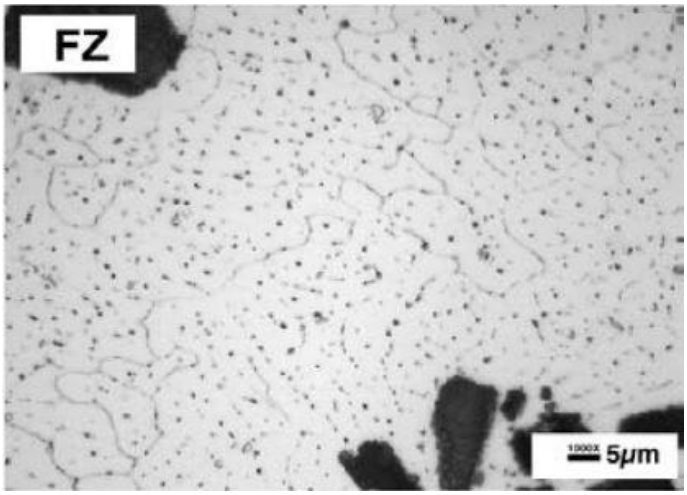


Figure 2-10 Optical micrograph of a fusion weld by LBW on AA 6061/Al_2O_3/20p [37]

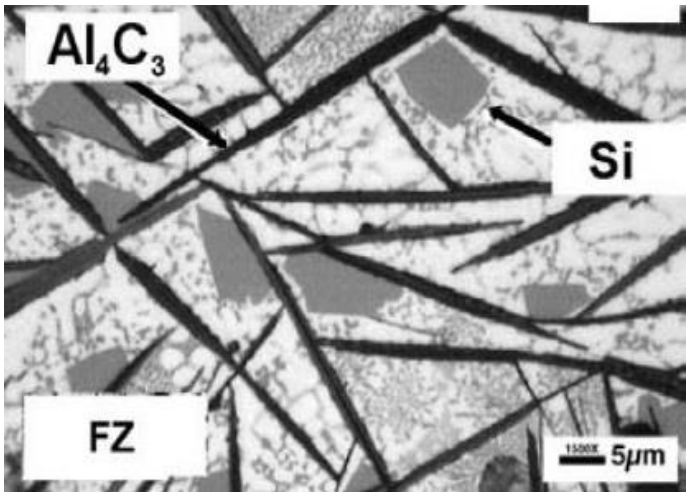


Figure 2-11 Optical micrograph of a fusion weld by LBW on AA 2124/SiC/20w [37]

2.6 Macrostructure and microstructure of FSW joints in AMCs

The quality of a weld joint can be assessed primarily by the evaluation of macrostructure and microstructure. The workpieces are exposed to thermal cycles and severe plastic deformation at high temperature through the rotation of the tool in FSW. As a result of either excessive or insufficient heat input in the weld zone, defects such as tunnel defects and kissing bonds may occur in the welded joint. Also, there are significant changes in the shape and structure of the welding zone. Hence suitable welding parameters need to be selected to avoid these defects. Therefore, the evaluation of macrostructure and microstructure of FSW joints has been carried out extensively.

2.6.1 Macrostructure of AMC joints

The macrostructure examination of welding zone can be used to reveal the quality of welded joints. Three different zones; nugget zone (NZ), thermo-mechanically affected zone (TMAZ), and heat affected zone (HAZ) can be identified in the macrostructure of AMC joints as shown in Figure 2-12. Wake effect, shape of the NZ, onion ring structure, and tunnel defect are typical features which can be examined visibly or at low magnification. Several conditions like types of BM, workpiece thickness, welding parameters, and shape of tool play a significant role in the formation of these features.



Figure 2-12 Cross-sectional macrostructure of FSW AA 2009/SiC/17p joint [38]

The first feature is characterised by the so-called wake effect at the surface of plates. Both Kalaiselvan et al. [39] and Ceschini et al. [40] reported that the formation of the wake effect by FSW of AA 6061/B_4C and AA 7005/Al_2O_3/10p plates, respectively. They considered that it was the friction action between the tool shoulder and the horizontal movement on the surface of the plate that led to the formation of wake effect during FSW.

The shape of NZ is the second feature which can be identified by macrostructural examination. Mishra and Ma [15] classified the shape of NZ into two profiles, basin and elliptical as shown in Figure 2-13. Feng et al. [41] reported the formation of the elliptical shape of the NZ in AA 2009/SiC/15p weldment at 600 rpm. They also noticed that the post weld heat treatment (PWHT) did not affect the profile of the NZ. Recently, Ni et al. [38] and Wang et al. [42] reported that the basin-shaped NZ was obtained by FSW using the same material (AA 2009/SiC/15p) at higher rotation speeds at 800 and 1,000 rpm,

respectively, which gives an indication about the effect of tool rotation speed on the NZ shape.

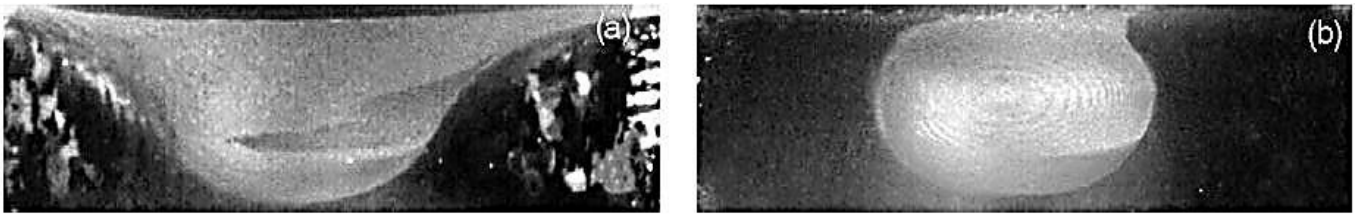


Figure 2-13 Nugget zone shape; (a) Basin, and (b) Elliptical [15]

The third feature that characterises the NZ is the appearance of onion ring structure in swirl pattern as shown in Figure 2-14. Cavaliere et al. [43] and Ceschini et al. [44] mentioned that the formation of the onion ring structure through the cross-section weld of AA 6061/Al_2O_3/20p plates. They considered that the flow behaviour of softened metals and the differences in dislocation density during the joining process are the main reasons for the formation of the onion ring structure. Bozkurt et al. [45] reported that the sweeping of softened metals and the horizontal movement of the FSW tool are the key mechanism for the formation of the onion ring structure when joining AA 2124/SiC/25p. Nami et al. [46] explained that the formation of the onion ring structure in FSW Al/Mg_2Si/15p depends on the effect of grain geometry and the difference in the size of the grain. They clarified that an alternating layer of Mg_2Si eutectic needle and fine particle Mg_2Si was found in rich and small bands, respectively. Also, they pointed out that the number of FSW passes can change the distribution and volume of Mg_2Si in the NZ.

However, the onion ring structure can partially appear or disappear entirely under certain conditions due to the type of AMCs, recrystallisation characteristics, and plate thickness. Chen et al. [47] and Marzoli et al. [48] found that the formation of the onion ring was not visible in the AS but clearly visible in the RS in FSW AA 6063/B_4C-T5 and 6061/Al_2O_3/20p, respectively, as shown in Figure 2-15. This was attributed to the partial recrystallisation which happened in the weld zone and hindered the flow of metal by reinforcement. Furthermore, Ni et al. [38] and Wang et al. [42] reported that there was no

visible onion ring in a basin shape welding zone in FSW AA 2009/SiC/17p-T351 and AA 2009/SiC/15p-T4, respectively. They reckoned that the reduction in thickness led to the disappearance of the onion rings.

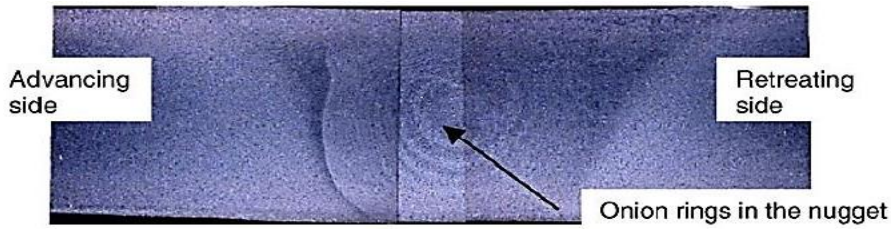


Figure 2-14 Optical micrographs of onion ring in FSW AA 6061/Al_2O_3/20p [44]

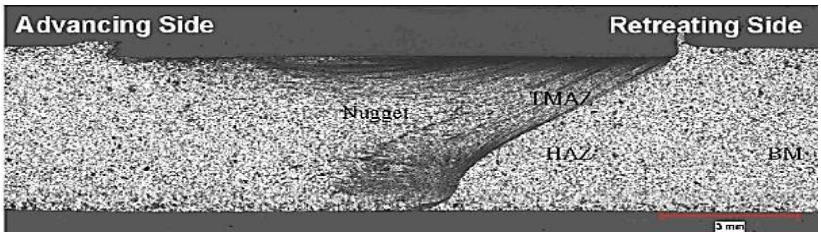


Figure 2-15 Partial appearances of onion ring in cross-section of AA 6063/B_4C/10.5p welded by FSW [47]

Figure 2-16 shows the tunnel defect that can be identified by macrostructure examination. It is found that the frequency of tunnel defect generation in FSW depends on the speed of tool rotation. The appearance of this type of defect can be attributed to insufficient heat input or inappropriate flow of plasticised metal. Cioffi et al. [49] identified clearly the appearance of tunnel defect in the AS of FSW AA 2124/SiC/25p at a low rotation speed of 300 rpm. The tunnel defect is less likely to happen as the rotation speed increases to 800 rpm which produces defect-free joints. They claimed that higher speed allowed higher energy input and hence sufficient plastic flow for minimised tunnel defects. Similarly, Nami et al. [46] reported tunnel defect in FSW Al/Mg_2Si/15p at low and high rotation speeds. They argued that tunnel defect occurred due to the improper flowability of metal in the stir zone as results of lack of heat input at low rotation speeds between 710 and 900 rpm or excessive heat at higher rotation speeds between 1,300 and 1,400 rpm.



Figure 2-16 Tunnel defect in cross-section morphology of an AA 6061/AlN/10p joint welded in 1,200 rpm and 85 mm/min [50]

Periyasamy et al. [51] studied the effect of heat input on the metallurgical properties of AA 6061/SiC/10p joint. The evaluation was carried out at five heat inputs of 755, 850, 945, 1,039, and 1,133 J/mm obtained by applying five tool rotation speeds through calculation. They found that the metal flows intermittently if heat input was below 1,039 J/mm, while turbulent flow behaviour occurred at a higher value of more than 1,039 J/mm. Tunnel defect appeared in the AS of the fabricated joint at a heat input of 1,133 J/mm as a result of the excessive flow of plasticised metal to the upper surface. Interestingly, this observation was confirmed recently by Fu et al. [52] when studying FSW of high strength aluminium alloy AA 7050. They indicated that the submerged FSW (plate under water by 3 cm) gave high-quality joint (tunnel defect free) than that welded in the air. In addition, the location of the tunnel defect in FSW in the air can occur either in the bottom or on the top region of the AS.

In conclusion, wake effect, nugget shape, onion ring, and tunnel defect are the main macrostructure features of AMCs welded by FSW. Rotation speed and the amount of heat input have a significant effect on the nugget shape and tunnel defects, while material flow behaviour, recrystallisation, and plate thickness effect are the main factors for the appearance of an onion ring. Hence the quality of AMC joints can be improved if the temperature of the weld zone can be carefully controlled.

2.6.2 Microstructure of AMC joints

The generated heat through the rotation of the FSW tool would ideally reach approximately 0.8 of the melting temperature of the joined AMCs. This leads to reinforcement redistribution and refinement, recrystallisation, and grain growth in the NZ. The microstructure of the AMC shows that the reinforcement materials clustered and distributed heterogeneously in the matrix as a result of production processes (casting or powder metallurgy). The inhomogeneous distributions of reinforcement materials in the microstructure of the BM can affect the isotropy of mechanical properties. It is accepted that the stirring action during FSW causes a break up of clustered reinforcement and homogenous distribution in the weld zone due to the mixing of material and severe plastic deformation [38, 39, 45, 46, 49, 53]. In contrast, Periyasamy et al. [51] reported that the NZ of AA 6061/SiC/10p joints fabricated at a heat input below 1,039 J/mm consisted of coarsely clustered SiC particles.

Meanwhile, the size of Al_2O_3 and SiC particles decreases obviously as compared to the original material, and the particle edges can be rounded or blunted in the NZ. As a result, the aspect ratio of the particles decreases noticeably. This phenomenon may be explained by the abrasion and stirring effect between particles and tool pin circumference, shoulder surface during welding process [37, 38, 48, 54]. Ceschini et al. [44] pointed out that finer particles were formed closer to the shoulder of the tool than the tip of the pin. However, if the size of the original reinforcement is small, it is not exposed to the refinement process. For example, Storjohann et al. [37] reported that no change was noticed in the size of SiCw reinforcement with a diameter of 1-2 µm and length of 5-7 µm. Instead, the whiskers were reoriented as shown in Figure 2-17, while 20 µm Al_2O_3 particles were subjected to refinement during FSW.

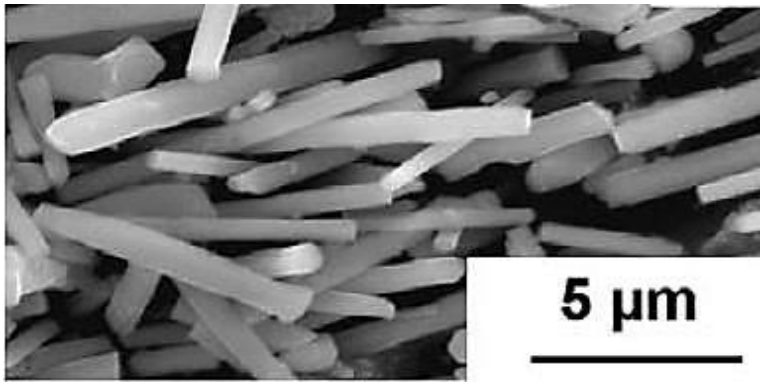


Figure 2-17 Reorientation of reinforcement in FSW AA 2124/SiC/20w [37]

The NZ may be characterised by equiaxed grains much smaller than those in the BM. This indicated that new grains nucleated in the NZ during FSW as a result of dynamic recrystallisation. Feng et al. [41] reported that an obvious reduction in grain size of the NZ reached about 5 µm in FSW of 8 mm thickness AA 2009/SiC/15p plate. Grain growth occurs after PWHT to a T4 condition which leads to a grain size of 8 µm. Similar observations were made by Wang et al. [42]. They reported that the reduction of grin size from 10 µm to 6 µm taking place in the NZ of FSW 6 mm thick AA 2009/SiC/15p plate. They believe that the high energy point on SiCp broken surface is the main location of the nucleation and growth of nano-sized grains to decrease the aluminium matrix/reinforcement interface free energy. However, the growth of new grains in T4 PWHT was restricted by the presence of SiC particles. In addition, Periyasamy et al. [51] indicated that a fine grain structure, fine eutectic, and the elimination of dendritic structure in the NZ were achieved at high heat input through the increase of tool rotation speed. On the other hand, faster cooling rate due to low heat input leads to the formation of coarse grains because of incomplete recrystallisation in the NZ of AA 6061/SiC/10p FSW joint.

In summary, the evaluation of microstructure of AMCs welded by FSW showed an improvement in reinforcement distribution and refined particles due to the stirring action in FSW. Also, the formation of new grains with equiaxed dimensions occurs as a result of dynamic recrystallisation process.

2.7 Mechanical properties of FSW joints in AMCs

For FSW of AMC joints, the evaluation of mechanical properties like microhardness, tensile strength, and fatigue is of considerable importance, particularly for critical components. It is also possible to optimise the welding parameters based on the evaluation of these properties which reflect the joint efficiency (the ratio of the tensile strength of joint to the tensile strength of base metal) of the weldment.

2.7.1 Microhardness of AMC joints

Transverse microhardness through the cross-section of a welded joint can indicate the change of various phases and reinforcement distribution in FSW of AMCs. Two different profiles of microhardness curves have been observed in the joint cross section of AMC weldment.

Firstly, it is well accepted that the highest hardness value occurs in the centre of the NZ followed by a gradual decrease across the TMAZ and HAZ until reaching the hardness value of the BM as shown in Figure 2-18 [39, 41, 43, 46, 51, 54-57]. This is attributed to more grain refinement in the NZ due to dynamic recrystallisation and more uniform distribution of finer reinforcement particles in the weld zone due to FSW action. These conclusions agreed with the Hall-Petch equation (inversely proportional relation between hardness and grain size) and the Orowan hardening mechanism (hardness can be improved if finer particles distribute homogenously) [56]. Also, it may be concluded from Figure 2-18 that lower heat input leads to the formation of coarse grains because of incomplete recrystallisation and thus a reduction of the NZ microhardness.

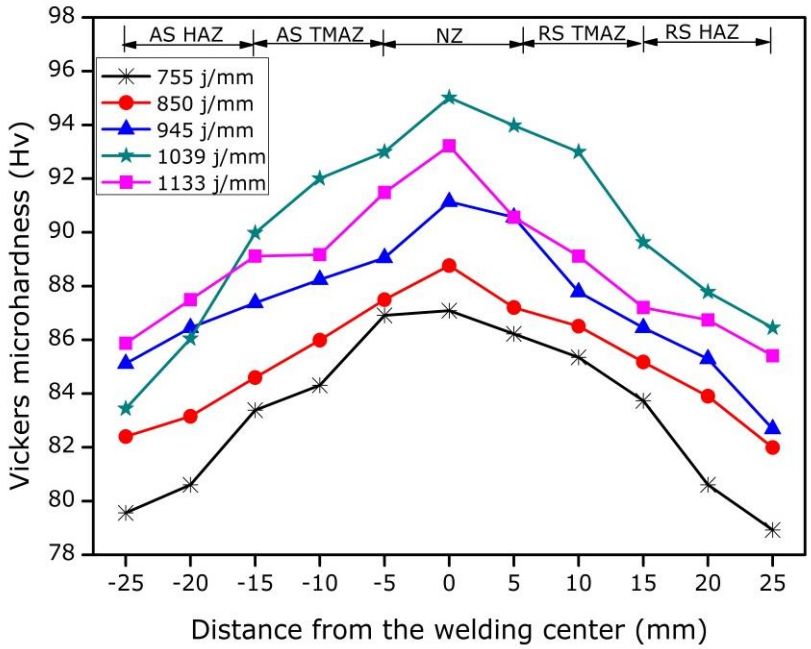


Figure 2-18 Microhardness profile across the weld region of AA 6061/SiC/10p at different heat input [51]

Secondly, Figure 2-19 shows the "W" shape profiles of microhardness curves which can be obtained in FSW of AMC joint, as reported by a number of researchers [38, 45, 49, 58]. Bozkurt et al. [45] explained that the behaviour of this curve depended on the amount of induced dislocation and particle refinement for AA 2124/SiC/25p–T4 FSW joint. The microhardness of the BM was nearly 185 Hv (Vickers hardness). Meanwhile, the hardness of the NZ was 170 and 165 Hv in the root and top of the joint, respectively. The generation of dislocation due to the difference in thermal expansion between the aluminium matrix and reinforcements particles was more significant in the NZ than in the HAZ. Therefore, the HAZ showed lower hardness on both the AS and the RS than that of the NZ, which was only about 155 Hv.

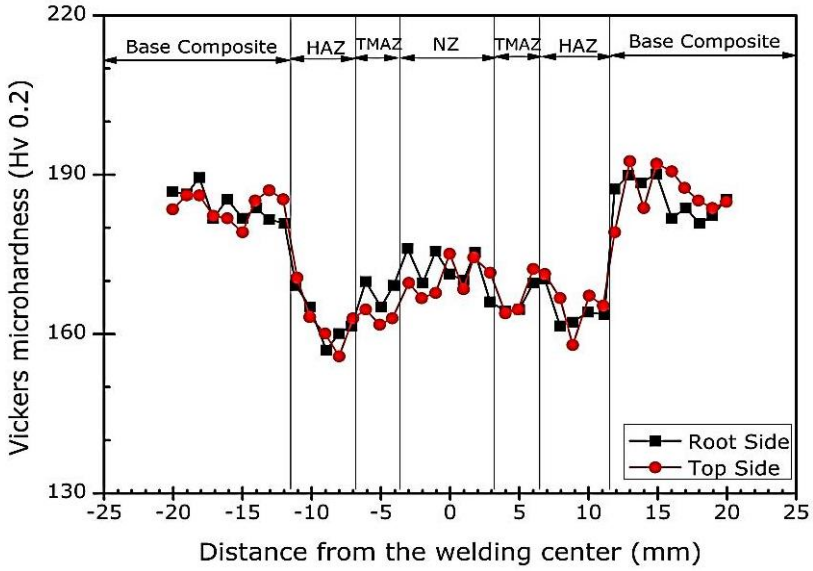


Figure 2-19 Microhardness profile across the weld region of AA 2124/SiC/25p [45]

2.7.2 Tensile strength of AMC joints

The tensile strength of AMC joints fabricated by FSW was compared to that of the BM composite. The efficiency of the joint produced by FSW is higher than that fabricated by conventional welding methods. Many factors influence the tensile strength of AMC joint including tool design, welding parameters, PWHT, and the formation of the intermetallic compound. Table 2-1 summarises the tensile properties of AMCs welded by FSW.

Table 2-1 Welding variables and tensile properties of AMC joints welded by FSW

Base metals	Base metals condition	Plate thickness (mm)	Rotation speed (rpm)	Traverse speed (mm/min)	Axial force (kN)	Tool Shape	UTS (MPa)	Yield stress (MPa)	EL (%)	Joint efficiency (%)
AA 6061/ZrB_2/10 [59]	cast	6	1155	48.8	5.9	square	243	-	-	95.8
AA 6061/B_4C/12 [60]	cast	6	997	78	9.3	square	208	-	-	96.83
AA 6061/B_4C/12 [39]	cast	6	1000	80	10	square	201	-	2.5	93.4
AA 6061/AlNp [61]	cast	6	1200	55	5	square	225	-	0.77	93.42
AA 7005/Al_2O_3/10p [43]	Extruded-T6	7	800	56	-	-	260	245	0.58	83.87
AA 6061/Al_2O_3/20p [43]	Extruded-T6	7	800	56	-	-	329	280	1.3	86.80
AA 6061/Al_2O_3/20p [48]	Extruded-T6	7	700	300	-	-	251	234	-	70
AA 6061/Al_2O_3/22p [54]	cast	4	880	260	-	cylinder smooth	227	-	-	99
AA 6061/SiC/10p [51]	cast	6	1100	45	6	cylinder thread	206	126	6.5	74
AA 6061/SiC/10p [56]	cast	6	1370	88.9	9.6	cylinder thread	265	-	-	92.3
AA 2124/SiC/25p [62]	Forged T4	3	1120	40	-	cylinder thread	366	-	-	81
AA 2124/SiC/25p [49]	Forged-T6	15	550	75	8.5	conical thread	642	478	2.9	86.5
Al/Mg_2Si/15p [46]	cast	6	1120	125	-	cylinder thread	110	-	-	95
AA 2009/SiC/15p [41]	Extruded-T4	8	600	50	-	cylinder thread	450	320	3	95
AA2009/SiC/17p [38]	Rolled-T351	3	1000	50	-	cylinder	443	274	4.7	76
AA 2009/SiC/15p [42]	Rolled-T4	6	800	100	-	conical	441	306	5.4	82
AA 2009/SiC/17p [58]	Extruded-T4	3	1000	800	-	conical thread	501	341	3.5	97
AA 6063/B_4C [47]	extruded	4.5	1500	600	-	conical	176	125	2.5	62
Al–4.5%Cu/TiC/10p [57]	rolled	5	500	20	6	cylinder thread	173	-	2.83	89

EL: Elongation; joint efficiency: the ratio of the tensile strength of joint to the tensile strength of the base metal

2.7.2.1 Effect of tool design

The shape of the tool shoulder and pin plays a significant role in the tensile strength of FSW joints. Vijay and Murugan [63] investigated the effect of different pin shapes (square, hexagonal, and octagon) in tapered and un-tapered profile on the tensile properties of FSW Al/TiB_2/10. The joint efficiency fabricated by un-tapered square pin exhibits a maximum tensile strength which reaches 99.47% of that of the BM in comparison to other profiles. This is attributed to the high ratios of static volume to dynamic volume of plasticised material, measured as 1.56 for the square pin, 1.21 and 1.11 for hexagon and octagon profiles, respectively. This result was confirmed in a later study by Hassan et al. [64]. They used un-tapered (square, hexagonal, and octagon) pin profiles to join hybrid AMC (Al-4%Mg, 1% SiCp and 1% graphite particles). Wang et al. [58] found that the use of conical threaded pin at high traverse speed at 800 mm/min rather than a flat cylinder in joining AA 2009/SiC/17p led to an increase of the joint efficiency to 97% due to the improvement of the flowability of softened material. In a study reported by Yigezu et al. [65] in FSW 5 mm thick Al-12%Si/TiC/10 plates, three shoulder diameters (18, 20, and 22 mm) and threaded cylinder pin were used as FSW tool. They reported that the tensile strength of the weld joints varied from 124 MPa to 172 MPa depending on the tool type and process parameters. A 20 mm shoulder diameter is preferable for obtaining the maximum ultimate tensile strength (UTS). More recently, Kumar et al. [57] investigated the tensile strength of 5 mm rolled Al-4.5%Cu/TiC/10. In order to reveal the effect of three shoulder surface geometries on mechanical properties, full flat surface, 1 mm flat surface, and 2 mm flat surface shoulder with a 7° concave angle were used in FSW. Among the three surface shoulders, the second shoulder configuration resulted in the highest tensile strength. They concluded that the higher heat

input as a result of the higher contact area between the second shoulder surface and the workpiece led to sufficient mixing in the stirring zone, as compared with the other two tool profiles.

2.7.2.2 Effect of welding parameters

In FSW process, the welding parameters including tool rotation speed (ω, rpm), traverse speed (V, mm/min) and axial force (F, kN) affect the amount of friction heat generation and mixing process. Therefore, optimum welding parameters must be selected in order to produce the best joint strength. The efficiency of AMC weld joints is generally in the range from 60% to 97% of those of the BM. It is accepted that the UTS of FSW joints of AMCs increases by increasing the rotation speed until a specific limit [46, 50, 51, 56, 59, 60, 62]. The maximum strength was achieved by using a rotation speed ranging from 1,000 to 1,200 rpm depending on the types of AMC. This leads to the conclusion that there is insufficient heat input in welding joint if the rotation speed is below 1,000 rpm, whilst excessive heat input is produced for the weld joint if the rotation speed is more than 1,200 rpm. Either the case of insufficient or excessive heat input produces an inadequate mixing of soft metal. On the contrary, both Yigezu et al. [65] and Kumar et al. [57] reported that the tensile strength decreases linearly when the tool rotational speed increases in FSW rolled Al-12%Si/TiC/10 and rolled Al-4.5%Cu/TiC/10, respectively.

In addition to the tool rotation speed, another important parameter is the traverse speed of the tool along the weld line. A suitable traverse tool stirs the material efficiently from the AS to the RS. Three possible behaviours for the effects of the traverse speed on the tensile strength of AMC joints are discussed below.

Firstly, the unsteady behaviour of the traverse speed on the tensile strength for different types of AMC has been noted. For example, researches [50, 56, 59] on AA 6061 composite aluminium as base matrices showed that the relation between the UTS and the traverse speed is not directly proportional. As traverse speed increases, the tensile strength increases and reaches a maximum value before it decreases. They assert that the amount of heat input due to friction action between the tool and BM is mainly affected by tool rotation speed. On the other hand, the cooling rate is determined by the traverse speed. Therefore, at lower traverse speed an increase in frictional heat generation and slow cooling rate is accompanied by coarse grains (grain growth). Tunnel defects may occur due to excessive stirring resulting from slow traverse speed. In contrast, at higher traverse speeds insufficient heat input is generated into the joint, which leads to inadequate stirring action of softened material from the AS to the RS also causing tunnel defects. Therefore, reduced tensile strength can be resulted from both low and high traverse speeds.

Secondly, a linear behaviour of traverse speed on the tensile strength for AA 2009/SiC/17p was reported by Wang et al. [58]. The maximum joint efficiency was achieved to reach 97% of the BM at a higher traverse speed of 800 mm/min. They pointed out that at lower traverse speed failure of the joint happened in the HAZ which was characterised by lowered hardness due to dissolution and precipitates growth. This led to a reduction in tensile strength. On the other hand, as the traverse speed was increased the clusters were partially dissolved in the matrix in the HAZ owing to the high cooling rate. Thus an increase in joint efficiency was achieved as a result of the increase of HAZ hardness and shift in fracture location from HAZ to NZ.

Thirdly, as reported by other researchers [57, 62, 65], the increase of the traverse speed slightly decreases the tensile strength of the joint (inversely proportional) for AMCs AA 2124/SiC/25p, Al-4.5%Cu/TiC/10, and Al-12%Si/TiC/10, respectively. The best welding speeds are 40 mm/min for AA 2124 and 20 mm/min for the other two AMCs. However, they mentioned that the influence of traverse speed on UTS is less obvious than the tool rotation speed and tool design.

Applied axial force is another important parameter in FSW. The heat generated by friction between the BM and the tool depends on the friction coefficient, which is also related to the applied force. Higher heat input is generated by a larger amount of applied force which causes sufficient flow. The defect-free joint can be achieved if a sufficient axial force which is higher than the flow stress of the BM is applied. Thus higher tensile strength can be obtained when an adequate force is selected. Despite the importance of the applied force on the amount of heat generation and the retention of the plasticised metal, few researchers have taken into account the effect of this parameter as one of the key welding variables on tensile strength.

Dinaharan and Murugan [59] reported that the maximum tensile strength of joint was obtained at 6 kN axial force when joining in-situ composite AA 6061/ZrB_2. Further increment in hydrostatic pressure leads to a reduction in the tensile strength. The appearance of micro-voids in the joint at lower force and excessive flash at larger force causes a reduction in the cross section of the joint and hence leads to a reduction in tensile strength of joint. Similarly, Murugan and Kumar [50] indicated that for the FSW joints of AA 6061/AlNp tunnel defects appeared in the cross-section of joint due to the lack of heat generation when using lower axial forces. Therefore, a reduction in tensile strength happened when the applied force was lower than 5 kN. On the other hand, if the applied

force was more than 5 kN, it led to thinning of the NZ and formation of the wormhole and therefore reduced the joint efficiency. A similar finding was reported by Kalaiselvan and Murugan [60] in FSW joints of AA 6061/B_4C with a different optimum axial force at 10 kN in their study.

In conclusion, welding parameters including tool rotation speed, traverse speed, and axial force affect significantly the UTS of AMC joints. Rotation speed has the greatest effect on joint efficiency, whilst traverse speed and axial force affect the tensile strength of AMC joints to a varying degree [62]. There is no general trend that can be related to welding parameters for all types of AMCs. Therefore, each material needs its own study to achieve its maximum tensile strength for the FSW joint.

2.7.2.3 Effect of other factors

There are other factors such as the formation of the intermetallic compound, PWHT, and strain rate which also affect the tensile strength of the FSW AMC joints. The formation of intermetallic compounds at the ceramic matrix interface lowers the inner bonding between the reinforcement and matrix. Feng et al. [41] studied the feasibility of joining AA 2009/SiC/15p by FSW under the annealed condition and followed by PWHT to T4 condition for further strengthening. The tensile strength of the joint was increased by 82% and 95% from the BM in the longitudinal and transverse directions, respectively. 100% joint efficiency in T4 condition cannot be achieved due to the formation of secondary phase (Cu_2FeAl_7) in the NZ as a result of interaction between the tool worn material and the BM. In contrast, Wang et al. [66] succeeded in preventing the formation of Cu_2FeAl_7 phase by using ultra-hard tool material in FSW AA 2009/SiC/15p. The strength of FSW joint was increased from 321 MPa to 521 MPa after PWHT to T4 condition, which is almost the same as the strength of BM at 543 MPa. Recently, Ni et

al. [67] studied the effect of strain rate on strain hardening and tensile properties of FSW AA 2009/SiC/17p joints. Because of little difference in hardening capacity of both the BM and the joint, slight reduction in tensile strength occurred when the strain rate increased and the fracture of most specimens happened in the HAZ of the RS.

2.7.3 Fatigue strength of AMC joints

Although many applications of AMC joints by FSW are designed to subject to dynamic loading conditions, there were few studies related to the fatigue properties of AMC joints. Ceshini et al. [44] studied the effect of strain amplitude on low cycle fatigue strength of AA 6061/Al_2O_3/20p FSW joints. The fatigue life of FSW joints is lower than the BM under all conditions. This is attributed to the factors such as the modification of welded surface, joint microstructure, and a higher amount of plastic strain induced by FSW. The roughness of surface affects significantly the fatigue life when the strain amplitude decreases. Also, the isotropic hardening value is higher under low strain amplitudes. At high strain amplitudes, the hysteresis loop area does not change. Moreover, more plastic strain happened in FSW joints than in the BM in low cycle fatigue due to progressive hardening as shown in Figure 2-20.

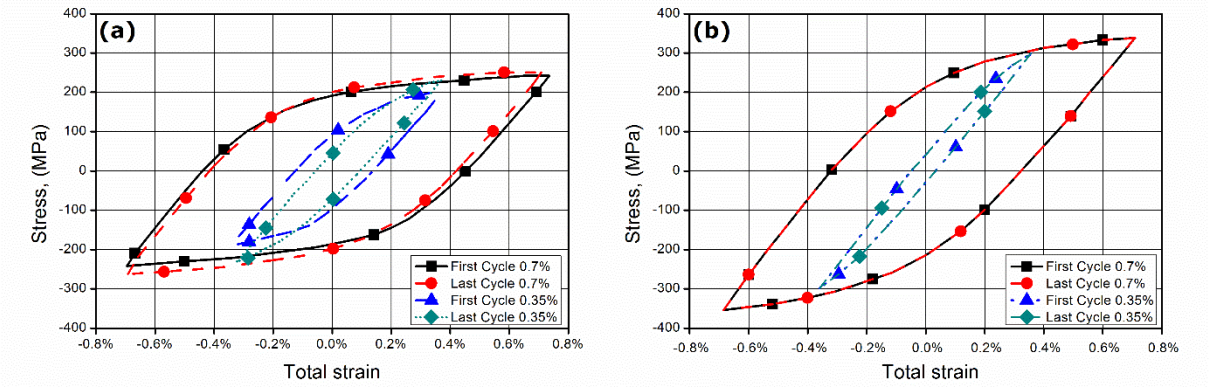


Figure 2-20 Hysteresis loops at different strain amplitudes for AA 6061/Al_2O_3/20p; (a) FSW joints, and (b) Base metal [44]

It is well known that the behaviour of fatigue is more sensitive to the homogeneity of microstructure than the behaviour of tensile. In an investigation on high cycle fatigue of FSW joint AA 7005/Al_2O_3/10p and AA 6061/Al_2O_3/20p [68, 69], it was reported that the FSW joint of the former material exhibited higher fracture toughness and lower fatigue crack growth, while the behaviour of the latter was opposite. Depending on the microstructure it was argued that the volume fraction of reinforcement in AA 6061/Al_2O_3/20p was double of that in the AA 7005/Al_2O_3/10p. More refined particles formed in the AA 6061 matrix after FSW led to increasing the number of stress raisers, embrittlement, and a reduction in the fracture toughness. Therefore, the fracture toughness of AA 7005/Al_2O_3/10p joint is higher than the BM by 10-20%, whilst in the case of AA 6061/Al_2O_3/20p, it is lower than the BM by 25%. However, the crack propagation rate of un-welded AA 7005 composite series is higher than AA 6061 composite series. Furthermore, Minak et al. [54] reported that the fracture location in the fatigue test shifted from the NZ to the BM as shown in Figure 2-21 in AA 6061/Al_2O_3/22p FSW joint, as a result of complete penetration.

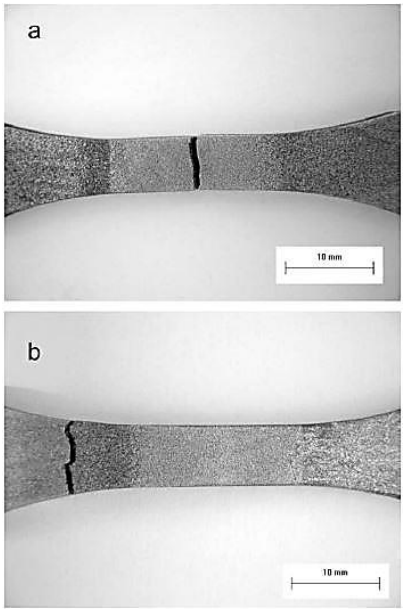


Figure 2-21 Fatigue failures in the FSW AA 6061/Al_2O_3/22p; (a) stirred FSW zone, and (b) Out of the FSW zone [54]

Furthermore, residual stresses are also induced into FSW joint due to severe plastic deformation of the workpiece through the joining process. Ni et al. [70] studied the effect of residual stress on the behaviour of high cycle fatigue of AA 2009/SiC/17p FSW joint. X-ray diffraction test showed that the maximum tensile residual stress of 54 MPa was induced in the centreline of the weld joint, whilst residual stresses were in compression being about 70 MPa and 60 MPa in the AS and the RS, respectively. At lower stress amplitudes below 150 MPa, the FSW fatigue samples fractured in the weld zone and gave nearly the same fatigue limit as of the BM due to the interaction between the residual stresses and the applied load. But at higher stress amplitude, the fatigue life of FSW joints was lower than that of the BM. Meanwhile, the fracture tended to occur randomly in either the AS or RS of the HAZ.

Finally, for critical engineering applications of AMCs, it is much more important to evaluate the fatigue properties of FSW joints in more depth. For FSW AMC joints, the fatigue strength and fatigue crack growth are affected by several factors such as surface roughness, microstructure homogenization, reinforcement volume fraction, and residual stresses in the weld zone. Also, the appearance of the reinforcement on aluminium matrices can play a role in stress concentration. Therefore, there is a need for more effort to understand the low cycle fatigue behaviour of AMC joints by FSW.

2.8 Tool wear in FSW of AMCs

The wear of FSW tool is a critical issue particularly for AMC materials, which occurs as a result of friction, rotation, and movement of the FSW tool along the base material. According to Rai et al. [26], plastic deformation, abrasion, diffusion, and reaction between the environment and the tool material are the major wear mechanisms that happen in FSW tools. Mishra and Ma [15] reported that FSW of soft metals such as

aluminium and magnesium did not exhibit significant wear of the tool. However, tool life issue becomes more significant when hard metals of high melting temperature or MMCs are welded by FSW. This phenomenon is characterised by the deformation and reduction in the pin diameter.

The appearance of hard reinforcement particles in AMCs makes abrasion a dominating factor for tool wear in FSW. Prado et al. [71, 72] studied the effect of welding parameters including rotation speed between 500 - 2,000 rpm and traverse speed between 1 - 9 mm/s on threaded ¼-20 / 01 AISI oil-hardened steel tool wear. Similar joints for AA 6061/Al2O3/20p and monolithic aluminium AA 6061-T6 were used in their studies. They pointed out that no wear was observed in the tool when welding a monolithic aluminium alloy, while severe wear started in joining AA 6061/Al_2O_3/20p when reaching its maximum value at 1,000 rpm then gradually becoming constant after a period of time (self-optimised tool shape). And thus the turbulent flow (vortex flow) of the worn tool is less than the unworn tool due to the eroded threads.

Figure 2-22 shows the wear features, the rate of tool wear at various weld lengths and the relationship between weld speed and tool wear rate. However, from microstructure evaluation, it was found that a sound joint could be produced continuously by using self-optimised shape tools.

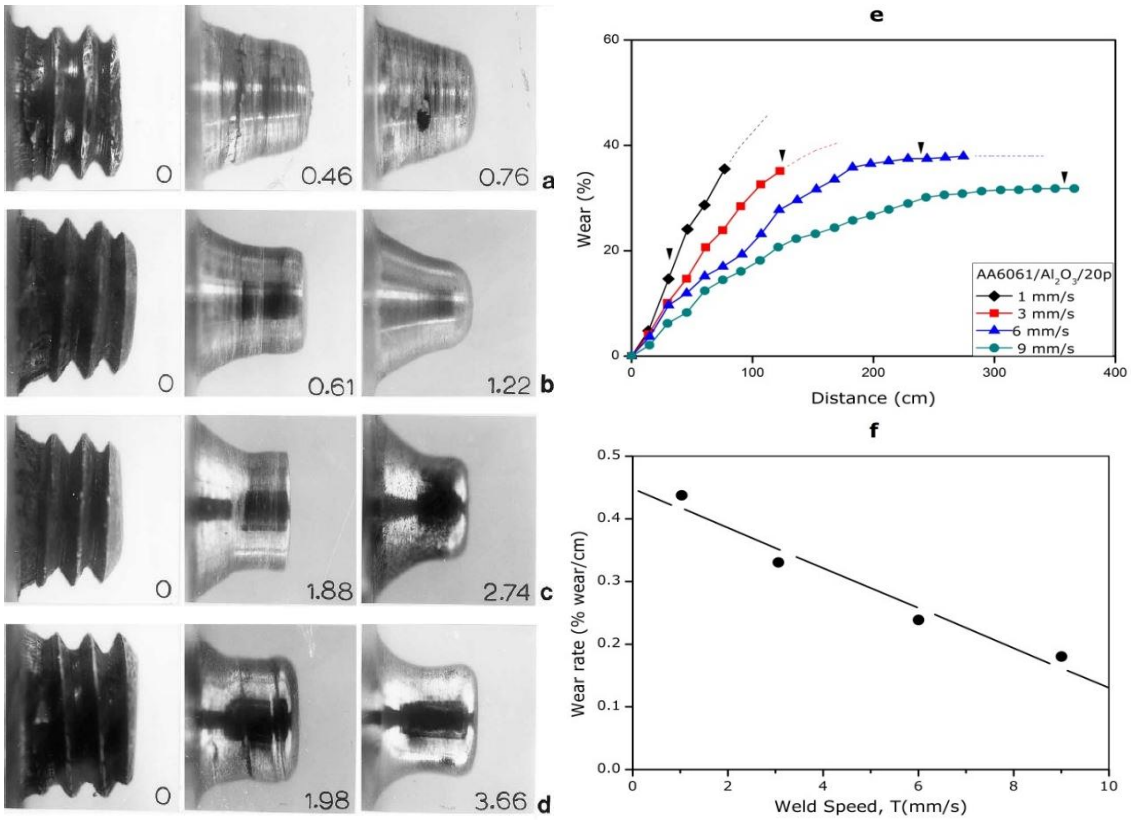


Figure 2-22 (a) through (d) Wear features of FSW tool pin at different weld distance (in meters) and constant tool rotation speed of 1000 rpm at different traverse speeds: a. 1, b. 3, c. 6, and d. 9 mm/s, (e) Wear rate versus weld length at different traverse speed, and (f) Wear rate versus weld speed [72]

The self-optimisation phenomenon of tool shape was confirmed by Shindo et al. [73] and Fernandez and Murr [74] in their experimental investigations by using cast AMC plate, AA 359/SiC/20p. An AISI 01 oil-hardened steel threaded ¼-20 tool was used. Shindo et al. [73] pointed out that there was an inverse relationship between traverse speed and wear rate at constant rotation speed. Fernandez et al. [74] reported that there was a linear relationship between the wear rate and the tool rotation speed. However, as a result of filling threads by base materials, the initial wear of the tool can be delayed by the reduction of rotation speed and the increase in traverse speed and after a period of time, the wear rate becomes constant as shown in Figure 2-23. They concluded that the self-optimised tool shape was evolved as a result of the complex solid-state flow of the

BM during FSW. Moreover, they indicated that homogeneous structure could be achieved with a worn pin.

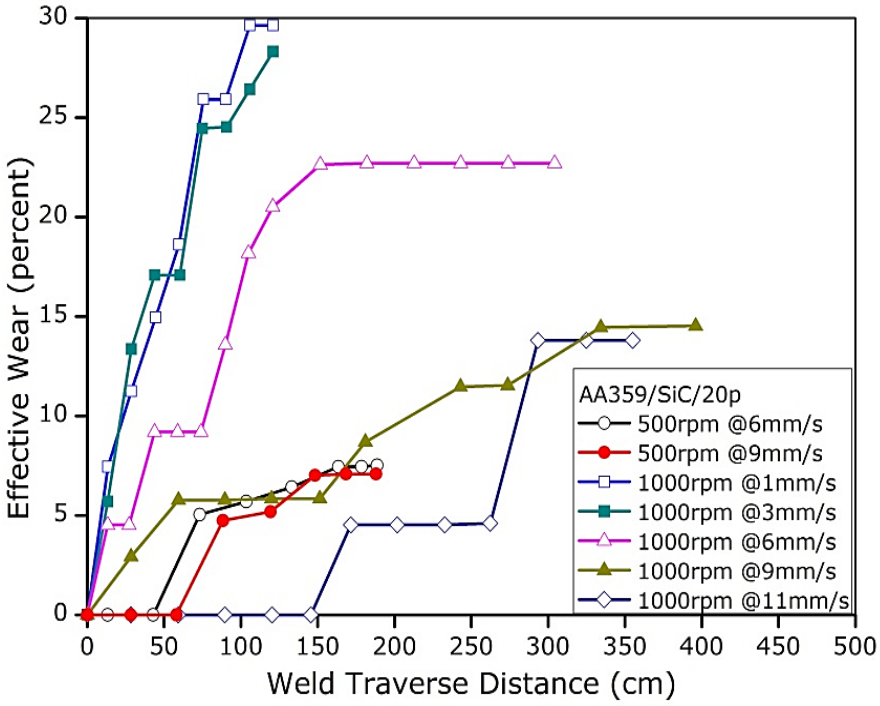


Figure 2-23 Pin tool wear as a per cent of initial tool shape projections versus weld traverse distance for different tool rotation and traverse speeds [74]

Further improvement of tool life cannot always be achieved by changing the type of steels. For example, Cioffi et al. [49] used MP159 and H13 as tool material for threaded pin and shoulder, respectively. At a rotation speed of 800 rpm, severe wear of the pin happened in welding 15 mm thick AA 2124/SiC/25p plates. Chen et al. [47] indicated that the reduction of tool wear could be achieved if tool design was changed. An AISI 4340 unthreaded conical tool was used for joining AA 6063/B_4C with limited wear rate. It is clear that significant wear can occur as steels are used in specific design as a FSW tool. Moreover, the formation of the intermetallic compound is produced as results of the interaction between the worn tool material and the BM. Feng et al. [41] showed that the interaction between Fe from the worn tool and AA 2009/SiC/15p resulted in the formation of Cu_2FeAl_7. The appearance of this compound in the weld zone proves to be

detrimental to the joint efficiency, i.e. a reduction of the strength of joint and change of failure modes from ductile to brittle.

Harder materials can be used as tool material rather than steels to reduce wear rate. Ni et al. [38] used cermit tool to weld AA 2009/SiC/17p. The tool was not visibly worn at 50 mm/min traverse speed and 1,000 rpm rotation speed. In the same manner, Wang et al. [66] reported that the formation of intermetallic compound (Cu_2FeAl_7) during welding AA 2009/SiC/15p was eliminated as a result of improved wear resistance of tool by using an ultra-hard material without giving detailed specifications of the tool material. Recently Prater et al. [75] compared wear resistance among different types of tool materials including 01 steel, Wc-Co micron, Wc-Co submicron, and Wc-Co coated by diamond to join AA 359/SiC/20p-T6 and AA 359/SiC/30p-T6. They observed that harder material could be used to reduce the wear of tool by 60-80%. However, the toughness of the tool is another problem that may cause tool pin fracture in FSW.

Alternatively, the surface coating may be used to reduce the occurrence of abrasive wear in the FSW tool. An experimental work was reported by Contorno et al. [76] to modify the wear resistance of the tool surface by generating a tribological layer to join AA 359/SiC/20p. They used AISI 1040 cone tool without thread, which has a 1,200 Hv substrate coated by a different nano-composite layer of AlSiTiN and AlSiCrN of 5100 and 5200 Hv, respectively. Although they used high hardness coated material, they found that there was no definitive advantage from the coating. On the other hand, Bozkurt et al. [45] reported that the tool wear was eliminated by using high-speed steel (HSS) coated by TiAlN. Based on these studies, it seems to be the case that the adhesion force between the substrate and the coated material has a significant effect on tool wear rate.

In conclusion, severe wear of FSW tool occurs especially in the pin when steels are used as tool materials for joining AMCs. Tool wear resistance can be improved by changing the design and the material of the pin. Also suitable coating material compatible with the substrate tool material can improve wear resistance. However, there is no work reported on the improvement of wear resistance by using a surface heat treatment technique. Therefore more effort in this field is needed for increased tool life and reduced the formation of an intermetallic compound which has a detrimental effect on joint efficiency.

2.9 FSW of aluminium alloy AA 6082

Aluminum-Magnesium-Silicon (Al-Mg-Si) (6xxx series) alloys specifically AA 6082 in T6 condition, has attracted considerable attention due to their high specific strength and stiffness-to-weight ratio, and excellent corrosion resistance, due to the high density of $\beta''(mg_5si_6)$ strengthening precipitates and the additions of Mg and Si that control the grain structure [77, 78]. So far, much effort has been carried on the welding of this alloy by metal inert gas (MIG) [79], tungsten inert gas (TIG) [80], and plasma arc welding (PAW) [81]. Even with good weldability of this alloy by fusion welding processes, the high heat input energy leads to very significant changes in the microstructural state within the welding zone in term of grain size, texture, segregation of silicon and magnesium, porosity, and dissolution or coarsening of strengthening precipitates [81-85]. Among these concerns, the mechanical properties of the welded joints deteriorate significantly and limit its full potential for industrial applications [21, 86-89].

Unlike fusion welding, FSW is considered as a viable method to weld aluminium alloy while maintaining mechanical properties of the joint and overcoming the

aforementioned problems. Despite remaining in the solid state, the development of microstructure, texture and strengthening precipitate across FSW joint proves to be extremely complicated, because of the combination of thermal exposure and intense levels of plastic strain, followed by different cooling rates experienced during the welding process, which results in complex physical metallurgical phenomena [8, 90-92]. FSW parameters control these thermo-mechanical conditions and subsequently affect the strength, fatigue and corrosion behaviour of FSW joints. Cavaliere et al. [93] studied the microstructural and mechanical properties of AA 6082 FSW joint. The variation in the nugget zone (NZ) microstructure depends strongly on the variation of the process parameters which lead to a wide range of possible performances. El-Danaf and El-Rayes [94] reported that post weld heat treatments could eliminate the negative effect of FSW on the strength and hardness in the NZ of AA 6082-T651 FSW joints by re-precipitation of $\acute{\beta}$ phase. Ericsson and Sandstrom [95] carried out a comparative study on MIG-pulse, TIG and FSW of AA 6082. It was found that in fusion welds the fracture propagated in the weld metal near the toe of the weld as a result of the formation of a dendritic cast microstructure in the weld zone with solute gradients near the dendrite boundaries leading to a reduction in fatigue strength. In contrast, the formation of very fine grains in the NZ of FSW joints helps improve the fatigue strength. While much effort has been focused on the effect of FSW parameters on the microstructure and corresponding tensile and hardness properties of AA 6082 joints , the fatigue which is considered the principal cause of failure for welded joints have been examined only in a few studies, mainly on the high cycle fatigue (HCF) regime [95-97], and fatigue crack propagation [97].

2.10 Conclusions and future challenges

This chapter aims to outline the current state-of-the-art of joining AMCs and aluminium alloy by FSW with a number of specific issues discussed including FSW process, the application of MMCs, weldability of aluminium and AMCs materials, macro and microstructure, mechanical properties of FSW joint, tool wear, and FSW of AA 6082. FSW, as a solid state welding process, is considered to be potentially a viable route for joining AMC materials and aluminium alloys. Its potential benefits in cost reduction, joint efficiency improvement, and high production accuracy make it even more attractive for the non-weldable series AA 2xxx, AA 6xxx and AA 7xxx. However, the maturity of using this joining process to weld AMCs is still at its infant stage in research and has not yet been fully implemented in industry.

The mechanical properties of AMCs joined by FSW are largely dependent on the combined effect of both the composition of AMCs and the FSW processing conditions. Therefore, the mechanical performance of FSW joints should be evaluated accordingly. Early researches showed that FSW is a potential welding process to achieve defect-free joints of AMCs. There is a clear need for more efforts to understand the effect of FSW on these materials in adequate depth to meet design and production requirements. For instance, there is a need for systematic studies which take into account the effects of reinforcement percentage and types of reinforcement on joint efficiency. More work is needed to understand the performance of FSW joint of AA 2124 and AA 6092 as base matrices for AMCs with different reinforcement percentages. Also, there is a need for joining AMCs to other materials rather than monolithic aluminium alloys such as magnesium alloy, a new candidate material for the aerospace application.

Furthermore, welding parameters such as tool rotation speed, traverse speed, and axial force have a significant effect on the amount of heat generation and strength of FSW joints. The macrostructural evaluation showed that the formation of tunnel defects due to the inappropriate flow of plasticised metal. Microstructural evaluation of FSW joints clearly showed the formation of new fine grain and refinement of reinforcement particles in the weld zone with different amount of heat input by controlling the welding parameters. However, there is no general trend between welding parameters and mechanical properties for different types of AMCs. Further work needs to be carried out to define the welding window of each composite metal for optimised mechanical properties.

Also, there is very limited data on fatigue strength and fracture toughness of friction stir welded of aluminium alloy and AMCs. More effort is needed to study these properties in more depth to establish the full potential of FSW joints of these materials. This is also confirmed more recently by Ma et al. [98]. They identified in their critical reviews that insufficient investigations had been carried out focusing on the LCF behaviour FSW joints, although many of the envisaged applications for the AMCs will undergo cyclic loading with high amplitude of strain and stress during service life resulting in fatigue damage and severely limit the useful life and the performance of the components [99]. Furthermore, the LCF in the composite metals may occur because of repeated localised yielding near stress raisers (strengthening particles) that lead to stress concentration, despite the bulk of the component under elastic deformation. Thus it remains an open question on how to improve the strength and fatigue behaviour of AMCs joints.

Finally, the wear of FSW tools especially in the pin is up to this time the main issue when joining AMCs and a significant hindrance for the application of FSW process in

the industry. Using new tool design which has frustum shapes (self-optimised shape), surface coating of the pin by` appropriate material compatible with the substrate, and surface heat treatment technique could be viable solutions to improve both the tool life and joint efficiency.

Chapter 3 Materials and experimental work

3.1 Introduction

This chapter provides the details of the material and facilities used in this work. The experimental work carried out on friction stir welding for different aluminium - magnesium-silicon (Al-Mg-Si) series AA 6xxx. The as-received materials and its properties are presented as well as the welding fixture, tool design, setup of the FSW machines, and welding temperature history measurements. Metallurgical inspections and mechanical characterisation used to evaluate the performance of FSW joints are also presented. Furthermore, the measurement techniques used to determine the welding-induced residual stresses by neutron diffraction techniques is described.

3.2 Materials

Three materials studied in the present work, which are based on an Al-Mg-Si series AA 6xxx. The first studied material is an aluminium alloy (AA 6082), the second studied metal is an aluminium matrix composite (AMC) (AA 6092/SiC/17.5p), and the third candidate material investigated in this work is a sandwich aluminium matrix composite (SAMC) (AA 6061B/SiC/20p). Their chemical composition and mechanical properties are illustrated in Table 3-1 and Table 3-2, respectively.

Table 3-1 Chemical composition of the alloys used in this study (weight %)

Alloy	SiC %	Mg	Si	Mn	Fe	Cu	Cr	Al
AA 6082	-	0.654	0.874	0.456	0.359	0.023	0.0247	Bal.
AMC 6092	17.5	0.79	0.4-0.8	0.35	<0.3	0.7-1	0.0261	Bal.
SAMC 6061	20	0.5	0.5	0.026	0.14	0.177	0.166	Bal.

Table 3-2 Mechanical properties of the alloys used in this study

Alloy	Temper	Tensile strength (MPa)	Yield strength (MPa)	Elongation %	Hardness Hv
AA 6082	T6	318	266	17	120
AMC 6092	T6	419	370	2.8	150
SAMC 6061	T1	288	130	8.5	120

The first studied material is heat treatable aluminium alloy AA 6082-T6 of 4 mm thick rolled sheet in a T6 metallurgical condition, which was solution heat treated, quenched to room temperature and artificially aged. This alloy is considered a medium strength alloy, and it has the highest strength in the AA 6xxx series alloys. It has attracted considerable attention for lightweight structures due to their high specific strength and stiffness-to-weight ratios, and excellent corrosion resistance [77]. The approach to strengthen this series is through the addition of magnesium and silicon as primary alloying elements, which promote the precipitation of a single metastable precursors

phase to the equilibrium ß (Mg_2Si) phase with a high density of β''strengthening precipitates [94, 100, 101].

The second studied material is an AMC (AA 6092/SiC/17.5p-T6), was manufactured by using the powder metallurgy technique and subsequently rolled into sheets. This metal is ideal for aero-structures applications, because of a combination of enhanced strength and stiffness, in the form of extruded profiles and control surfaces. A high strength aluminium alloy AA 6092 (Al-Mg-Si) was used as a matrix reinforced with 17.5 % vol. of silicon carbide particles having an average size of around 6 µm. The composite metal supplied as 3.1 mm thick rolled sheet in a T6 metallurgical condition, which was solution heat treated, quenched to room temperature and artificially aged [102].

The third studied material is SAMC (AA 6061B/SiC/20p-T1), manufactured via a powder metallurgy route using a mechanical alloying process to ensure a homogeneous reinforcement distribution, providing a refined grain structure enhancing mechanical properties. A high-quality aerospace grade aluminium alloy (AA 6061B) was used as a matrix reinforced with 20% vol. ultrafine silicon carbide particles having an average size of around 700 nm. The composite metal supplied as a rolled sheet with an aluminium skin on top and bottom surface up to 0.5 mm. The sandwich material has a thickness of 4 mm in a T1 metallurgical condition, which was cooled from an elevated temperature shaping process and naturally aged to a substantially stable condition [103].

3.3 Friction stir welding

3.3.1 Friction stir welding fixture

Welding fixture is exposed to extreme work conditions such as high forging force, thrust force, and high temperature. Therefore, careful design for the fixture is needed to withstand the deformation and deflection processes. The main features that put into account when designing FSW fixture include the flexibility of fixture to be compatible for different plate thicknesses and width and appropriate holding to avoid gap and divergence between two plates. The fixture was designed as shown in Figure 3-1 and manufactured from mild steel.

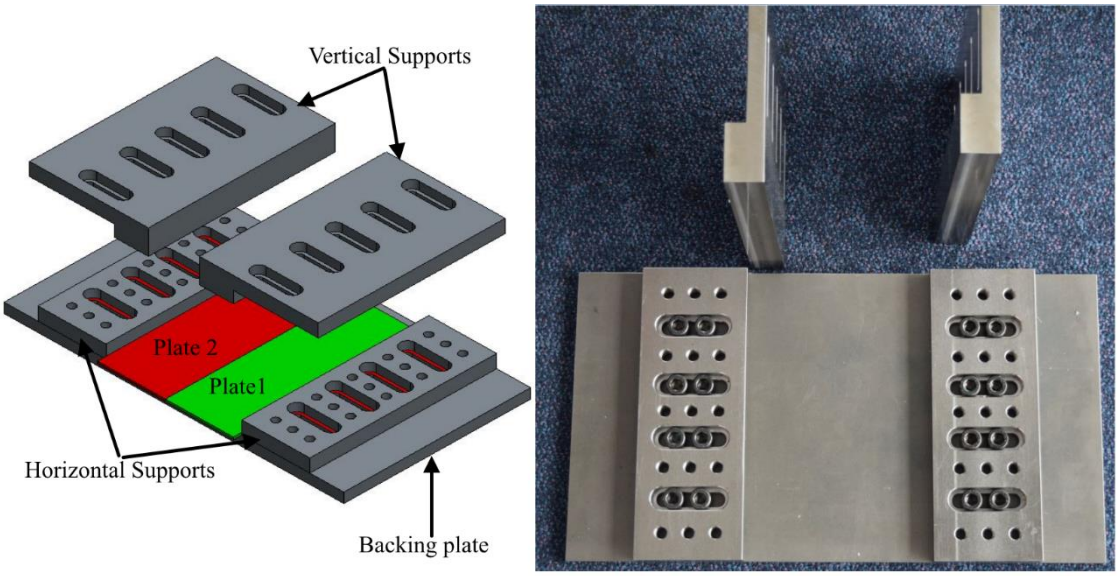


Figure 3-1 Friction stir welding fixture

3.3.2 Friction stir welding tool design and machine setup

Even though FSW consistently gives high-quality welds, proper use of the process and control of some parameters are needed to achieve this. The use of a proper FSW tool design is a crucial factor to ensure high-quality welding joints, as the rate of heat generation and the flow of plasticised metal are experienced by tool geometry [28].

According to the literature, three main criteria should be followed when designing FSW tools including tool material, shoulder shape and dimension, and pin profile and dimension. The FSW tool was manufactured from chromium hot-work tool steel (AISI H13) with 6° flat edge featureless concave shoulder of 16 mm in diameter and right-threaded cylindrical pin 6 mm in diameter (M6) with a dome end, as shown in Figure 3-2. The length of the pin was chosen based on the thickness of the base metal, a 3.3 mm for AA 6082-T6 and SAMC sheets, while for AMC a 2.8 mm pin length was used. Wear of FSW tool is a critical issue particularly for joining aluminium reinforced by ceramic particles, which occurs as a result of friction, rotation, and movement of FSW tool along the base material [8]. Therefore, to minimise the wear of the tool, a plasma nitriding heat treatment was done with the tool surface to achieve a hardness of 950 Hv. To set up the machine, in term of the tilt angle, rotation direction, and plunge depth, some initial welding test has been done. The surface morphology of the FSW joints in term of flash formation, and surface appearance has been investigated visually and used to assess the setup conditions. It is noticed that the increase of tool tilt angle from 0° to 2° and inverse tool rotation direction from clockwise to counter-clockwise (push softened metal down) reduces dramatically the appearance of flash for the same welding conditions as shown Figure 3-3. Therefore, for all welding samples, the tool rotation axis was tilted by 2° from the sheet normal (the front of the tool was higher than the rear) and rotated counterclockwise. The tool plunge depth, which means the depth of the rear of tool shoulder into the top surface of the workpiece was controlled to be 0.2 mm for AA 6082 and SAMC and 0.05 mm for AMC

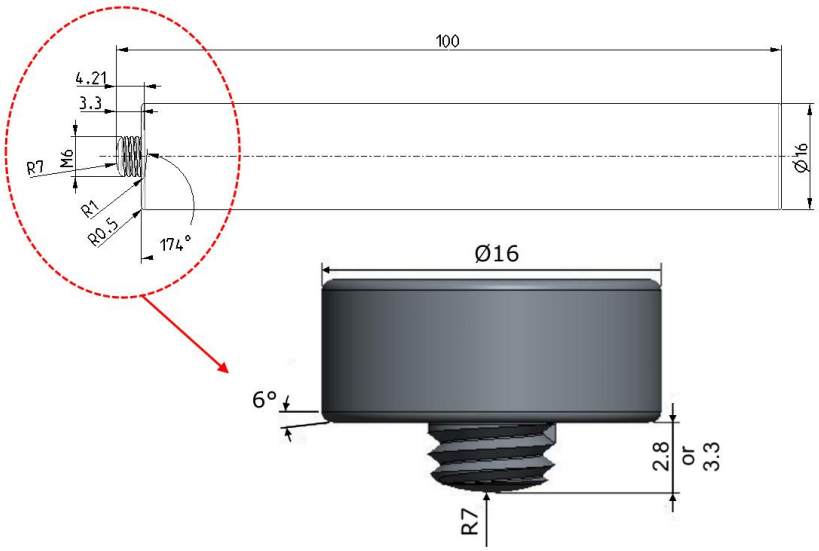


Figure 3-2 Geometry of FSW tool (dimensions in mm)

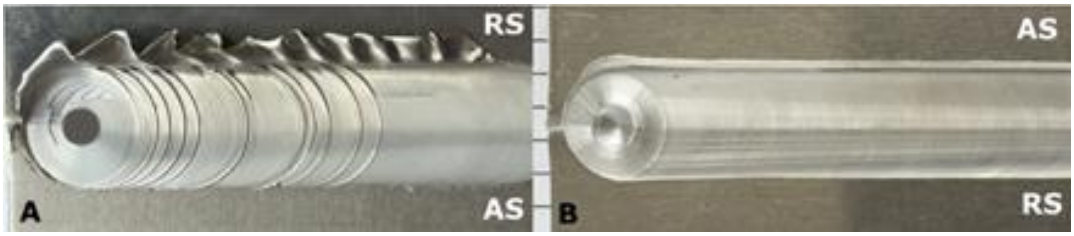


Figure 3-3 Effect of tilt angle and rotation direction on flash formations at a tool rotation speed of 1500 rpm and tool traverse speed of 75mm/min; (A) 0° tilt angle with clockwise rotation, and (B) 2° tilt angle with anticlockwise rotation

3.3.3 Design of friction stir welding experiments

FSW was performed parallel to the rolling direction for all studied materials in a single-pass butt weld configuration. The principal directions of FSW geometry are denoted as welding direction (WD), normal direction (ND) and transverse direction (TD). As the amount of heat generation and dissipation during FSW depends mainly on the FSW parameters including tool rotation speed (ω) (rpm), and traverse speed (V) (mm/min), a series of FSW runs were conducted to identify the FSW window. The range of welding parameters was optimised after several trials to achieve high weld quality in

term of surface finish and penetration. Thus, different welding parameters of tool rotation and traverse speeds were used for different materials.

For aluminium alloy AA 6082-T6, a total of twenty joints denoted as W1–W20 were investigated by using four levels of tool rotation speed ranging from 800 to 1800 rpm and five levels of traverse speeds ranging from 20 to 200 mm/min as shown in Table 3-3 to examine the metallurgical and mechanical properties of welded joints at a diversity of welding temperatures. The welding process was conducted for sheets having dimensions of 150 mm x 60 mm x 4 mm by using a conventional milling machine as shown in Figure 3-4.

Table 3-3 Summary of welding matrix of AA 6082-T6

		Tool rotation speed (rpm)			
		800	1100	1500	1800
Tool traverse speed (mm/min)	20	W1	W6	W11	W16
	40	W2	W7	W12	W17
	75	W3	W8	W13	W18
	125	W4	W9	W14	W19
	200	W5	W10	W15	W20



Figure 3-4 Conventional milling machine

For AMC and SAMC, a total of nine joints for each material denoted as W1–W9 were carried out by using three levels of tool rotation speed ranging from 1500 to 2100 rpm, and three levels of traverse speeds ranging from 25 to 100 mm/min as shown in Table 3-4. The welding window of AMC and SAMC was chosen based on the obtained metallurgical results of the aluminium alloy AA 6082. The welding process was carried out for sheets having dimensions of 110 mm x 50 mm x 3.1 mm (AMC), and 100 mm x

50 mm x 4 mm (SAMC) at TWI-UK by using a bespoke FSW machine as shown in Figure 3-5.

Table 3-4 Summary of welding matrix of AMC and SAMC

		Tool rotation speed (rpm)		
		1500	1800	2100
Tool traverse speed (mm/min)	25	W1	W4	W7
	50	W2	W5	W8
	100	W3	W6	W9



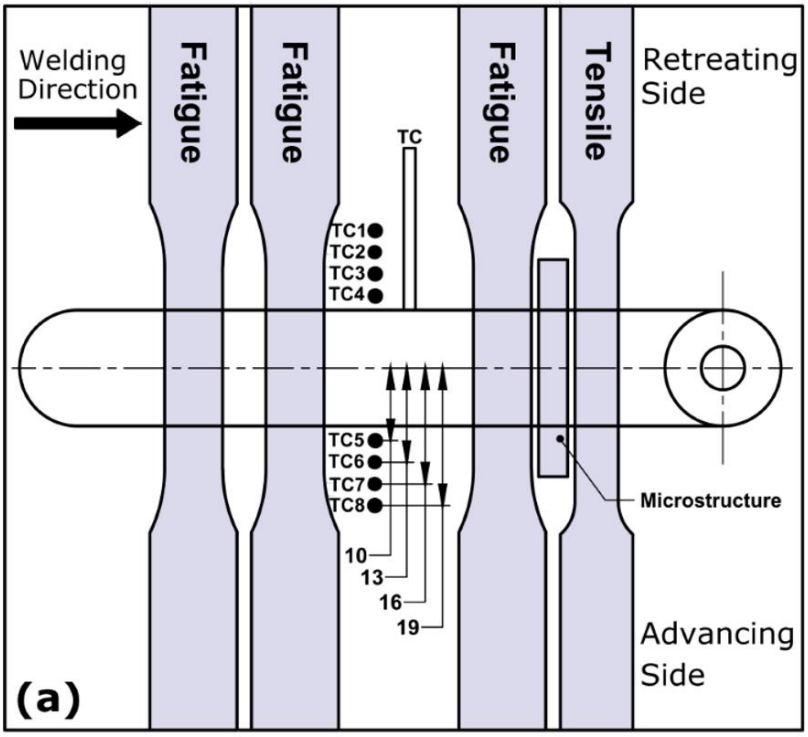
Figure 3-5 Bespoke friction stir welding machine

3.3.4 Measuring welding temperature and thermal history

For aluminium alloy AA 6082, the maximum welding temperature in the NZ was measured by a K-type thermocouple (90 % nickel and 10 % chromium) having measuring range of -40 to 1300° C, and infrared camera system (FLIR). Thermocouple (TC) having a diameter of 1.6 mm embedded in the middle of the joint line as shown in Figure 3-6 (a) and Figure 3-7 to measure the peak temperature during the welding process. Meanwhile, the maximum welding temperature in AMC and SAMC was measured by the infrared camera system as shown in Figure 3-8. The infrared data was processed by FLIR Tools software.

To measure the thermal distribution across all FSW joints during welding process eight TCs having a diameter of 1.6 mm were embedded in 1.5 mm depth holes at a different distance from the centre of weld on the retreating (RS) (TC1-TC4) and advancing (AS) (TC5-TC8). The positions of the TCs were in the mid-length of the weld line, 10 mm away from the weld centre and 3 mm between each of them as shown in Figure 3-6 (a) and Figure 3-7. The TCs temperature was recorded digitally using TM-747D thermometer connected to the computer that contained a data acquisition system.

To assess the accuracy and calibrate the setting of the infrared camera a compression has been made between the temperature results obtained from thermocouples (TC1, TC2, and TC3) and infrared camera reading (Ir1, Ir2, and Ir3) as shown in Figure 3-9. It is clear that a good agreement between the reading recorded by infrared camera and thermocouples is obtained. Also, the sensitivity of the camera to change in temperature is faster than thermocouples.



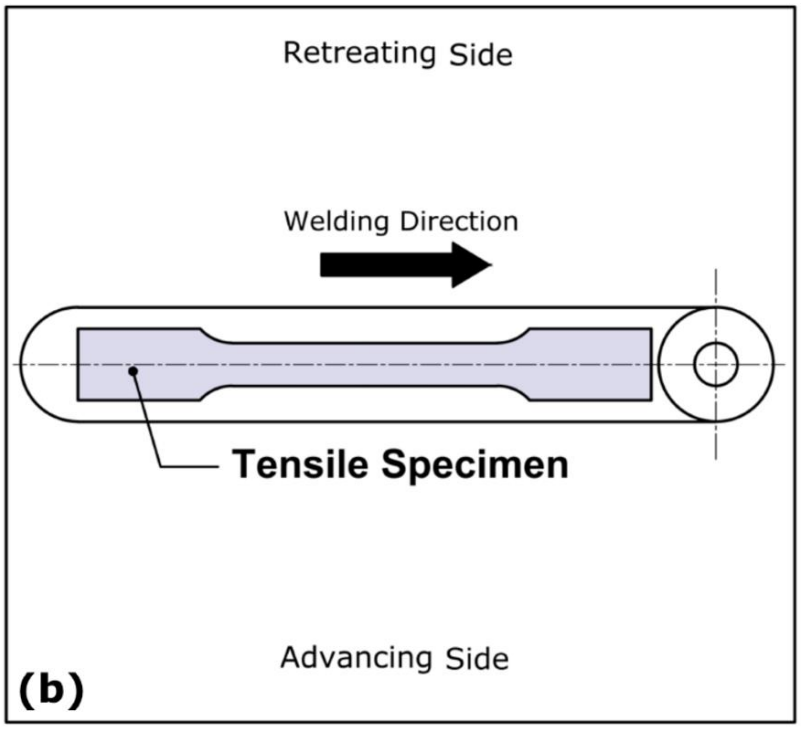


Figure 3-6 (a) Illustration of friction stir welds and the positions of the thermocouples attached on the samples and the extraction of cross-weld testing sample locations are highlighted, and (b) The extraction of longitudinal tensile sample locations is highlighted (all dimensions in mm)

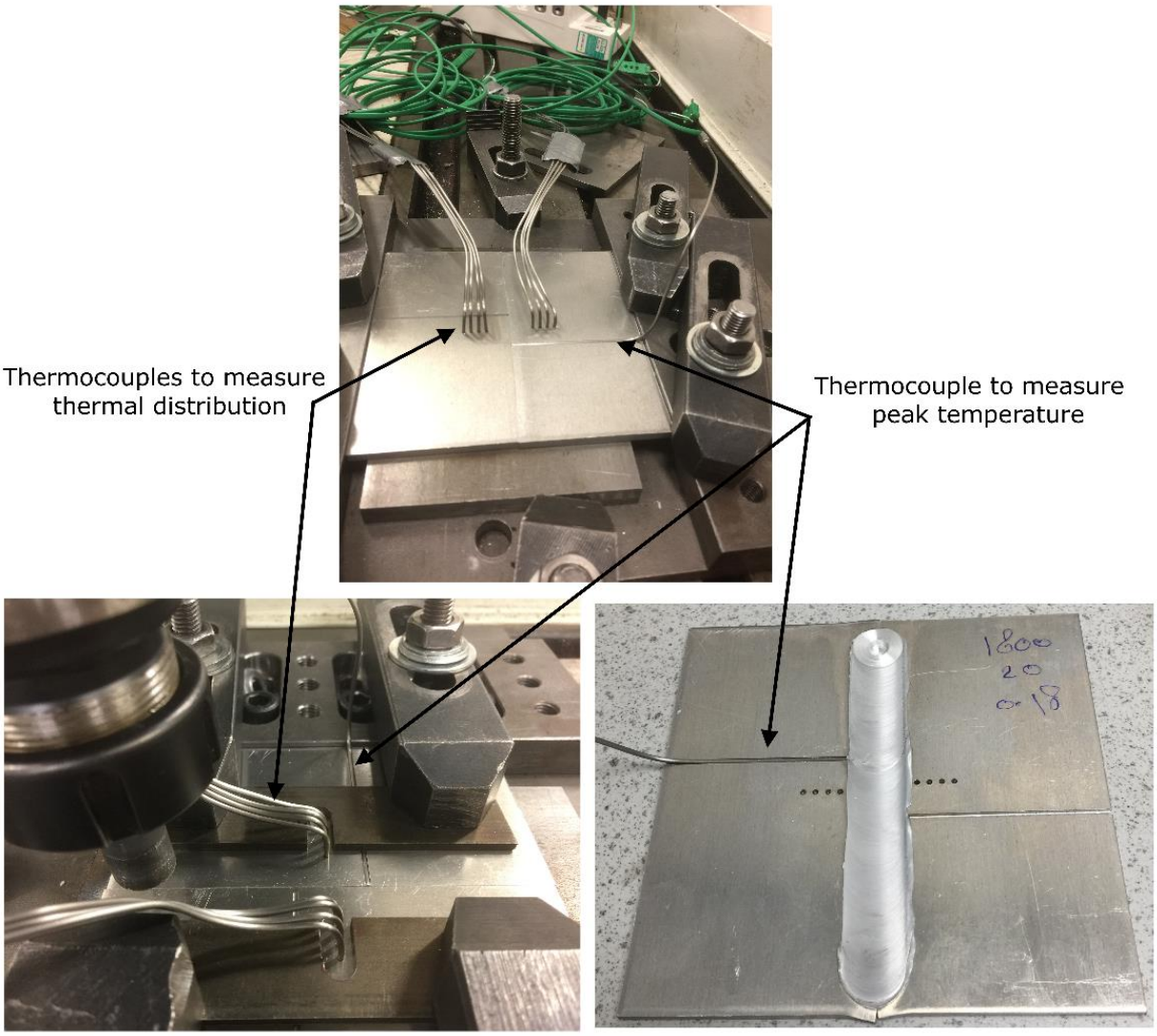


Figure 3-7 Photograph of the experimental setup and thermocouples locations



Figure 3-8 Infrared camera

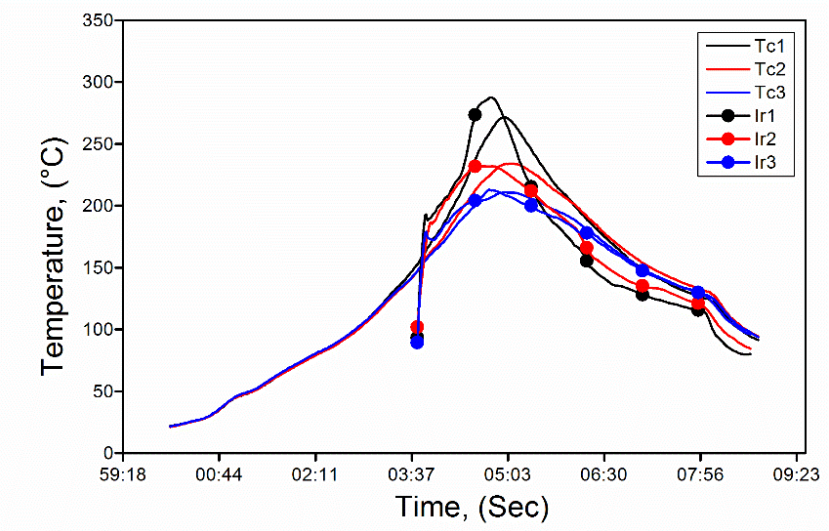


Figure 3-9 Temperature gradients through FSW joint measured by thermocouples and infrared camera

3.4 Metallurgical inspection

3.4.1 Optical microscope and Scanning Electron Microscopy (SEM)

Metallographic investigations were carried out for cross-weld joints to quantify the joint soundness and formation of macro defects. Samples were cut perpendicular to the welding direction (cross-welds) (Figure 3-6 (a)) using a slow speed diamond cutter to minimise deformation. The samples then hot mounted in conductive resin and prepared according to the standard metallographic techniques for specimen preparation consisting of grinding with 220, 400, 800, 1200, 2000 and 4000 grit emery papers followed by cloth polishing with 6 and 1 μm diamond. The macrostructural samples etched by Poulton's reagent and investigated by a Nikon optical microscope.

Scanning electron microscope (SEM) examinations were carried out by FEI Quanta 600 SEM with a tungsten filament was employed to analyse the cross-section of welds. A high-energy electron beam imaged the samples at an accelerating voltage of 20 with a spot size of 6 and a working distance of 10 mm. A range of signals produced from the interaction between the electrons and the sample's atoms. Microstructures were imaged through backscattered electron (BSE) imaging. Also, Energy Dispersive X-Ray Spectroscopy (EDS) mapping and the spectrum was used to determine the element distribution in the FSW joints.

3.4.2 Electron Backscattered Diffraction (EBSD)

The use of electron backscattered diffraction (EBSD) in the scanning electron microscope (SEM) has progressed over the past decade because of it is accuracy in quantitative analysis of grain and subgrain structures, as well as texture determination, with the development of field emission gun (FEG) SEM [104]. The sample preparation was carried out similarly to that for metallographic specimens, but a high surface finish

was obtained by using BUEHLER vibratory polisher with 0.06 µm colloidal silica to obtain a high surface finish as an extra step. The Microstructure and texture observations were carried out by high-resolution electron-backscatter diffraction (HREBSD). The EBSD analysis conducted by using a JEOL 7100F field-emission gun scanning electron microscopes (FEG-SEM) equipped with an HKL channel 5 Oxford EBSD system. The microscope was operated at 15 kV with stage tilted at an inclination of 70°, and a step size of 0.25 µm was used to scan the specimens. A lower limit boundary misorientation angle cut off 3° was used to avoid spurious boundaries, which is caused by misorientation noise. For grain-size measurements, a 15° misorientation criterion was used to differentiate between low-angle grain boundaries (LAGBs) and high-angle grain boundaries (HAGBs).

3.4.3 Transmission Electron Microscope (TEM)

Transmission electron microscope (TEM) was used in the current study to investigate the precipitate and intermetallic compound formed in the FSW joint of AA 6082-T6. Nano-scale transparent foils were extracted from the base metal, heat affected zone, and nugget zone by using a focused ion beam (FEI Quanta 200 3D FIB-SEM). The FIB system is provided with a liquid metal ion source (LMIS), (Gallium Ga* ions), that can be operated at high beam currents to deposit material onto a defined area typically of the order of microns, or to mill (cutaway) a specific site on the surface. In the current work, platinum (Pt) was deposited on the surface of the sample to protect the surface of the sample during milling processes, which was monitored continuously using SEM, then followed by milling steps to extract the sample and thinning as shown in Figure 3-10. The SEM was operated at accelerating voltages of 20kV; a probe current of up to 200 nA was used for imaging. The FIB system was operated at accelerating voltages of 30 kV

and a current of 1pA-20 nA for fast material removal. Bright-field imaging and selected area electron diffraction (SAED) TEM experiments were carried out by JEOL 2000 operating at an accelerating voltage of 200 kV using the 2-beam condition. The analysis of the fine precipitates composition was carried out by EDS.

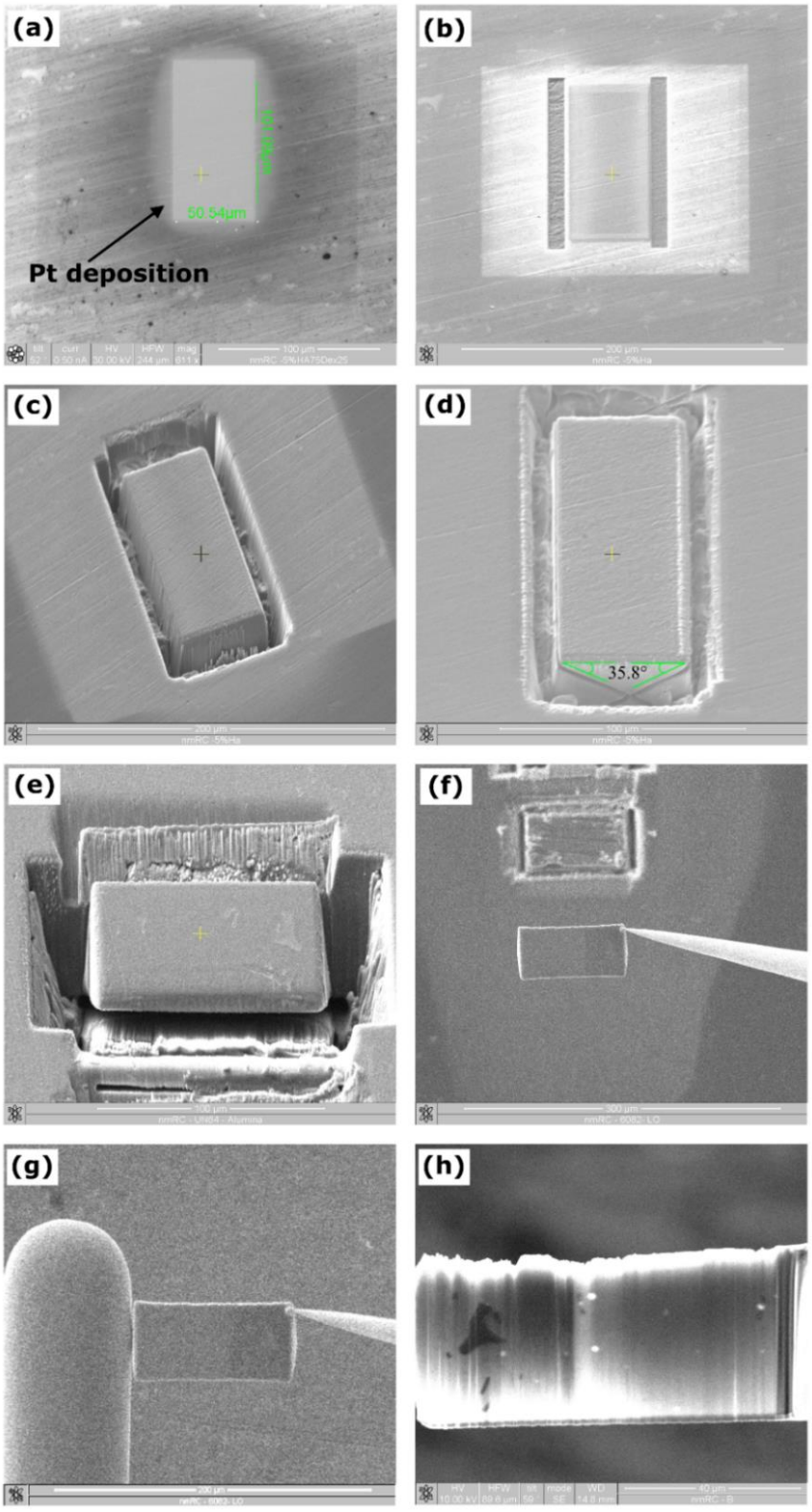


Figure 3-10 SEM micrographs showing the stage of TEM samples preparation by FIB machine; (a) Platinum coating, (b through f) Sample extraction steeps, (g and h) Sample thinning

3.5 Mechanical testing

3.5.1 Hardness testing

Microhardness testing was performed on the cross-weld FSW joints to establish the effect of thermal distribution on the hardness of joints. Before hardness measurement, samples were mounted and polished using standard metallographic techniques, with particular attention being paid to keeping the top and bottom surfaces parallel. A Vickers micro-indentation automated Buehler machine was used with the pyramid-shaped indentation and applied a load of 100 gf over a 30s dwell time. As a general rule, the spacing between the indentations has to be 2-5 times larger than the diagonal of the indentation. Therefore, 1 mm distance between successive indentations were used and the average Vickers microhardness mapping through the NZ of weld cross-sections was obtained from three readings at cross-weld; in the mid-thickness of the weld and above and under by 0.5 mm.

3.5.2 Tensile testing

For tensile testing, cross-weld flat dog-bone specimens were extracted from the FSW joints as shown in Figure 3-6 (a) using an electrical discharge machine (EDM). In addition to this, one longitudinal tensile sample was extracted from the weld line as shown in Figure 3-6 (b) to compare the influence of the tensile strength along the longitudinal and transverse direction of the weld. The samples prepared according to ASTM E8M-13a as shown in Figure 3-11 [105]. As the mechanical properties are severely affected by the introduction of stress raiser (stress concentration) such as surface roughness, thus, the surfaces of samples were ground by silicon carbide paper to 4000 grit and polished parallel with the direction of the principal tensile (par bars specimen) to produce a smooth surface. The tensile tests were carried out on an INSTRON 5581-50KN

servo-hydraulic test machine at a constant strain rate of 1 x 10^{-4} s^{-1}, with extensometer having a gage length of 25 mm as shown in Figure 3-12. Also, for some samples, Dantec Q-400 DIC (Digital Image Correlation (DIC)) system as shown in Figure 3-13 was used to measure the displacement on the surface of the sample and then map the variation of strain through the cross-weld (BM, HAZ, TMAZ, and NZ). A speckle pattern marker was applied to the surface of the tensile sample with white paint, then a random black speckle as shown in Figure 3-14 to enable data to capture by coupled charge device (CCD) camera. One image per four seconds was captured during deformation processes, then processed by using the ISTRA-4D software to provide two-dimensional strain map.

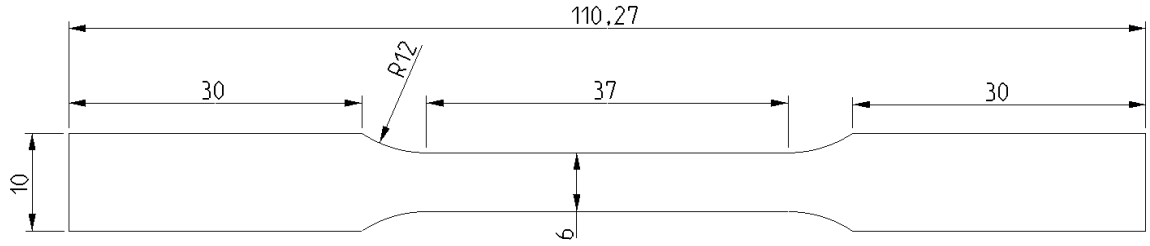


Figure 3-11 Tensile sample (all dimensions in mm)



Figure 3-12 Tensile with an extensometer

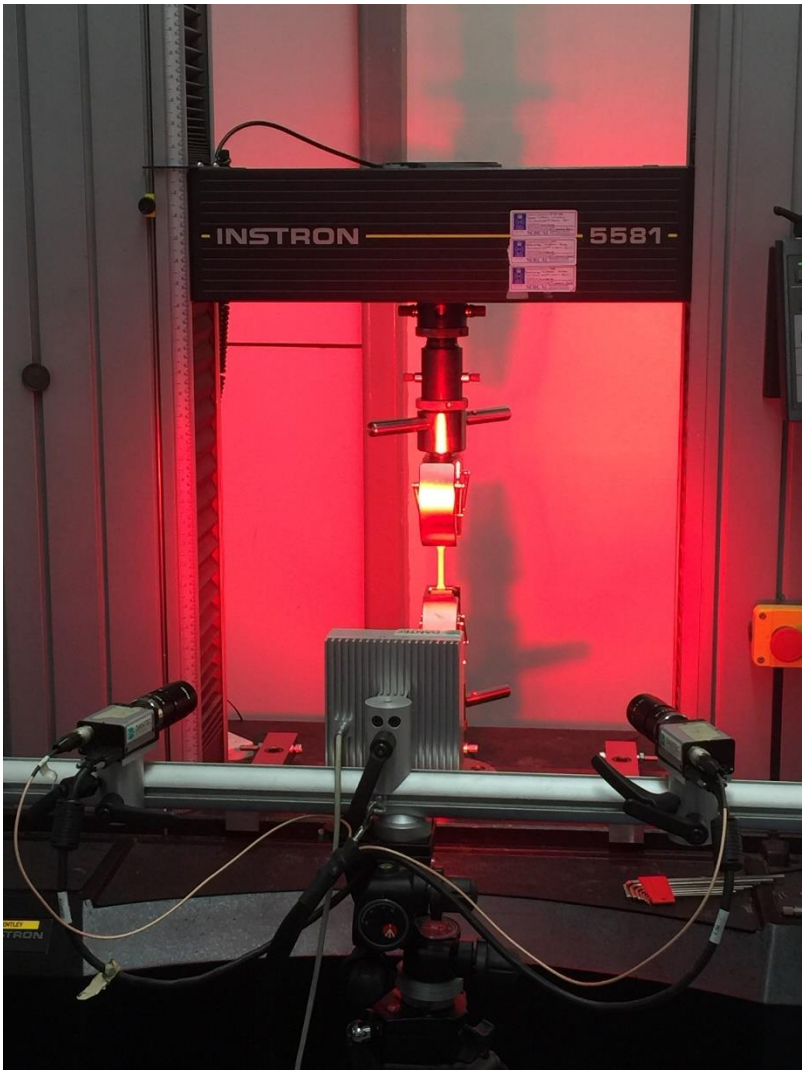


Figure 3-13 Tensile with DIC system

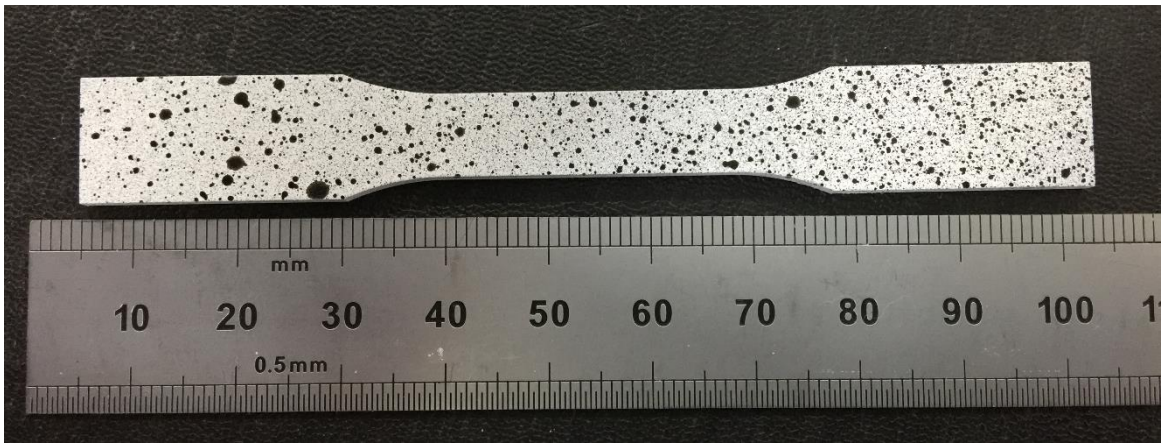


Figure 3-14 DIC tensile sample

3.5.3 Low cycle fatigue (LCF) testing

For fatigue testing, cross-weld flat dog-bone LCF specimens were extracted from the FSW joints as shown in Figure 3-6 (a), using an electrical discharge machine (EDM). The specimens were prepared according to BS ISO 12106:2017 as shown in Figure 3-15 [106]. The samples then ground and polished parallel to the principal load direction to exclude the effect of stress concentration, and non-homogeneous distribution of thicknesses caused by the FSW. The fatigue tests were performed on INSTRON 8801-50KN servo-hydraulic test machine in a fully reversed total strain-controlled condition (R= -1) (symmetric tension-compression strain cycle), with triangular waveforms conducted at a constant total strain rate of $5x10^{-4}s^{-1}$ at ambient temperature. An INSTRON axial clip extensometer made of alumina with a gage length of 12.5 mm was attached to the gauge section of the test specimen to control the amount of applied strain as shown in Figure 3-16. The extensometer converts the mechanical displacement of the test specimen into an electrical signal with the conditioned signal permitting the monitoring and/or controlling of the specimen applied strain. Different range of strain amplitudes were used for different material and cross-weld joints ranging from 0.2 % to 0.7%. The fatigue failure criteria were defined when the maximum tensile stress had dropped by 30% below that at initial life. As the test was done for flat specimen under completely cyclic test, thus the samples are significantly influenced by the bending stresses. The first issue appeared to be the dominant factor is a failure by buckling as shown in Figure 3-17. Therefore an anti-buckling restraints with a lubricant to reduce friction action was used for LCF test.

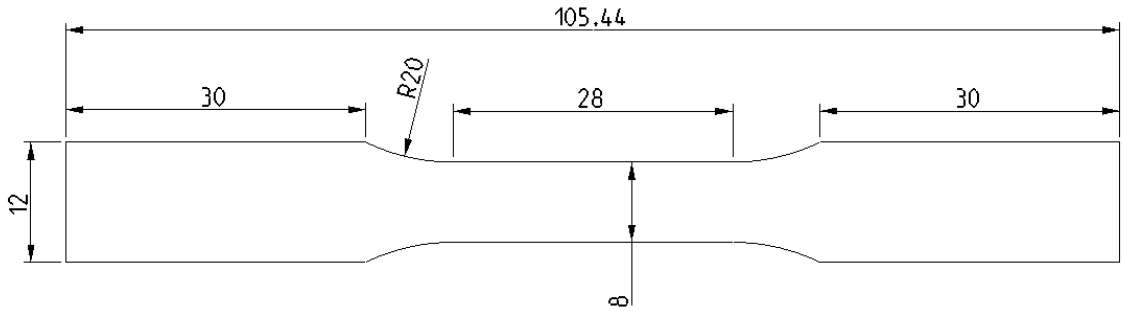


Figure 3-15 LCF sample (all dimensions in mm)

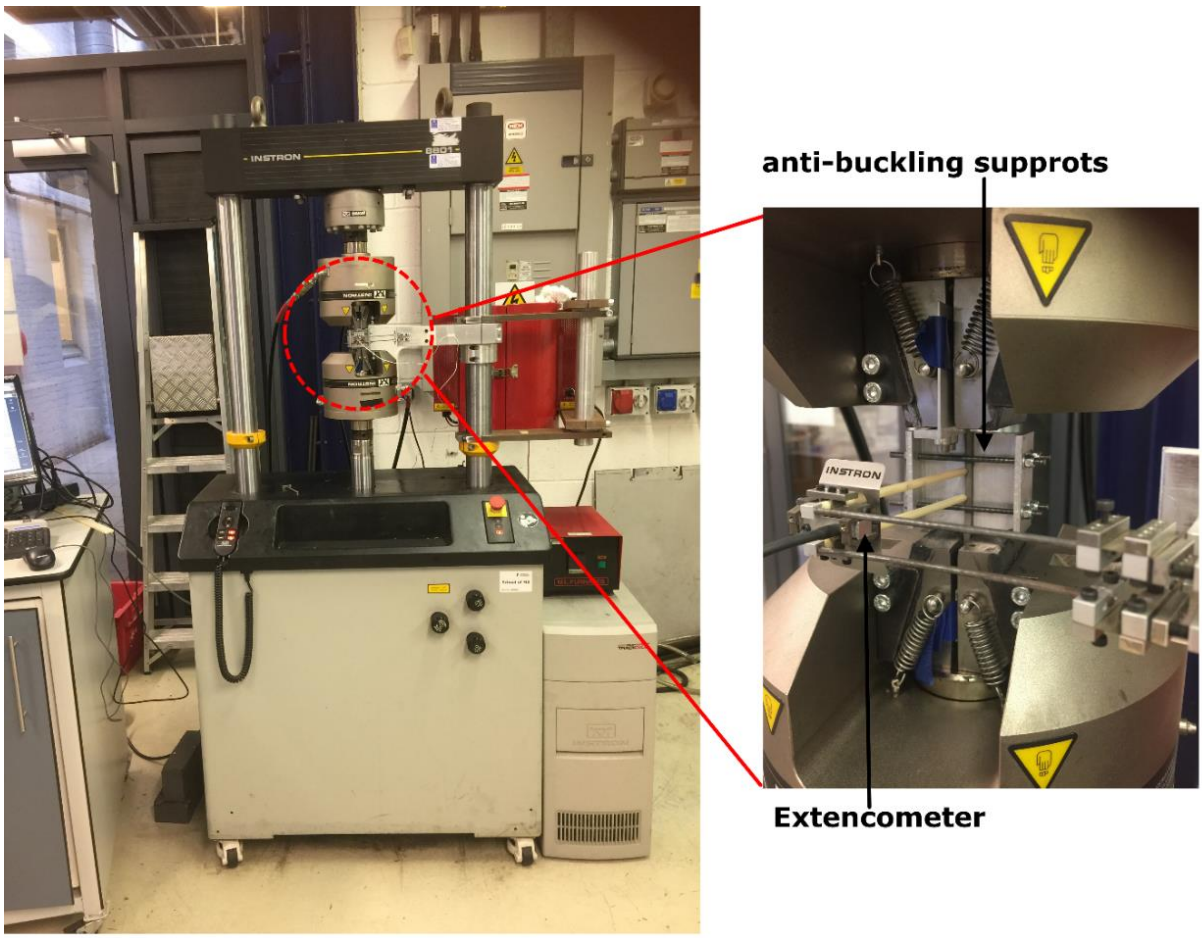


Figure 3-16 Fatigue machine and anti-buckling



Figure 3-17 Low cycle fatigue buckling sample

3.6 Residual stress measurement

3.6.1 Overview of instrument

Residual stress measurement has been done by neutron diffraction using the beamline ENGIN-X, ISIS, Rutherford Appleton Laboratory, Oxford, United Kingdom (Figure 3-18). ISIS owns the world's brightest pulsed neutron source [107]. The concept of measuring of residual stress in this instrument is based on the measurement of the macroscopic elastic strain tensor as it is defined by the time-of-flight (TOF) neutron strain scanner at definite locations in the bulk of the sample. A pulsed neutron beam with a wide energy range travelling to the sample and being scattered into detectors at an angle of 2θ as shown in Figure 3-19 (a) [108].

The instrument consists of four major components. A collimated incident pulsed neutron beam (moderator), xyzω positioner (to position the gauge volume within the sample), secondary flight-path radial collimators (which define the gauge volume), and neutron detectors. These components are illustrated in Figure 3-19 (a and b). In addition to two telescopes (theodolites) and a laser/CCTV system to enable the sample to be accurately aligned, and monitoring the motion of the sample. When measuring the strain within an engineering component, it is essential to know where the measurement has been taken. For this reason, the position of the gauge volume must be well characterised by using the positioner. In pulsed instrument the volume of material contributing to the diffraction pattern (gauge volume) is defined by the intersection between the incident and diffracted beams, which typically defined by slits and collimators, respectively (Figure 3-19 (a)). The two radial collimators each have 40 vertical foils vanes made from gadolinium oxide coated Mylar, which constrains the detectors to receive neutrons from a small volume. As can be seen in the figure, the instrument has two banks of detectors

to count neutrons as a function of time, each centred on a Bragg angle (2θ) of ±90°, when the Bragg's Law is satisfied for some lattice spacing d_{hkl}, diffraction peaks occur and are measured at times t_{hkl} elapsed after the initial pulse [107, 108].

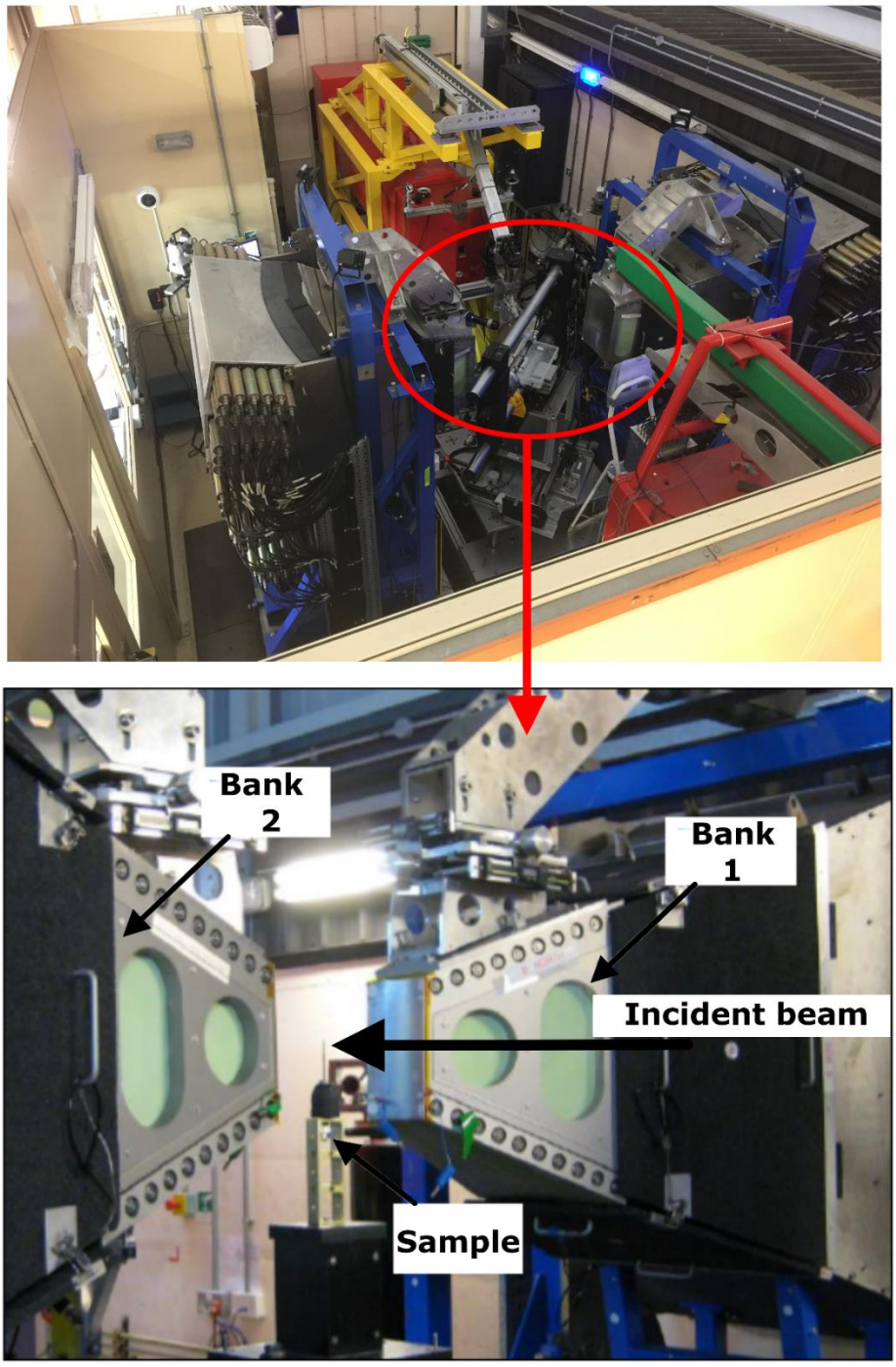


Figure 3-18 ENGIN-X

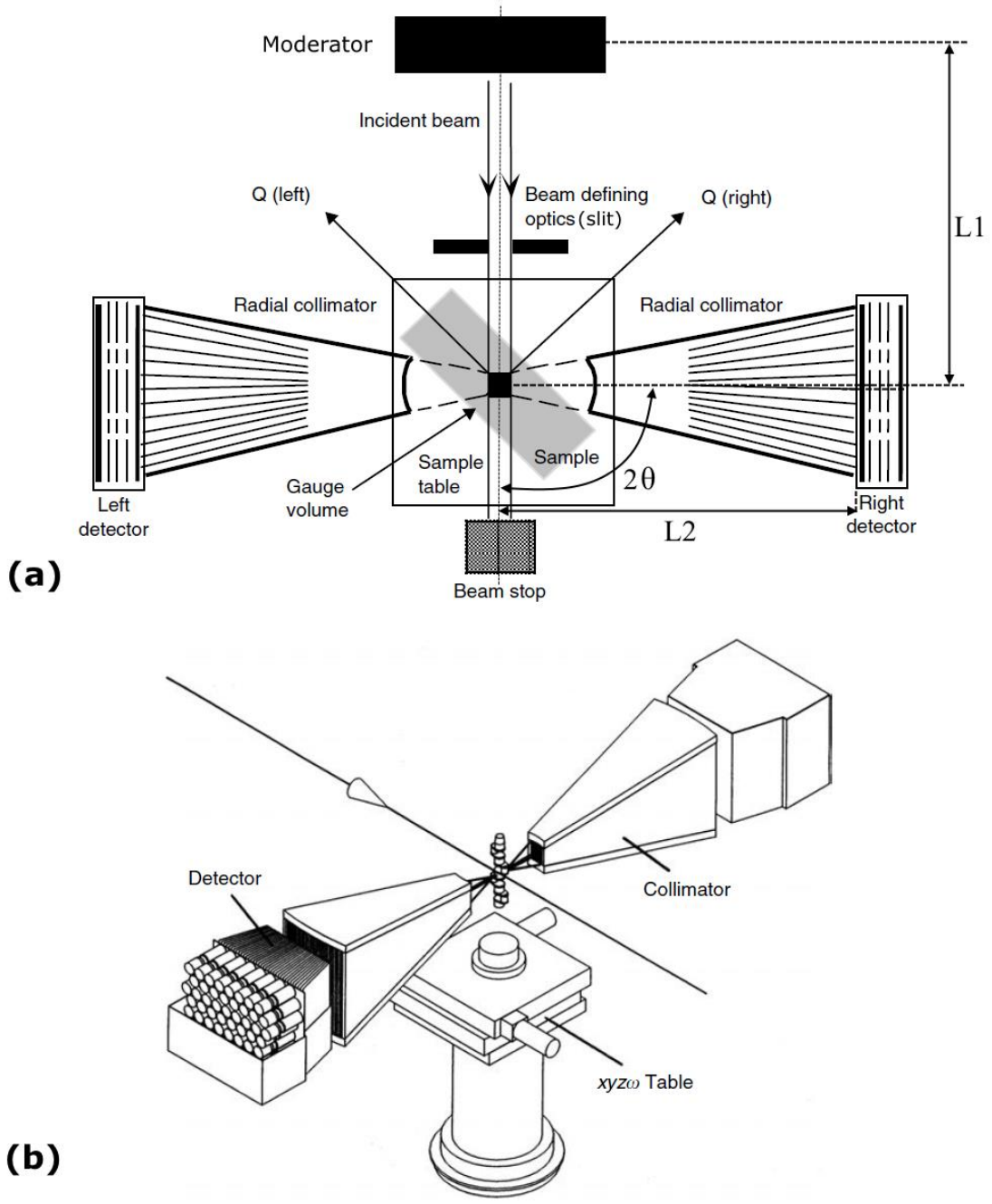


Figure 3-19 (a) Plan view of the ENGIN instrument. The arrows marked 'Q' indicate the directions in which strain is measured by the two detectors, and (b) Schematic view of the ENGIN instrument [107]

3.6.2 Samples

The cross-welded residual stresses were measured in AA 6082, AMC, and SAMC FSW joints by the ENGIN-X. For AA 6082 one welded joint has been examined, while for AMC and SAMC two joints for each were tested, in total five samples. For all tested

joints, the location of cross-weld measurement line was in the middle of the joint line as shown in Figure 3-20. The measurements were taken in the mid-thickness of the joint. To obtain the strain-free lattice spacing d_o, thin samples were cut from the same joints and locations after testing by EDM. As the thickness of sample and welding temperature is not too high, thus the cutting process is enough to release the induced residual stresses and gives strain free lattice.

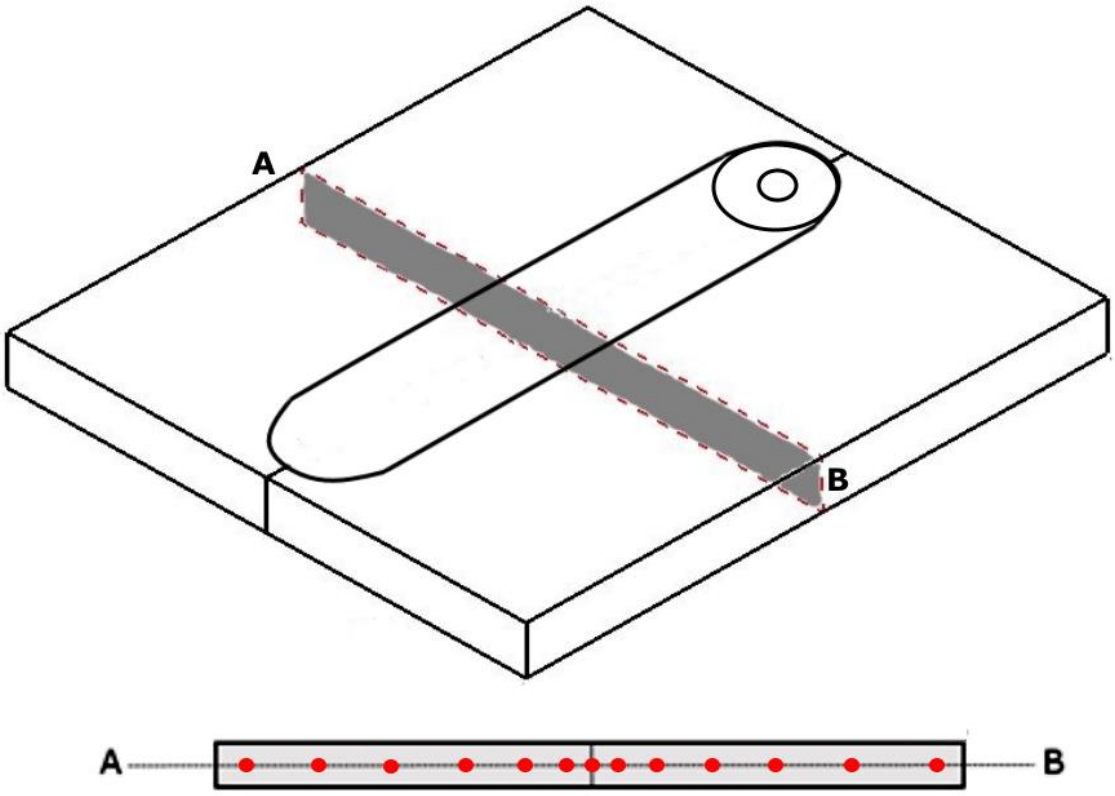


Figure 3-20 Schematic drawing FSW sample measured by neutron diffraction the grey shaded area and red dot show the positions of measurement

3.6.3 Measurement set-up

Due to the configuration of the ENGIN-X, with a single scan, the strain is measured in normal (X-X), and longitudinal (Y-Y) or transverse (Z-Z) direction based on the position of the sample (Figure 3-21 (a)). Therefore, to measure both longitudinal and transverse strain, the scan was repeated twice for each sample with changing the weld

line direction. When the weld is horizontal and the angle between the incident beam and the plate surface plane was 45°, resulting in one of the two vectors was in the direction of the longitudinal (Y-Y) strain and the other vector in the direction of the normal (X-X) strain as indicated in the Figure 3-21 (b). On the other hand, when the weld line in the vertical position this leads to measure the transverse (Z-Z) and normal (X-X) strain as shown in Figure 3-21 (c). The transverse measurements were taken with a gradual increase in a spatial resolution from the weld centre at points located at the middle layer of the thickness as shown schematically in Figure 3-20.

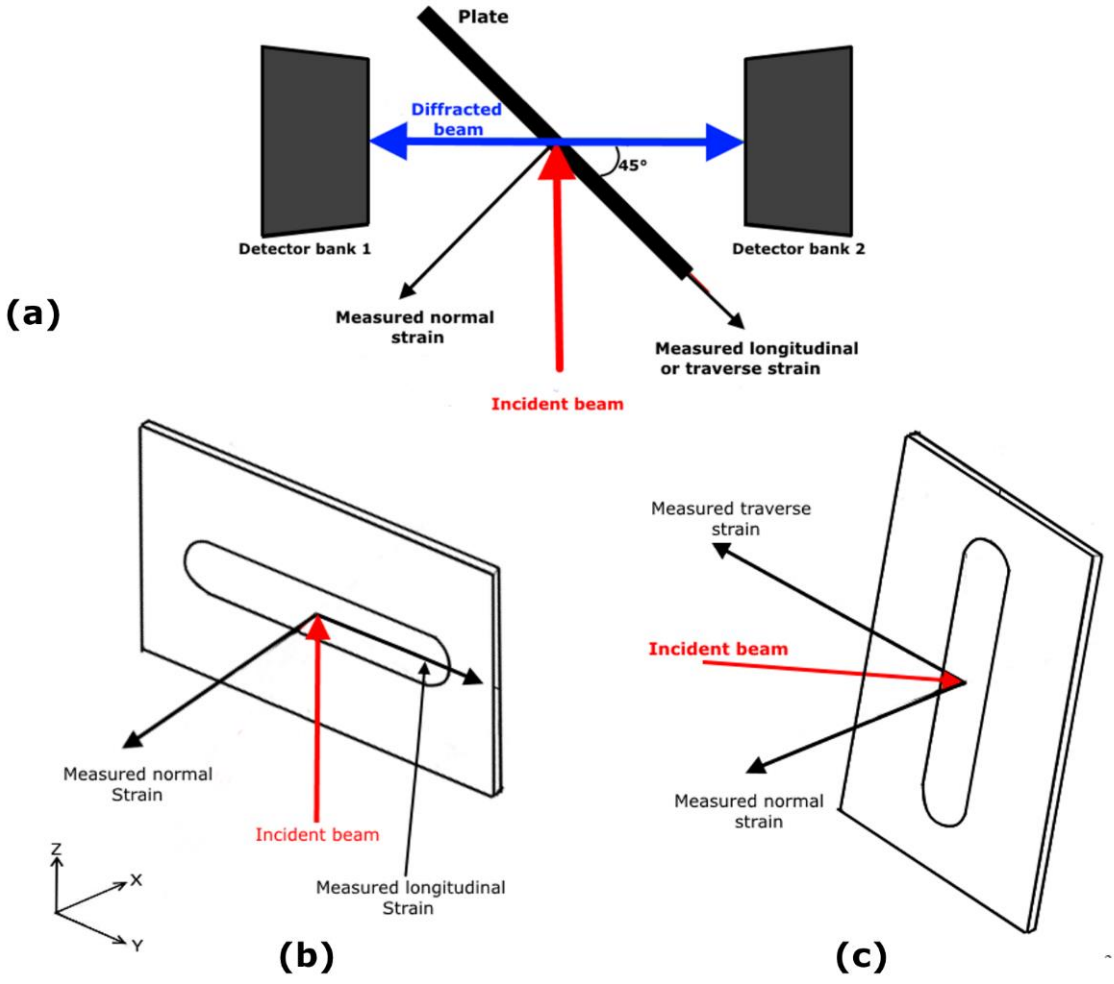


Figure 3-21 (a) Sample position of ENGIN-X measurement, (b) Sample position to measure longitudinal strain, and (c) Sample position to measure traverse strain

3.6.4 Data analysis of neutron measurements

The ISIS pulsed neutron source is a time-of-flight facility. Thus a full diffraction spectrum was obtained from each point and measured by ENGIN-X. The Diffraction profiles were analysed using multiple peaks fitting Pawley refinement with the software package 'Open Genie' which utilises GSAS. Neutron diffraction measurements use lattice-spacing as a strain gauge, which is obtained from Bragg's law. From the measured lattice-spacing of the welded specimen and stress-free reference the strain was calculated from:

$$\varepsilon = \frac{d - d_o}{d_o}$$

Where d is the lattice parameter for each measurement point and d_o is the measured stress-free lattice parameter. For the welding samples, because of the symmetry of principle directions coincide with the normal, transverse, and longitudinal directions, so that the strain was measured in these three principal strain directions. The measured strain were combined with a Young's modules E, and Poisson's ratio v to calculate the principle stresses in each direction using Hooke's law, given by the following equations.

$$Normal\ direction: \quad \sigma_{11} = \frac{E}{1+v}[\varepsilon_{11} + \frac{v}{1-2v}\ (\varepsilon_{11} + \varepsilon_{22} + \varepsilon_{33})]$$

$$Longitudinal\ direction: \quad \sigma_{22} = \frac{E}{1+v}[\varepsilon_{22} + \frac{v}{1-2v}\ (\varepsilon_{11} + \varepsilon_{22} + \varepsilon_{33})]$$

$$Tranverse\ direction: \quad \sigma_{33} = \frac{E}{1+v}[\varepsilon_{33} + \frac{v}{1-2v}\ (\varepsilon_{11} + \varepsilon_{22} + \varepsilon_{33})]$$

For all tested joints, in order to maximise data acquisition rates, the gauge volume was adjusted depending on the orientation of the measurement. When measuring in the transverse plane directions, 2 mm x 2 mm x10 mm 'matchstick' gauge was used aligned

with the weld direction. While for the longitudinal measurements the matchstick was shortened and the gage volume was 2 mm x 2 mm x2 mm.

3.7 Summary

The chapter gives an overview of the experimental methods used in this study. FSW has welded three different material based on aluminium-magnesium-silicon series alloy (AA 6xxx), namely aluminium alloy AA 6082-T6, AMC (AA 6092/SiC/17.5p), and SAMC (AA 6061B/SiC/20p) under different welding conditions of tool rotation and traverse speed. Welding fixture and tool design has been presented, as well as the setup of the FSW machine and the technique of measuring the peak welding temperature and thermal history during the welding process. Both metallurgical and mechanical characterisation has been done to assess the effect of welding parameters on the final weld quality. Optical microscope, SEM, EBSD, and TEM have been used to quantify the evolved macrostructure and microstructure in the FSW joints. Also, microhardness, tensile, and low cycle fatigue test have been done to evaluate the mechanical properties of the welded joints. Furthermore, the residual stresses measurement technique by neutron diffraction for the welded joints has been presented. These tests have made a significant contribution to life assessment of the welded components and have provided useful directions to the process development and improvement.

Chapter 4 Thermal history and metallurgical characterisations of AA 6082, AMC, and SAMC FSW joints

4.1 Introduction

This chapter aims to determine the influence of FSW parameters (tool rotation and traverse speeds) on the heat input and thermal cycle and subsequently on the metallurgical characterisation of FSW joints, to provide insight for the microstructural development under different welding conditions. The characterised welds divided into three groups based on the type of alloy; the first is the aluminium alloy (AA 6082-T6) welds, which was welded by using the welding parameters shown in Table 3-3. The second was the AMC (AA 6092/SiC/17.5p-T6) welds, and thirdly SAMC (AA 6061B/SiC/20p-T1), which were welded using same welding parameters as shown in Table 3-4. For all groups, the metallurgical results cover the characterisation of joints in term of joint soundness, grain size, grain structure, along with the grain substructure, and misorientation angle distributions. Furthermore, as the all studied materials in this work are based on Al-Mg-Si (AA 6xxx). Thus more detailed investigations are conducted for the first group as a benchmark thorough metallurgical characterisation in term of grain texture, and microstructural-strength (strengthening precipitate).

4.2 Aluminium alloy AA 6082-T6

4.2.1 Welding temperature and thermal history

In order to evaluate the effect of tool rotation and traverse speeds on the thermal history of the welded joints, detailed temperature measurement in the NZ and cross-weld in the AS and RS was conducted by thermocouples. Figure 4-1 depicts the NZ peak temperature under different FSW parameters. The higher the tool rotation speed, the higher the generated temperature. For example, as the tool rotation speed increased from 800 to 1800 rpm at a constant tool traverse speed of 20 mm/min, the peak temperature increased from nearly 442°C to 593°C (~from 0.67 to 0.9 Tm) (where Tm is the melting point). On the other hand, the increase of tool traverse speed from 20 to 200 mm/min with a lowest tool rotation speed of 800 rpm leads to the rise of peak temperature from about 442°C to 451°C. This trend can be attributed to the higher heat generation due to friction than shearing at the interface between the tool and the BM at higher tool traverse speed, which is resulted from the higher slip. While opposite trend is noticed with higher tool rotation speed, i.e., less heat input was generated with higher tool traverse speed.

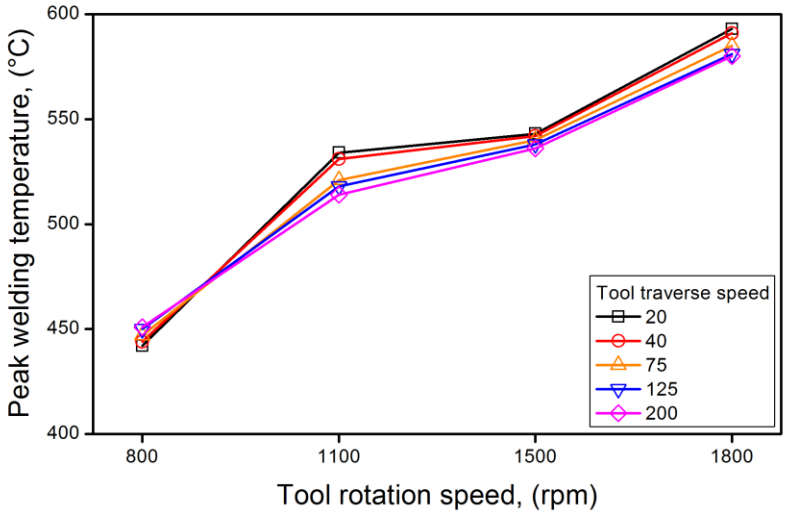


Figure 4-1 Effect of FSW parameter on the peak temperature of AA 6082 FSW joints

Although the tool rotation speed dominated the FSZ temperature, the exposure time at high temperature and heating and cooling rate were more influenced by the tool traverse speed. Figure 4-2 compares the thermal cycle at the centre of NZ from the peak temperature concerning the welding time for four joints (welding matrix corners). Each of these curves can be divided into three stages; plunge and preheating, welding and cooling. For instance, the denoted lines t1, t2, and t3 represent these stages, respectively for the W1 and W16 joints. The lower the tool traverse speed, the slower changes in the temperature during both heating and cooling (slower heating and cooling rate).

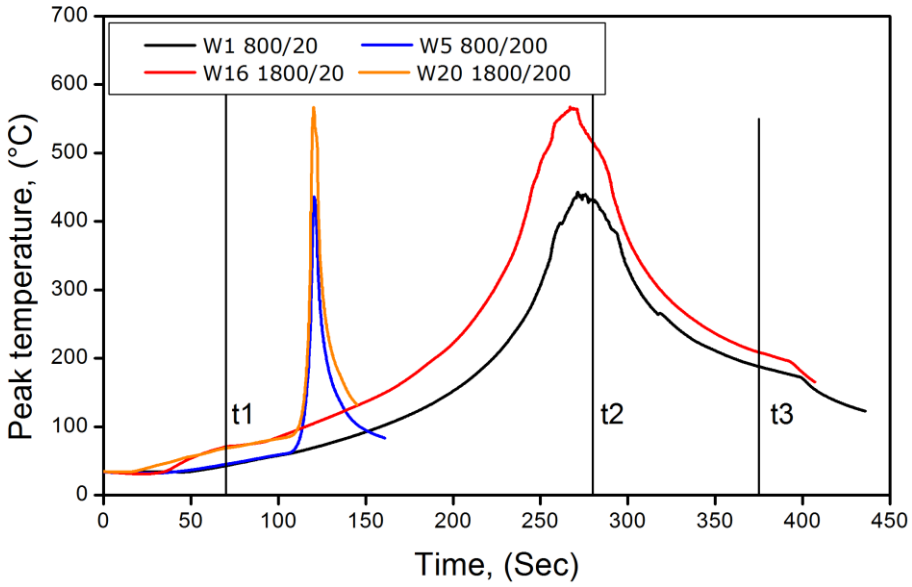


Figure 4-2 Effect of FSW parameters on thermal history in the NZ of AA 6082 FSW joints

Figure 4-3 presents the cross weld thermal cycles of the joint welded at highest and lowest tool rotation and traverse speeds (corners of the welding matrix) in the middle of welding line at several monitoring locations on the retreating side (RS) (TC1-TC4), and advancing side (AS) (TC5-TC8) (as presented in Figure 3-6) [Thermal history for all joints are found in Appendix A]. The results of the four joints show an unsymmetrical distribution in the temperature concerning the weld line; a higher temperature is conducted in the RS than the AS. Also, the thermal cycles are characterised by higher

heating rate followed by a relatively slower cooling rate as the tool moves away from the locations of TCs. Consistency with a measured peak temperature in the centre of the NZ, the induced temperature on the RS and AS is higher as the tool rotation speed increases.

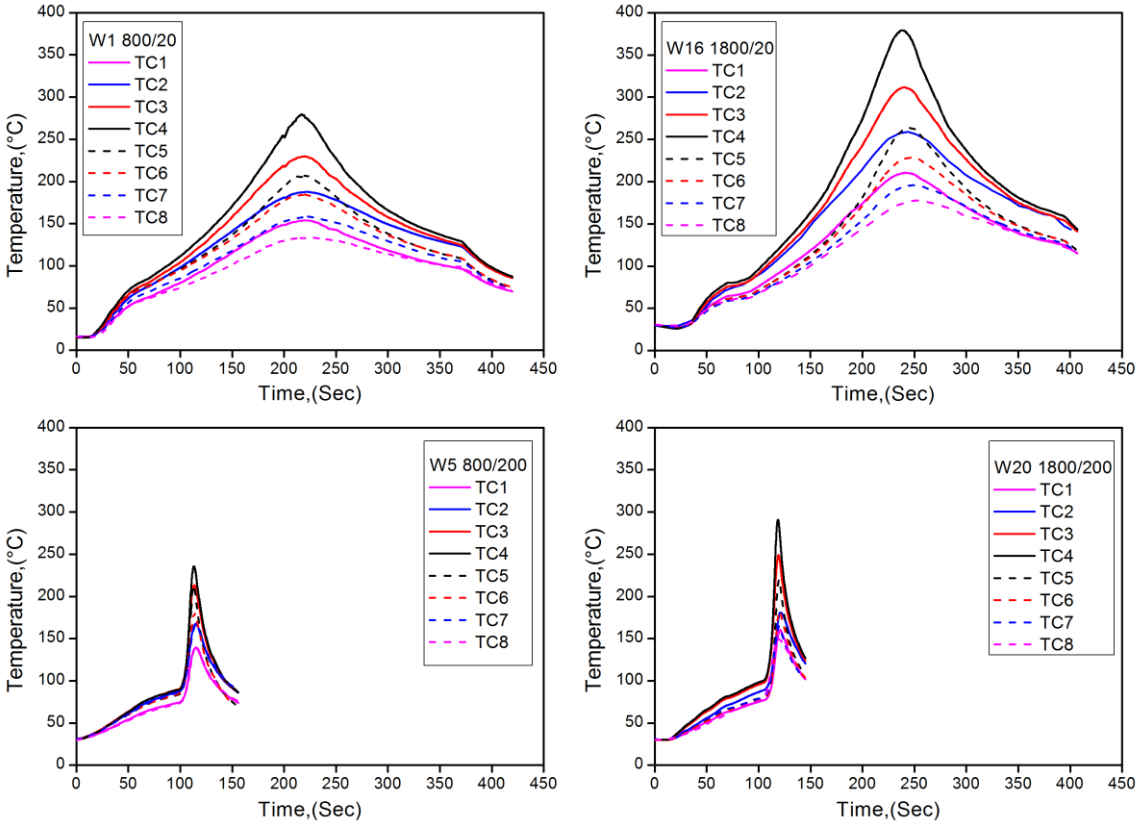


Figure 4-3 Thermal cycles on the RS and AS of W1, W5, W16, and W20 AA 6082 FSW joints

4.2.2 Metallurgical characterisations of the as-received AA 6082

Figure 4-4 shows the microstructure of the as-received AA 6082, including the EBSD Euler map, grain size distribution, and misorientation angle. The EBSD map is shown in Figure 4-4 (a), where the red and black lines represent the LAGBs and HAGBs, respectively. It is seen that the BM exhibits a highly elongated pancake shape grain structure with a mean grain diameter of 45 μm (see Figure 4-4 (b)) highly dominated by HAGBs as shown in Figure 4-4 (c), which is the typical structure resulted from the rolling process.

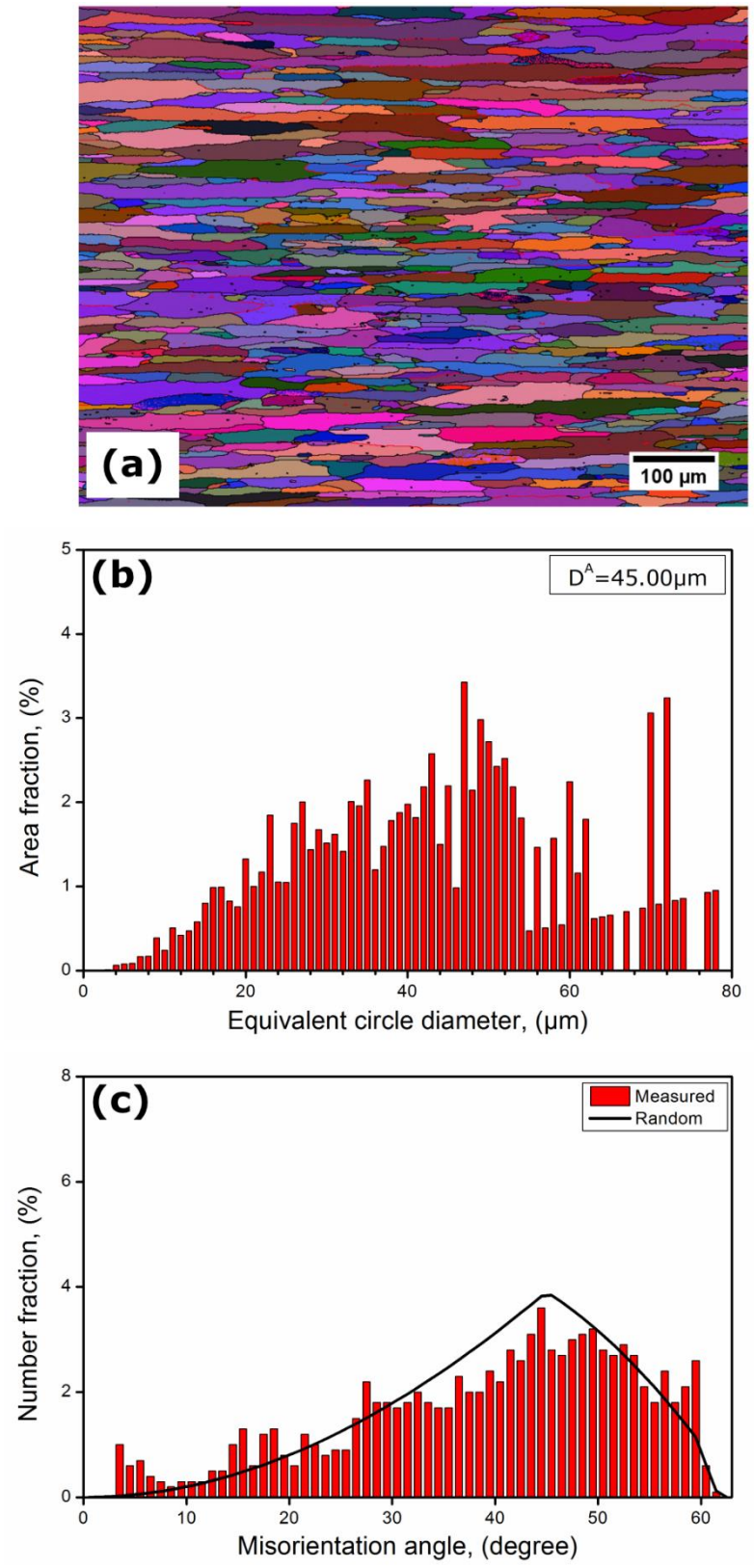


Figure 4-4 Microstructure characterisation of AA 6082; (a) EBSD map, (b) Grain size distribution, and (c) Misorientation angle

Based on the EBSD maps, pole figures of the BM calculated over areas 93,000 μm^2 with a step size of 0.25 μm are shown in Figure 4-5. The pole figures were generated using Oxford Instruments CHANNEL 5 software, by equal area upper hemisphere projection, contoured with a half-width of 20° and 5° data clustering. It is seen that cube texture is the dominant orientation in BM, which is known as a typical recrystallised texture in FCC. Also, the BM has a coarse grain structure dominated by HAGBs (see Figure 4-4) so that recrystallisation generated during the production characterises the BM.

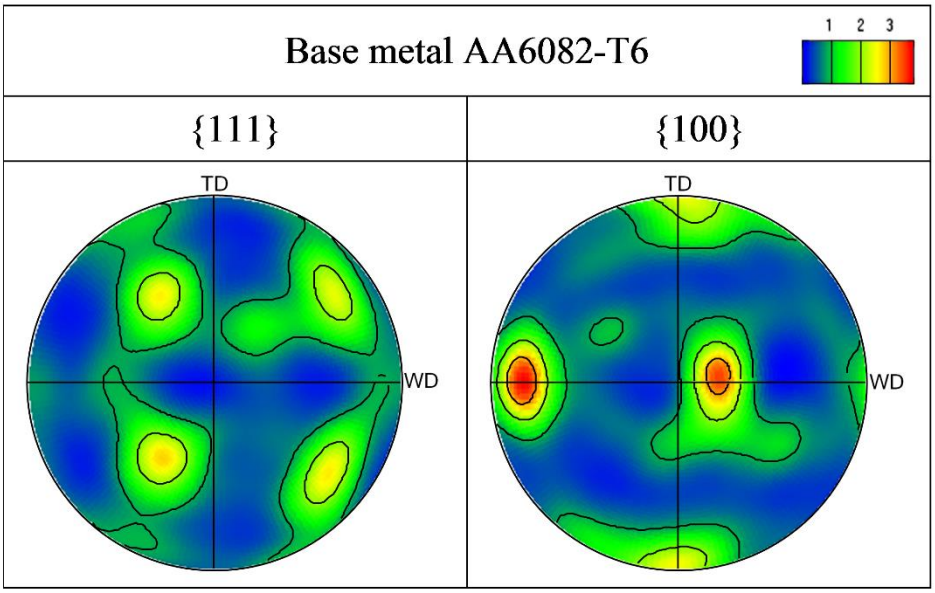


Figure 4-5 Pole figures of the as-received AA 6082

Furthermore, TEM observations made in the BM as shown in Figure 4-6 to characterise the strengthening precipitate as this alloy in T6 conditions. Three different types and shapes of precipitate are revealed in these TEM micrographs. Firstly, coarse irregularly shaped precipitates more than one μm in size was found as shown in Figure 4-6 (a). This phase is consisted of Al, Fe, Si, Mn, Cu, Cr, and Ni, as revealed by the Energy Dispersive X-Ray Spectroscopy (EDS) spectrum (see Figure 4-7-phase 1). The EDS results indicate there must also be some substitution of Cu, Cr and Ni into the

lattice. The red circle in Figure 4-6 (a) shows approximately the related selected area electron diffraction patterns (SAED) (Figure 4-6 (e) (SAED 1)). All patterns match well with an $Al_{57}Mn_{12}$ type structure with space group 200($Pm\bar{3}$), with the substitution of Si into some or all Al sites in the lattice and substitution of Fe into Mn sites. Secondly, Fine homogenously distributed rounded precipitates up to 500 nm in size were observed in the BM as shown in Figure 4-6 (a and b). The typical EDS spectrum detected Al, Mn, Si, Fe, Cr, Cu; sometimes also a little Mg, Ni or V as shown in Figure 4-7-phase 2. The EDS results indicate there must also be some substitution of Fe, Cr, and Cu into the lattice. The related SAED patterns (Figure 4-6 (f) (SAED 2)) showed well match with an $Al_{57}Mn_{12}$ type structure with space group 200 ($Pm\bar{3}$) same as irregularly shaped precipitates, with the substitution of Si into some or all Al sites in the lattice. Thirdly, very fine linear precipitates structure with high density were observed as shown in Figure 4-6 (c and d) white arrow, both Zandbergen et al. [109] and Marioara et al. [78] proven that the ideal structure and composition of this phase in an Al-Mg-Si alloy was determined to be Mg_5Si_6 ($\acute{B}$), which occurred as precipitates and were related with a mainly strong increase in the mechanical strength.

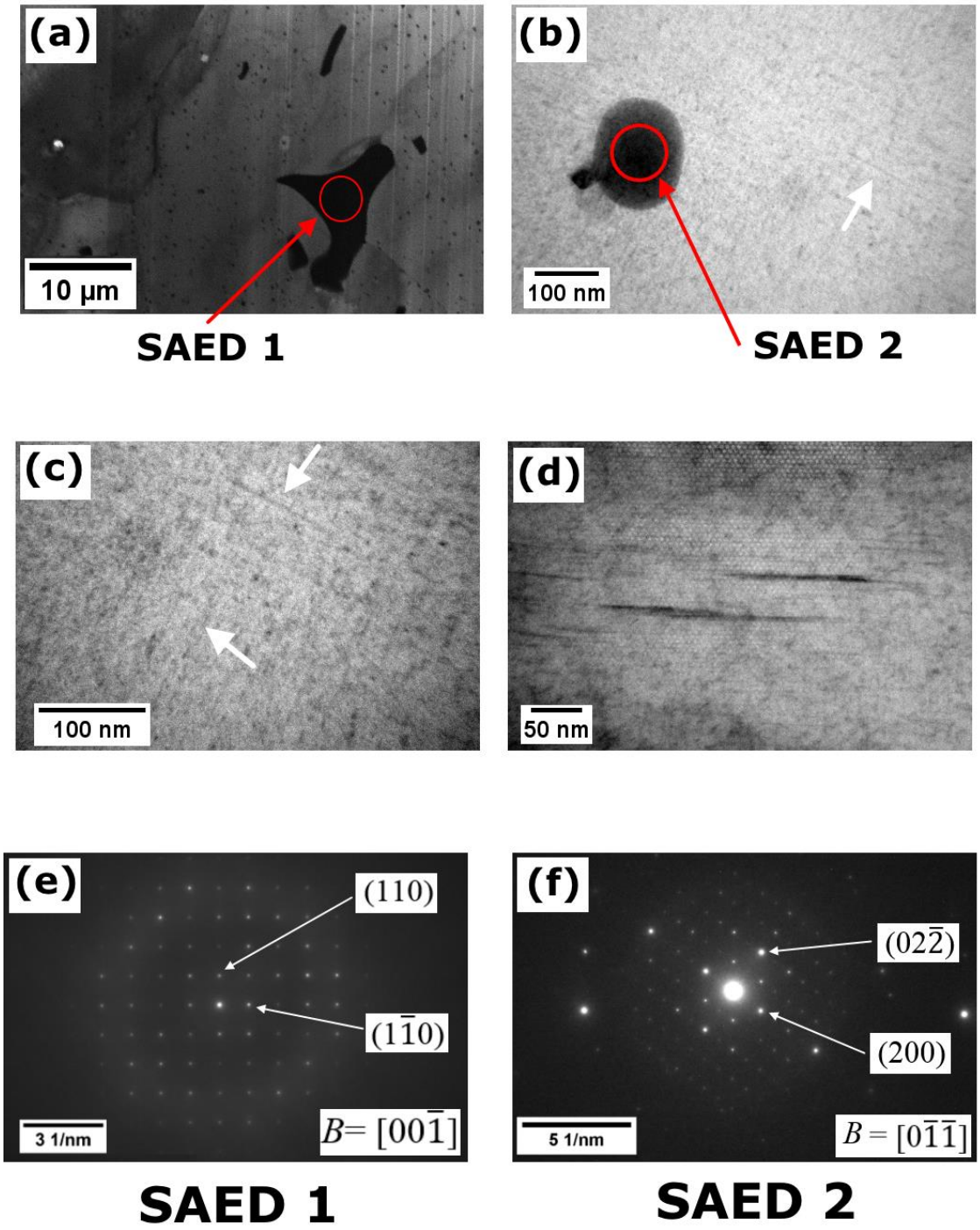


Figure 4-6 (a-d) TEM bright field micrographs in the as-received AA 6082, and (e-f) Related selected area electron diffraction (SAED)

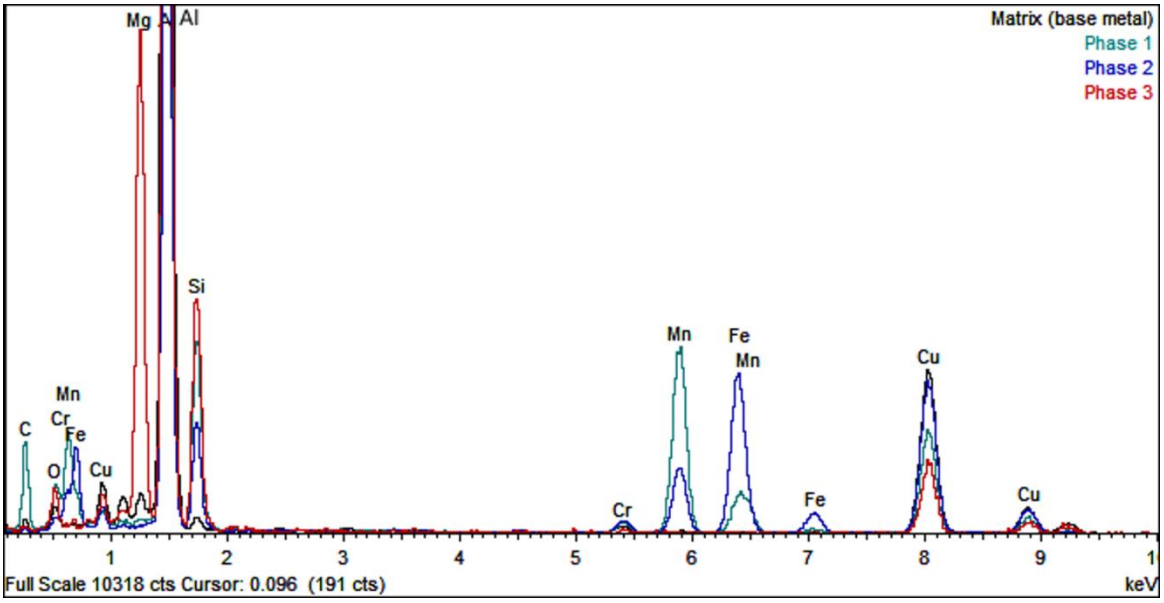


Figure 4-7 EDS spectrum related to the TEM

4.2.3 Metallurgical characterisations of AA 6082 FSW joints

4.2.3.1 Macrostructure and surface morphologies of the weldment

The metallurgical characteristics of AA 6082 FSW joints were significantly affected by the variation in the thermal history and plastic flow. Typical features such as exit hole profile, NZ profile, tunnel defect, lack of penetration, onion ring structure, flash (wake effect) and surface appearance were examined for all FSW joints. Figure 4-8 shows the surface morphology and exit hole profile of friction stir welded joints obtained at a different combination of tool rotation and traverse speed, while Figure 4-9 presents the related cross-weld macrostructure images.

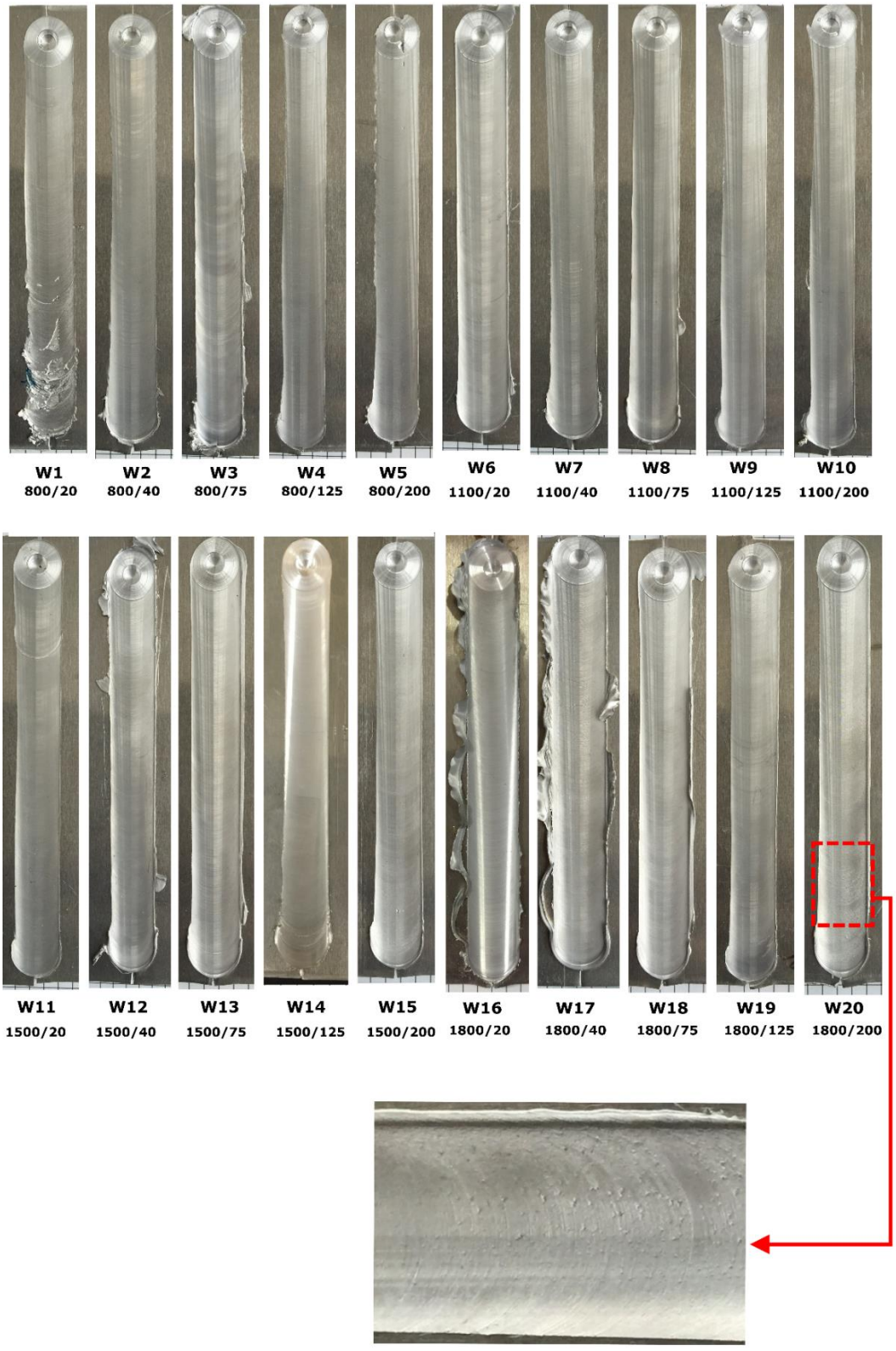


Figure 4-8 Surface morphology and exit hole profile of AA 6082 FSW joints under different welding parameters (AS on the right)

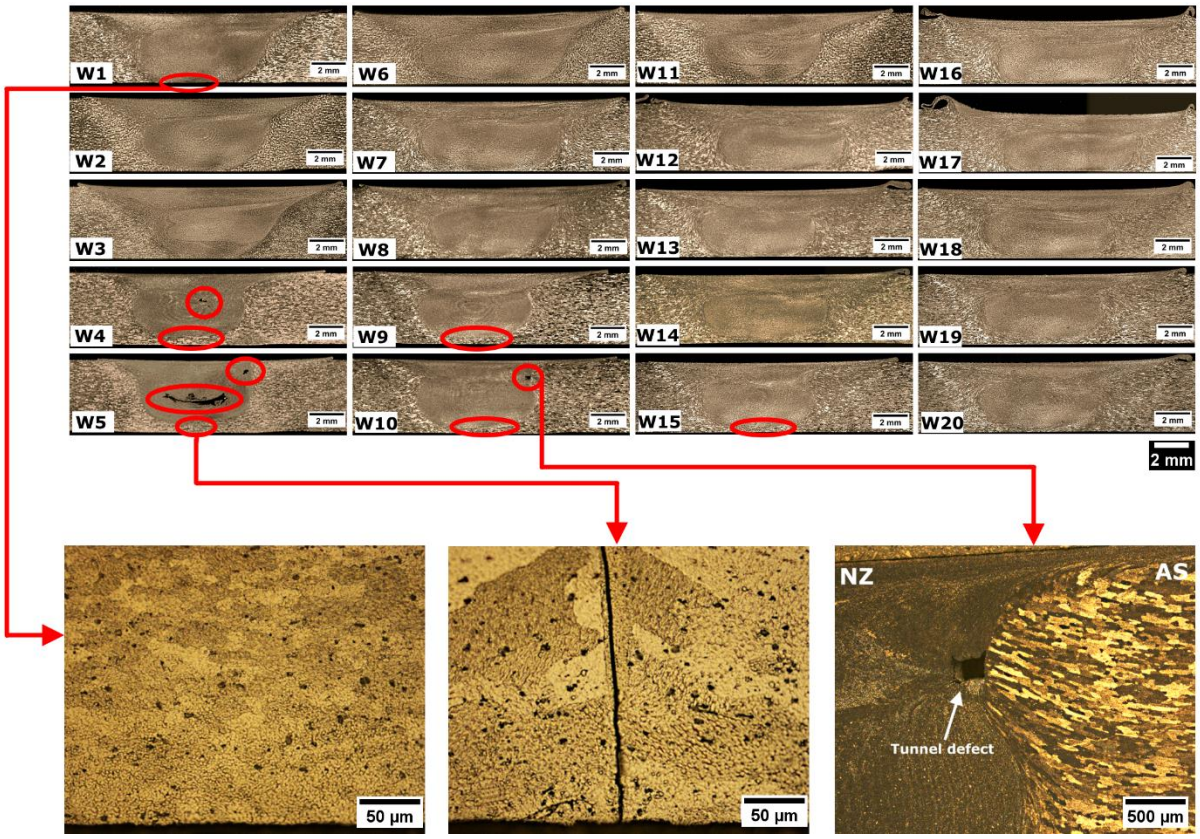


Figure 4-9 Cross-weld macrostructure of AA 6082 FSW joints under different welding parameters (AS on the right)

The profile of the exit hole (thumbprint of tool shoulder) at un-plunge step can give a good indication of weld quality. Mostly, defect-free joints are achieved when a complete circle around the exit hole is formed [110]. When unsuitable FSW parameters are used (lower heat input and insufficient stirring time), inhomogeneous shapes of exit hole are formed, for example, Figure 4-8 (W5, and W10) combined by narrow NZ contains macro defects (poor weld quality) such as tunnel defects (Figure 4-9 W4, W5, and W10), cavity (Figure 4-9 W5), and incomplete penetration along with non-recrystallisation of the grains (Figure 4-9 W4, W5, W9, W10, and W15). The formation of these defects is profoundly affected by the tool traverse speed and more likely to happen when higher traverse speeds (125 and 200 mm/min) were used. Under such conditions, the material received lower energy input per unit length of the weld (fewer

tool rotations per millimetre) resulting in a lower volume of softened material in the NZ, inappropriate flow of plasticised metal and insufficient stirring time. From these observations, it can be concluded that in FSW the cavity is formed in trailing position (behind the tool) of the AS then filled by sweeping of plasticised material from the leading position, and the tunnel defect is more likely to happen if the cavity is not filled with plasticised material.

On the other hand, by increasing the stirring time and lowering the cooling rate through decreasing the traverse speed from 200 to 20 mm/min at a constant rotation speed of 800 rpm, this leads to improve the flowability of softened metal and form a homogeneous circle shapes of exit hole (Figure 4-8 W1) with elliptical NZ shape exhibits a high degree of continuity and entirely joint free defects (Figure 4-9 W1).

Figure 4-10 shows the typical cross-weld macrostructure of W6 FSW joint. It is seen that the friction stir zone (FSZ) consists of three different zones namely; HAZ, TMAZ, and NZ, which were identified explicitly in all FSW joints. An elliptical shape characterises the NZ with onion structure consist of alternating layers of coarse and fine grains. Also, the FSZ is widened on the upper surface, as a result of high contact frictional area and plastic flow in the shoulder/plate interface.

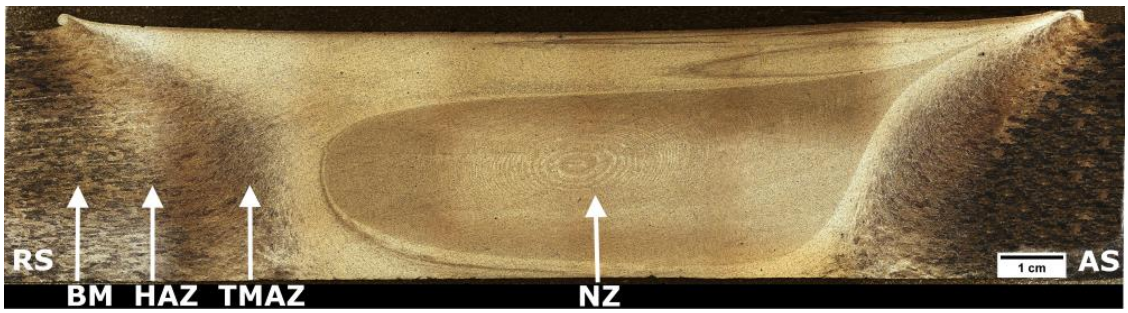


Figure 4-10 Typical cross weld section macrostructure of AA 6082 FSW joint welded at 1100 rpm - 20 mm/min (W6)

The surface morphology of the FSW joints in terms of flash formation and surface appearance has been investigated visually. Despite pushing the softened metal down by rotating the tool in a counter-clockwise direction, excessive release of stirred material to the upper surface as the flash was formed at the highest temperature in the range of 593°C (1800 rpm / 20 and 40 mm/min) (Figure 4-8 W16 and W17) with a wider softened area. On the other hand, a noticeable reduction in the amount of flash, as well as narrower softened area, were obtained when the traverse speeds increased to 75, 125 and 200 mm/min (Figure 4-8 W18, W19, and W20).

Also, it is noticed that a smooth surface is observed from most weldments. However, a weld surface covered by aluminium particles was obtained at higher heat input (hot weld) when using the highest tool rotational speed (1800 rpm). More aluminium particles were spread on the surface of the joint when the traverse speed increased to 200 mm/min as shown in Figure 4-8 (W20). This feature can be assigned for the following reasons. (i) The formation of more aluminium softened particles, which are stuck to the shoulder surface of the tool and then picked up to the surface by centrifugal force to another location [8, 111]. (ii) The excessive softening of the BM when using the highest heat input during FSW. (iii) The stirring action between the tool shoulder and the horizontal movement on the surface of the plate [112].

4.2.3.2 Microstructure evolution in AA 6082 FSW joints

The EBSD maps of the transition zones (TZ) from the BM to the NZ of a typical weld (W1) revealed a heavily deformed microstructure as shown in Figure 4-11. These zones have experienced partial recrystallisation, which consists of rotated elongated grains and equiaxed grains. The softened elongated grains in the AS (Figure 4-11 (a)) can be clearly seen rotating sharply where it passes into the NZ in the form of substantial

plastic stirring as lamellar shear bands, coincided with increased dislocation densities within the deformed grains [113]. While in the RS much more diffused interface is observed (see Figure 4-11 (b)).

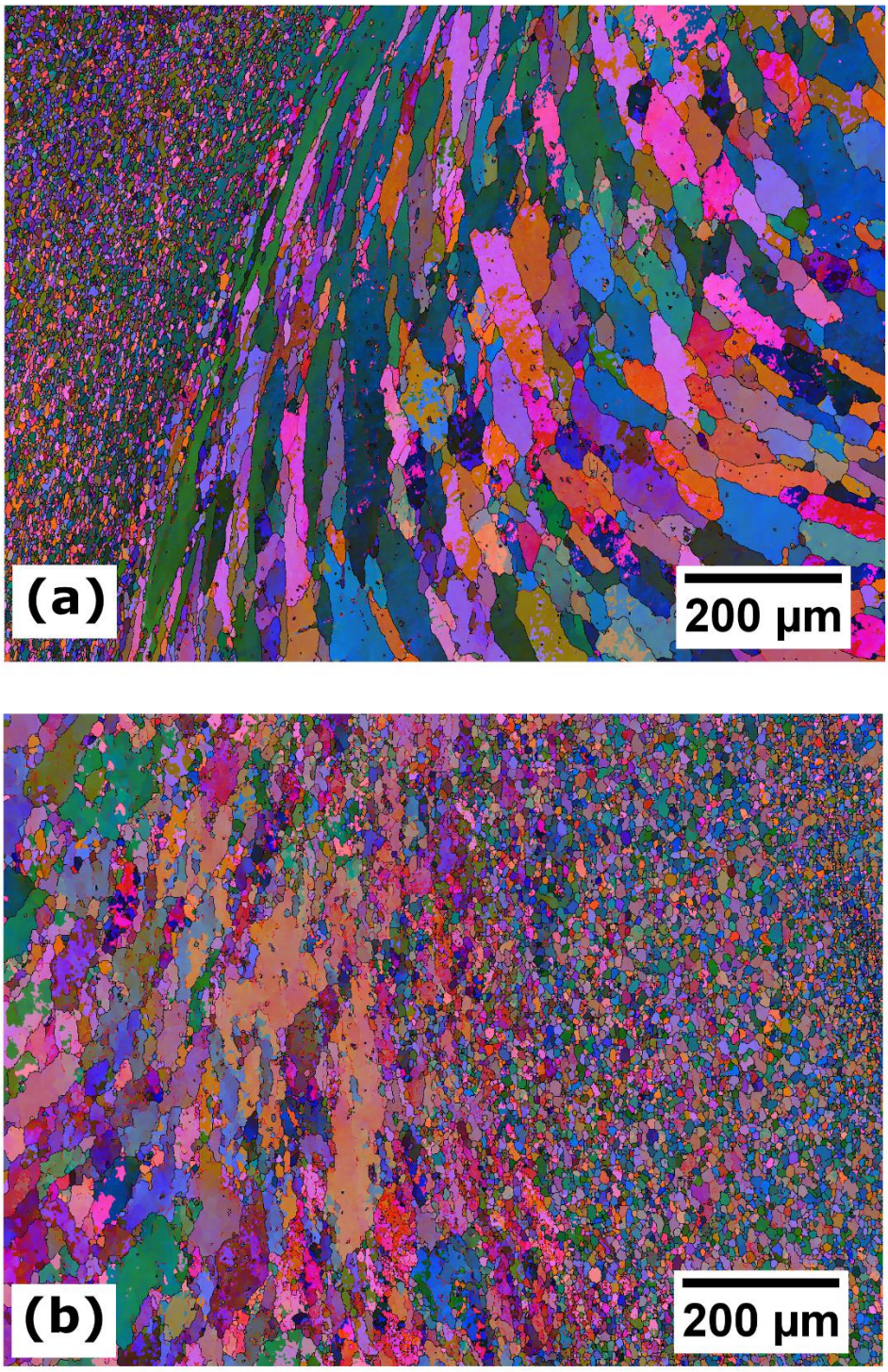


Figure 4-11 Transition zone of the W1 joint cross-section; (a) AS, and (b) RS

Figure 4-12 presents the EBSD orientation and grain boundary maps obtained in the centre of the NZ under different welding conditions. The morphology of grain structures which evolved in the NZ under different welding conditions was clearly different from that of the BM, and recrystallised equiaxed grains were evolved. The related grain size distribution is shown in Figure 4-13 and the area-weighted mean size D^A is plotted as a function of welding temperature as shown in Figure 4-14. It is seen that as the welding temperature increased either by increasing tool rotation speed or decreasing the tool traverse speed, the size of grain was increased. For example, by increasing rotation speed from 800 to 1800 rpm at a constant tool traverse speed of 20 mm/min, the grain size increased from around 7.4 to 20.5 µm as a result of higher heat input, longer exposure time and slower cooling rate. Meanwhile, when the tool traverse speed increase from 20 to 200 mm/min at a constant rotation speed of 800 rpm, the grain size decreased from about 7.4 to 5 µm due to the higher cooling rate.

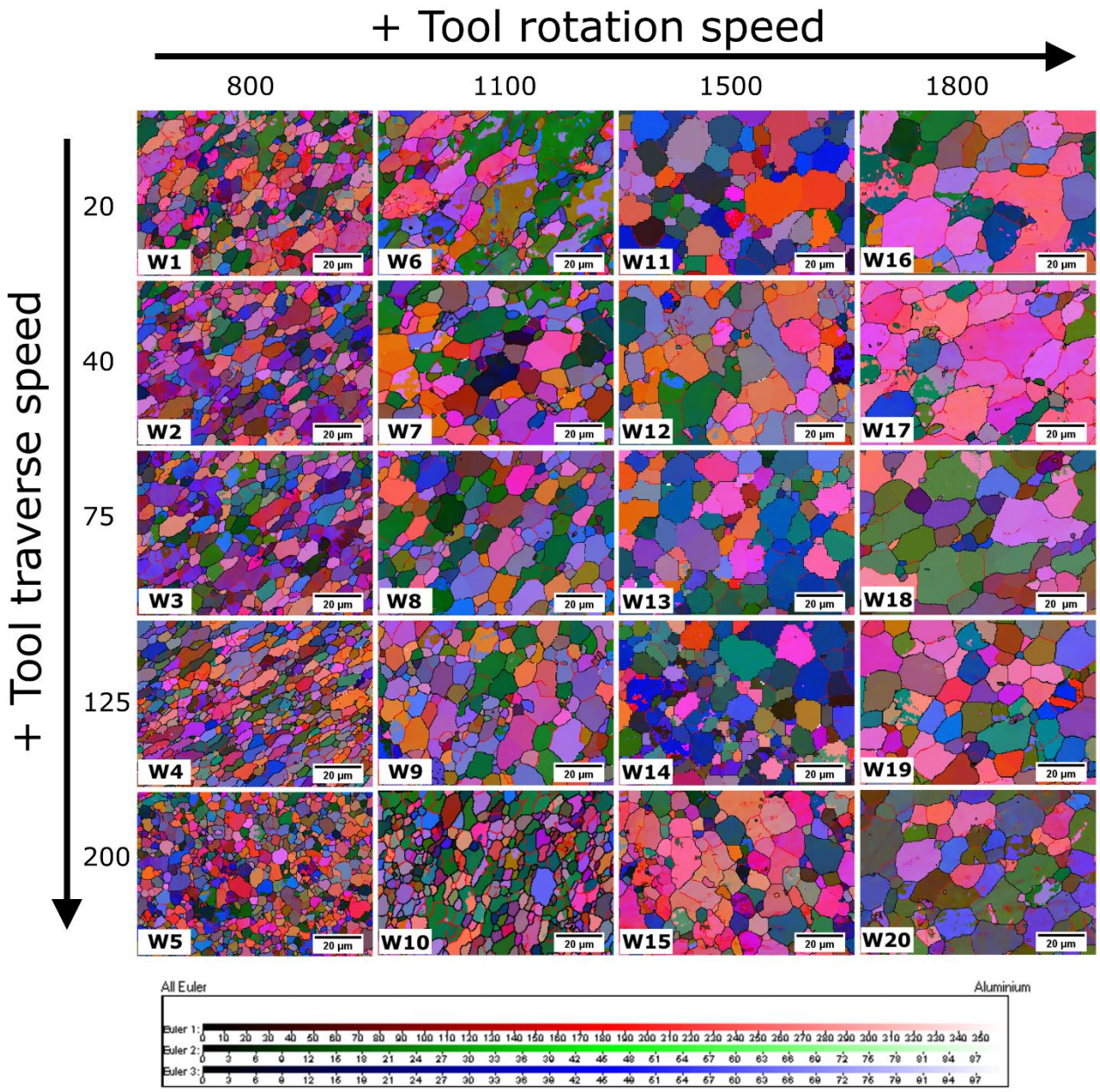


Figure 4-12 EBSD maps obtained in the centre of NZ of AA 6082 under different FSW conditions. In the maps, HAGBs and LAGBs are depicted by black and red colour, respectively

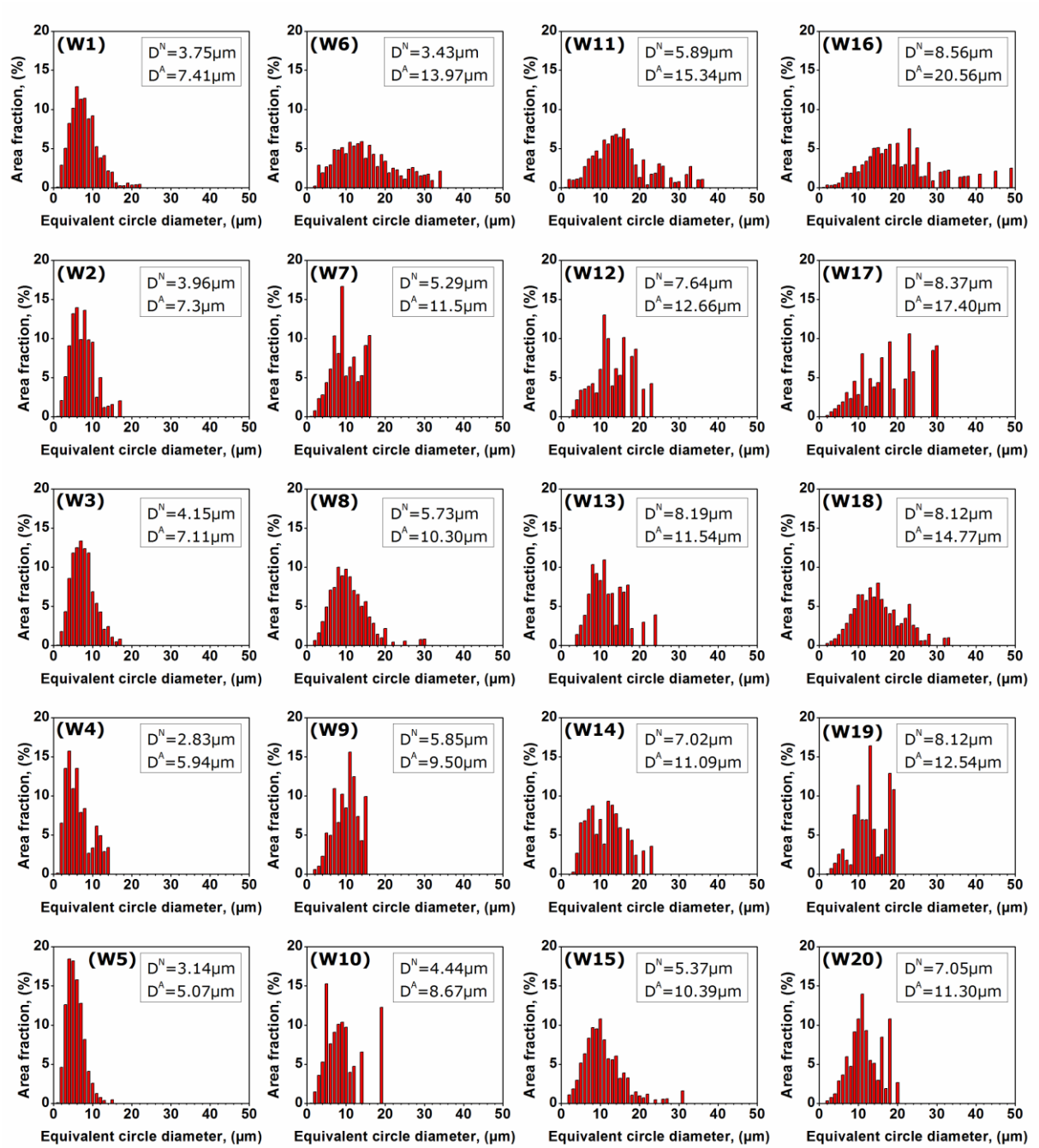


Figure 4-13 Grain size distribution in the NZ of AA 6082 under different welding conditions

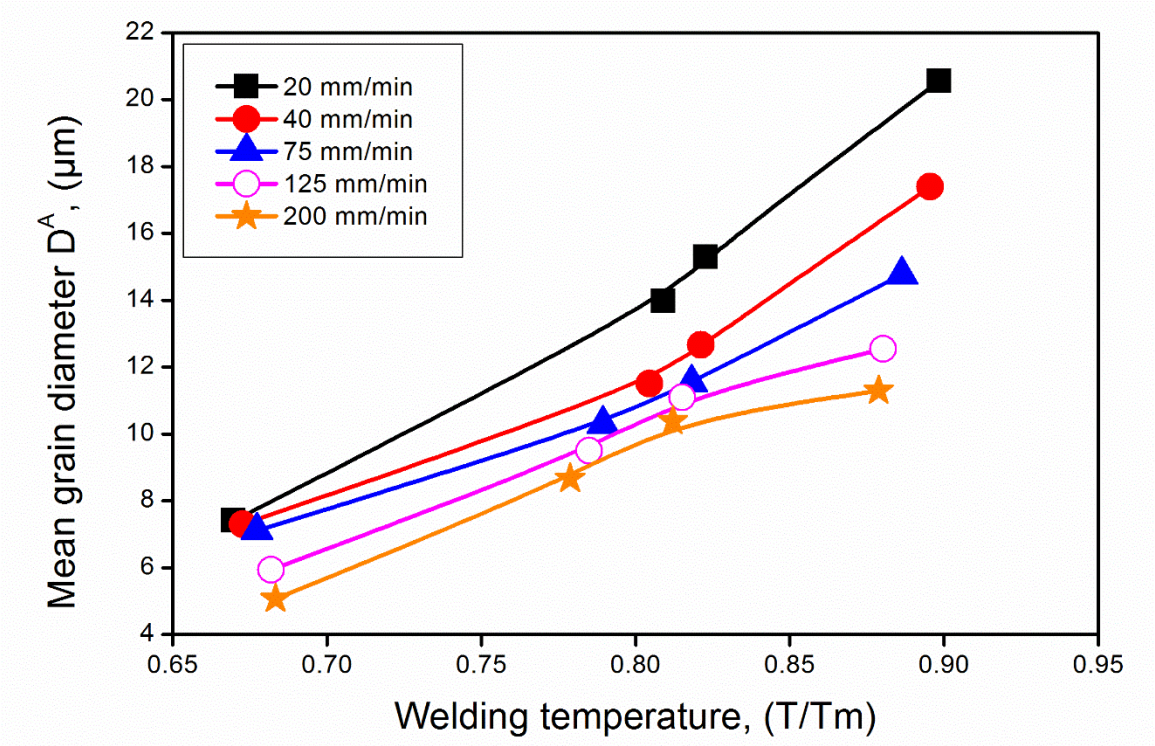


Figure 4-14 Effect of welding temperature on the grain size

In a polycrystalline material, the grain boundaries are categorised based on the difference in crystallographic orientation between two crystallites (misorientation). Figure 4-15 shows the related misorientation distribution angle of FSW joints. The grain structures which evolved under all welding conditions are a mixture of LAGBs and HAGBs. As the tool rotation speed decreased, the fraction of the HAGBs increased indicating that grain refinement happened simultaneously with accumulation LAGBs. For most examined cases, at a low angle, sharp angle peak characterised the misorientation distribution, resulted from the accumulation of dislocation introduced by the plastic deformation during the FSW whereas a broader peak was observed in the angular range of 5 – 60° [114].

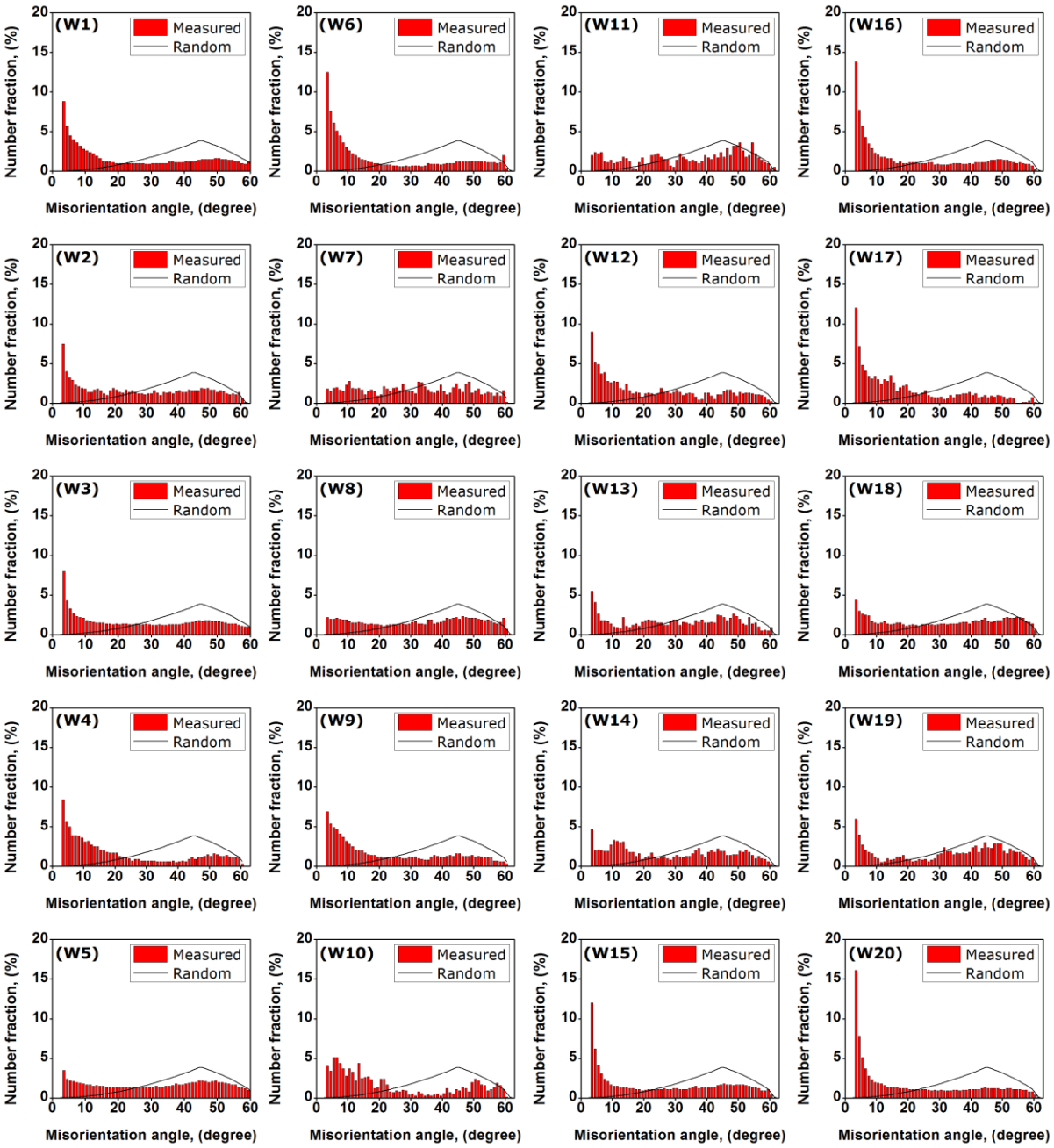


Figure 4-15 Misorientation angle distribution in the NZ of AA 6082 under different welding conditions

4.2.3.3 Grain texture in AA 6082 FSW joints

Based on the EBSD maps, pole figures of the centre of the NZ for specific joints collected in the TD-ND plane and calculated over areas between 69,000 μm^2 and 93,000 μm^2 with a step size of 0.25 µm are shown in Figure 4-16 (a and b). The evolution of texture is associated with the deviatoric stress states. Thermal and mechanical stresses introduce in the material during the welding resulted from the thermal history and rotation of tool and forward motion. Under all welding conditions, the pole figures exhibit preferred orientation, mostly dominated by <111> fibre textures (Figure 4-16 (a)), but with considerable variation in the direction of the fibre axis, the texture strength and the degree of preferential orientation around the fibre axis. At 800 rpm tool rotation speed and lowest tool traverse speed of 20 mm/min, the <111> fibre texture is moderately strong, with the direction of the fibre axis angling further from the ND as tool traverse speed increases (19° at 20 mm/min, 40° at 75 mm/min), towards the WD. This trend appears to break down at 200 mm/min tool traverse speed when the rate of heat input and induced stresses are lowest, and there is a weakening of the texture. At the opposite corner of the matrix, 1800 rpm tool rotation speed and 20 mm/min tool traverse speed (W16), when the rate of heat input and stresses is highest, the <111> fibre texture is very strong, closely aligned with the ND, and is dominated by a single orientation around the fibre axis, approximating to a $(111)[0\bar{1}1]$ or $(111)[2\bar{1}\bar{1}]$ texture. As the tool traverse speed increases, there is a weakening of the texture and a shift of the fibre axis about 16° away from the ND, backwards from the WD. At the same time, there is a strengthening of a <100> fibre texture, which dominates the <111> fibre texture at 200 mm/min tool traverse speed (see Figure 4-16 (b)). The <100> fibre axis is angled about 71° from the ND, backwards from the WD and TD. For a tool traverse speed of 75 mm/min, increasing

the rotation speed gradually changes the direction of the <111> fibre axis, while the texture strength remains about the same. At 800 rpm the fibre axis is angled towards the WD, 40° from the ND, but at higher tool rotation speed it is angled backwards from the WD, 4° from the ND at 1100 rpm and 17° at 1800 rpm.

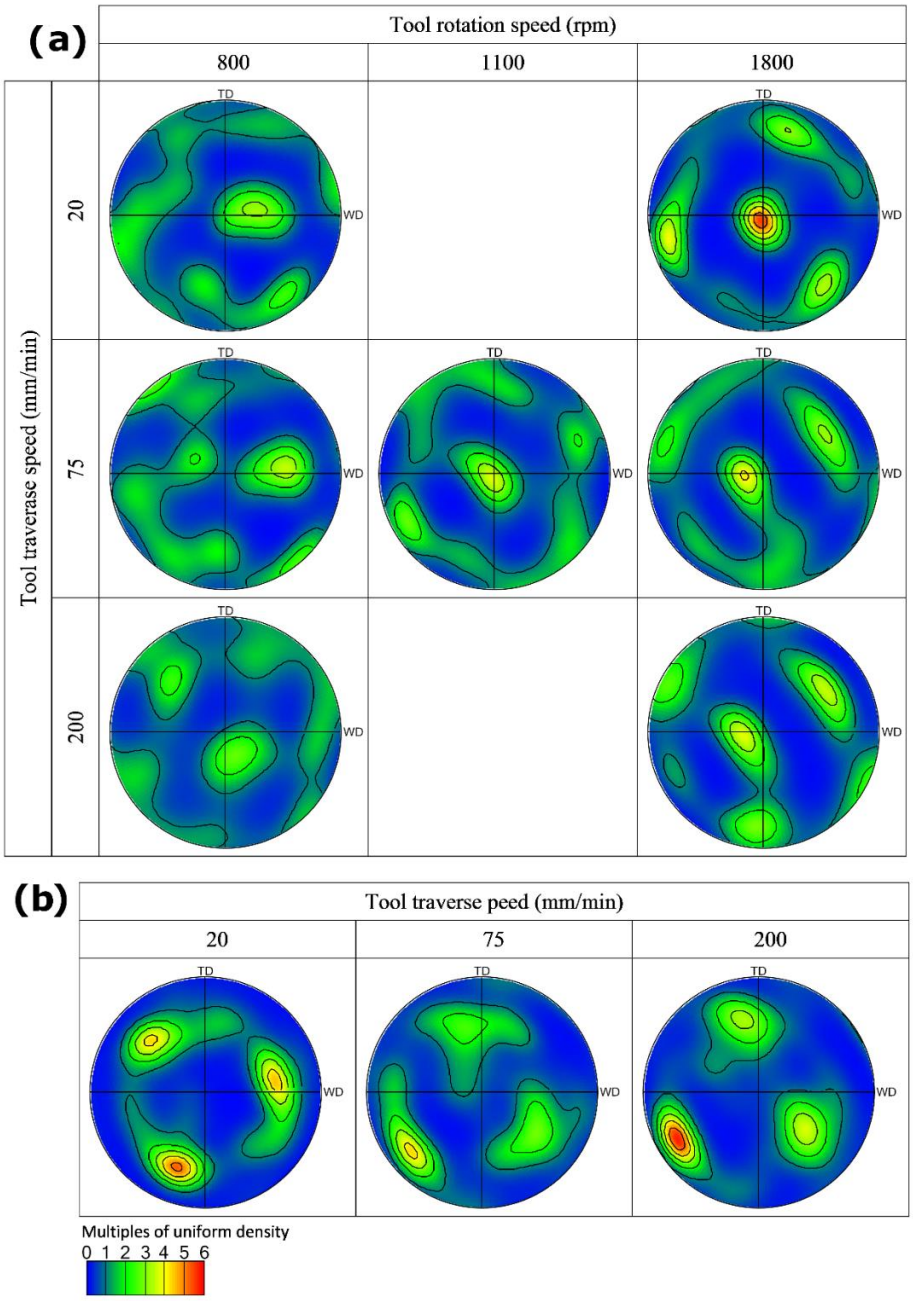


Figure 4-16 Pole figures generated from EBSD maps of AA 6082 FSW joints; (a) {111} pole of the NZ, showing the variation in texture with welding parameters, and (b) {100} pole of the NZ for 1800 rpm tool rotation speed, showing the variation in texture with tool traverse speed

4.2.3.4 Strengthening precipitate in AA 6082 FSW joints

Since the BM used in this study strengthened by precipitation hardening (T6-conditions) and it is affected by heat input and thermal history, TEM observations made in the HAZ (Figure 4-17), and NZ (Figure 4-18) of the joint welded at highest heat input and slowest cooling rate (W16). Different types and shapes of precipitate are revealed in these TEM micrographs. Coarse irregularly shaped precipitates more than one μm in size and homogeneously distributed rounded precipitates up to 500 nm in size were observed in HAZ as shown in Figure 4-17 (a and b). These precipitates were identified as $Al_{57}Mn_{12}$ type structure with space group 200($Pm\bar{3}$) same as the one identified in the BM (see Figure 4-6). Compared to the BM the fine linear strengthening precipitates have coarsened severely in the HAZ with the size of about 400-1000 nm long, 50-100 nm wide and well aligned with or perpendicular to each other (see Figure 4-17 (b and c)). The EDS spectrum of this precipitate (see Figure 4-7-phase 3) detected Al, Mg, and Si with probably a large contribution of Al from the matrix because of the small size of the precipitate. The related SAED (Figure 4-17 (d)) matches well with a Mg_9Si_5 ($\acute{B}$) type structure with space group 173 ($P6_3$) or 176 ($P6_3/m$) and this is consistent with the EDS results. The pattern also contains a line of $(h00)$ diffraction spots from the matrix, which are very closely aligned to the $(71\bar{8}0)$ precipitate spot, indicating that these planes are parallel. This alignment with the matrix explains the orthogonal alignment of the precipitates observed in the BF images. The appearance of this phase give much less contribution to the hardness and strength [115].

Figure 4-18 shows the precipitate morphologies in the NZ, which is characterised by the appearance of rounded precipitates (see Figure 4-18 (a and b)) up to 500 nm same as the BM and HAZ, as well as, both coarse ($\acute{B}$) (Figure 4-18 (c)) with high density and fine

$\acute{B}$ (Figure 4-18 (d)) with less density linear precipitate. Furthermore, from the comparison of spot intensities, it is found that for the base metal and HAZ spot intensities are fairly even, suggesting a relatively disordered solid solution, whereas for the weld centres the intensities vary (e.g. (100) less than (200)) suggesting a more ordered solid solution.

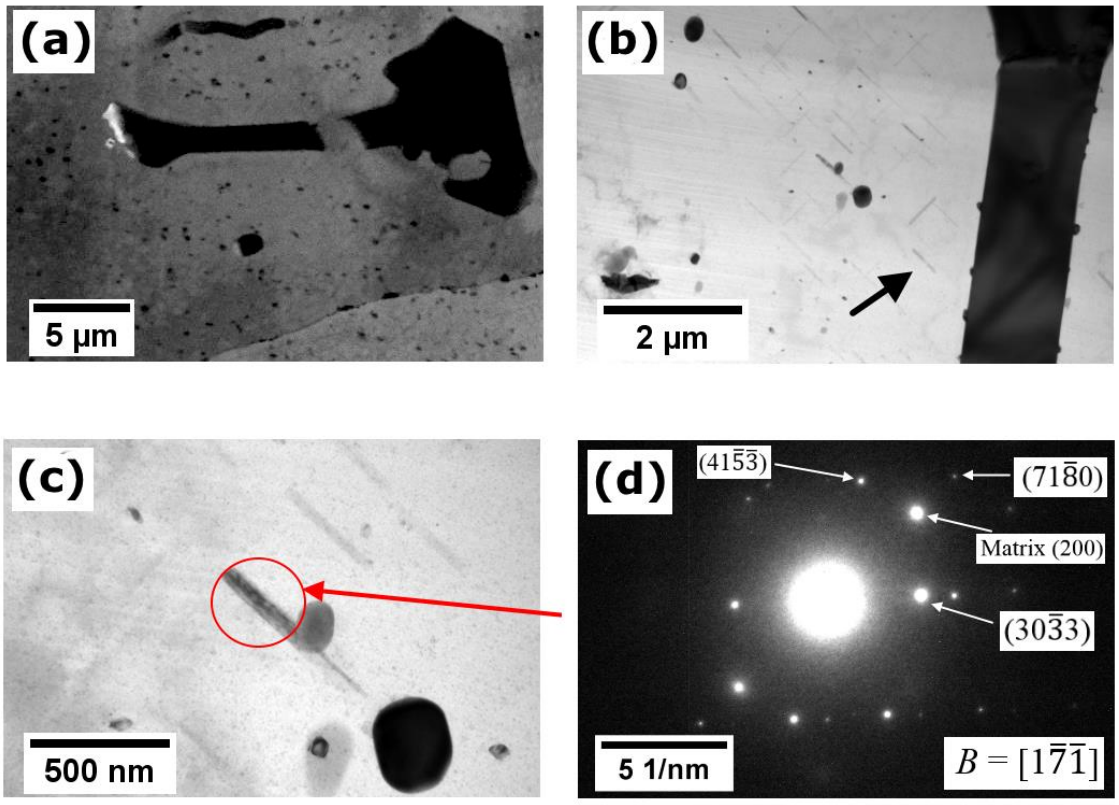


Figure 4-17 (a-c) TEM bright field micrographs in the HAZ, and (d) Selected area electron diffraction (SAED)

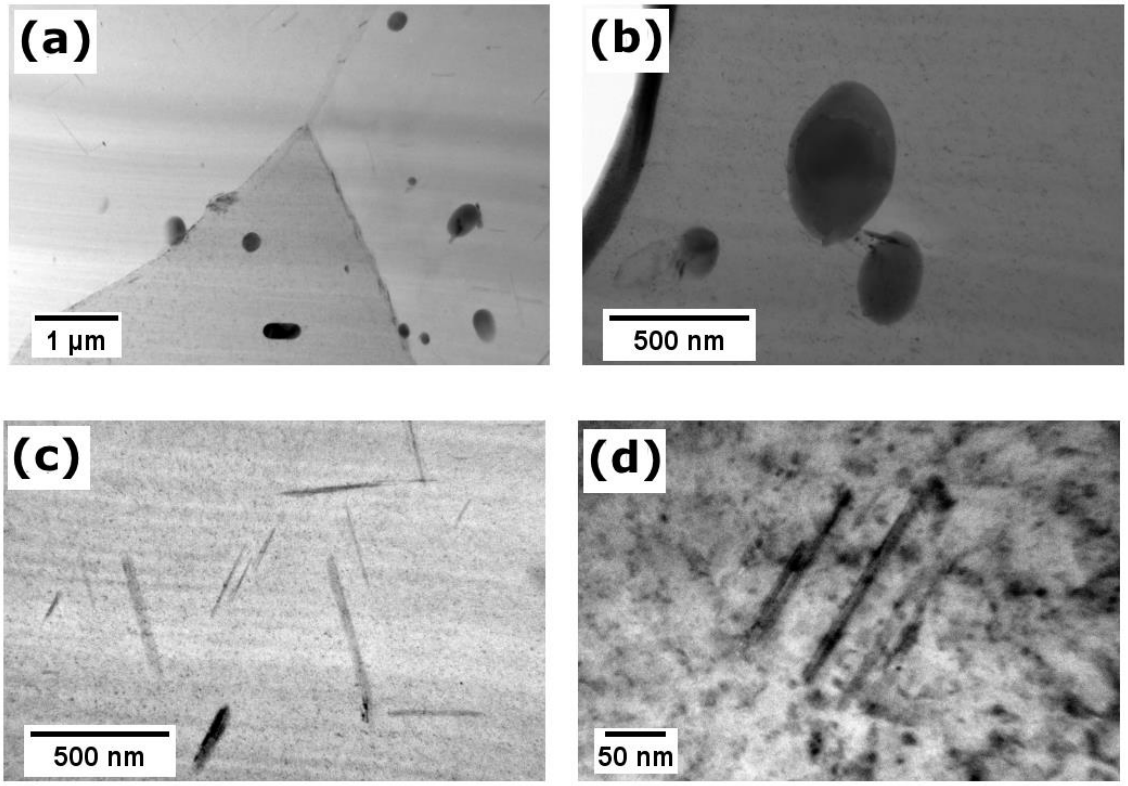


Figure 4-18 TEM bright field micrographs in NZ; (a and b) round precipitate, (c) Coarse precipitate $\acute{B}$, and (d) Fine precipitate $\acute{\acute{B}}$

4.3 Aluminium matrix composite AA 6092/SiC/17.5p-T6

4.3.1 Welding temperature and thermal history

Detailed temperature measurements with thermocouples and infrared camera have been done to map out the temperature field during FSW. Figure 4-19 shows the maximum temperature in the centre of the weld (NZ). It is seen that the peak temperature in the NZ increased from around 500 to 605 °C with the increasing of tool rotation speed from 1500 to 2100 rpm at a constant tool traverse speed of 25 mm/min. On the other hand, the rises of tool traverse speed from 25 to 100 mm/min lead to a reduction of the peak temperature from about 500 to 488 °C using a constant tool rotation speed of 1500 rpm. Furthermore, there is no significant change in the welding temperature, and it tends to be saturated when the tool rotation speed rises from 1800 to 2100 rpm.

Figure 4-20 compares the effect of the different tool traverse and rotation speed on the thermal history in the centre of NZ for the welds produced with 1500 and 2100 rpm at a tool traverse speed of 25 and 100 mm /min (corners of welding matrix). It is evident that the temperature gradient from the peak temperature of the NZ decreases with the reduction of tool traverse speed (lower cooling rate from high temperature). The increase of tool traverse speed from 25 to 100 mm/min at a constant rotation speed of 1500 rpm reduces the cooling time from peak temperature from about 150 sec to around 40 sec. Figure 4-21, Figure 4-22, and Figure 4-23 show the cross-weld thermal history measured in the AS and RS as a function of distance from the welding line for the joints welded by using tool rotation speed of 1500, 1800 and 2100 rpm, respectively. The recorded temperature field shows the highest temperature is closest to the weld line, and it is nearly symmetric on both sides concerning the weld line. However, it is clear that the temperature at the RS is higher than that at the AS.

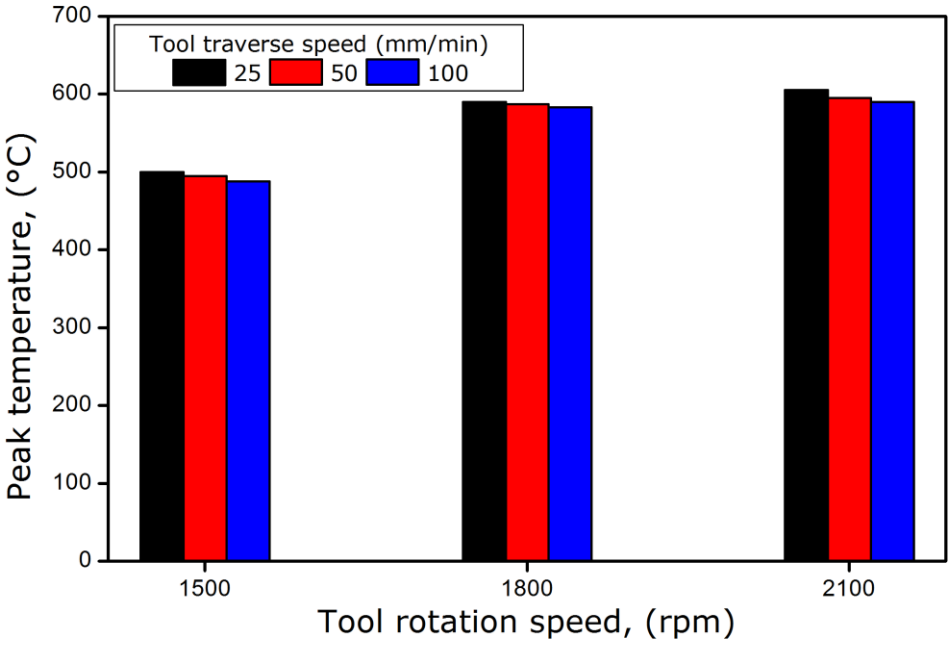


Figure 4-19 Effect of FSW parameters on the peak generated temperature in the NZ of AMC

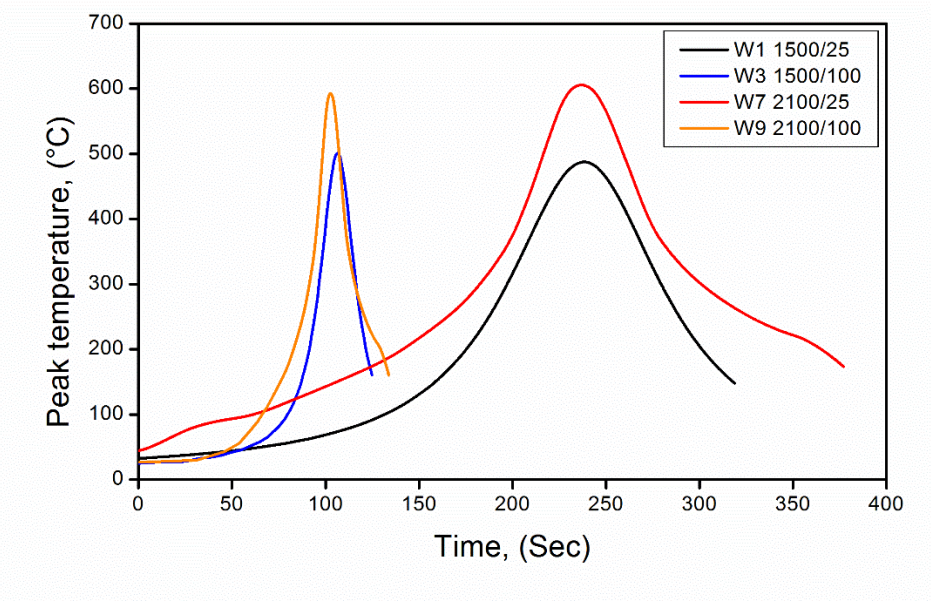


Figure 4-20 Effect of FSW parameters on thermal history in the NZ of AMC

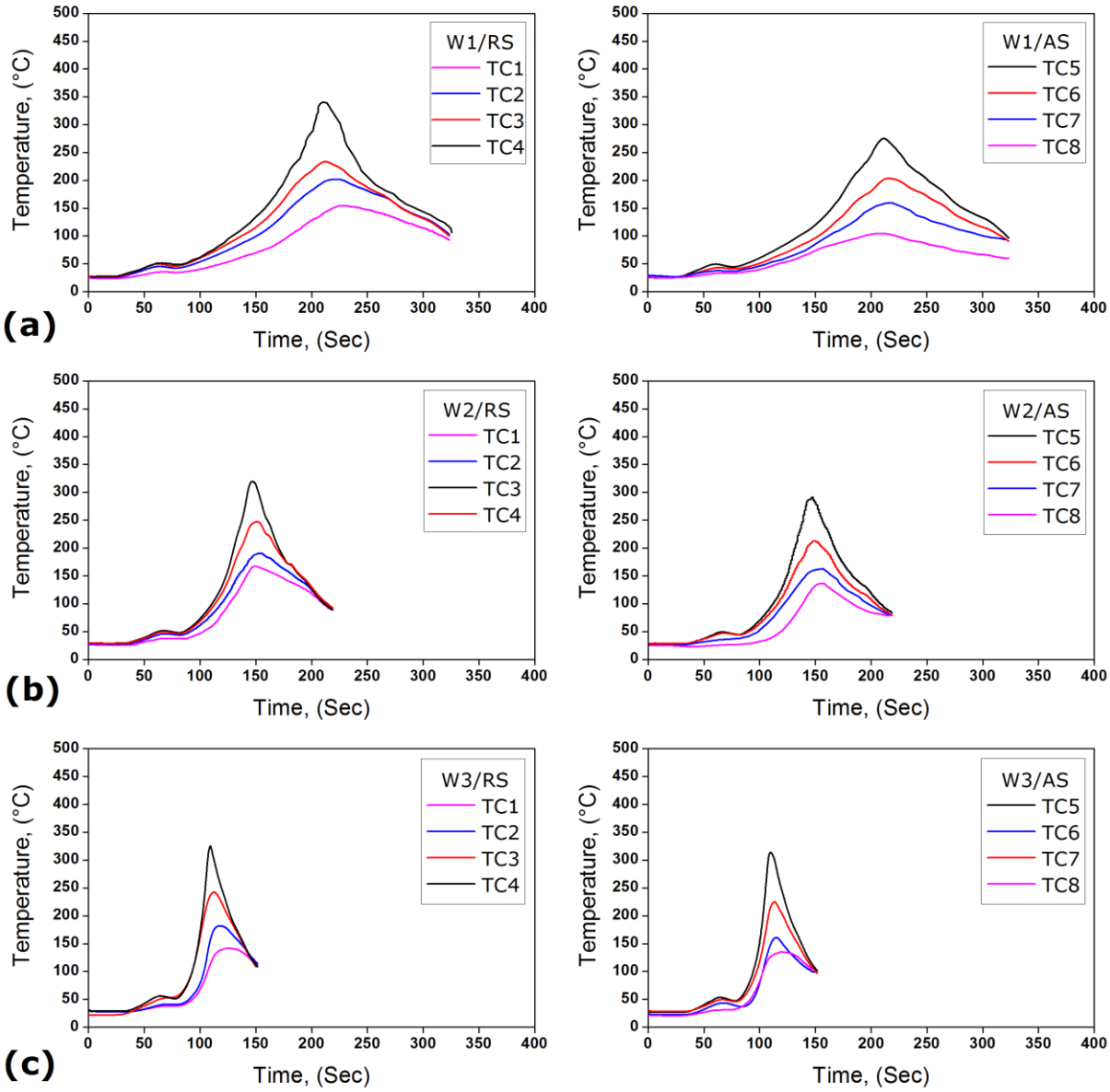


Figure 4-21 Thermal histories of AMC joints welded at a tool rotation speed of 1500 rpm and different tool traverse speed; (a) 25, (b) 50, and (c) 100 mm/min

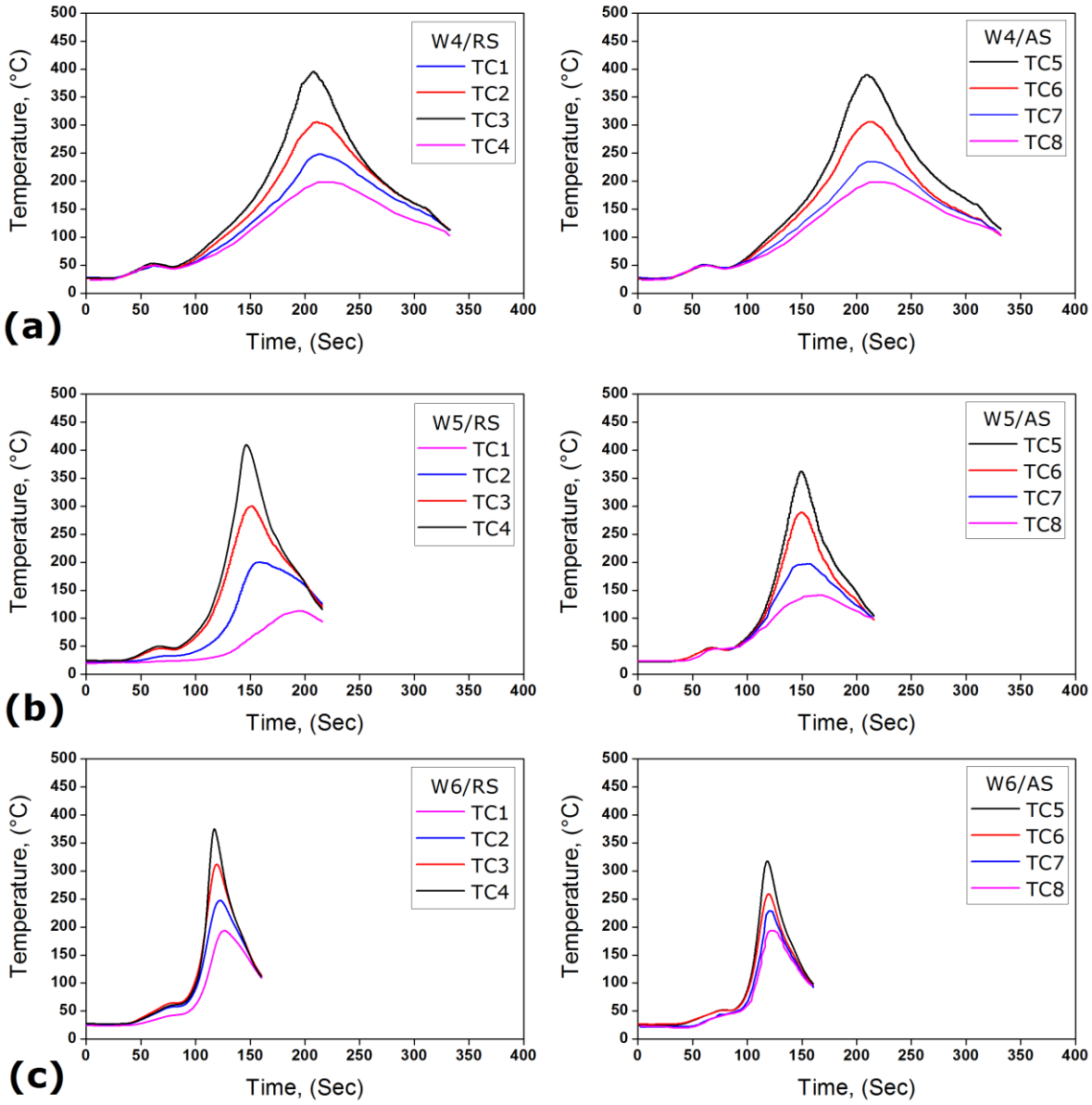


Figure 4-22 Thermal histories of AMC joints welded at a tool rotation speed of 1800 rpm and different tool traverse speed; (a) 25, (b) 50, and (c) 100 mm/min

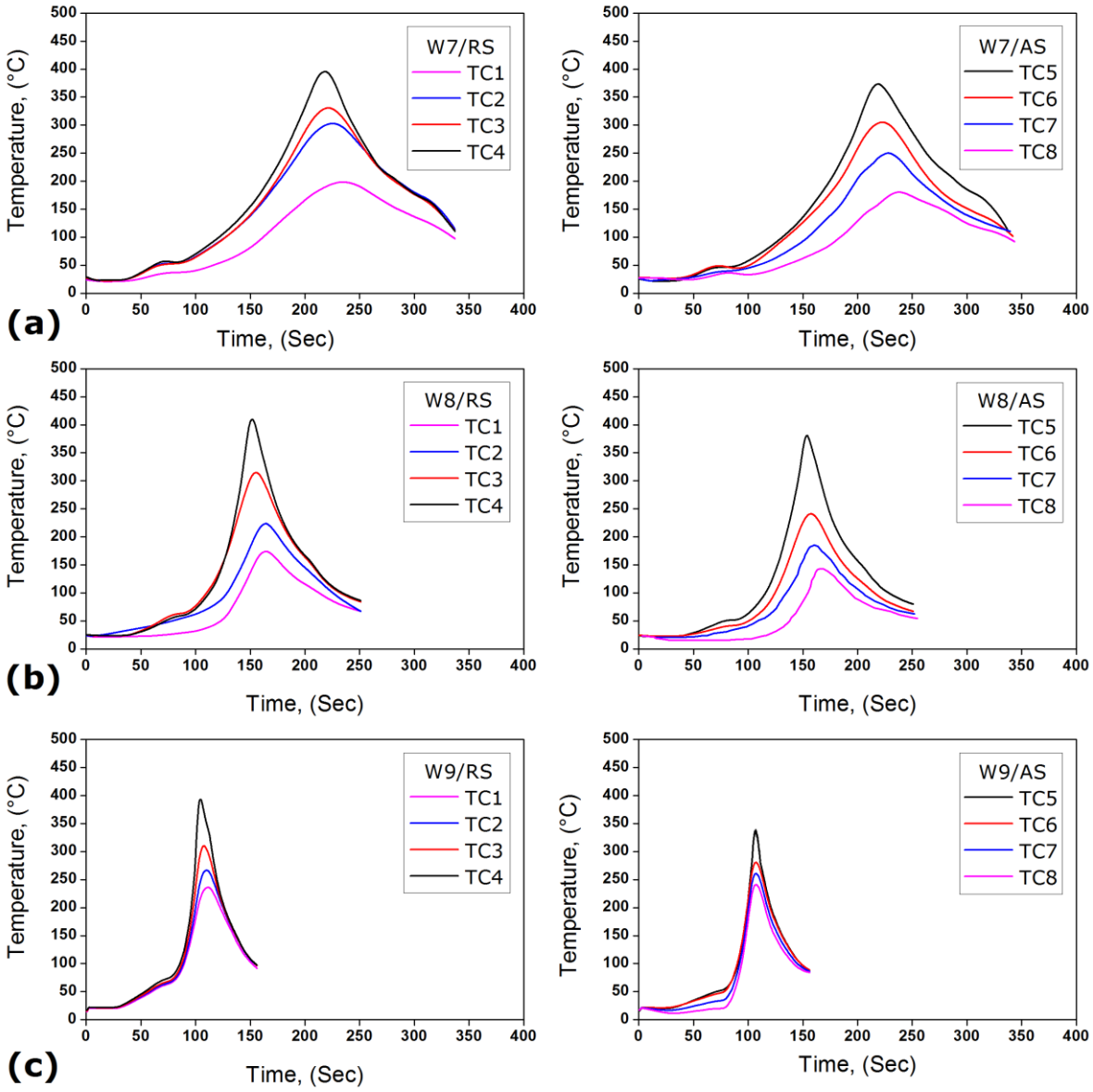


Figure 4-23 Thermal histories of AMC joints welded at a tool rotation speed of 2100 rpm and different tool traverse speed; (a) 25, (b) 50, and (c) 100 mm/min

4.3.2 Metallurgical characterisations of the as-received AMC

Figure 4-24 shows the microstructure of the as-received AMC, including the SEM image, EBSD map, grain size distribution, and misorientation angle. As shown in Figure 4-24 (a), the microstructure of the BM shows a reasonable distribution of the reinforcement particles (SiC) in the matrix alloy having an average size of around 6 µm. Figure 4-24 (b) represents the EBSD Euler map; individual grains were coloured

according to their crystallographic orientations, which is indicated by the colour code legend in Figure 4-24 (e), and the black and red lines represent the HAGBs and LAGBs as well as, the white area represents the SiC. BM microstructure shows a significant variation in the grain size ranging from 3 to 39 µm having a mean diameter of around 13 µm, with a mixture of HAGBs (high surface energy) and a high fraction of low energy substructure network LAGBs (subgrains) as shown in Figure 4-24(c and d). This can be related to the fact that when the polycrystalline metal deformed a large number of LAGBs are formed, as the LAGBs consist of arrays of edge dislocations and its structure and properties depend on the misorientation angle [116].

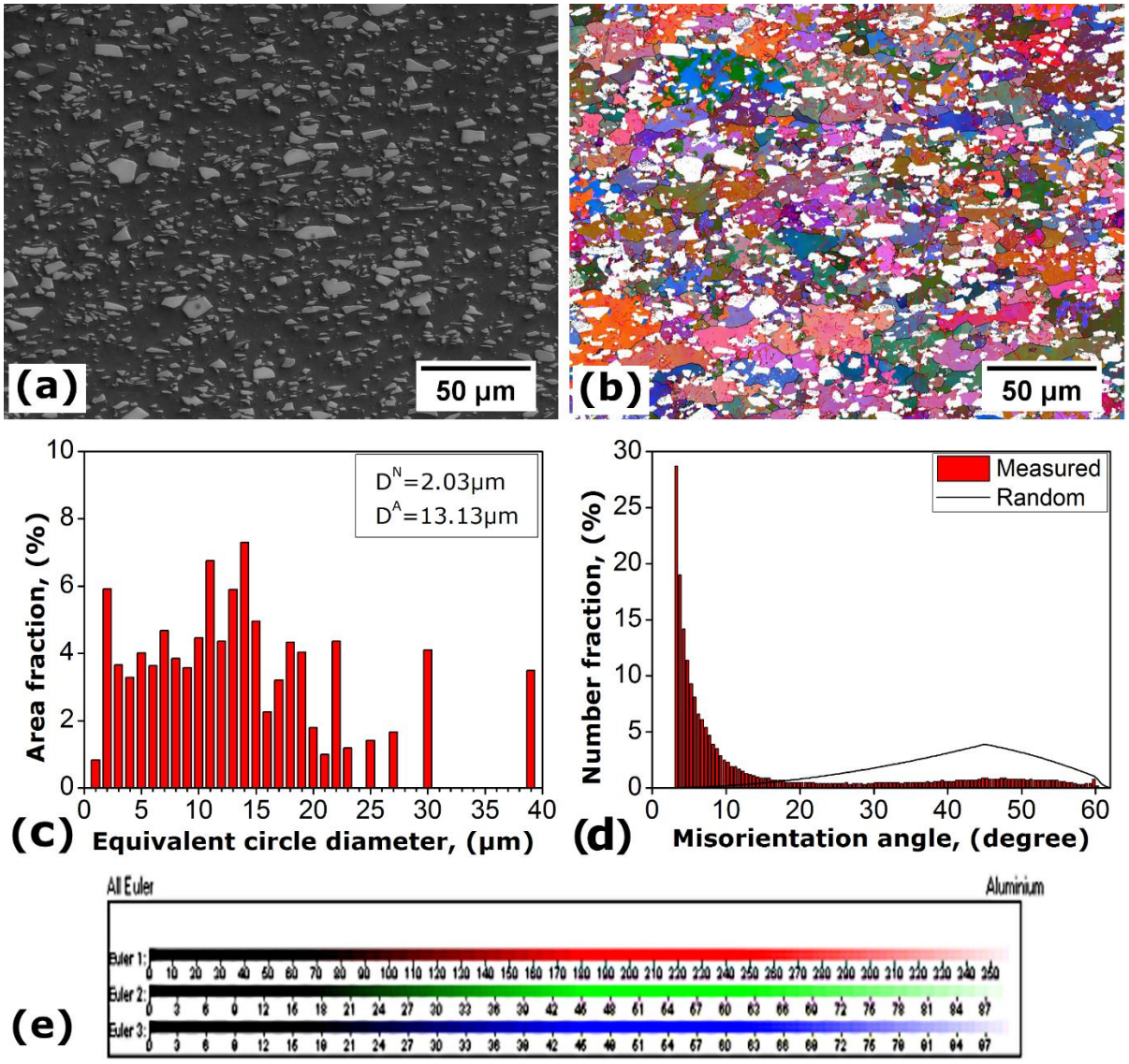


Figure 4-24 Microstructure characterisation of AMC; (a) SEM image, (b) EBSD map, (c) Grain size distribution, (d) Misorientation angle, and (e) EBSD legend

4.3.3 Metallurgical characterisations of AMC FSW joints

4.3.3.1 Macrostructure and surface morphologies of the weldment and FSW tool

Figure 4-25 shows the surface morphologies of AMC FSW joints with various welding parameters of tool rotation and traverse speeds. Visual observations revealed that a rough surface was formed in contact with the tool shoulder same as demonstrated by Ceschini et al. [40], with the formation of the so-called wake effect feature (flash) as

similarly reported by Kalaiselvan et al. [39]. Smoother surface joints obtained for hotter welds that are fabricated with higher tool rotation speed and lower tool traverse speed.

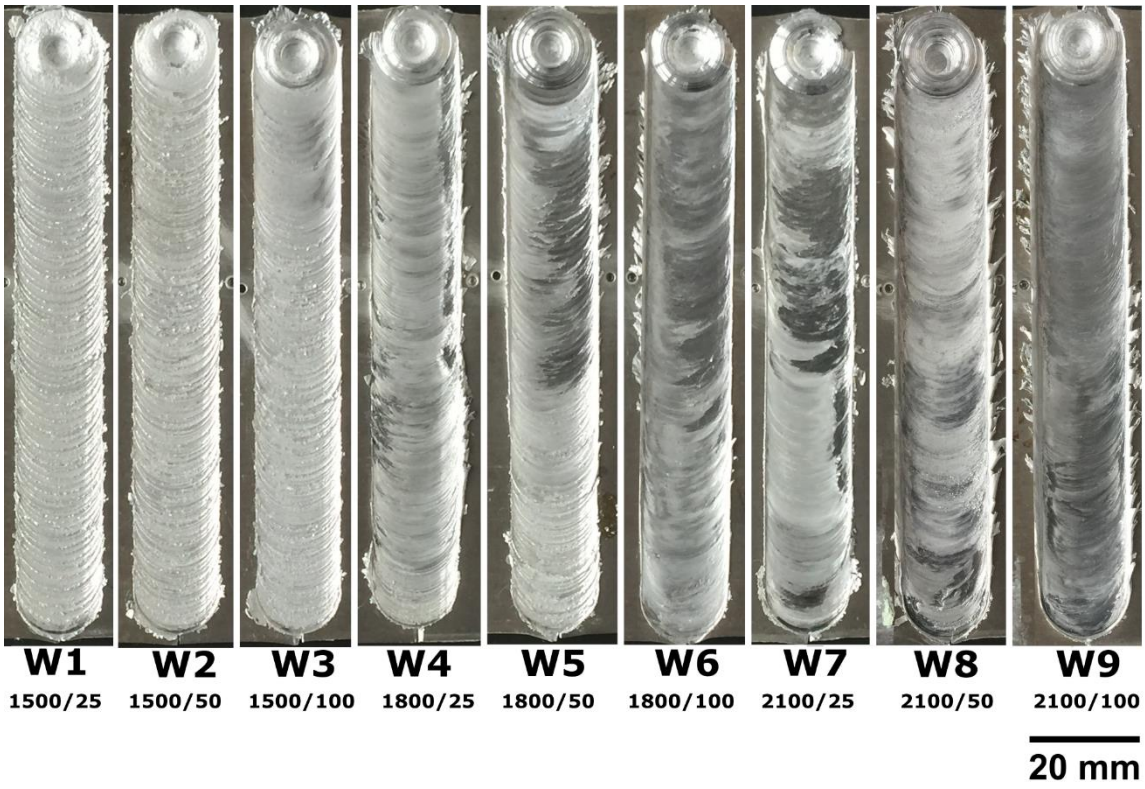


Figure 4-25 Surface morphologies of AMC FSW joints under different welding parameters (AS on the right)

Figure 4-26 reveals the cross-weld macrostructure of the welded joints; it is clear from the figure that a complete penetration and joint entirely formed under all welding parameters. Also, it can be seen from the figures that the increase of tool rotation speed and reduction of the tool traverse speed can increase the width of the FSZ. The macrographs further depict that the formation of joints is free of defects and there are no significant volumetric defects such as tunnels, pinholes, and wormholes in the NZ. However, macro defect under the top surface was identified in the joints welded at 2100 rpm - 50 mm/min (Figure 4-26-W8) with the precipitate of the iron layer as shown in EDS map and spectrum Figure 4-27. This defect is attributed to the fretting damage of

the nitrided layer due to rubbing action between the tool shoulder and reinforcement particles, which is lead to precipitate iron layer on the top surface.

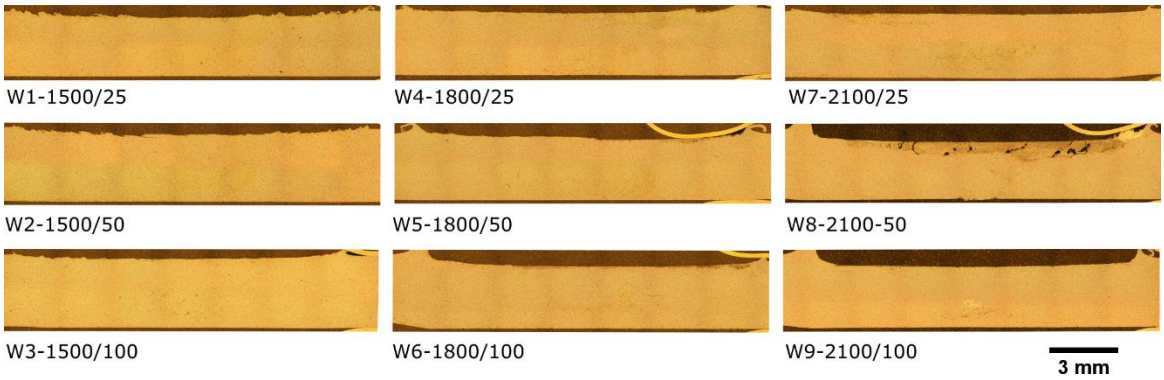


Figure 4-26 Cross-weld macrostructure of AMC FSW joints under different welding parameters (AS on the right)

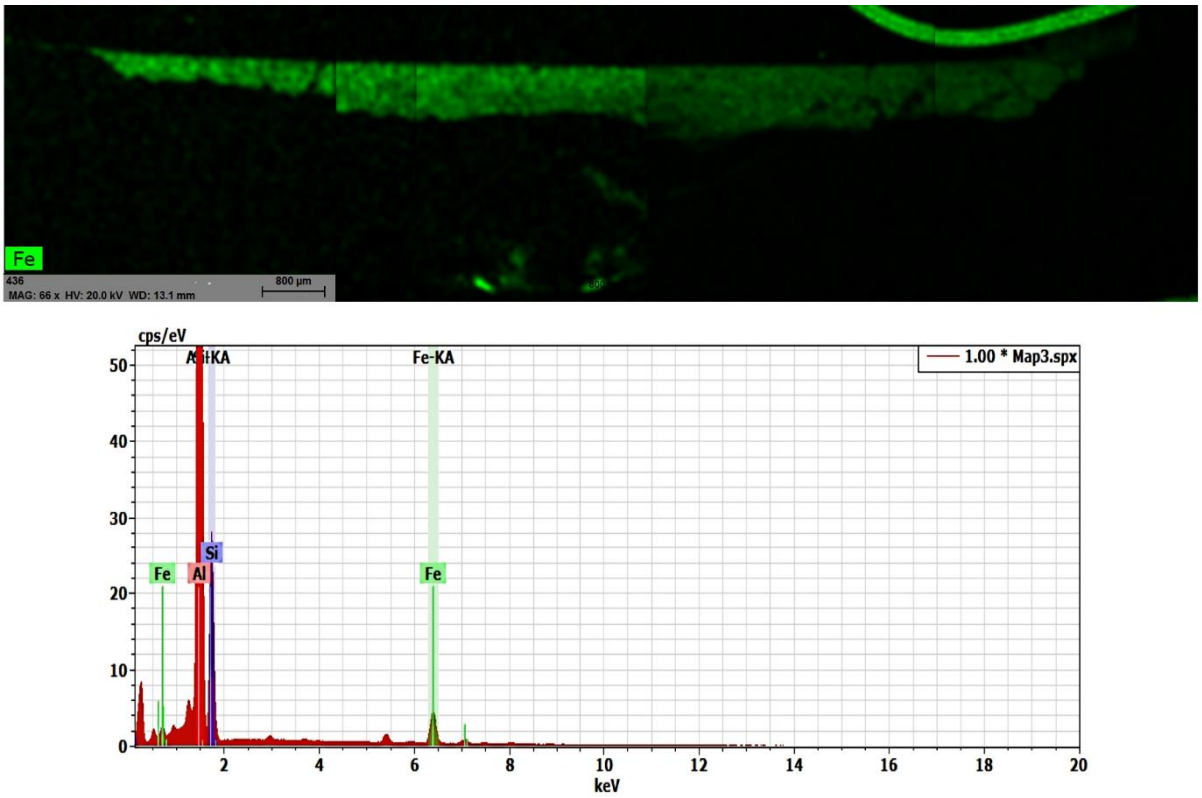


Figure 4-27 EDS map and spectrum of AMC joint welded at 2100 rpm and 50 mm/min (W8)

Figure 4-28 shows the surface morphology of the welding tool before and after the welding process. As a result of filling threads by BM, a delay in the wear of the tool pin was achieved, and the tool was still maintained the original shape. However, due to the large contact area between the shoulder of the tool and the surface of the BM, some abrasion was detected on the tool shoulder. This result indicates that the surface heat treatment (plasma nitriding) for the tool surface can improve the wear resistance and increase the life of the tool.

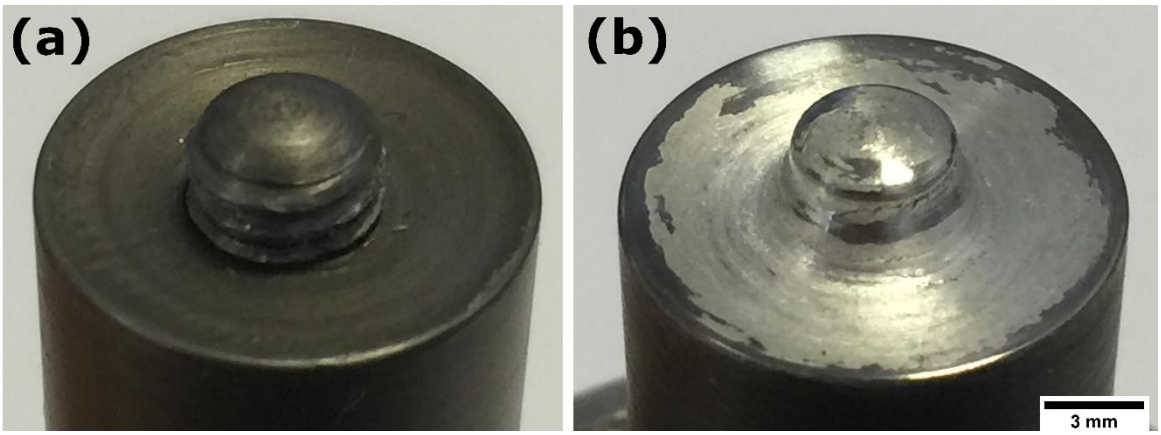


Figure 4-28 Surface morphology of FSW tool; (a) Before welding, and (b) After welding

Figure 4-29 shows the typical cross-weld macrograph of the AMC FSW joint (W5). It can be seen clearly that the FSZ consists of three different zones namely; HAZ, TMAZ and NZ, which are identified in all joints. The NZ exhibited an elliptical shape and onion ring structures with the widened area on the upper surface for all examined joints, same as reported by Feng et al. [41] and Cavaliere et al. [117]. This indicates that there is sufficient frictional heat, stirring action, and material plastic deformation available for complete plasticization and material flow for proper coalescence.

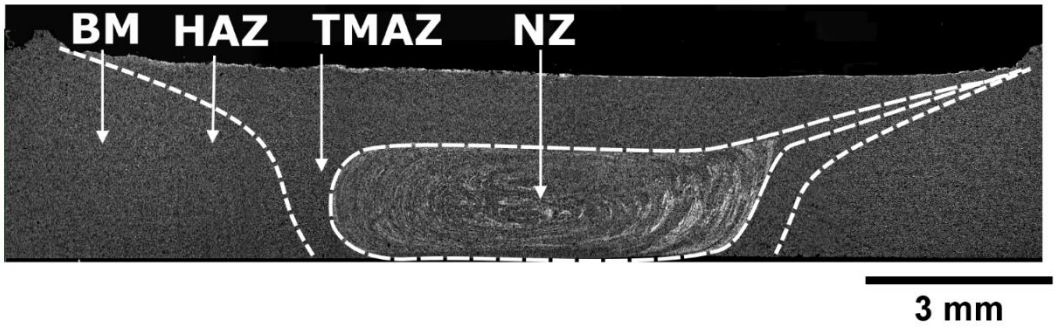


Figure 4-29 Typical cross-weld of AMC joint W5 (AS on the right)

The flow lines within the NZ (onion ring patterns) are related to the tool design, welding parameters, and process of friction heating due to the rotation of the tool and the forward movement extruding the material around the RS of the tool. Figure 4-30 (a) shows the EBSD band contrast of the onion ring structure in the NZ. It is distinguished with alternating layers of refined grains in addition to subgrain with various stages of development. The variations in grain evolution as shown in Figure 4-30 (b), which is a higher magnification from the subregion from Figure 4-30 (a), show different grain size characteristics of the banded structure and a network of LAGBs spread throughout the structure. It was suggested that the FSW process could be thought to be simply extruding one cylindrical sheet of material in one rotation of the tool and the cutting through the section of the material results in the formation onion ring structure [118].

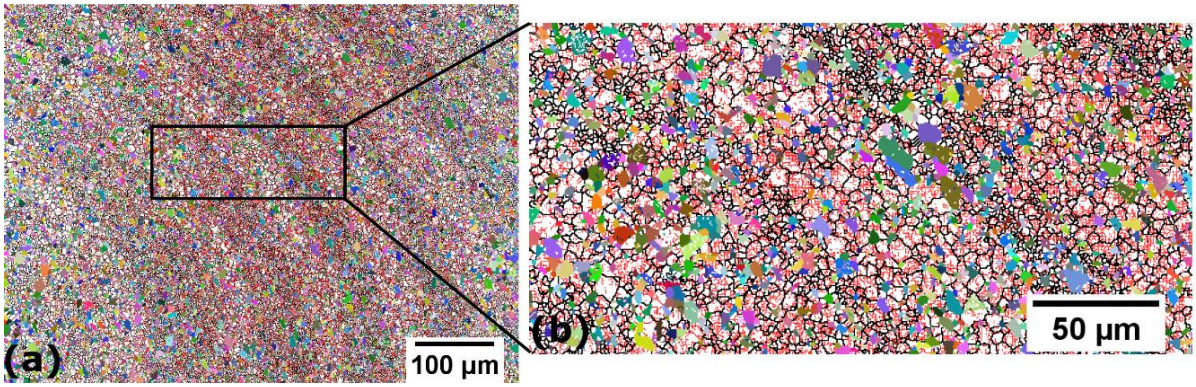


Figure 4-30 (a) Typical onion ring microstructures in AMC FSW joint at the centre of NZ for W3 welds, and (b) Higher magnification from the indicated region in (a)

4.3.3.2 Microstructure evolution in AMC FSW joints

Due to the effect of reinforcement particles (SiC) size and distribution on the isotropy and local mechanical properties, a homogeneous particle distribution is a critical factor to achieve in FSW joints. The SiC distribution after the welding process in the centre of the NZ is given in Figure 4-31. It can be seen from this figure that all samples show a homogenous distribution of SiC in the stirred zone as a result of stirring action and mixing the metal during the welding process. More homogeneity was achieved at lower welding traverse speed. Also, it was observed that the SiC particles were fractured in the NZ (white arrow) and the edges of the particles were blunted compared to the sharp SiC particles in the BM. This leads to refinement of SiC, for example, W1, W3, and W7 having an average size of around 1, 3, and 1.7 µm, respectively with the presence of small rounded particles, which did not appear in parent composite metal. This phenomenon can be related to the abrasion and stirring action between the SiC particles and tool pin circumference, as well as, to the extremely high plastic deformation which occurred during FSW [45]. The EBSD map of the FSZ in the AS of a typical weld (W1) shown in Figure 4-32. In this figure, there is a clear gradient in the cross-weld microstructure (grain

size), and it is consist of three significant parallel area namely; BM, TZ, and NZ inclined by around 45°.

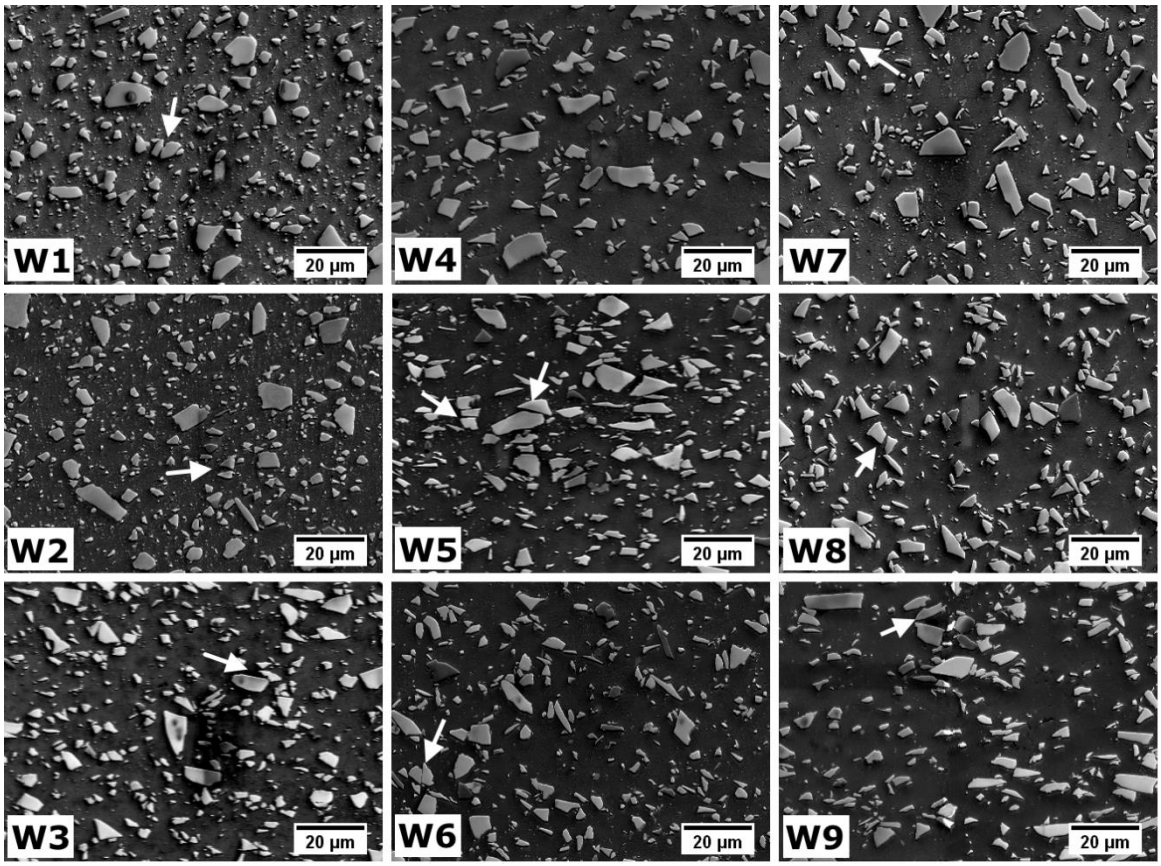


Figure 4-31 SiC distribution in the NZ of AMC joints under different welding conditions

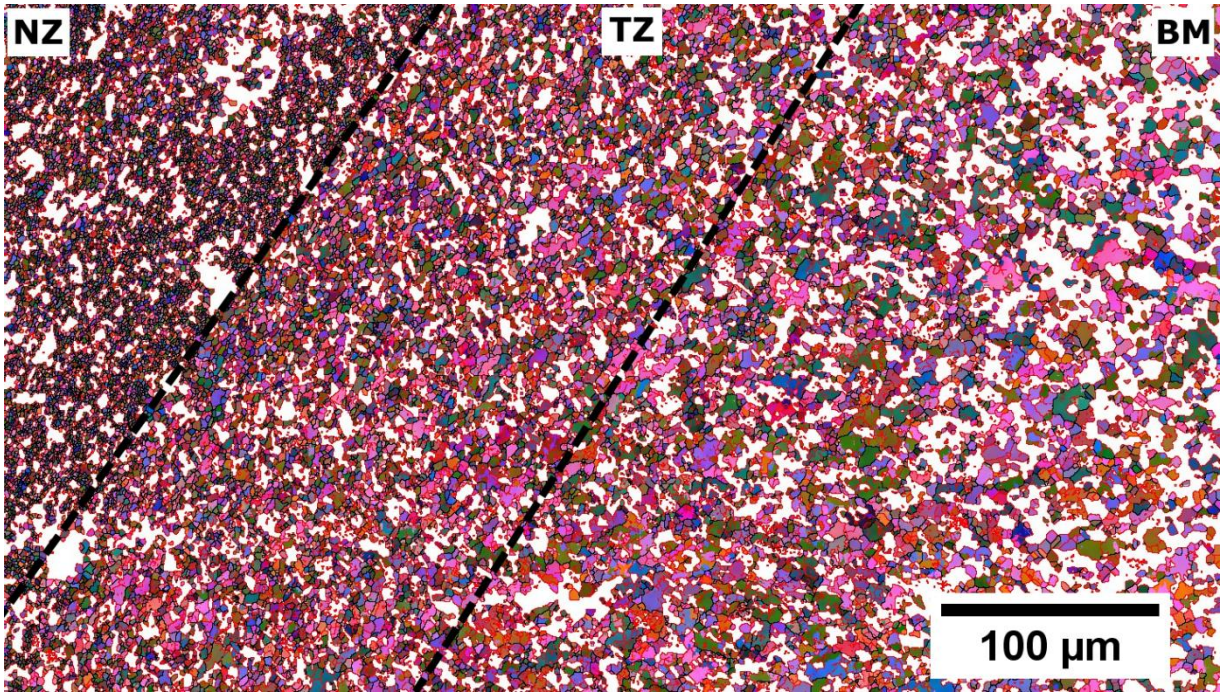


Figure 4-32 Gradient in the grain size of the AMC cross-weld sample (W1)

Figure 4-33 shows the EBSD Euler orientation and grain boundary maps in the NZ for welds obtained under different welding conditions. These maps present a clear visualisation of the grain size. In comparison with BM, more homogeneous microstructures with fine equiaxed grains were formed in the NZ as shown in Figure 4-34. Furthermore, to analyse the grain boundary characteristics, the selected misorientation angle distributions are shown in Figure 4-35. At lowest tool rotation speed (1500 rpm) fine equiaxed grains were formed in the NZ combined by a low fraction of LAGBs. Grain growth happened with the increase of tool rotation speed to 1800 and 2100 rpm as a result of high welding temperature. In both cases, the grain boundaries are highly dominated by HAGBs. Consequently, the LAGBs increases with the increase in tool traverse speed, while the local misorientation change in a few grains, and it is more evident with 1500 rpm rotation speed. From Figure 4-24 (d), and Figure 4-35 five important observations can be made: (i) The BM consists of HAGBs and a high fraction of LAGBs. (ii) The

fraction of HAGBs increases under all welding conditions in comparison to BM. (iii) For all examined cases, at a low angle, the misorientation distribution is characterised by a sharp angle peak whereas a broader peak was observed in the angular range of 5-60°. (iv) The HAGBs are close to the random distribution under most welding conditions. (v) The formation of LAGBs is more affected by tool traverse speed than tool rotation speed.

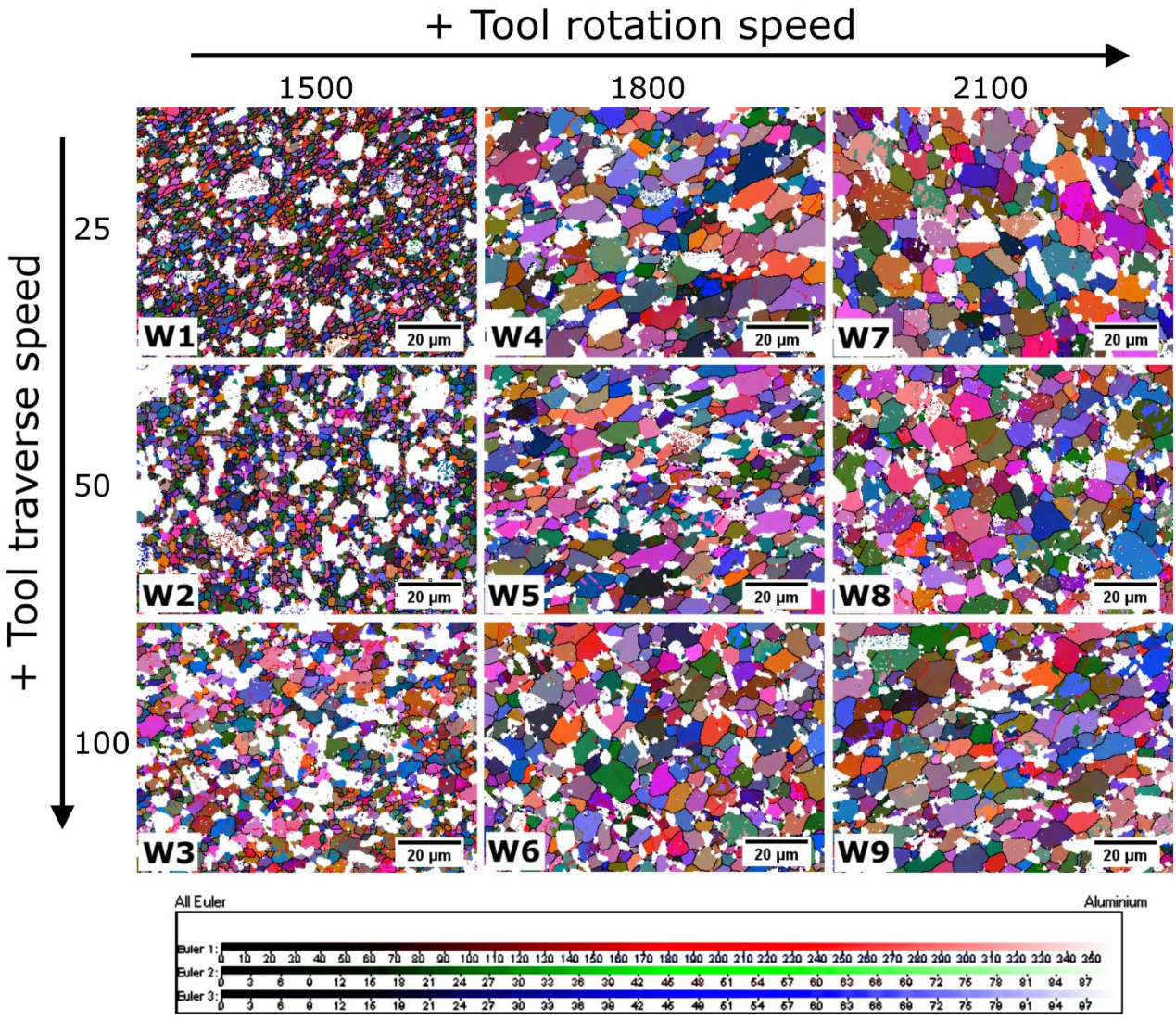


Figure 4-33 EBSD images of grain morphology and the distribution of HAGBs (black line), and LAGBs (red line) under different welding conditions

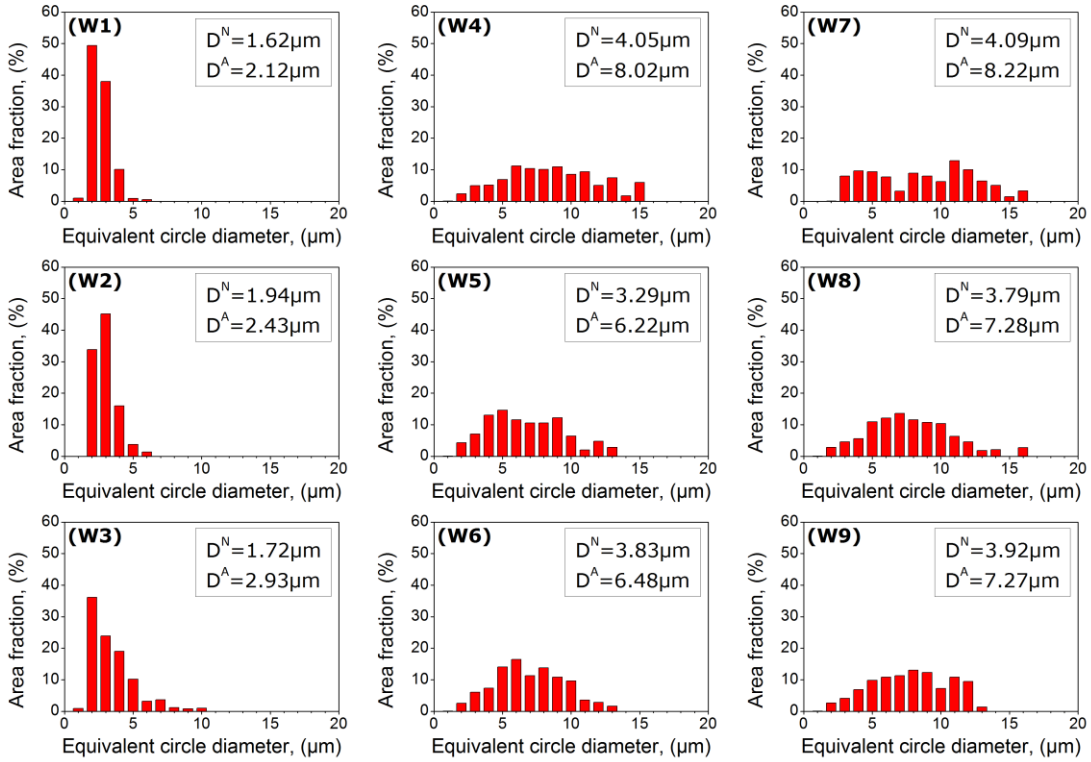


Figure 4-34 Grain size distribution in the NZ of AMC joints under different welding conditions

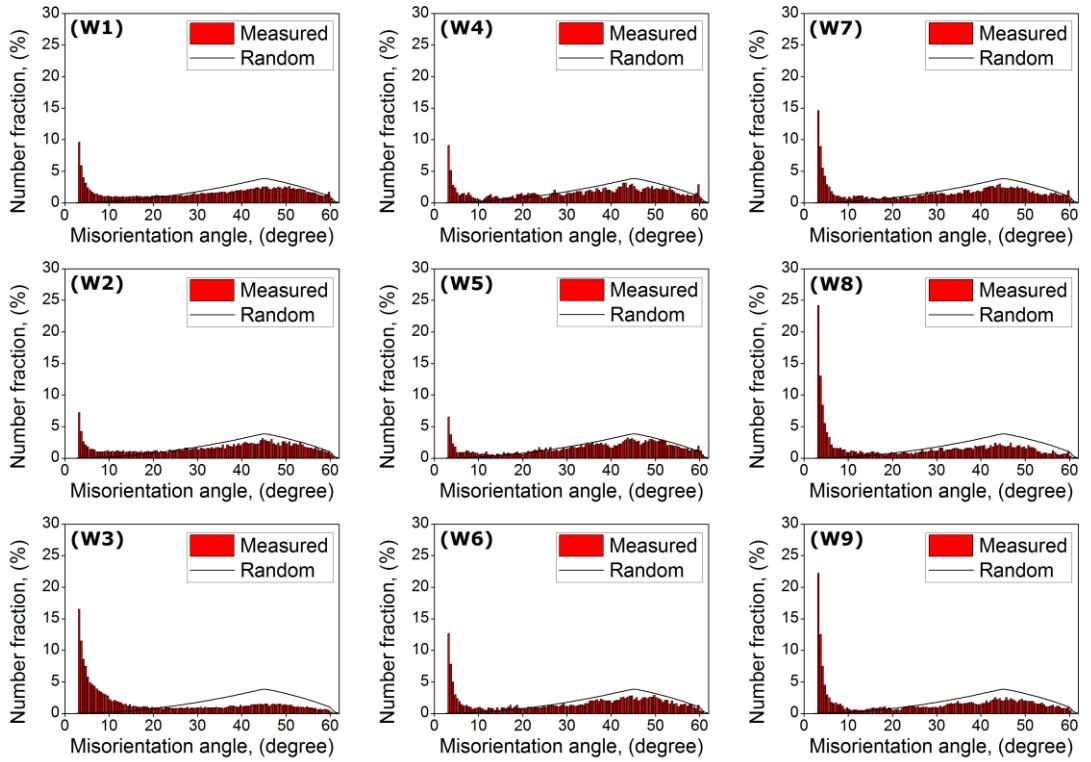


Figure 4-35 Misorientation angle in the NZ of AMC joints under different welding conditions

4.4 Sandwich aluminium matrix composite AA 6061B/SiC/20p-T1

4.4.1 Welding temperature and thermal history

The maximum temperature generated in the centre of the NZ is measured by the infrared camera and presented in Figure 4-36. Similar to the general trends for AA 6082 and AMC, the increase of tool rotation speed from 1500 to 2100 rpm leads to increase the peak temperature from around 530 to 610 °C at 25 mm/min traverse speed and from about 512 to 585°C at 100 mm/min traverse speed. Under all used rotation speeds, the rises of tool traverse speed lead to reduce the peak temperature, for example, the temperature dropped from around 530 to 512 °C when tool traverse speed increased from 25 to 100 mm/min at a constant tool rotation speed of 1500 rpm. Similarly to AMC, the peak temperature tends to be saturated as the tool rotation speed increase from 1800 to 2100 rpm. The cross-weld thermal histories were measured by thermocouples in the middle of welding line at several monitoring locations on the retreating side (RS) (TC1-TC3), and advancing side (AS) (TC4-TC6) as shown in Figure 4-37, Figure 4-38, and Figure 4-39. The distribution of temperature recorded on both sides is nearly symmetrical, with higher induced temperature on the RS, consistent with AA 6082 and AMC.

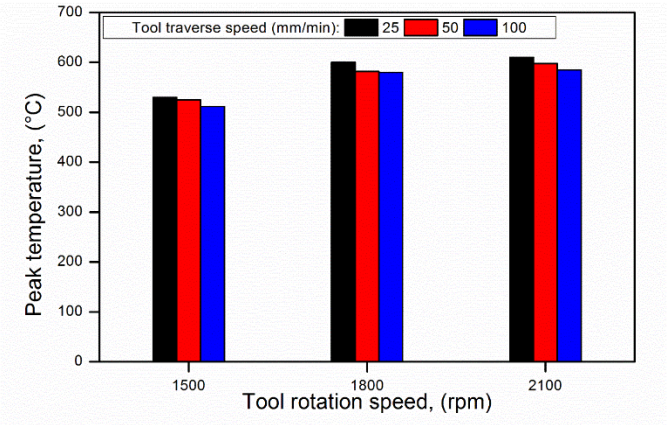


Figure 4-36 Effect of FSW parameters on the peak temperature in the NZ of SAMC

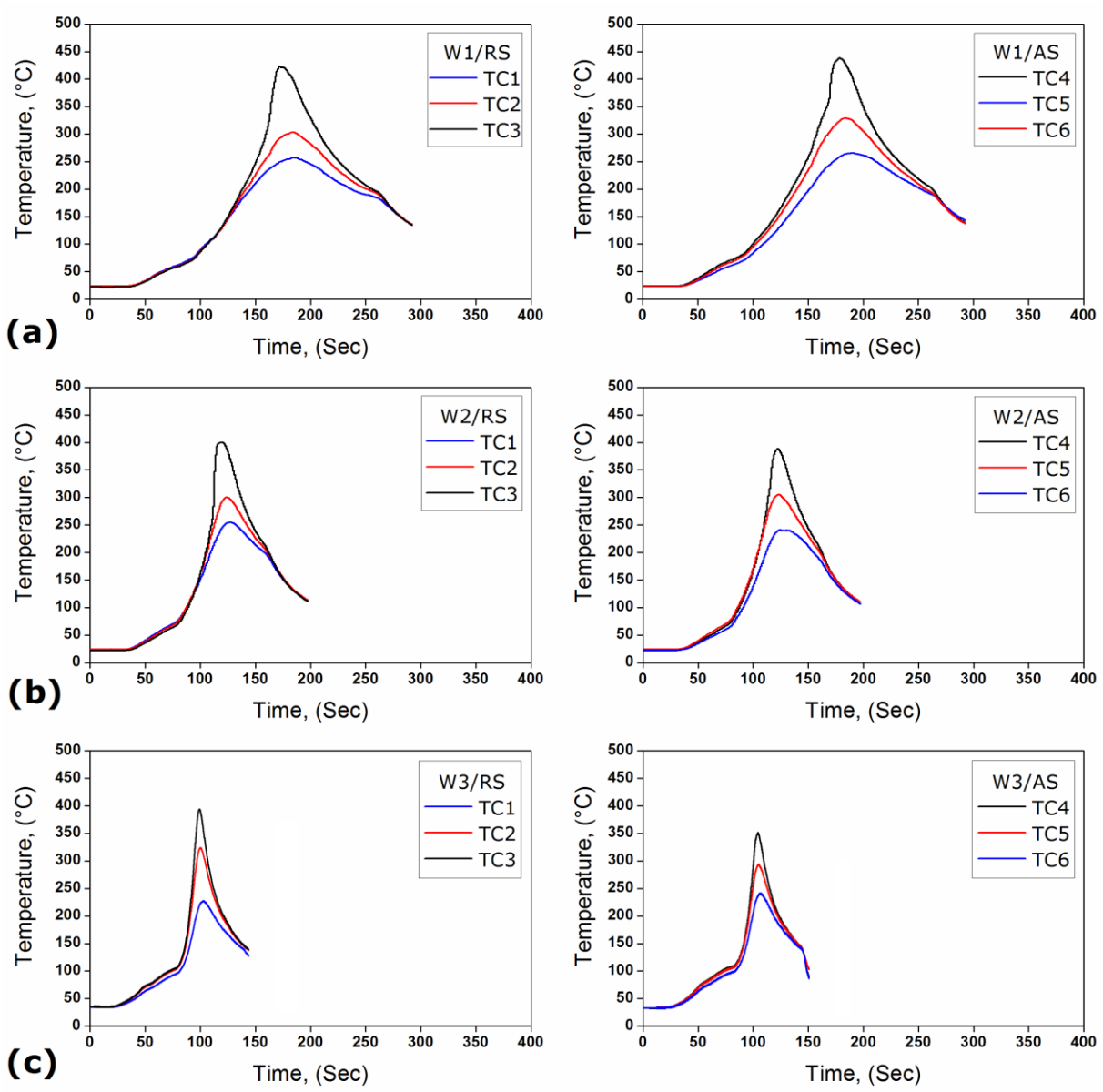


Figure 4-37 Thermal histories of SAMC joints welded at a tool rotation speed of 1500 rpm and different tool traverse speed; (a) 25, (b) 50, and (c) 100 mm/min

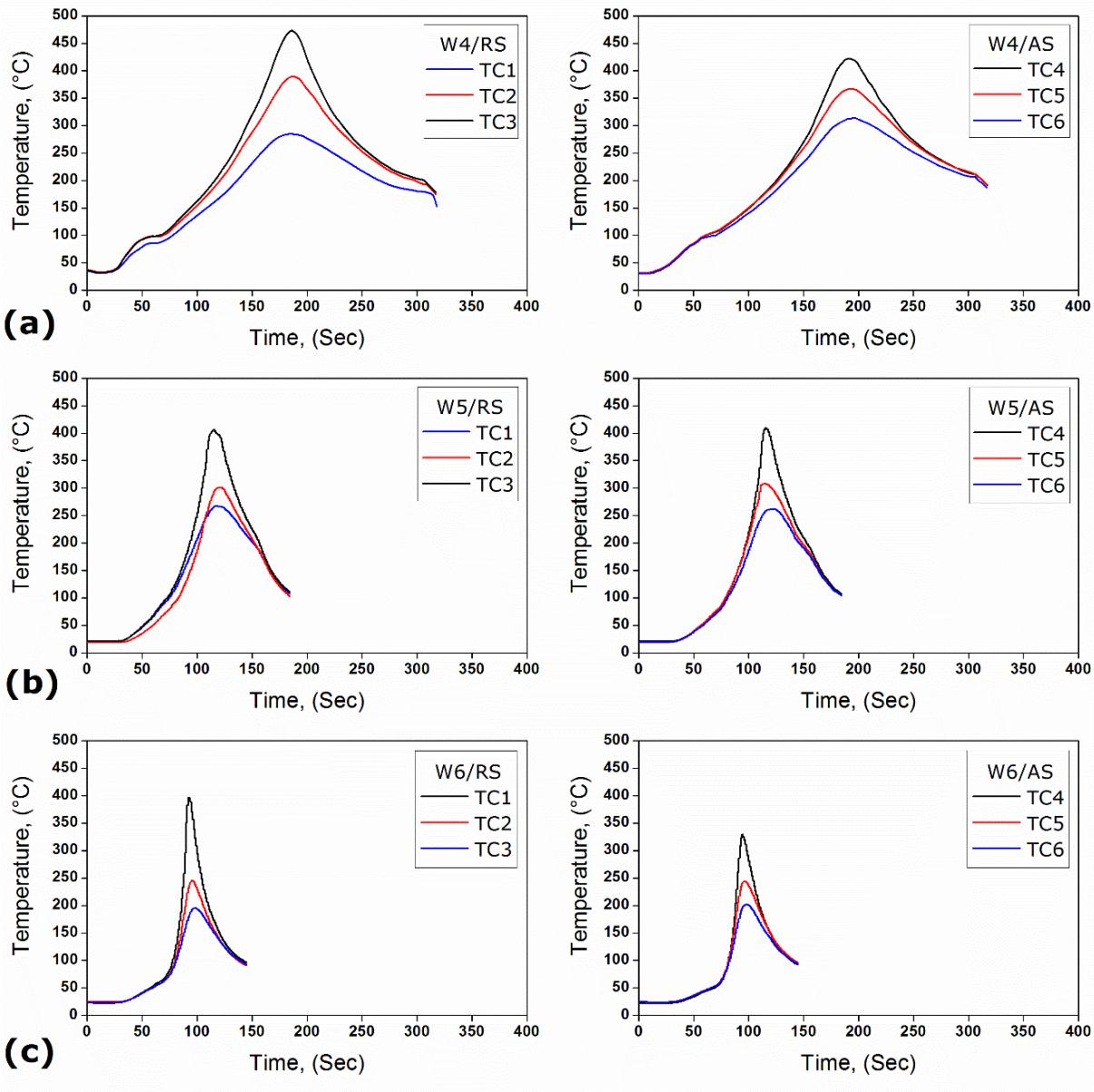


Figure 4-38 Thermal histories of SAMC joints welded at a tool rotation speed of 1800 rpm and different tool traverse speed; (a) 25, (b) 50, and (c) 100 mm/min

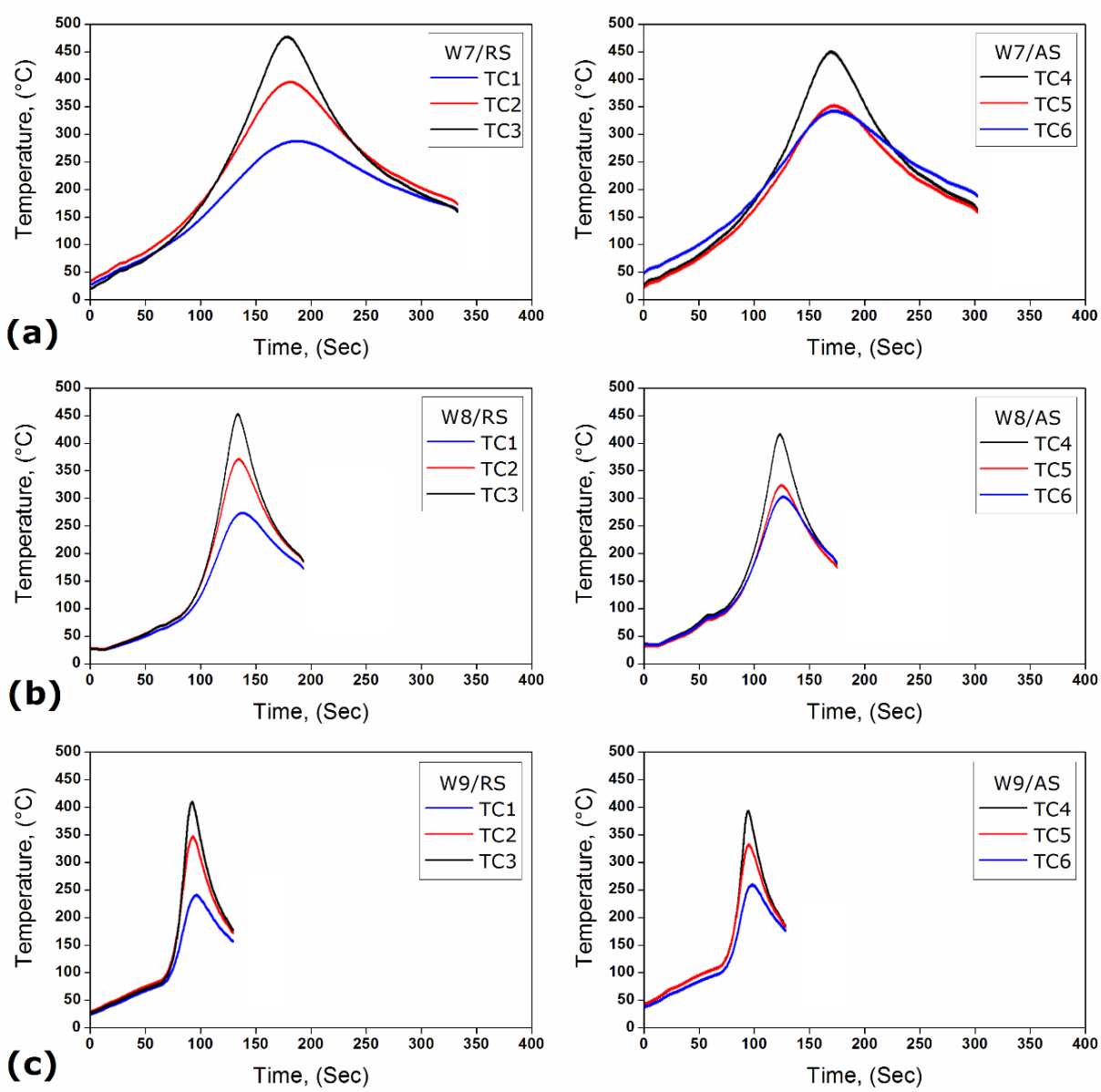


Figure 4-39 Thermal histories of SAMC joints welded at a tool rotation speed of 2100 rpm and different tool traverse speed; (a) 25, (b) 50, and (c) 100 mm/min

4.4.2 Metallurgical characterisations of the as-received SAMC

Figure 4-40 shows the optical and SEM microstructure of the cross-section of SAMC. It is seen that this material consists of aluminium matrix composite as a core (hard) covered by two layers of aluminium (soft) on the top and bottom surface having a thickness of around 0.5 mm. The SEM image of the core composite shows a reasonable distribution of the SiC reinforcement particles in the matrix alloy having a size ranging

from around 200 to 700 nm. Also, it is pointed out that there are some SiC particle clusters in the BM. This phenomenon is more likely to happen with the increasing of SiC particles volume fraction [119].

Figure 4-41 presents the EBSD Euler map, grain size distribution, and misorientation angle of the core metal. In the EBSD map, the white area represents the SiC, while the black and red lines represent the HAGBs and LAGBs, respectively. The core microstructure is dominated by a fine grain having a size ranging from around 2 to 6 µm with a mean diameter of around 1.6 µm (see Figure 4-41 a and b), as well as, there is some elongated grain (green oval) due to incomplete recrystallisation. This is confirmed by the distribution of misorientation angle as shown in Figure 4-41 (c), as it is consist of a mixture of a high fraction of HAGBs and LAGBs (subgrains).

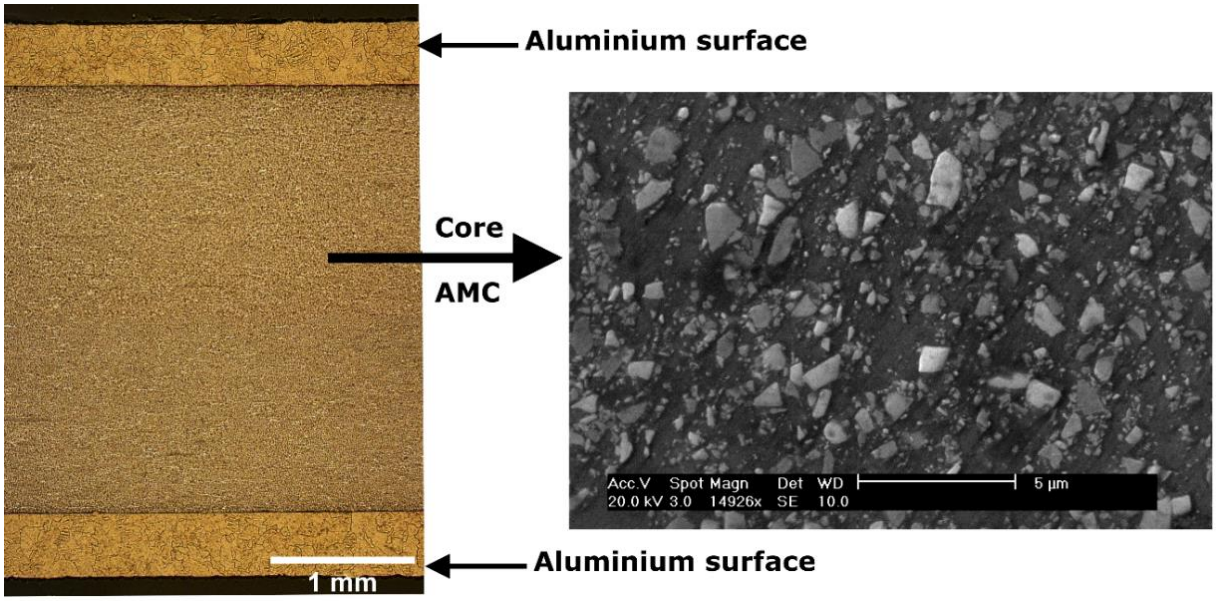


Figure 4-40 Optical and SEM microstructure observed at the cross-section of SAMC

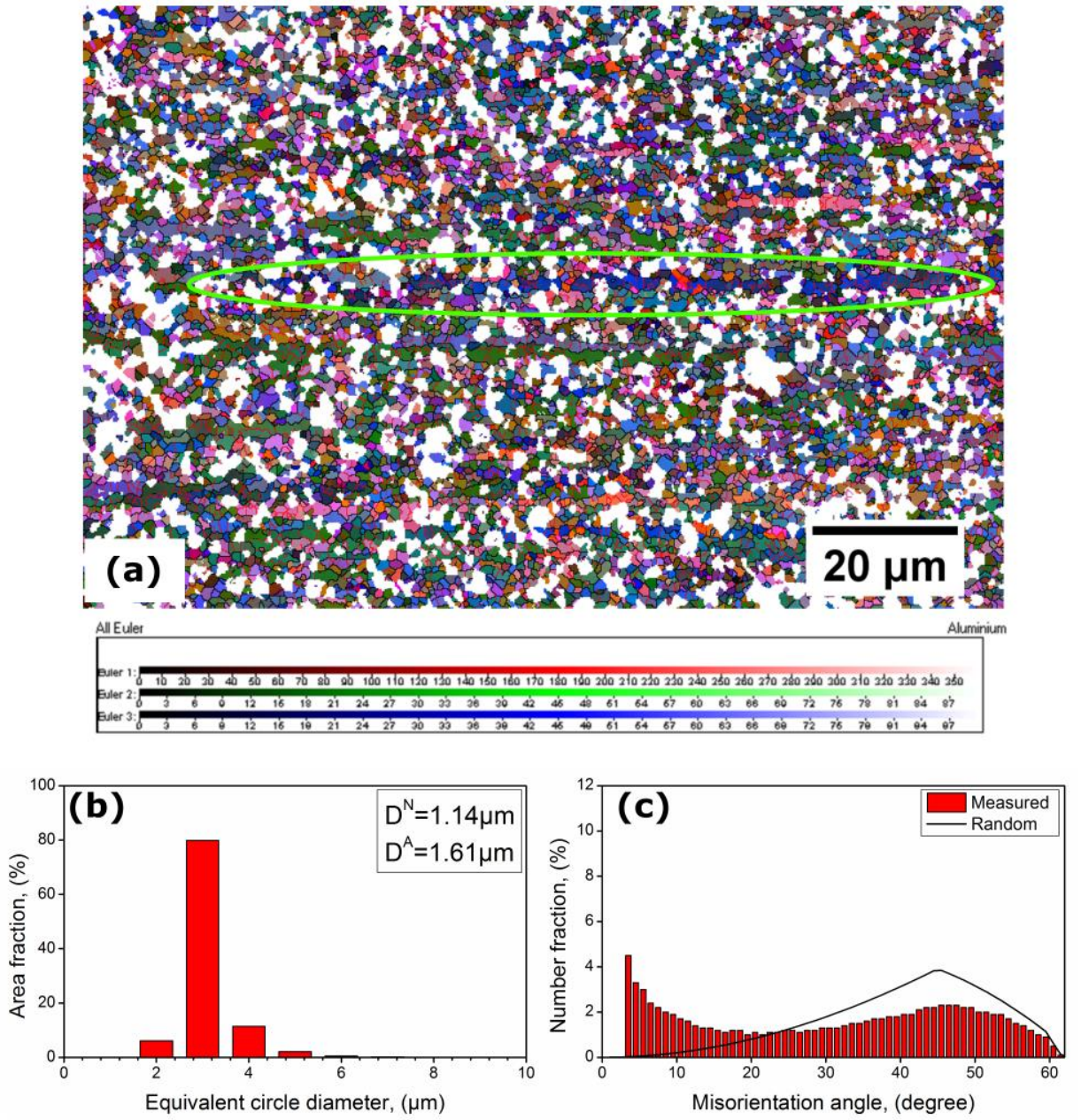


Figure 4-41 Microstructure characterisation of SAMC; (a) EBSD map, (b) Grain size distribution, and (c) Misorientation angle

4.4.3 Metallurgical characterisations of SAMC FSW joints

4.4.3.1 Macrostructure and surface morphologies of the weldment

Figure 4-42 presents the surface morphologies of SAMC FSW joints under different welding parameters of tool rotation and traverse speeds. Visual observations revealed that a smooth surface was mostly formed in contact with the tool shoulder combined with the

formation of excessive flash, as the top surface layer characterised by softening. Figure 4-43 displays the related cross-weld macrostructure of the welded joints. The macrographs reveal that joints free defect were formed with no significant volume defects such as tunnels, pinholes, and wormholes under all welding parameters. However, joints welded at 1800 rpm – 50 and 100 mm/min (see Figure 4-43 W5 and W6) show a flowing arm of soft aluminium alloy generated from the bottom surface to the centre of weld forming continuous elliptical shape not mixed with core metal and segregate between the NZ and TZ. This feature has been confirmed by EDS map and spectrum as shown in Figure 4-44. Also, it can be seen from the macrograph figures that the increase of tool traverse speed leads to keep a thinner layer of aluminium on the top surface.

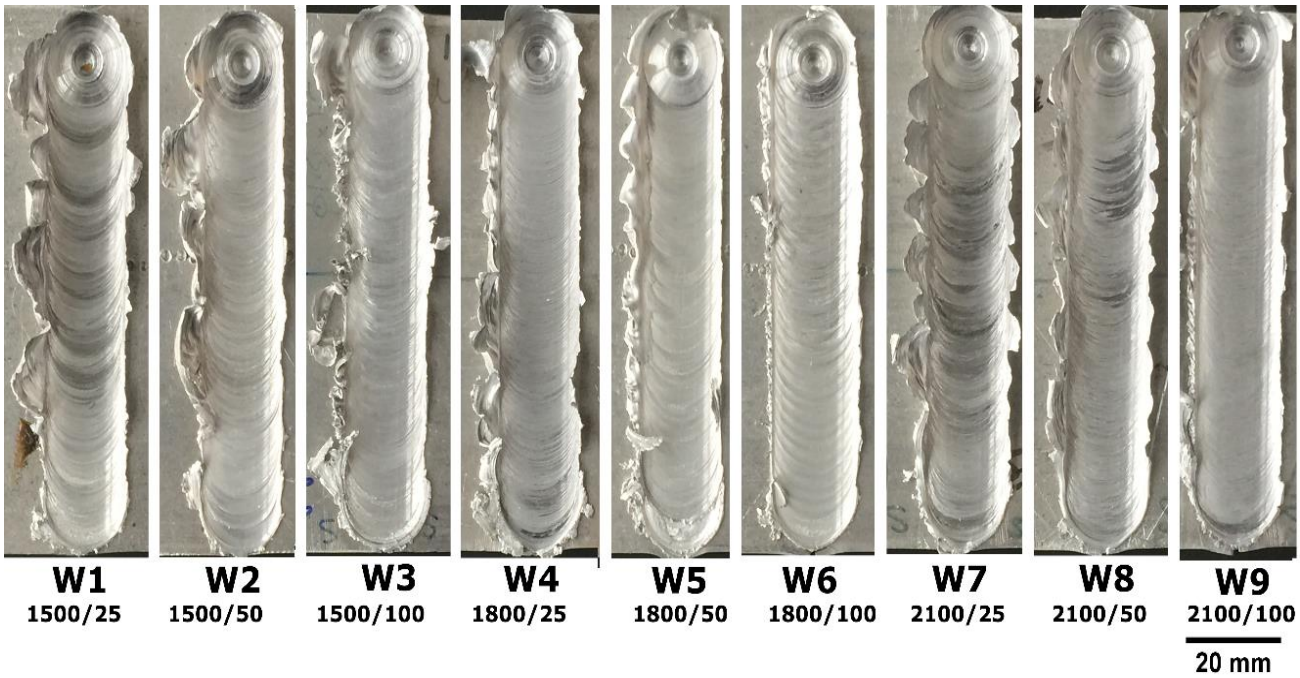


Figure 4-42 Surface morphologies of SAMC FSW joints under different welding parameters (AS on the right)

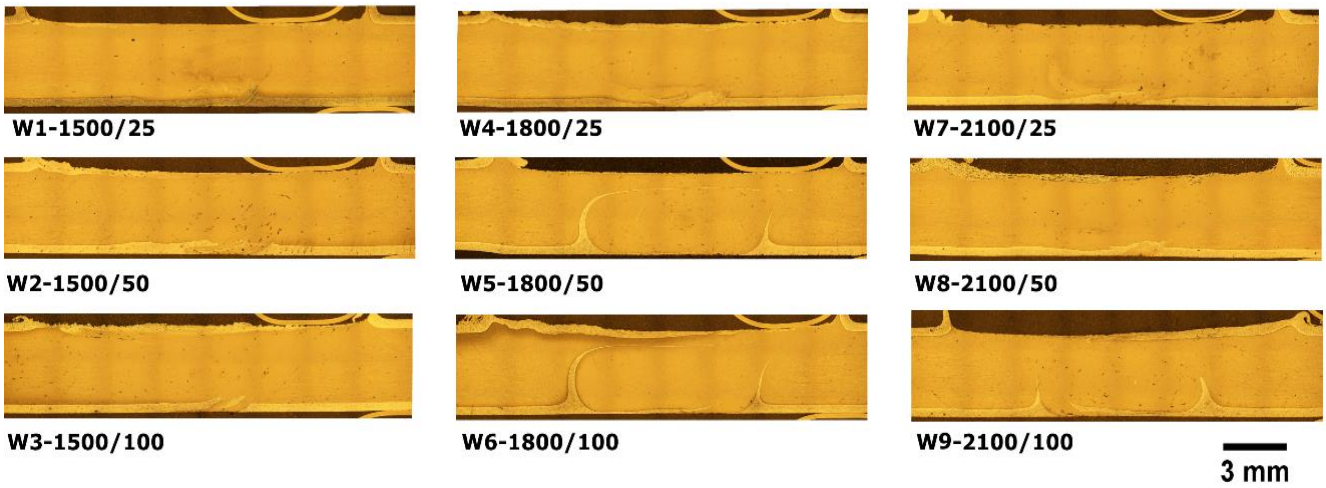


Figure 4-43 Cross-weld macrostructure of SAMC FSW joints under different welding parameters (AS on the right)

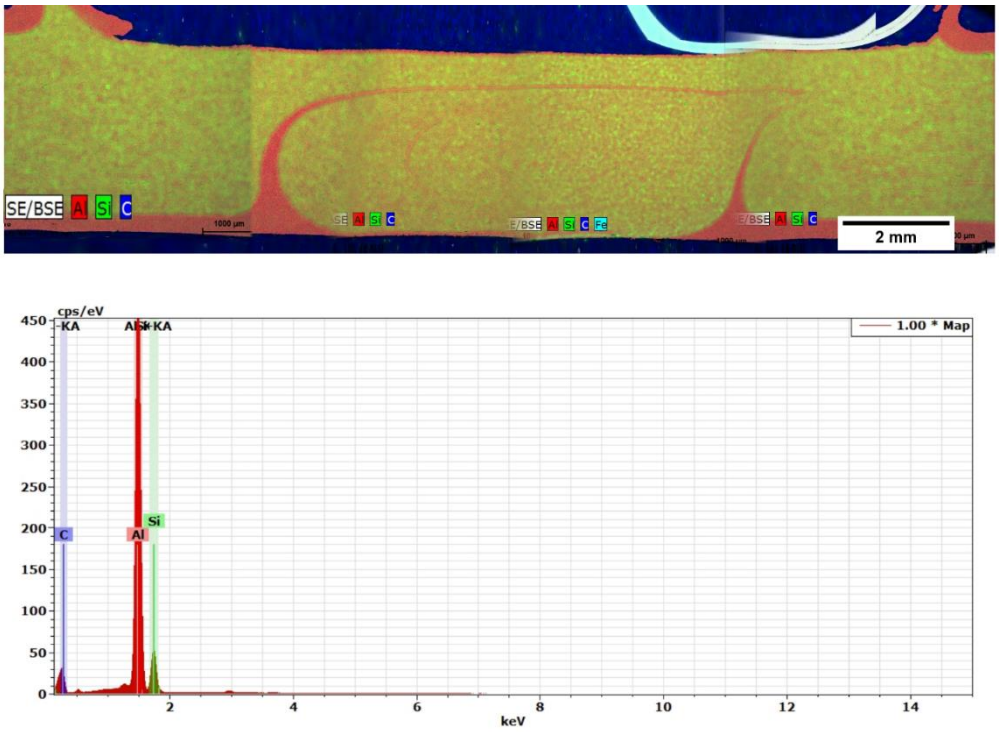


Figure 4-44 EDS map and spectrum of SAMC joint welded at 1800 rpm and 50 mm/min (W5)

Figure 4-45 shows the onion ring structure in the NZ. Because there are two different materials in SAMC; the formation of a composite structure within the NZ is inevitable. Typically, it appears in the forming of onion ring in the NZ alternating layers of the soft aluminium and hard AMC as shown in Figure 4-45-b, which is a higher magnification from the subregion from Figure 4-45-a. Figure 4-45-c presents the related EBSD map; it clearly shows the variations in grain evolution as it is consist of different grain size characterise the banded structure with a network of LAGBs spread throughout the structure.

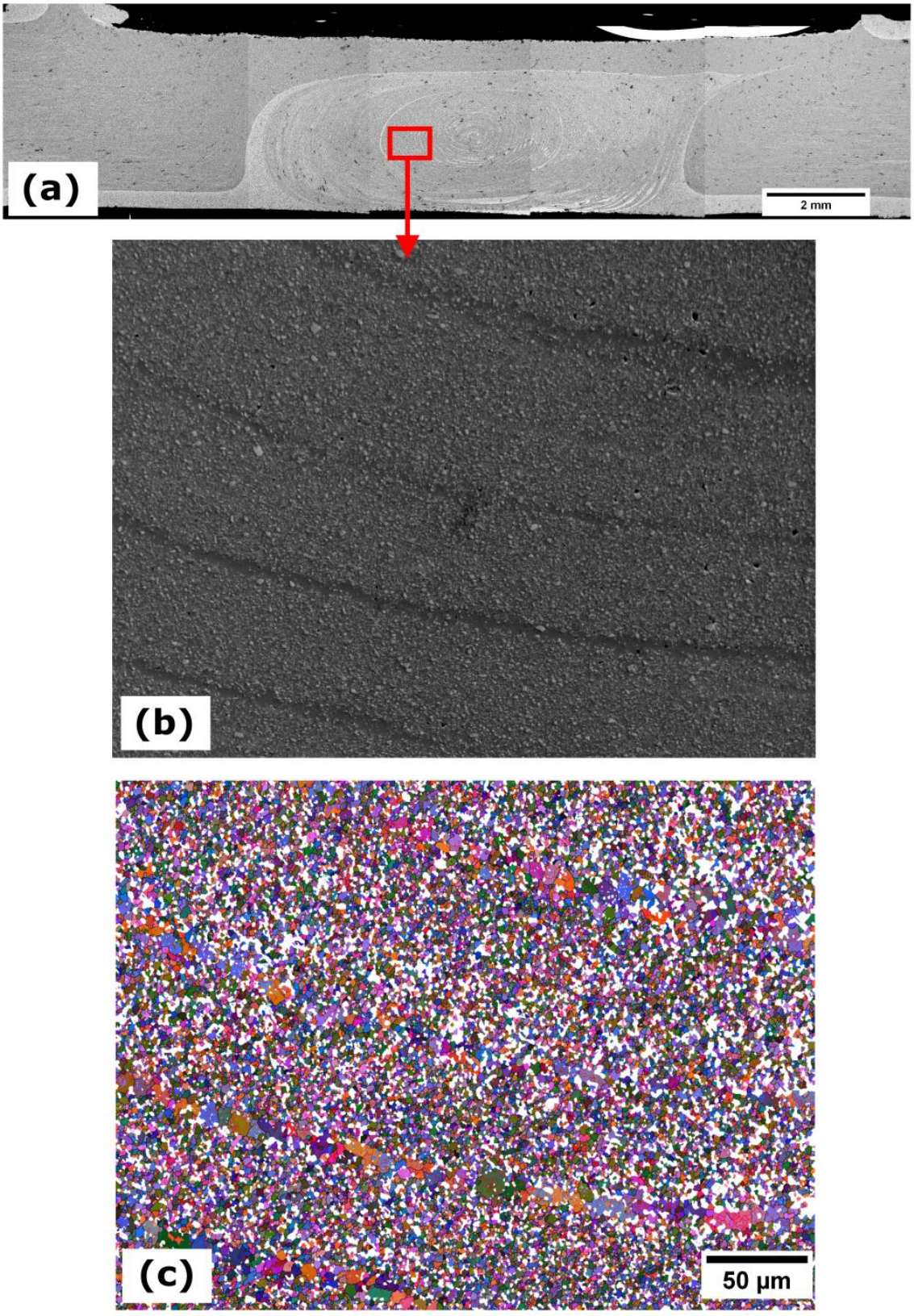


Figure 4-45 Typical onion ring microstructures of SAMC in the centre of NZ for W5 welds; (a) SEM, (b) Higher magnification from the indicated region in (a), and (c) Related EBSD map

4.4.3.2 Microstructure evolution in SAMC FSW joints

Due to the main application of SAMC in the aerospace industry, a homogeneous particle distribution is needed to achieve consistent mechanical properties. The SiC distribution in the NZ is given in Figure 4-46. After FSW, the SiC particles were more homogeneously distributed in the NZ, except the area that contained aluminium alloy in the onion ring structure as discussed above. It is interesting to note that a lower concentration of clusters is observed in the NZ than in the BM. It was reported that a reduction in the particle clusters in composite metals happens in the extrusion process [120]. In the same way, it appears that the stirring action of FSW can be beneficial to produce homogenous particles distribution in the NZ. Thus, it is reasonable to believe that the clusters present in the BM are broken down during the welding process.

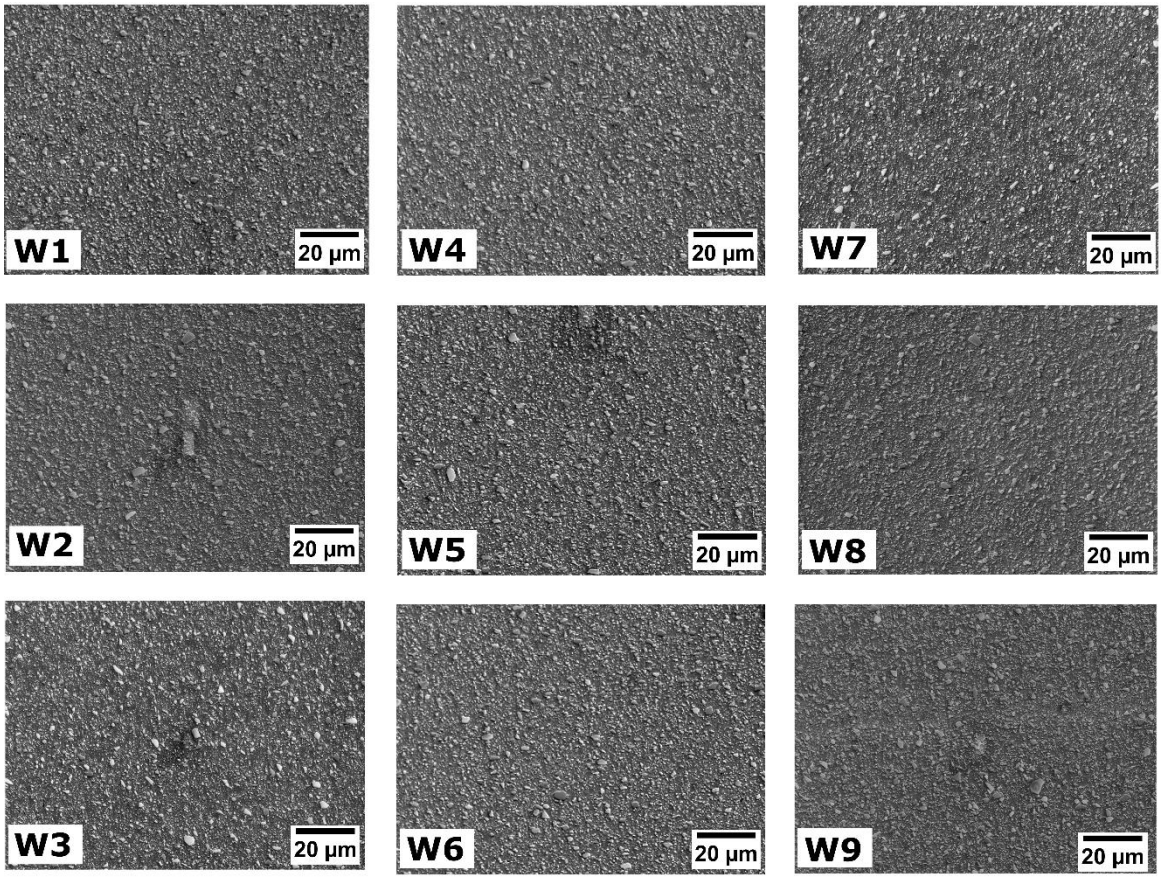


Figure 4-46 SiC distribution in the NZ of SAMC joints under different welding conditions

The EBSD Euler orientation and grain boundary maps in the NZ for welds obtained at different welding conditions are presented in Figure 4-47. In comparison with as-received material more homogeneous microstructures with fine equiaxed grains were formed in the NZ within a range of around 1.5 to 2.6 μm as shown in Figure 4-48. Figure 4-49 presents the related misorientation angle distributions. Under most of welding conditions grains, refinement dominated by a high fraction of HAGBs close to the random distribution were formed due to complete recrystallisation processes. However, there is an increase in the LAGBs of W5, W6, and W9 joints, which is resulted from the heterogeneity in grain sizes exhibited in the form of bands containing coarse grains (soft aluminium alloy) of size ranging from about 6 to10 μm, and fine grains (AMC) having an average size of around 1.7 μm (see Figure 4-47 W5).

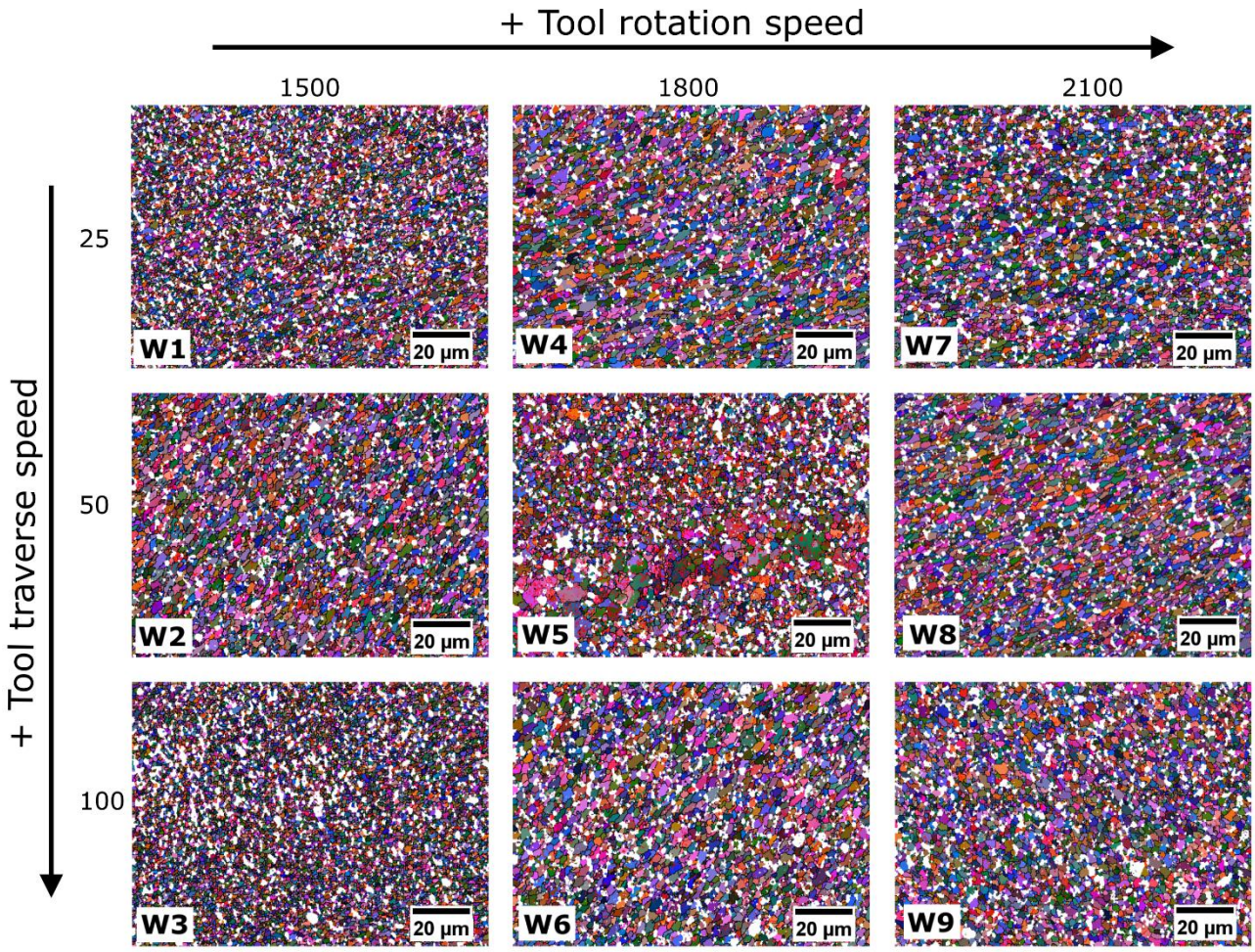


Figure 4-47 EBSD images of grain morphology and the distribution of HAGBs (black line), and LAGBs (red line) under different welding conditions

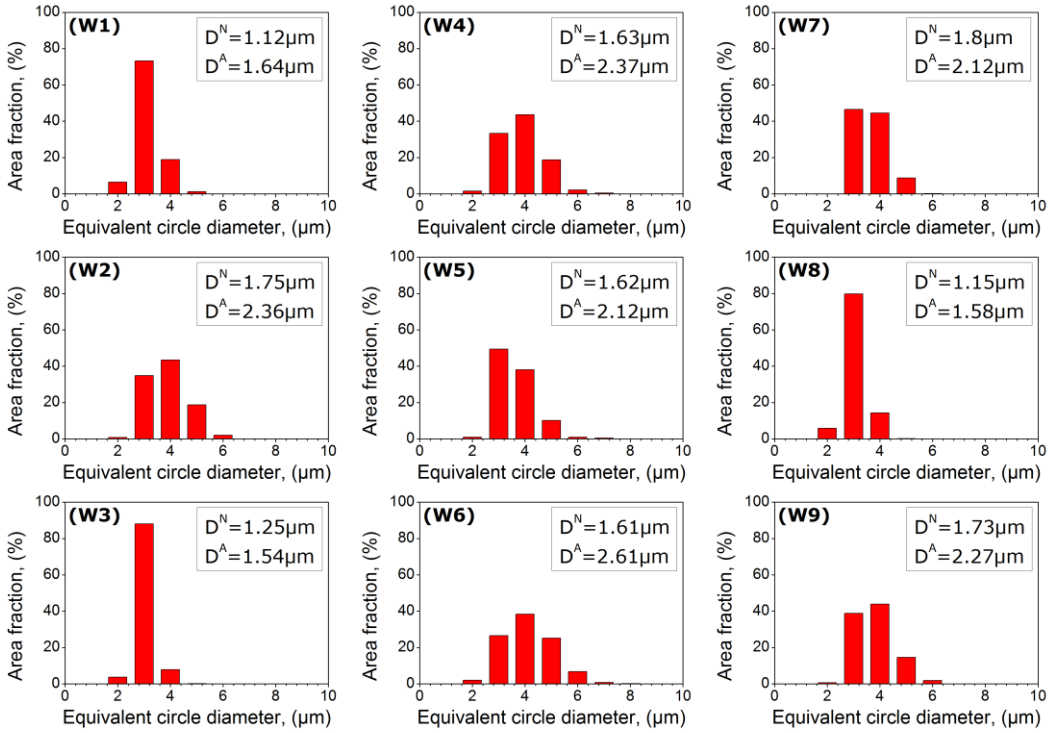


Figure 4-48 Grain size distribution in the NZ of SAMC joints under different welding conditions

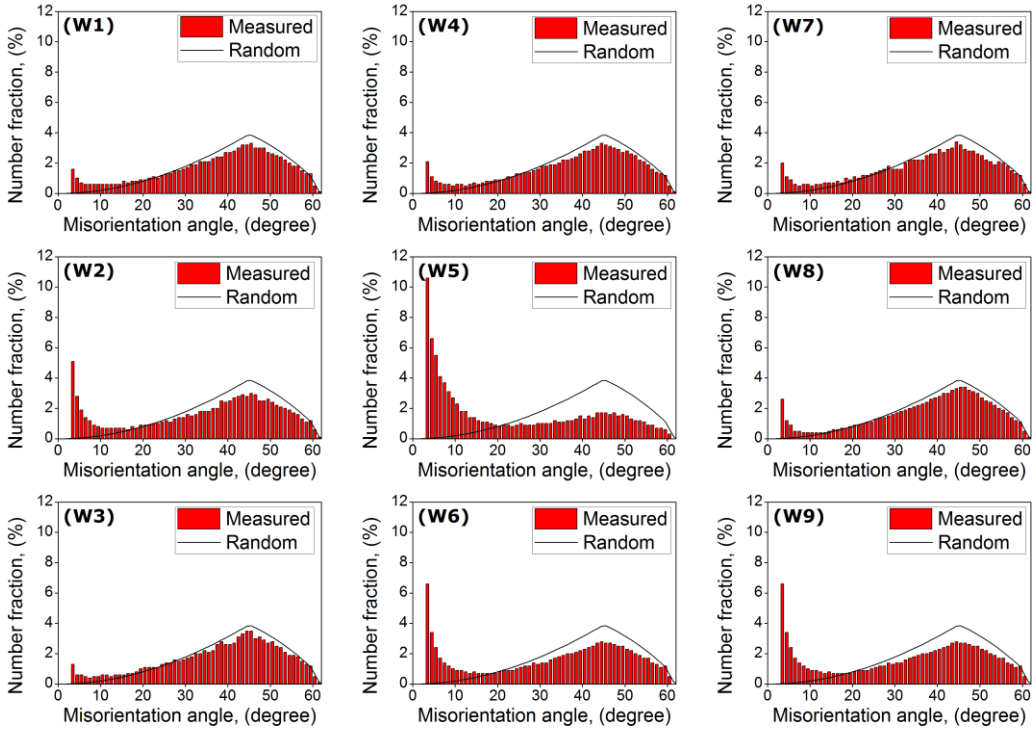


Figure 4-49 Misorientation angle in the NZ of SAMC joints under different welding conditions

The EBSD map of the TZ from the BM to the NZ in the AS of a typical weld (W6) is shown in Figure 4-50. It is seen that this zone consists of three significant microstructure characteristics; firstly, very fine completely recrystallised equiaxed grain in the NZ. Secondly, the soft aluminium alloy flow arm with very large grain segregate between the NZ and TZ. Thirdly, a heavily deformed microstructure with sharply rotated elongated grains in the form of substantial plastic stirring as lamellar shear bands in the TZ.

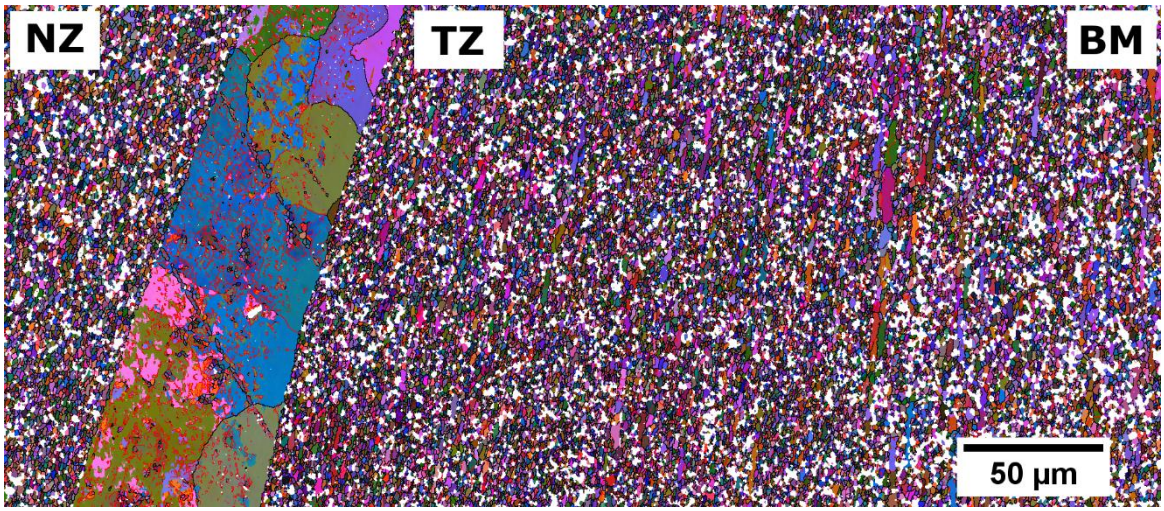


Figure 4-50 Friction stir zone on the AS of the W6 SAMC FSW joint

4.5 Analysis and discussion of results

The properties and performance (weld quality) of the FSW joints are strongly controlled by FSW parameters (tool rotation and traverse speed). As the relationship among the process parameters, heat generation, material flow and plastic deformation, are so complicated [7], this contributes to form a complex structure, and development of texture within the stirred zone [15] and dissolve and/or re-precipitated strengthening precipitate in the FSZ [121]. This study has demonstrated that the variation in the FSW parameters plays a significant role in the recrystallisation and grain refinement, crystallographic texture, strengthening phase transformation, and joint soundness and

these aspects obviously influence the overall quality of the FSW joints. An interaction diagram (Figure 4-51) has been developed to relate the quality of weldments to the experimental parameters investigated in this study; this is accomplished by looking into the basic physics of how the experimental parameters influence the physical parameters that control the quality of weldments. For example, an increase in tool rotation speed will increase the amount of heat input, material flow and plastic deformation and thus a variation in the metallurgical and mechanical properties.

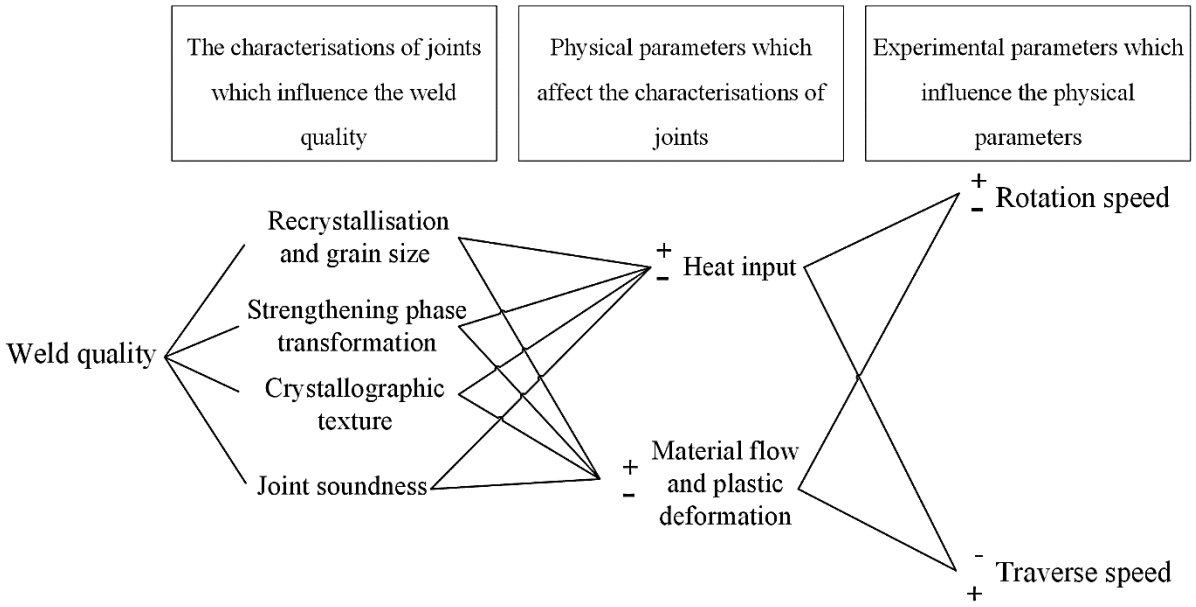


Figure 4-51 Interaction diagram linking the experimental parameters with the physical parameters and joint characterisations, which are influence the weld quality

The in-depth metallurgical characterisation of the aluminium alloy (AA 6082-T6), AMC (AA 6092/SiC/17.5p-T6), and SAMC (AA 6061B/SiC/20p-T1) as base metal and FSW joints have revealed several microstructural features that can be linked to the influence of the base metal microstructure and FSW parameters. The effect of FSW parameters on the heat input and thermal history for all studied materials is reported.

Moreover, the investigations also highlighted the microstructural characterisations under different welding conditions. Based on the developed interaction diagram, it was

found that the relationship among welding parameters, heat input and metallurgical characterisations is quite complex. The correlations between these effects and the observed microstructural features will be discussed in this section.

4.5.1 Effect of FSW parameters on the heat input and thermal cycle

Understanding the effect of FSW parameters on the thermal histories is a critical issue as it has a significant effect on post-weld metallurgical characteristics and subsequently on the mechanical properties. FSW differs from conventional welding processes such as arc and laser welding, since these use an external heat source of a specified power, whereas in FSW heat is generated from friction action between tool surfaces (shoulder, and pin) and BM, as well as from the severe plastic deformation of welded materials. The heat input is, therefore, a complex function of the welding parameters, the alloy being welded, and the tool design [122]. A higher amount of heat is generated from the tool shoulder than the tool pin due to the larger contact area between shoulder and BM surface and the higher linear velocity of the shoulder than that of the pin. Except for the plunging and retracting tool steps, heat is generated at a constant rate during the intermediate period, and similar geometry, structure and properties are formed in the cross-welds, which indicates a quasi-steady behaviour [123-125]. Thus in this study, the peak temperature and thermal history were measured in the mid-length of the welded joints. In FSW the combined effect of the tool traverse speed and tool rotation speed is defined as the weld pitch (WP), as it is the ratio between tool traverse speeds to tool rotation speed (mm/rev). WP controls the thermal cycle during the welding process, i.e., the FSW joint exposed to higher cooling rate and lower exposure time at high temperature when higher WP is used. The peak temperature generated in the NZ of FSW joints of the three studied materials are plotted as a function of tool rotation speed (see Figure 4-1, Figure 4-19, and

Figure 4-36) and as a function of the WP as shown in Figure 4-52. In AA 6082 (Figure 4-52 a) the increase of WP by rising the tool traverse speed from 20 to 200 mm/min (ten times) at a constant tool rotation speed of 1800 rpm results in a decrease in the peak temperature by nearly 2%. In comparison, decreasing the WP by increasing the tool rotation speed from 800 to 1800 rpm (2.25 times) caused the peak temperature to rise by about 25% and 22% at a constant tool traverse speed of 20 and 200 mm/min, respectively. Also, there are considerable variations in the peak temperature for the combinations of tool rotation and traverse speed corresponding to the same WP.

A similar trend has been noticed in the AMC and SAMC (Figure 4-52 b and c), these figures indicate three tendencies for attention. Firstly, for joints welded with the same tool traverse speed, the reduction in peak temperature as a function of WP was so sharp. For AMC, the increase of WP by decreasing the tool rotation speed from 2100 to 1500 rpm (29%) caused the peak temperature to decrease by about 17 %. Secondly, for joints welded with a similar tool rotation speed, a lower sharpness in the drop of welding temperature has obtained. The rises of tool traverse speed from 25 to 100 mm/min (300%) increase the WP, leading to a reduction of the peak temperature by nearly 2.5,1.2 and 1.5 % for tool rotation speed of 1500, 1800 and 2100 rpm, respectively. Thirdly, there is no significant change in the welding temperature, and it tends to be saturated when the tool rotation speed rises from 1800 to 2100 rpm. Sato et al. have experimentally confirmed this phenomenon [126]. They demonstrate that the maximum temperature rises gradually beyond 2000 rpm. This observation can be related to the reduction of the friction coefficient and torque when the weld metal softens at a high temperature [15]. This leads to reduce the heat generated in the metal by mechanical work and stabilise the temperature to avoid the melting of metal.

As a result, from these facts, it can be clearly seen that the induced temperature on the workpiece is influenced by both tool rotating and traverse speeds with considerable variations in the peak temperature for the combinations of tool rotation and traverse speeds corresponding to the same WP. Also, the important general observation that can be revealed from these figures is that the tool rotation speed has a more significant effect on the generated peak temperature than the tool traverse speed. These findings are in agreement with the finding of Seidel and Reynolds [127]. They reported that the amount of energy input (Joules/meter) relates to the specific WP, as the WP increase, a reduction in the energy per unit length of weld occurred.

Regarding the cross-weld thermal history in the AS and RS for the three investigated materials, it is seen that the highest temperature is closest to the weld line, and it is nearly symmetric on both sides concerning the weld line. However, it is clear that the temperature at the RS is higher than that at the AS. Schneider, J. A [128], and Rui-dong Fu et al. [129] have reported a similar thermal history trend. This trend can be explained from a metal flow mechanism viewpoint in FSW. The FSW tool swept the hot softened material from the AS to the RS, as the tool moves ahead more heat generated on the RS.

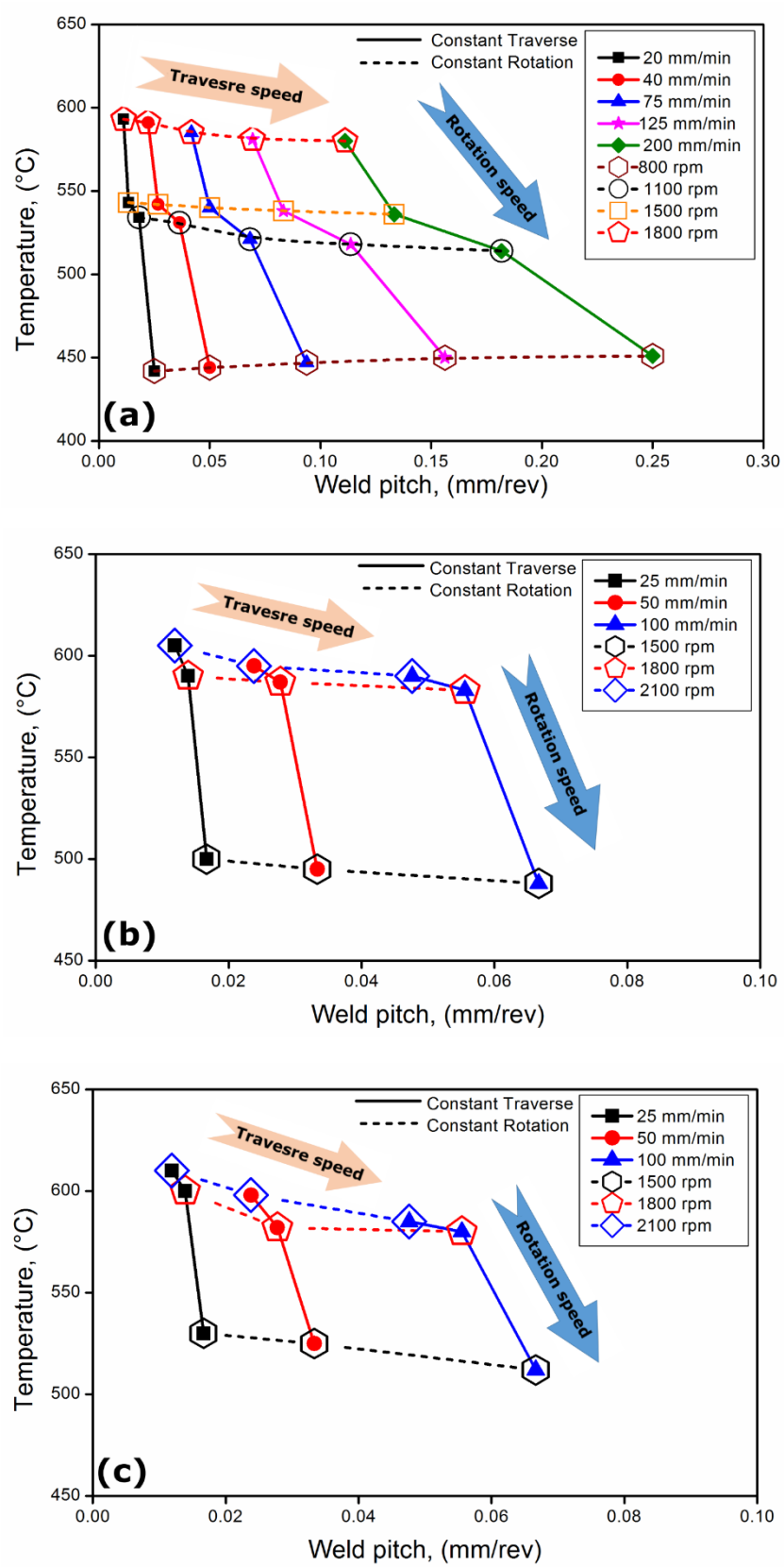


Figure 4-52 Relationship between peak temperatures and weld pitch at constant traverse and rotation speeds for different materials; (a) AA 6082, (b) AMC, and (c) SAMC

4.5.2 Effect of thermal history on the metallurgical characteristics of FSW joints

The initial microstructure of the BM influences the final microstructure evolution of the FSW joints. Also, the observed microstructural difference between the BM and FSW joints are believed to be related to the peak temperature, exposure time at highest temperature, temperature gradient, and plastic deformation, which is controlled by welding parameters (tool rotation and traverse speeds) [42, 130]. As previously shown in this chapter, the initial state microstructure of the three studied materials (AA 6082, AMC, SAMC) consisted of inhomogeneous grain structure as presented in Figure 4-4, Figure 4-24, and Figure 4-41, respectively. The BM sheets were prepared with different processing routes, which has resulted in different microstructural homogeneity specific to the processing routes, for example a highly elongated pancake shape grain structure dominated by HAGBs in AA 6082, coarse grain dominated by LAGBs in AMC, and very fine equiaxed grain with a mixture of HAGBs and LAGBs in SAMC. In FSW, the evolution of microstructure, texture and plastic flow within each subzone of the FSZ is highly dependent on the thermal cycle and stress states [113, 131]. Thermal and mechanical stresses are induced during the welding process from thermal history and tool stirring action, respectively. Microstructure evolution near the top surface of FSZ is mainly affected by the stresses induced from the tool shoulder, while the rest of NZ is affected by the induced stresses from the rotating pin. Thus to avoid the complicated effect of thermal cycle and material flow in the top and bottom part of the FSZ, a systematic investigation was carried out on the centre of the NZ.

4.5.2.1 Influence of FSW parameters on the macrostructural characterisation

The FSZ of most welded joints (AA 6082, AMC, and SAMC) showed the formation of joint free defects with complete penetration (see Figure 4-9, Figure 4-26, and

Figure 4-43). However, volumetric defects and incomplete penetration were formed in the FSZ of AA 6082 FSW joints fabricated at low tool rotation speed (800 and 1100 rpm) and high traverse speed (125, and 200 mm/min) as a result of insufficient frictional heat, stirring action, and material plastic deformation. Thus, for AMC and SAMC, higher tool rotation speed starts from 1500 rpm, and tool traverse speed up to 100 mm/min was used to achieve complete plasticization and material flow for proper coalescence and avoid defects formation.

So far, it is broadly identified that three different deformation zones in FSW joints, namely NZ, TMAZ, and HAZ. However, on a finer scale, this deformation is associated with a more intricate feature generally known as the "metallurgical band" or "onion rings", which is a unique feature in the NZ of FSW. Microscopically, this feature is observed as a repetitive pattern on the cross-weld of the joints in a swirl pattern. In this study, two structures are found for the onion ring based on the used BM. For AA 6082 and AMC, the onion rings structure arises due to a rhythmic variation in grain size as shown in Figure 4-30. Meanwhile, in the SAMC, it is formed due to precipitate alternating layers of soft aluminium and hard AMC with different grain size as shown in Figure 4-45. The appearance of onion ring structure in the NZ is direct evidence of material flow phenomena occurring during the FSW, and it is associated with the oscillation of the tool rotation axis about its linear travel axis [112].

Furthermore, for all studied materials, the NZ exhibits an elliptical shape as a result of using high tool rotation speed. This is in agreement with an investigation of friction stir processing (FSP) of cast aluminium A356 conducted by Ma et al. [132]. They reported that the NZ profile is highly depending on process parameters, at a higher tool

rotation speed of more than 700 rpm elliptical NZ was observed; meanwhile, the lower tool rotation speed of 300–500 rpm resulted in the formation of basin-shaped NZ.

The TMAZ has experienced partial recrystallisation processes, as the peak temperature and plastic deformation is not quite sufficient to cause complete recrystallisation. Meanwhile, there are no significant plastic deformations in the HAZ, and it is only affected by the thermal cycle generated during the welding process. However, even though this zone is experienced a thermal cycle, it is not influenced by the heat regarding grain size. Instead, the most common metallurgical phenomena happened at higher temperature are decomposition of strengthening precipitates [94, 133, 134].

4.5.2.2 Influence of FSW parameters on the microstructural characterisations

The contribution of intense plastic deformation and high-temperature exposure during welding process results in the generation of a recrystallised fine equiaxed dislocation-free grains microstructure within the NZ in comparison to the initial BM microstructure. The relationship between the mean grain size measured by EBSD and the peak temperature in the NZ for the investigated materials are displayed in Figure 4-53.

In aluminium alloy (AA 6082), two tendencies can be noticed on the effect of welding parameters on the grain size as shown in Figure 4-53-a. Firstly, by increasing the tool rotation speed, the mean grain size increases with the generated welding peak temperature under the studied conditions, and it is more pronounced at the highest rotation speed of 1800 rpm. However, the evolved grain is finer than that of the BM. Secondly, it is evident that the increases of the traverse speed lead to decreases the grain size. This is attributed to the lower soaking time at peak temperature and a high cooling rate (the amount of heat input is mainly affected by tool rotation speed, while, the tool

traverse speed determines the cooling rate). According to Heidarzadeh et al. [135], this result shows that the relationship between grain size and the peak temperature of the welds is similar to the static grain growth equation.

According to the Figure 4-53 (b), two behaviours are observed in AMC; firstly, at lowest tool rotation speed (1500 rpm), larger grains were formed at highest tool traverse speed. This behaviour can be related to the incomplete recrystallisation in the NZ, as a result of lower heat input, insufficient stirring time, and a high cooling rate. This behaviour is confirmed by the formation of a low fraction of HAGBs (see Figure 4-35 (W3)). Secondly; at the higher tool rotation speed (higher heat input) the mean grain size coarsened (grain growth) with the generated welding peak temperate under the studied conditions, and this effect was found to be more pronounced at the highest rotation speed (temperatures exceeding 0.75 from melting temperature). It is evident that the grain size decreases accompanying increases of the traverse speed, as a result of low exposure at high temperature, which leads to form finer recrystallised grain in the NZ with a high fraction of HACBs.

The effect of peak temperature on the mean grain size in the NZ of SAMC is shown in Figure 4-53-c. It can be seen that the increase of tool rotation speed did not show a significant effect on the size of the evolved grain in the NZ. This can be related to the initial BM microstructure, as it consists of very fine equiaxed grain. However, the welding process leads to increase the fraction of the HACBs in comparison to the BM (see Figure 4-49).

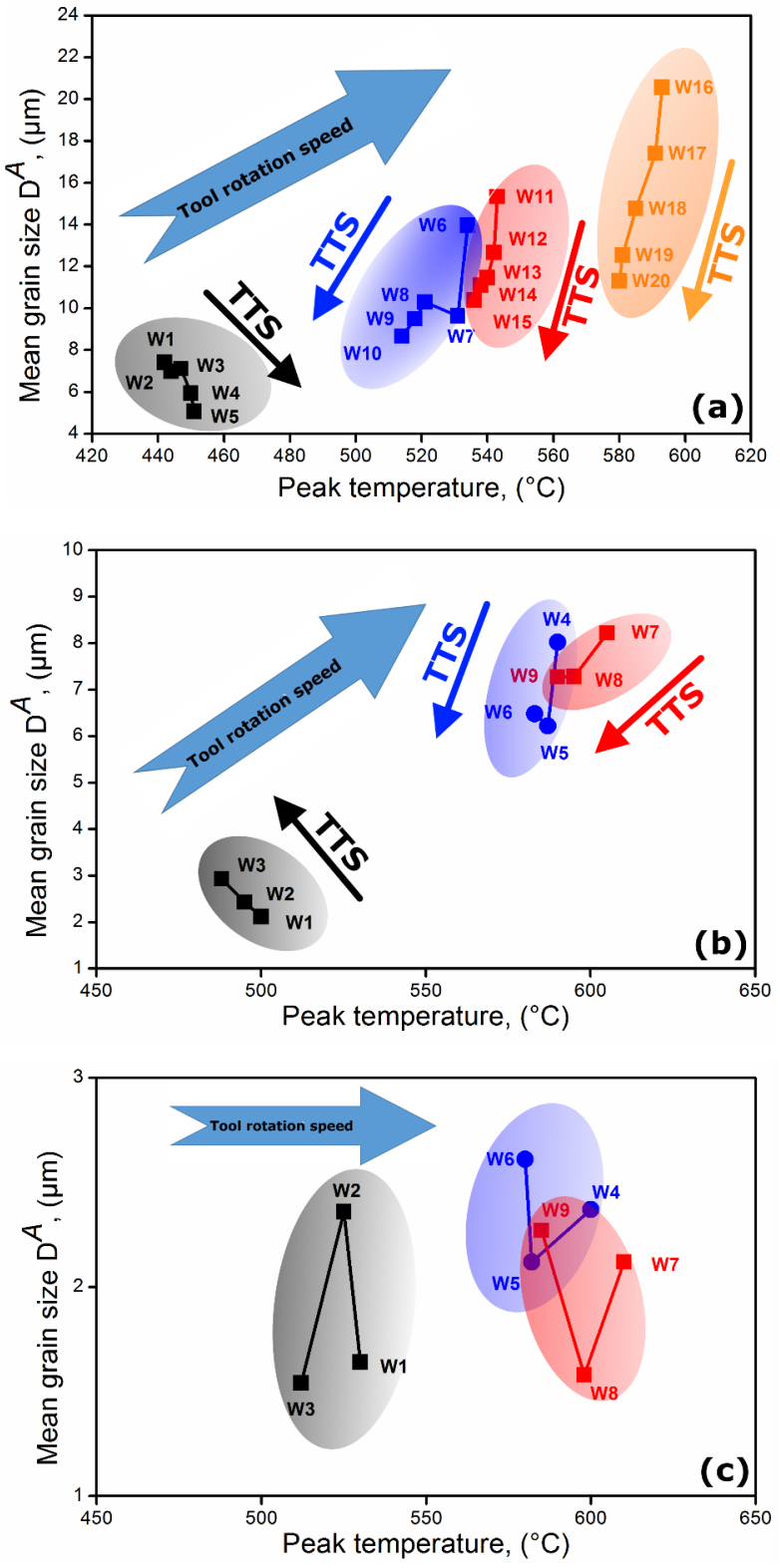


Figure 4-53 Relationship between peak temperatures and grain size for investigated materials; (a) AA 6082, (b) AMC, and (c) SAMC. [TTS: tool traverse speed]

The understanding of local grain structure and properties are necessary for the understanding of its behaviour and effect on the mechanical properties. The mechanisms of recovery and recrystallisation that happened in the NZ are so complicated, and it can be considered as a combination of both cold and hot working. From metalworking viewpoint, Mishra et al. [112] pointed out that these mechanisms occurred during FSW in the NZ as a result of both static recovery (SR) - static recrystallisation (SRC), which happens in cold working and dynamic recovery (DR) - continuous (geometric) dynamic recrystallisation (CDR), which is associated with hot working. Figure 4-54 illustrated the relationship between temperatures/strain and time with three zones to be identified based on thermal cycle and strain. The regions A and C experience only thermal cycle when the tool is plunging and removing from the workpiece, respectively, and it is exposed to SR - SRC. While, region B is the period when the tool traverses along the weld joint, which experiences thermal cycle and plastic deformation leading to dominated DR and CDR.

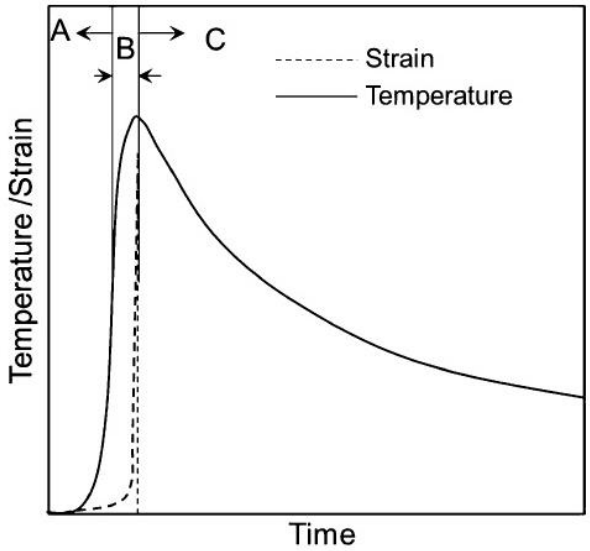


Figure 4-54 Schematic variation of temperature and strain in the NZ of friction stir process [112]

Thus, it is believed that the refinement of the grain in the NZ can be related to the DR and CDR process, which occurs during severe plastic deformation at elevated

temperature. The stages of the development of microstructure continuously and uniformly are; DR by subgrain (low angle boundaries) growth without nucleation and growth stages, CDR, and grain growth. These processes are essential in FSW, as they lower the flow stress of the material, so enabling it to be deformed more efficiently and to influence the grain size and texture. The microstructure of the BMs showed a variation in the grain size with a mixture of HAGBs (high surface energy) and low energy substructure network LAGBs (subgrains). This can be related to the fact that when the polycrystalline metal deformed a large number of LAGBs are formed, as the LAGBs consist of arrays of edge dislocations [116]. On the other hand, during FSW, the NZ microstructure showed fine equiaxed recrystallised grains with more homogenous grain distribution and a high fraction of HAGBs replacing the original grain and subgrain boundaries.

The mechanism of the evolution of microstructure in the NZ by DR and CDR can be explained by the hot working process at large strain deformation viewpoint as follow: The deformation process associated with FSW introduces a large number of dislocations. The dislocation climb, cross-slip, and glide occur quickly at high temperatures in metals of high stacking fault energy (SFE) such as aluminium (around 170 mJm^{-2}), which is the mechanism of DR process. This process is rapid and extensive and results in the formation of more organised dislocations arrangement (LAGBs), and subgrain aligned on the plane of high shear stress and contain a significant number of dislocations which are not associated with the LAGBs. As the evolution of microstructure at an elevated temperature where the deformation and softening processes occur depends on the deformation temperature, strain rate, and strain. Thus, the subgrain size is a function of the Zenner-Hollomon parameter $Z = \dot{\varepsilon}\ \exp(\frac{Q}{RT})$ in which $\dot{\varepsilon}, T, and\ Q$ denoting the strain

rate, temperature, and activation energy, respectively. The developed grain boundary during DR contains serrations with a wavelength nearly equal to the subgrain size resulted from the local migration of the grain boundary (as shown schematically in hot rolling Figure 4-55). CDR process then occurs as the increasing of applied strain resulting in more flattening in the original grain without a significant change in the serrations wavelength, and dislocations are continuously introduced to the subgrains by further deformation. As the subgrain size is almost independent of the strain during deformation at high temperature, instead the subgrains rotate as they accommodate more dislocations into their boundaries, forming fine equiaxed grains having a size comparable to the subgrain with HAGBs evolve from the interpenetration among the scalloped boundaries, followed by dynamic grain growth [122, 136, 137]. Based on the above discussions this can give an explanation of the formation of fine equiaxed grain dominated by HAGBs in the NZ of welded joints.

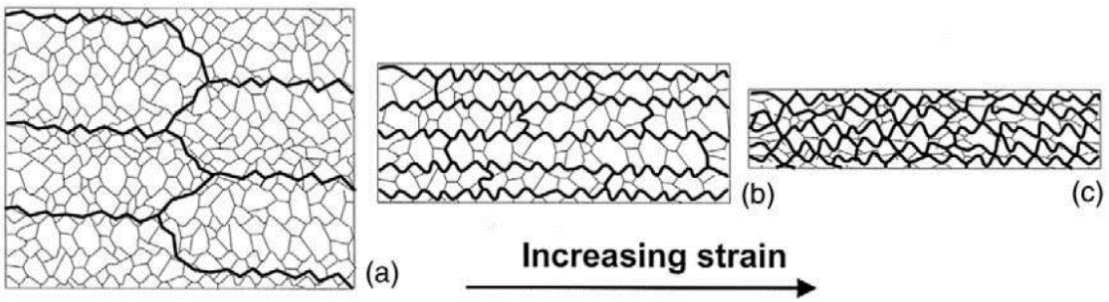


Figure 4-55 Continuous dynamic recrystallisation. As deformation progresses, the serrated HAGBs (thick lines) become closer, although the subgrain size remains approximately constant [136]

4.5.2.3 Influence of thermal history on the strengthening precipitate

The changes in the shape, density and distribution of strengthening precipitates occurred in the FSZ, which are strongly influenced by the thermal hysteresis during FSW [134]. Ageing precipitation strengthening is the key strengthening mechanisms in Al-Mg-Si alloy, and it is accepted that the precipitation sequence was as follows: $\alpha\ (ssss) \rightarrow$

$GP\ zones \rightarrow \acute{\acute{\beta}}\ (needle\ shaped) \rightarrow \acute{\beta}\ (lath\ shaped) \rightarrow \beta\ (Mg_2Si\ + Si)$,where SSSS is supersaturated solid solution [138, 139]. $\acute{\acute{\beta}}$ (Mg_5Si_6) phase is the main source of strengthening, as it is a semi coherent interface with the aluminium matrix, which is more effective for dislocation pinning [109, 140]. As shown in Figure 4-6 (c-d), the fine needle shaped $\acute{\acute{\beta}}$ primary strengthening precipitates were detected in the BM. A complete decomposition process of $\acute{\acute{\beta}}$ phase to $\acute{\beta}$ (Mg_9Si_6) occurred in the HAZ (see Figure 4-17 (b-c)), as the temperature in the HAZ above the decomposition temperature of about 250 °C [139]. On the other hand, the dissolution and re-precipitation process is more likely to happen within the grains in the NZ and form both phases, as the maximum temperature in the NZ was ranging from around 442 to 605° C (as discussed in sections 4.2.14.3.1), which is above the solvus line and below the eutectic temperature of the BM that lead to form SSSS. Thus, the fraction of fine or /and coarse precipitates are formed based on the exposure at high temperature and cooling rate.

4.6 Summary

The chapter provides a detailed evaluation of the effect of two key FSW parameters, namely the tool rotation speed, and tool traverse speed and their interaction on the thermal histories and metallurgical characterisations in the FSW of AA 6082, AMC, and SAMC alloys. Experimental testing was used in order to evaluate the significance of each parameter on the fabricated joints. The evaluating processes have been done by an optical microscope, SEM, EBSD, TEM, and EDS. Furthermore, this chapter highlighted the welds microstructure differences among the investigated alloys.

The results showed that the tool rotation speed has a more significant effect on the generated peak temperature, while the tool traverse speed controls the exposure time and

subsequent cooling rate. From the evaluation of cross-weld macrostructure and surface morphology of welded joints, it can be concluded that the combination of FSW parameters has a significant effect on the stirring process and the flow of softened material in the NZ, which resultantly influences the joint soundness and the quality of the FSW joints. The use of higher weld pitch leads to increase the tendency of formations tunnel defects, cavity, and incomplete penetration in the FSW joints, as a result of insufficient plastic flow and mixing time and improper heat input.

The initial BMs microstructure showed inhomogeneous grain structure with a mixture of HAGBs and LAGBs. On the other hand, the different zones of the weld exhibit very different microstructure, and it is significantly affected by frictional heat and plastic flow. The microstructure of NZ exhibits an elliptical shape, and fine equiaxed grains resulted from the CDR process with an increase in the fraction of HAGBs. Also, the NZ microstructure of all studied joints showed the formation of the onion ring structure. In AA 6082 and AMC this structure consists of alternating layers of different grain size. Meanwhile, in SAMC, it is consist of alternating layers of aluminium alloy and core AMC.

The TMAZ consists of rotated elongated grains inclined by around 45°, which is resulted from severe plastic deformation. In conclusion, the macrostructure and microstructure of FSW joints and in particular the NZ is dependent mainly on the welding parameters, which affect the flow of softened materials, recrystallisation and grain growth, and strengthening precipitates.

Chapter 5 Mechanical characterisations and residual stresses of AA 6082, AMC, and SAMC FSW joints

5.1 Introduction

The complex microstructural evolution during FSW is expected to result in various mechanical properties. This chapter aims to determine the influence of the evolved microstructure on the mechanical behaviour of AA 6082, AMC, and SAMC FSW joints. The mechanical testing results for all studied materials cover the microhardness, tensile, and low cycle fatigue (LCF) that includes the evolution of the maximum and minimum stress per cycle, and the stress versus mechanical strain hysteresis loops. This allows a detailed evaluation of the influence of local microstructure in the NZ on the strength and ductility of joints and its implication on the LCF performance. Finally, the residual stresses induced in FSW joints during the welding process are also studied.

5.2 Microhardness distribution

To evaluate the effect of the FSW parameters on the hardening or softening of the welded joints, Vickers microhardness test has been done. The hardness distribution was obtained by taking the average measurement of three readings. The distance between successive indentations was 1 mm along the cross-section of the FSW joints at the mid-length of the welding line.

5.2.1 Microhardness distribution in AA 6082 FSW joints

To correlate among thermal history, microstructure, and microhardness development, the distribution of hardness at the cross-weld, alongside the measured temperatures for joints welded at maximum and minimum values of tool rotation (800 and 1800 rpm) and traverse (20 and 200 mm/min) speeds (corners of the welding matrix W1, W5, W16, and W20 (see Table 3-3)) are presented in Figure 5-1.

In comparison to the BM's hardness (120 Hv), which is consist of elongated grain and fine needle precipitate, the NZ hardness dropped significantly regardless of welding parameters. Meanwhile, the hardness of transition zones varied between those of the BM and NZ. Figure 5-1(a) compares between the hardness profiles of samples welded at the lowest tool rotation speed of 800 rpm with different tool traverse speed of 20 and 200 mm/min. It can be seen that the hardness profile for both welds exhibits a V-shape, i.e., the minimum hardness value recorded in the middle of NZ. At lower traverse speed (20 mm/min), the hardness drops progressively before reaching a minimum of about 45Hv in the NZ. As the traverse speed is increased to 200 mm/min, the minimum hardness increases to nearly 60Hv, without significant change in the width of the TMAZ and HAZ. This indicates that the temperature within the welding zone was high enough (around 450° C) to allow for complete dissolution of strengthening precipitates ($\acute{\beta}$) in the case of

low tool rotation speed (20 mm/min). At high traverse speed (200 mm/min), the welding zone is exposed to less exposure time at high temperature, which leads to the coarsening of strengthening precipitate and transformed completely to ($\acute{\beta}$) as shown in the inset TEM images. In addition, the formation of fine grain structure at higher traverse speed contributes to the increase of the hardness.

When the tool rotation speed increases to 1800 rpm, the hardness distribution is more complicated and changed to W-shape with the wider softened region as shown in Figure 5-1(b), which is consistent with the increase of the induced temperature. As the tool traverse speed increased, higher hardness with a narrower softened region was obtained. This indicates that the generated heat (ranging from 580 to 593°C) in the FSZ was sufficient to cause dissolution/re-precipitation effect and precipitate both $\acute{\acute{\beta}}$, and $\acute{\beta}$, as shown in the inset TEM images, in addition to grain refinemnt, which accordingly resulted in the observed increase in the hardness.

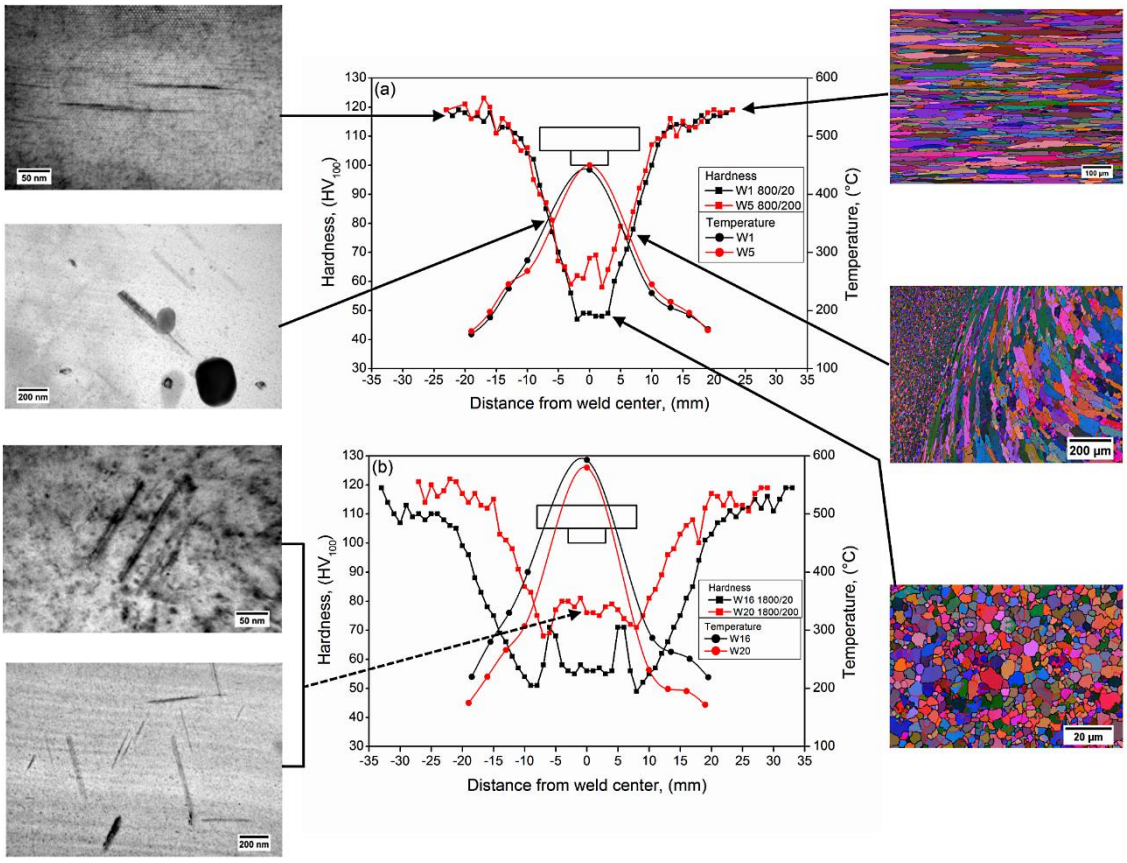


Figure 5-1 Cross-weld microhardness profile of AA 6082 FSW joints with the measured temperature and microstructure at different tool rotation speed; (a) 800 rpm, and (b) 1800 rpm

5.2.2 Microhardness distribution in AMC FSW joints

Figure 5-2 presents the distributions of hardness along the mid-thickness of the AMC cross-weld joints welded at tool rotation speed of 1500, and 2100 rpm with traverse speed of 25 and 100 mm/min (corners of welding matrix W1, W3, W7, and W9 (Table 3-4)). The hardness profile exhibit symmetric distribution with a typical "W" shape for all joints, like to that seen in AA 6082 as discussed in the previous section and same as reported by Wang et al. [58] and Ni et al. [70] in AA 2009/SiC FSW joints. Regardless of the welding parameters, a softening process occurred in the welding zone, and the hardness value of the as-received BM was much higher than that of the welding zone of around 150 HV. For the joints fabricated at the lowest traverse speed of 25 mm/min, a wider TMAZ and HAZ were formed with the increase of tool rotation speed from 1500

to 2100 rpm (Figure 5-2 (a)), associated with a higher peak temperature and exposure time. However, the hardness value in the NZ was nearly same and ranging from 95 to 110 HV. As the traverse speed increased to 100 mm/min (Figure 5-2 (b)), the average hardness of the NZ increased by about 20 HV combined by a reduction in the TMAZ and HAZ. Furthermore, the width of the high hardness zone in the joints fabricated at a traverse speed of 100 mm/min was larger than that of the joints welded at 25 mm/min. It is believed that this variation in the hardness of welded joints is a result of the difference of microstructures characterisations, which are controlled by welding parameters [141].

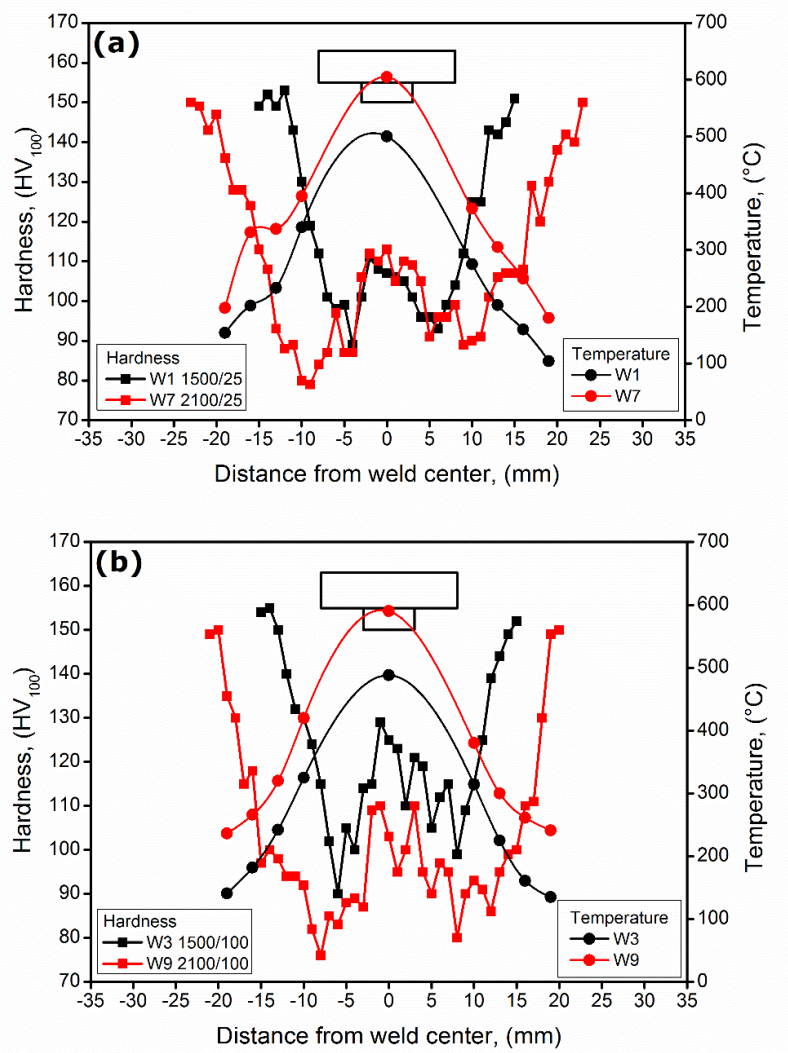


Figure 5-2 Cross-weld microhardness profiles of AMC at a traverse speed of; (a) 25 mm/min, (b) 100 mm/min

5.2.3 Microhardness distribution in SAMC FSW joints

The hardness profiles of SAMC welded joints fabricated by using tool rotation speed of 1500, and 2100 rpm with traverse speed of 25 and 100 mm/min (corners of welding matrix W1, W3, W7, and W9 (Table 3-4)) are illustrated in Figure 5-3 (a and b). As indicated in the figures, unlike the results of the hardness obtained from AA 6082 and AMC welded specimens. The NZ hardness is observed approximately similar to that of the base material (around 120 Hv) regardless of welding parameters. A similar trend has been reported by Öztoprak et al. [142] in FSW of AA 6061/SiC/20p-T1. Also, the hardness distribution in the FSZ is nearly symmetric concerning the tool rotation axis, and there is little scatter, which can be attributed to the presence of varied size of SiC nanoparticles within measuring points. However, the obtained profiles are associated with both the microstructure evolution of the material and the dispersion of the particles. It can be seen that in the transition zone from the base metal to the stirring zone (the flowing arm), the hardness variation was more drastic, and it is dropped to around 30 Hv, as shown in Figure 5-3 (b), due to the appearance of the softer aluminium layer.

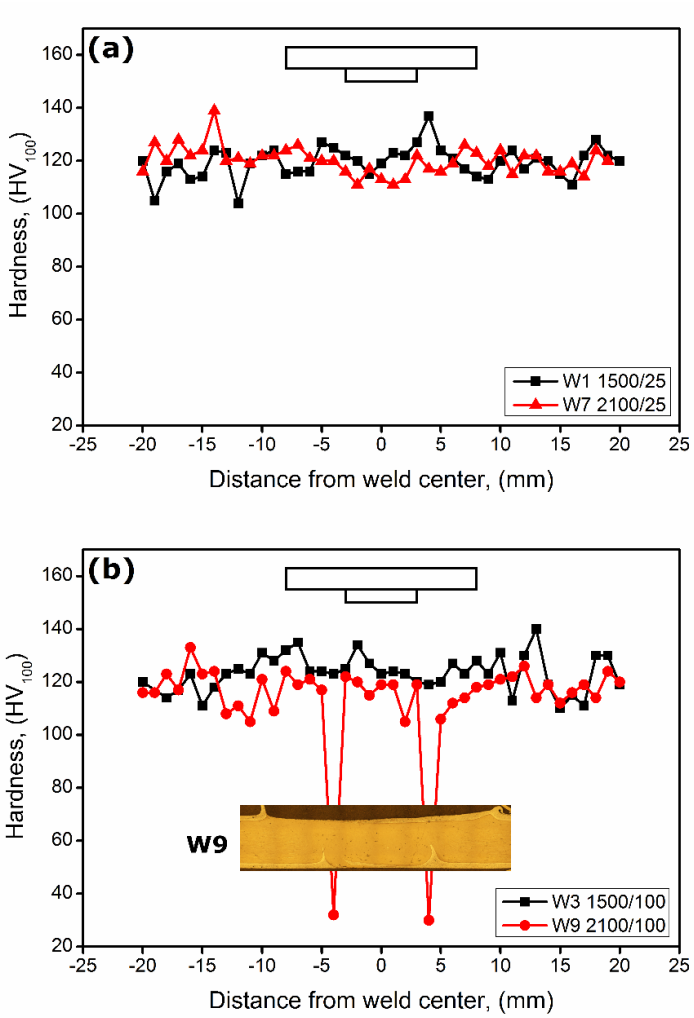


Figure 5-3 Cross-weld microhardness profiles of SAMC at a traverse speed of; (a) 25 mm/min, (b) 100 mm/min

5.3 Monotonic tensile properties

5.3.1 Tensile properties of AA 6082 FSW joints

The cross-weld samples (W1-W20) underwent tensile tests at room temperature to examine the mechanical response according to the variations in FSW parameters; their engineering stress-strain curves are shown in Figure 5-4 (a-d), together with those of the as-received BM, and the weld line of W12 joint (W12-WL). Furthermore, for more quantitative analysis of the test results the ultimate tensile strength (UTS), yield stress (YS), and fracture elongation (El) are presented in Figure 5-5. The as-received BM

exhibited a tensile strength of about 318 MPa with a high total elongation to failure of around 17%. On the other hand, the cross-weld specimens exhibit lower tensile strength and ductility than the BM, and they vary with the FSW parameters due to their variation in the evolved microstructure. Also, it is observed that at constant tool rotation speed the flow stress increases gradually with the increases of traverse speed, which means that the amount of strain-hardening is dependent on the tool traverse speed (for example Figure 5-4 (d)). This hardening effect is combined by a reduction in the elongation specifically at lower tool rotation speed (800, 1100, and 1500) owing to the reduction in heat input per unit length of the weld and insufficient stirring time. This leads to inappropriate stirring in the NZ and forms volumetric defects, and incomplete penetration (as presented in Figure 4-9). The joint efficiency of cross-weld sample ranges from 40 to 71 % with a reduction in the elongation ranging from around 38 to 72 %. However, comparing to the tensile properties of AA 6082-T6 welded by fusion welding [79, 95], the FSW joints in this work shows a higher improvement in the tensile properties remarkably in the percentage of elongation to failure. Under most welding conditions, the cross-weld FSW samples exhibited shear fracture mode occurred mostly in the HAZ (AS). By comparison, the weld line sample (W12-WL) with the cross-weld samples exhibits a moderate strength (60 % joint efficiency) and higher ductility nearly the same as the BM (95%). Surprisingly, the cross-weld samples show the formation of the step-like discontinuities in stress (serration) “jerky flow phenomenon”. This phenomenon is less pronounced at higher traverse speed, and it is not pronounced in the BM, and WL-W12 samples (smooth curve).

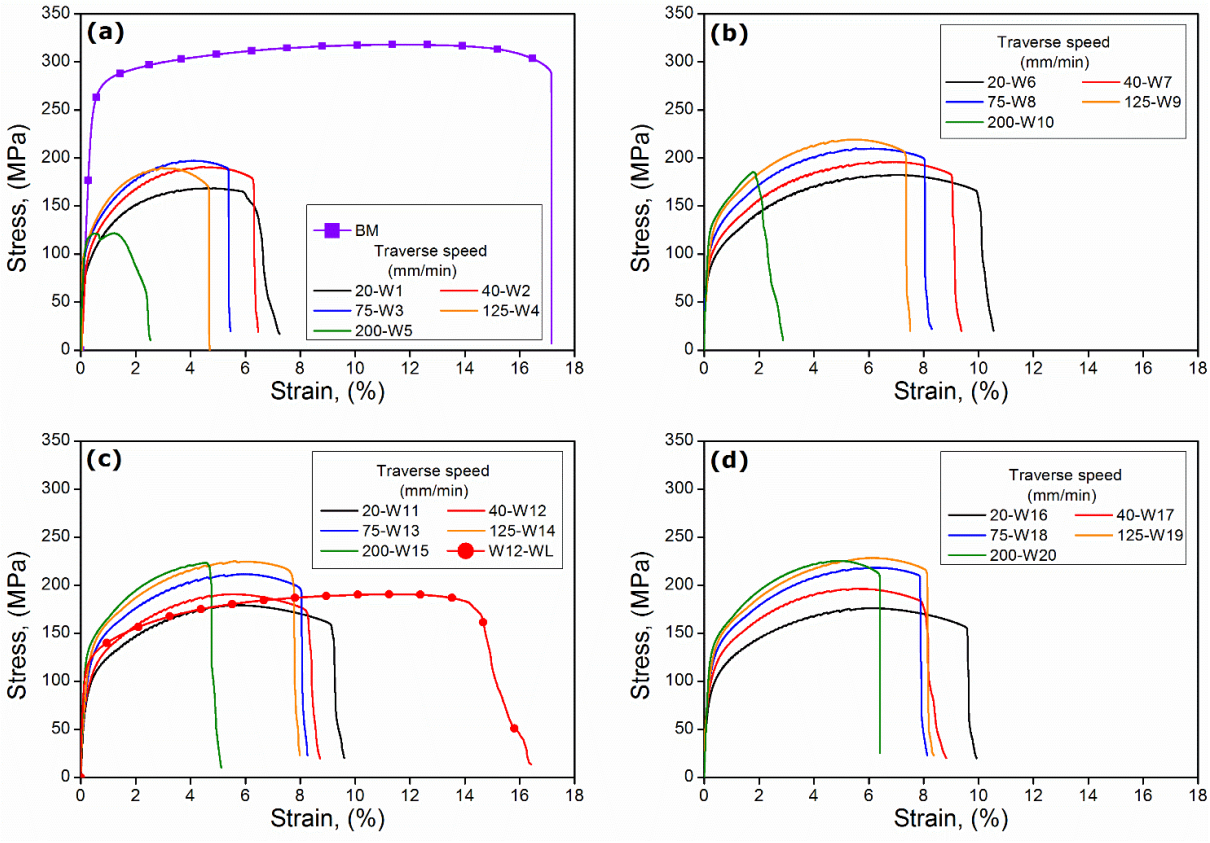


Figure 5-4 (a-d) Engineering stress-strain curves of AA 6082 FSW joints at various tool rotation speed; (a) 800, (b) 1100, (c) 1500, and (d)1800 rpm, respectively, including BM and weld line (W12-WL)

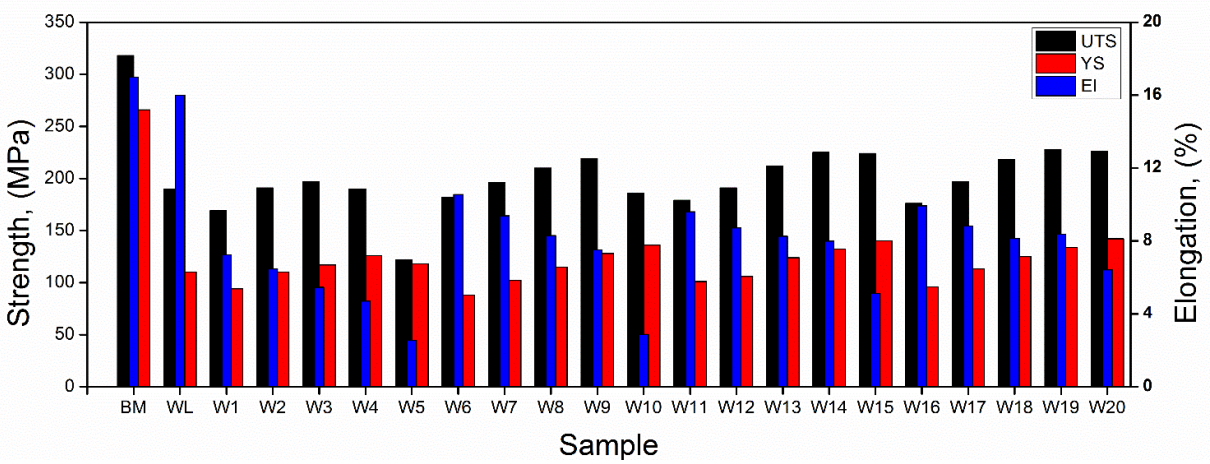


Figure 5-5 Bar graph compare among UTS, YS, and fracture elongations of AA 6082 BM, weld line (WL), and FSW joints

5.3.2 Tensile properties of AMC FSW joints

Figure 5-6 (a) shows the stress-strain curves of the BM, cross-weld (W1-W9) [welding matrix Table 3-4], and longitudinal weld (WL3). Their UTS, YS, and El are compared in the bar graph (Figure 5-6 (b)). According to the results, the as-received AMC shows a tensile strength of 419 MPa with a total elongation to failure of around 2.8%. In contrast, the cross-weld samples exhibit a higher ductility reached to around 6% (increasing 112%) with a drop in the tensile strength (joint efficiency ranging from about 52 to 75 %) as compared with BM. The reduction in tensile strength of AMC (AA 6061/Al_2O_3) FSW joints was also reported by Cavaliere et al. [43]. Furthermore, the stress-strain curve related to BM shows continuous yielding, while most of the welded samples exhibit a distinct yielding serration "jerky flow" phenomenon and similar findings have been reported by Mahmoudiniya et al. [143] and Pathak et al. [144]. Judging from Figure 5-6 (b), the mechanical properties of FSW joints are affected significantly by the welding parameters. It is shown that the joint fabricated at lowest heat input (W3) showing a higher strength (joint efficiency reaches about 75 %) with the adequate elongation of around 5 %. On the other hand, the joint welded at highest heat input and lower cooling rate (W7) shows a lowest joint strength (joint efficiency of about 52 %) with a severe drop in the elongation. Remarkably, the longitudinal welded samples (WL3) shows smooth curve characterised by a moderate combination between strength and elongation of about 361 MPa (86 % joint efficiency), and 8.5 % (201% increase in elongation) than the BM, respectively. The location of the fracture in the typically tested samples is shown in Figure 5-6 (c and d). Under most welding conditions, the FSW joints exhibited shear fracture mode occurred in the HAZ (AS) (see Figure 5-6 (c)) oriented at an angle of about 45°, same as AA 6082 and as also reported by Moreira et al. [145],

because of the loss of strength in this area as observed in the microhardness measurements. The DIC image shows the local strain concentration before fracture, which indicates the fracture location. However, in W8 FSW joints fracture occurred in the stirring zone (see Figure 5-6 (d)), which can be related to macro defects on the top surface of the joint (as presented in Figure 4-26). This is confirmed by the DIC image, as it can be seen that there is no strain concentration in the welded joints and the fracture happened in the middle of NZ.

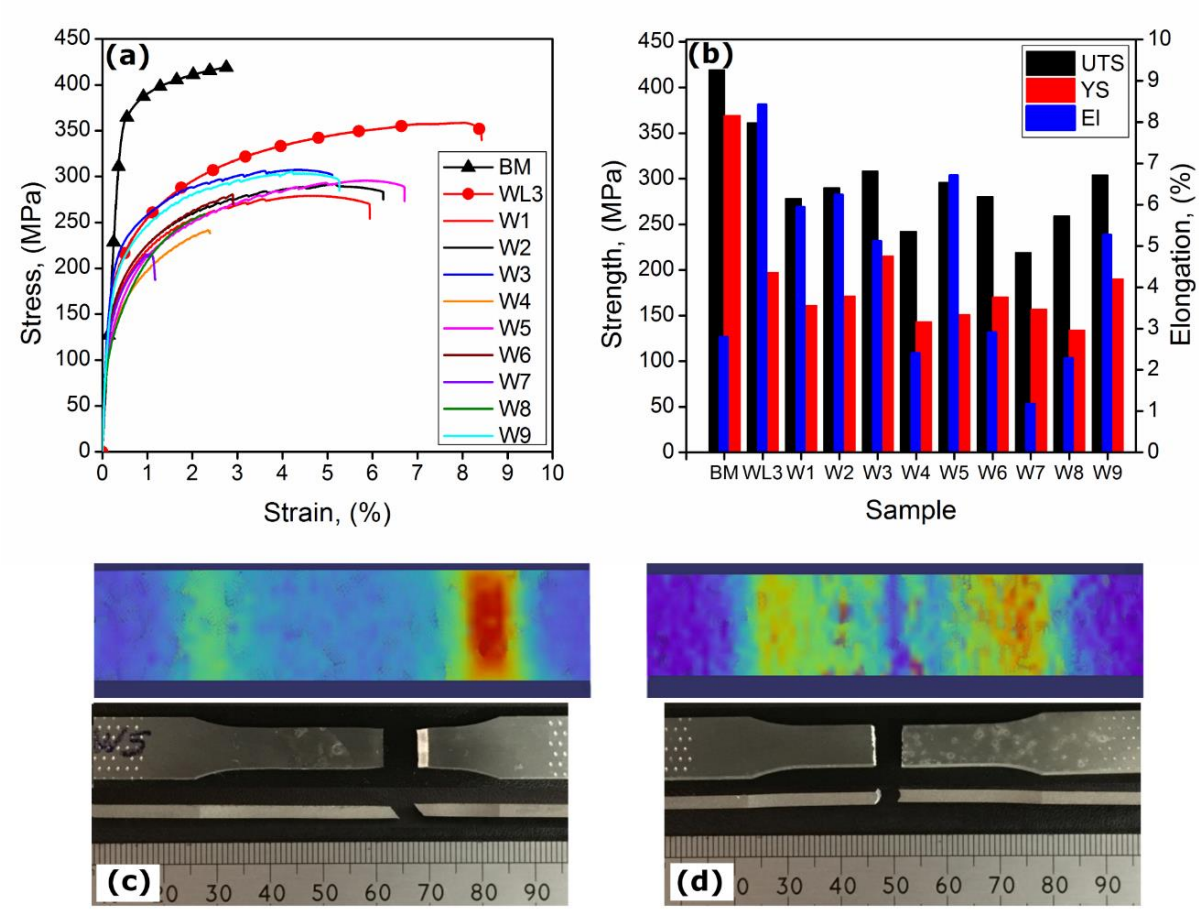


Figure 5-6 Tensile properties of AMC including BM, cross-weld under different welding conditions (w1-W9), and longitudinal weld (WL3); (a) Stress-strain curves, (b) Bar graphs representing strength and elongation, and (c and d) Fracture locations and DIC images of typical samples

5.3.3 Tensile properties of SAMC FSW joints

Figure 5-7 (a) shows the engineering stress versus engineering strain curves of the SAMC in the as-received condition (composite with two aluminium layers), BM without two aluminium layers, and cross-weld (W1-W9) FSW joints graphically. Their tensile strength and elongation to fracture are presented in Figure 5-7 (b). The UTS of the as-received BM was obtained to be 288 MPa, with a total elongation to failure of around 8.5. By removing the top and bottom surface layers of aluminium alloy by grinding (sample labelled BM without surfaces), and keeping just the core part (composite aluminium), the UTS increase to around 344 MPa, with drop in the elongation to about 6.5 %, which shows a significant effect of soft aluminium layers on the strength of the base metal. Regarding the FSW joints, it is seen that after welding both the strength and elongation reduced, and the position of most of the tensile curves are between the as-received BM and BM-without surfaces, as a result of mixing core composite with aluminium layers during the welding process. The joint efficiency the FSW joints varied approximately from 63% to 108% than that of the as-received BM. On the other hand, the elongations were relatively low compared to the as-received BM, ranging from approximately 0.7 to 2%. Welds W5, W6 and W9 show a substantial difference in trends for tensile strength along the cross-welds to the rest of the specimens. They show a decrease in tensile strength, and in particular W6, and W9, show an increase in the slope of tensile curves. This is contrary to the behaviour shown by the other welds, which can be related to the flow arms resulted from improper mixing process between the core and surface of the metal.

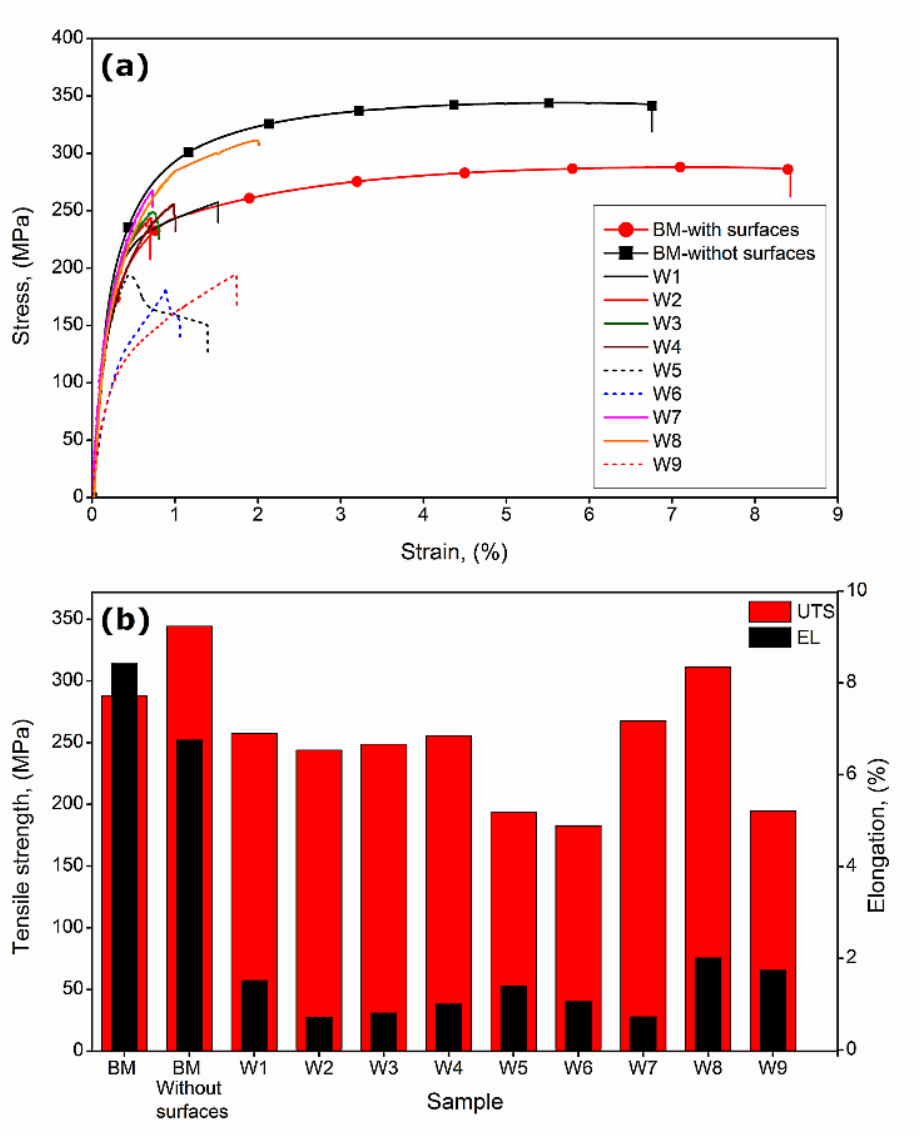


Figure 5-7 Tensile properties of SAMC including the as-received BM, BM without aluminium layers, and cross-weld under different welding conditions (W1-W9); (a) Stress-strain curves, (b) Bar graphs representing strength and elongation

5.4 Low cycle fatigue properties of FSW joints

The fatigue properties of the BMs and cross-weld FSW joints were studied through full tension and compression testing under ambient conditions to assess the effect of welding parameters on the fatigue performance. The fatigue loading was applied in a direction perpendicular to the weld line with a constant strain amplitude and a strain ratio of R = -1. The strain amplitudes range is chosen based on the number of cycles to failure,

i.e. the failure occurs at a number of cycles less than 10000 cycles. Therefore, for each studied materials, some samples have been examined at extra strain amplitudes to identify the test window as presented later. Firstly, for aluminium alloy AA 6082 FSW joints subset of original welding matrix highlighted in red as shown in Table 5-1 has been chosen for the assessment of fatigue behaviour. This subset is chosen based on the macrostructure characterisation of FSW joints, i.e. for the samples free defects. The test has been done at different strain amplitudes ranging from 0.35 to 0.8% for the BM and from 0.4 to 0.7% for FSW joints. Also, one FSW joint (W7) has been examined with an extra strain rate of 0.35%. Secondly, for AMC, the test has been done at strain amplitudes ranging from 0.3 to 0.7% for the BM and from 0.3 to 0.5% for all FSW joints. Also, two FSW joints (W2, and W6) has been examined with an extra strain rate of 0.6 and 0.2%, respectively. Thirdly, for SAMC, the strain amplitudes ranging from 0.2 to 0.5% for the BM and from 0.2 to 04% for all FSW joints. Also, three FSW joints (W2, W5 and W8) have been examined with an extra strain rate of 0.5%.

Table 5-1 Fatigue matrix of AA 6082

		Tool rotation speed (rpm)			
		800	1100	1500	1800
Tool traverse speed (mm/min)	20	W1	W6	W11	W16
	40	W2	W7	W12	W17
	75	W3	W8	W13	W18
	125	W4	W9	W14	W19
	200	W5	W10	W15	W20

5.4.1 Fatigue life of FSW joints

The total strain amplitudes ($\Delta_{\varepsilon t}/2$) as a function of the fatigue life (i.e., the number of cycle to failure, Nf) of the BM and FSW joints of AA 6082, AMC, and SAMC are plotted in Figure 5-8, Figure 5-9 and Figure 5-10, respectively. As seen from the figures, the general trend is consistent with general expectations. The shortest fatigue life is observed for most heavily deformed specimen at the largest plastic strain amplitude. In addition, the FSW specimens reveal lower fatigue lives than the BMs at the same total strain amplitudes. However, the results witnessed that there is a specific trend related to the fatigue behaviour of each material, which is discussed in details in the following paragraphs.

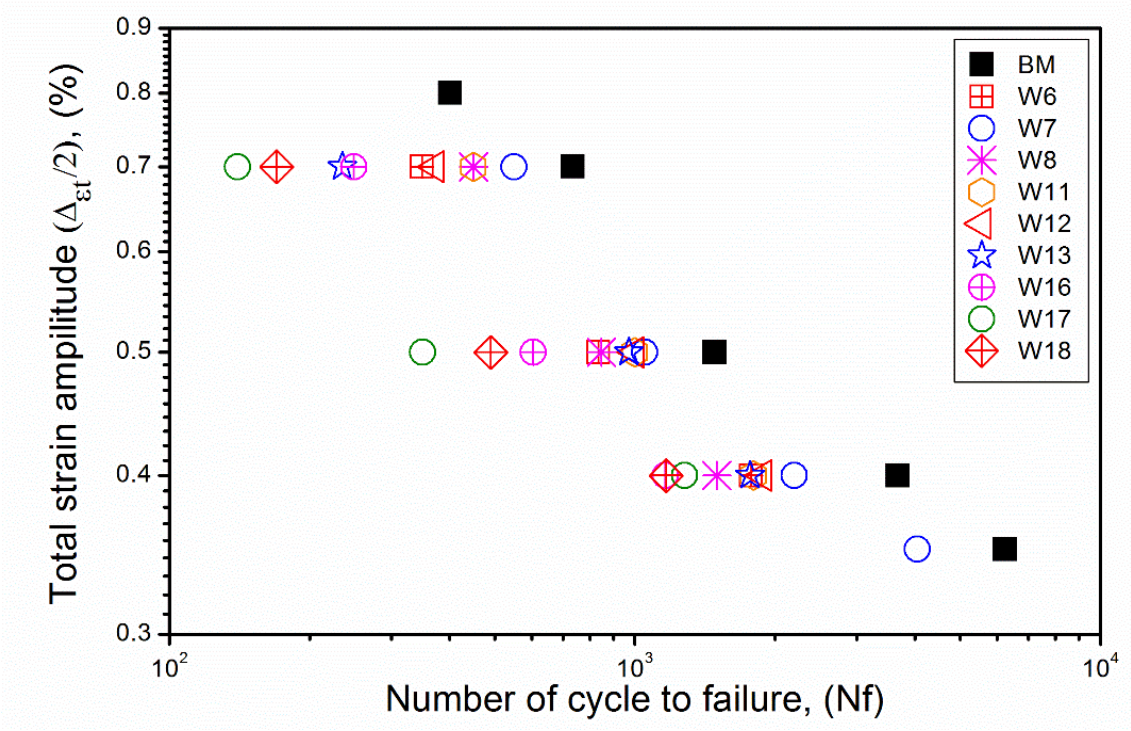


Figure 5-8 Total strain amplitude versus fatigue life of AA 6082 for BM and FSW joints

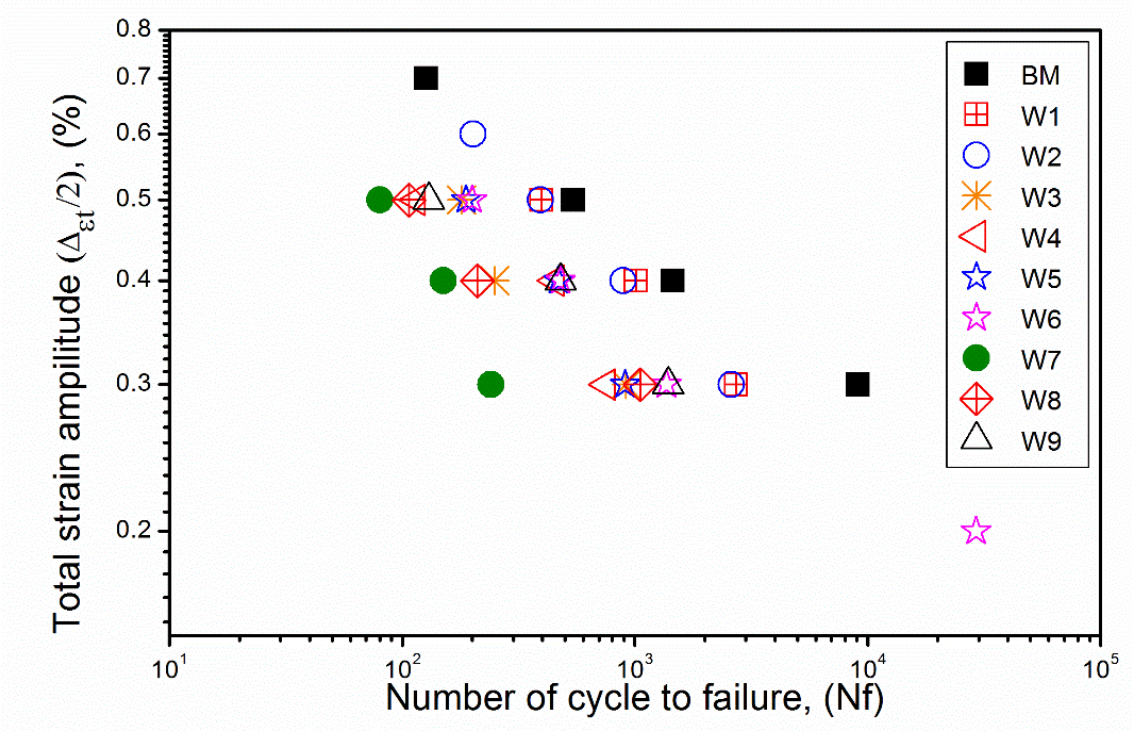


Figure 5-9 Total strain amplitude versus fatigue life of AMC for BM and FSW joints

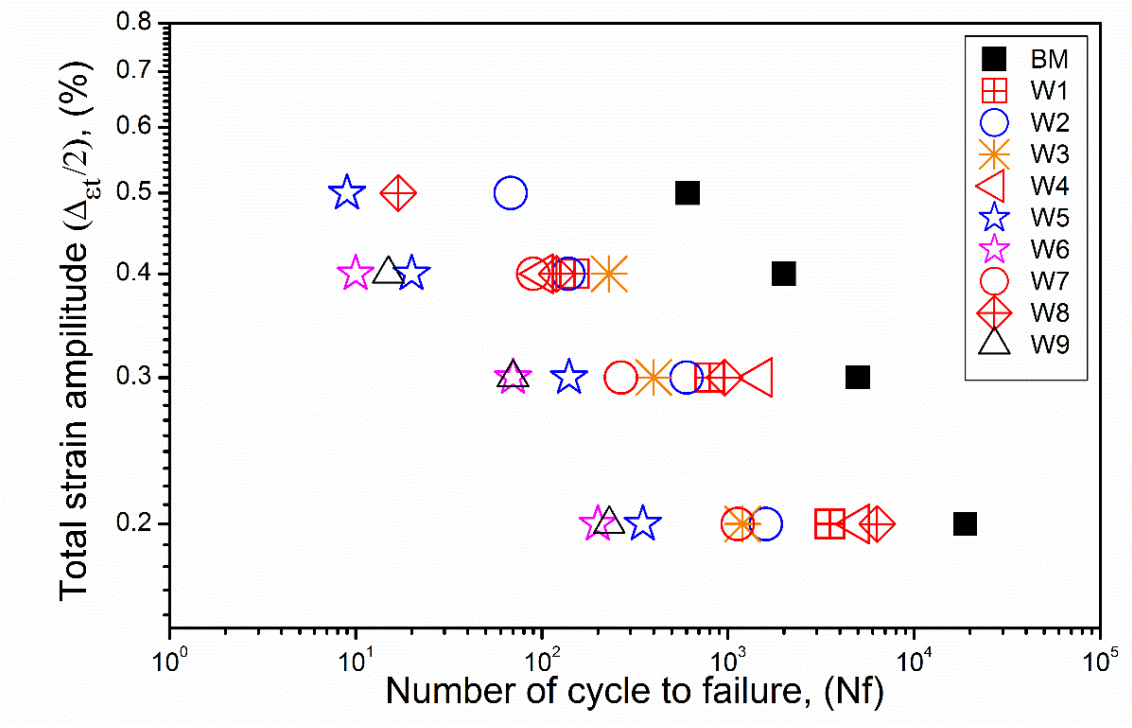


Figure 5-10 Total strain amplitude versus fatigue life of SAMC for BM and FSW joints

As seen from Figure 5-8, the results of AA 6082 witnessed that, at lower strain amplitude the difference in the number of cycles to failure is small, and the fatigue life shows an apparent convergence in the BM and the welded joints. A similar trend has been reported by Feng et al. [139] in strain-control fatigue test of AA 6061, as well as, by Sano et al. [146] and Zhou et al. [147] in stress-controlled fatigue tests of AA 6061 and AA 5056 aluminium alloy FSW joints, respectively. This behaviour can be attributed to the softening of the welding zone resulted from the deterioration of strengthening precipitates, as well as, to the low ductility of the FSW in comparison to the BM [146]. At high plastic strains amplitude, the cyclic ductility of the material limits the amount of induced plastic strain, and thus, the number of cycles that can be generated before fracture. Also, it is seen that the fatigue life of FSW joints depends strongly on the welding parameter and subsequently on the evolved microstructure. The reduction in the fatigue life was more evident on the joints fabricated by using the highest tool rotation speed of 1800 rpm, as a result of large grain size (as presented in Chapter Four).

On the other hand, significant enhancements of LCF properties were achieved in the joints welded at lower tool rotation speed, for example, W7, even so at high strain amplitude (0.7%). This can be related to the formation of fine equiaxed grain dominated by a high fraction of HAGBs. This indicated that the combination of tool rotation speed of 1100 rpm with a traverse speed of 40 mm/min resulted in optimal joints performance.

Regarding the AMC (Figure 5-9), the results witnessed completely different trend than that of AA 6082, i.e. at high strain amplitude, the fatigue life show an apparent convergence in the BM and the welded joints. A similar trend has also been reported by Ceschini et al. [44] in FSW of AA 6061 composite reinforced with Al_2O_3. This behaviour can be attributed to the lower ductility of the composite metal. Also, this behaviour is

consistent with the general concept of the fatigue behaviour of AMC, as the improvement of the fatigue life of AMC is most pronounced in the high cycle fatigue (HCF) regime than in low cycle fatigue (LCF) as a result of ductility exhaustion [148-150]. The reduction in the fatigue life was more evident on the joints fabricated by using tool rotation speed of 1800 and 2100 rpm.

On the other hand, significant enhancements of LCF property are achieved in the W1, and W2 even so at high strain amplitude (0.5%). This distinctive LCF performance is due to the fact that the formation of very fine equiaxed grains dominated by HAGBs in the NZ combined with a high fraction of ultra-fine reinforcement particles can restrict the movement of dislocations most effectively [151]. This showed that the optimal joints performance could be achieved when the tool rotation speed of 1500 rpm is used with a traverse speed of 25, and 50 mm/min.

The fatigue life of SAMC FSW joints is presented in Figure 5-10. The results witnessed an entirely different trend than that of AA 6082 and AMC with more complexity. The fatigue life shows no convergence either at low strain amplitude or high strain amplitude between the BM and most of FSW joints. However, the W1, W4, and W8 FSW joints show some convergence with the base metal at lower strain amplitude. These different behaviours can be related to the microstructure of welded joint as it is consist of two different materials having different grain size, which can be postulated as dissimilar FSW joint. This trend is more likely to happen in dissimilar FSW welding, and it is reported by Rodriguez et al. [152] in FSW of AA 6061 to AA 7050, and Cavaliere and Cerri [153] in FSW of AA 2024 to AA 7075. The reduction in the fatigue life was more evident on the W5 (1800-50), W6 (1800-100), and W9 (2100-100) FSW joints. This can be related to the flow arm of softened aluminium alloy and the big difference between

the grain size of core composite and aluminium alloy. Based on the results, it can be concluded that the fatigue performance of SAMC FSW joint is depended significantly on the mixing process between the core composite and aluminium layers more than the grain size of the core composite. Because there is no significant difference between the grain size of the as-received core composite and FSW joint. Therefore, fatigue performance can be improved if there is less mixing between the core and surfaces.

5.4.2 Cyclic deformation response and hysteresis loop of the base materials and FSW joints

The low cycle fatigue tests were performed with a constant cyclic strain amplitude, as mentioned earlier. One aspect of stress-strain history is the evolution of the maximum and minimum stresses recorded during the LCF tests. This is done by plotting the maximum and minimum tensile and compressive peak stresses respectively from the hysteresis loops against the respective number of cycles. The evolutions of stress over a range of total strain amplitudes for the as-received base metals of AA 6082, AMC, and SAMC with a typical FSW joint for each material are presented in Figure 5-11, Figure 5-12, and Figure 5-13, respectively. The response of all FSW joints including the photographic images of the tested samples is found in Appendix B, C, and D.

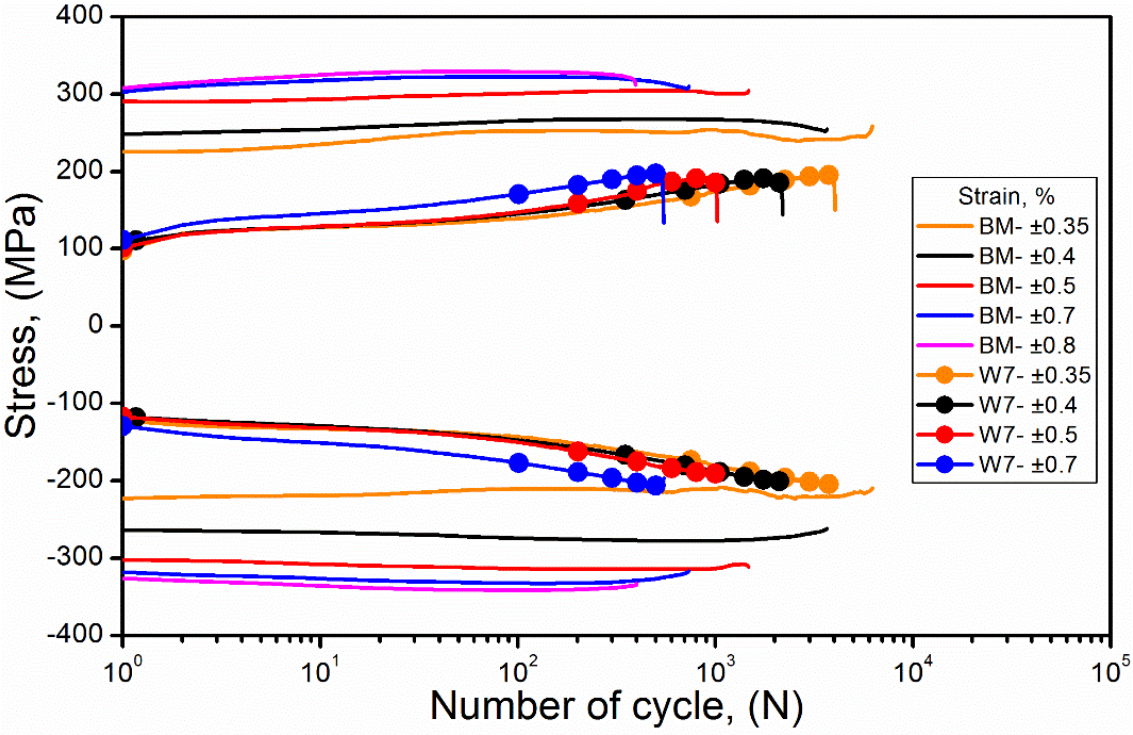


Figure 5-11 Cyclic stress response under different strain amplitudes of the as-received AA 6082 and typical FSW joint (W7/1100 rpm – 40 mm/min)

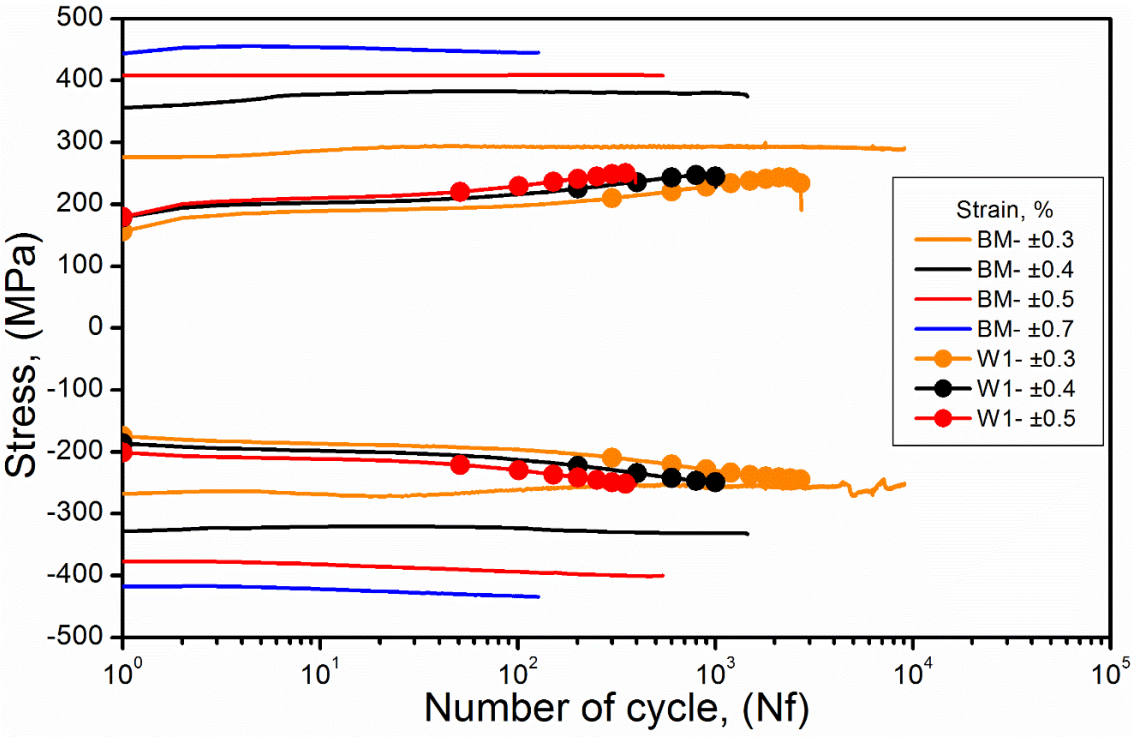


Figure 5-12 Cyclic stress response under different strain amplitudes of the as-received AMC and typical FSW joint (W1/1500 rpm – 25 mm/min)

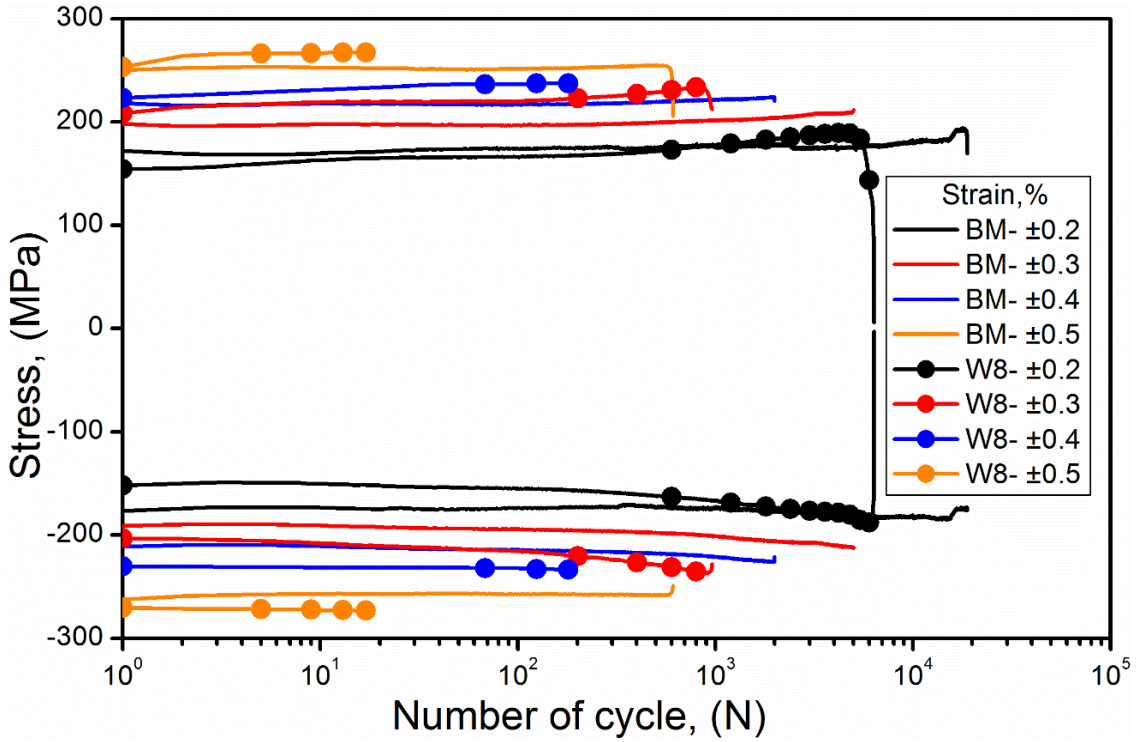


Figure 5-13 Cyclic stress response under different strain amplitudes of the as-received SAMC and typical FSW joint (W8/2100 rpm – 50 mm/min)

A similar trend has been observed for the evolution of the stress with the number of cycles of the as-received and FSW joints of AA 6082 (Figure 5-11) and AMC (Figure 5-12). Several features can be observed from these figures. Firstly, in the as-received AA 6082, the increases in stress are more pronounced when the strain amplitude increase from 0.35 to 0.7%, while there is no significant change when the strain amplitude increases to 0.8%. In contrast, in the as-received AMC, the increases of stress is pronounced when the strain amplitude increase from 0.3 to 0.7%, and it is higher than the AA 6082 at a given strain amplitude. Secondly, in the as-received AA 6082, it can be seen that a pronounced cyclic hardening effect was observed at strain amplitudes of 0.7 and 0.8, whereas at lower strain amplitudes the cyclic hardening particularly pronounced on the early stage of cycling followed by the saturated state. For both behaviours, the material is softened rapidly before failure.

On the other hand, the evolution of the stress in the as-received AMC with the number of cycles was found to rise slightly to a short period of rapid cycling hardening followed by stabilising with low plastic deformation then sudden fracture. Thirdly, as the total strain amplitude increases, the stress increases and fatigue life decreases for both base metals and FSW joints. Fourthly, the stress evolution of the BMs is higher than the FSW joints for a given strain amplitude. Fifthly, the evolution of the stress with the number of cycles in FSW joints was found to be different from that encountered at the BMs. For all FSW joints test results, the cyclic hardening was more evident through the entire test regardless of strain amplitudes. It starts with an initial stress hardening and then gradually reaches the maximum level that is followed by a rapid drop in stress amplitudes due to the degradation of hysterics curves caused by the crack expansion.

Sixthly, the cyclic hardening in BMs and FSW joints was isotropic, and it is amount higher at the higher strain-amplitudes and resultant short fatigue life.

Regarding the cyclic deformation response of the as-received and FSW joint of SAMC (Figure 5-13), it is found that the cyclic deformation is entirely different from that of AA 60282, and AMC. It can be seen that the stress for the BM remains almost constant, ranging from 180 to 250 MPa, under the strain-controlled fatigue cycling at the strain amplitudes ranging from 0.2% and 0.5% respectively. On the other hand, a very slight cyclic hardening is seen in the FSW at the same strain amplitude. Also, there is no significant difference in the initial stress between the BM and FSW joints under specific total strain amplitudes.

Based on these observations, it is evident that in AA 6082 and AMC the FSW resulted in much stronger cyclic hardening, while a decrease in the initial cyclic stress and an increase in the initial plastic strain amplitude happened after the FSW, regardless of the change in the total strain amplitudes. On the other hand, in SAMC, there is no significant effect of FSW on the cyclic hardening. These observations are supported by Figure 5-14, Figure 5-15, and Figure 5-16, where the typical stress-strain hysteresis loops of the first, mid-life, and last cycles at a given strain amplitude for the AA 6082, AMC, and SAMC are shown, respectively, including the as-received BM and typical FSW joint. By comparison of these figures, several features can be pointed out. As can be seen in these figures, the stress-strain hysteresis loops of all studied materials in the as-received condition are shown nearly constant and symmetrical area during the specimen life, which is in agreement with cyclic deformation properties. Similar symmetrical behaviour was reported by Hamada et al. [154] and Ceschini et al. [44]. Because the elastic strain predominantly controls the entire fatigue life at the studied strain amplitudes under

consideration, the hysteresis loops obtained here are therefore constant in the whole fatigue process, i.e., the tensile stress is necessarily the same as the compressive stress at each cycle [154].

On the other hand, there is a significant change in the loop area in the case of AA 6082 (Figure 5-14) and AMC (Figure 5-15) FSW joints under all studied strain amplitude. The maximum/minimum peak stress becomes higher through the test, which means an increase in strain hardening and it corresponds well to the cyclic deformation characteristics. Furthermore, the shape of hysteresis loops changed from fusiform to similarly rectangular gradually by increasing the applied strain, and for a given total strain, the amount of plastic strain is much higher for the FSW joints than for the BM, and this is in agreement with its lower fatigue life. Meanwhile, the hysteresis loop area of the SAMC FSW joint was nearly constant during the specimen life, and this is consistent with the cyclic deformation behaviour. Furthermore, under all test conditions, the cyclic behaviour for all of the BMs and FSW joints is exhibited nearly symmetrical hysteresis loops at both the outset and mid-life, representing an isotropic cyclic hardening response.

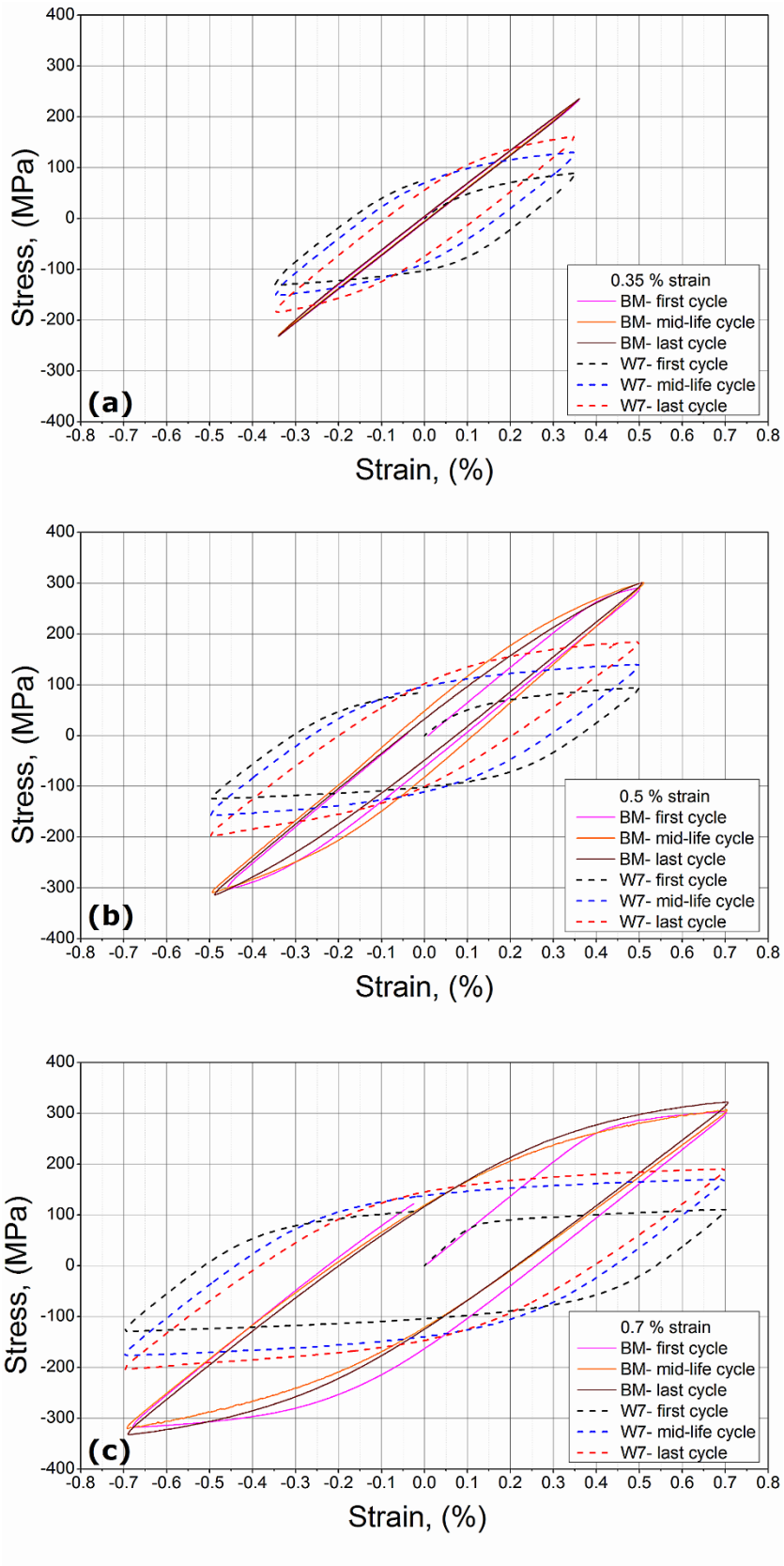


Figure 5-14 Hysteresis loops of the as-received AA 6082 and typical FSW joint (W7) at different strain amplitudes; (a) 0.35%, (b) 0.5%, and (c) 0.7%

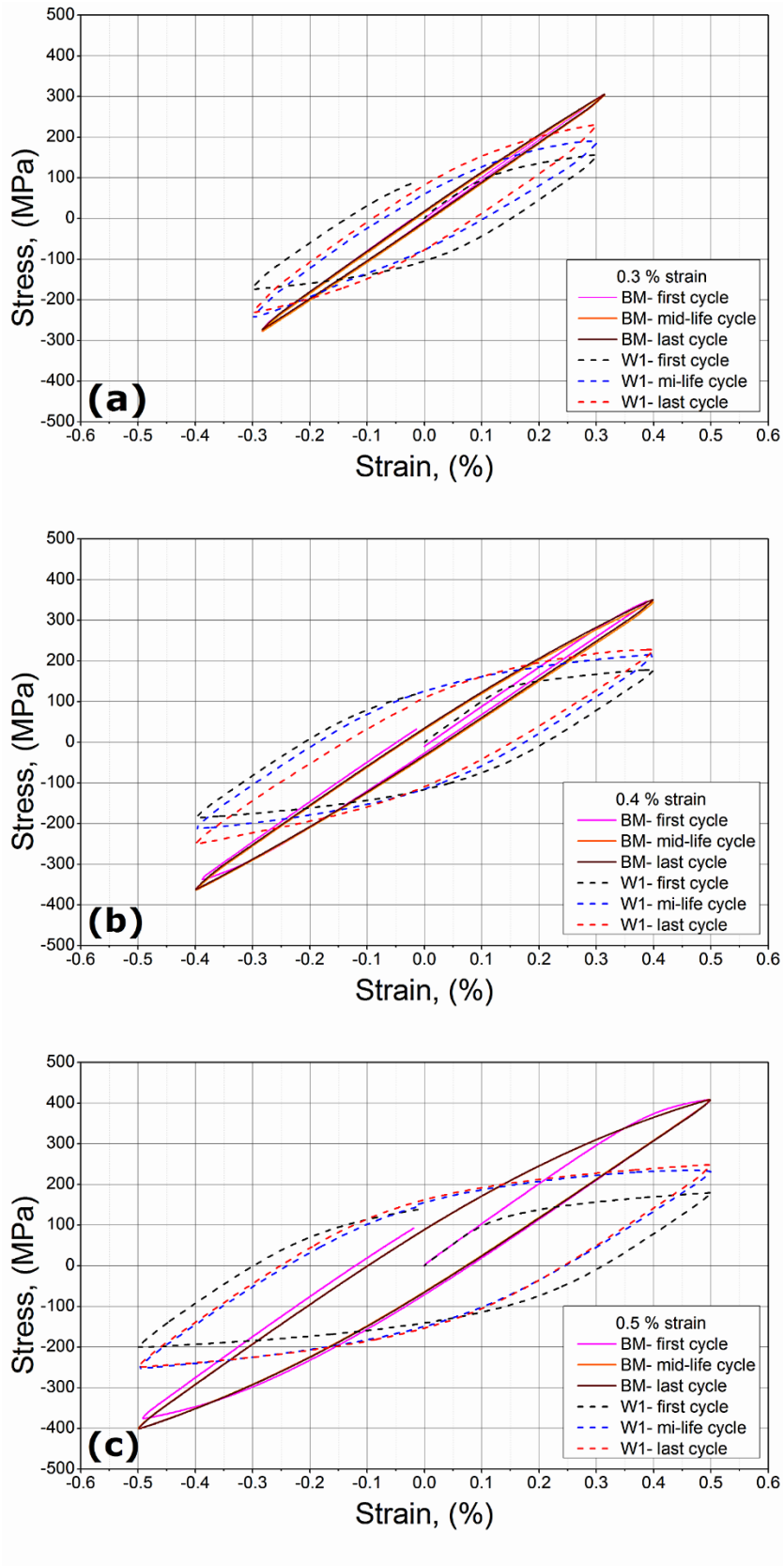


Figure 5-15 Hysteresis loops of the as-received AMC and typical FSW joint (W1) at different strain amplitudes; (a) 0.3%, (b) 0.4%, and (c) 0.5%

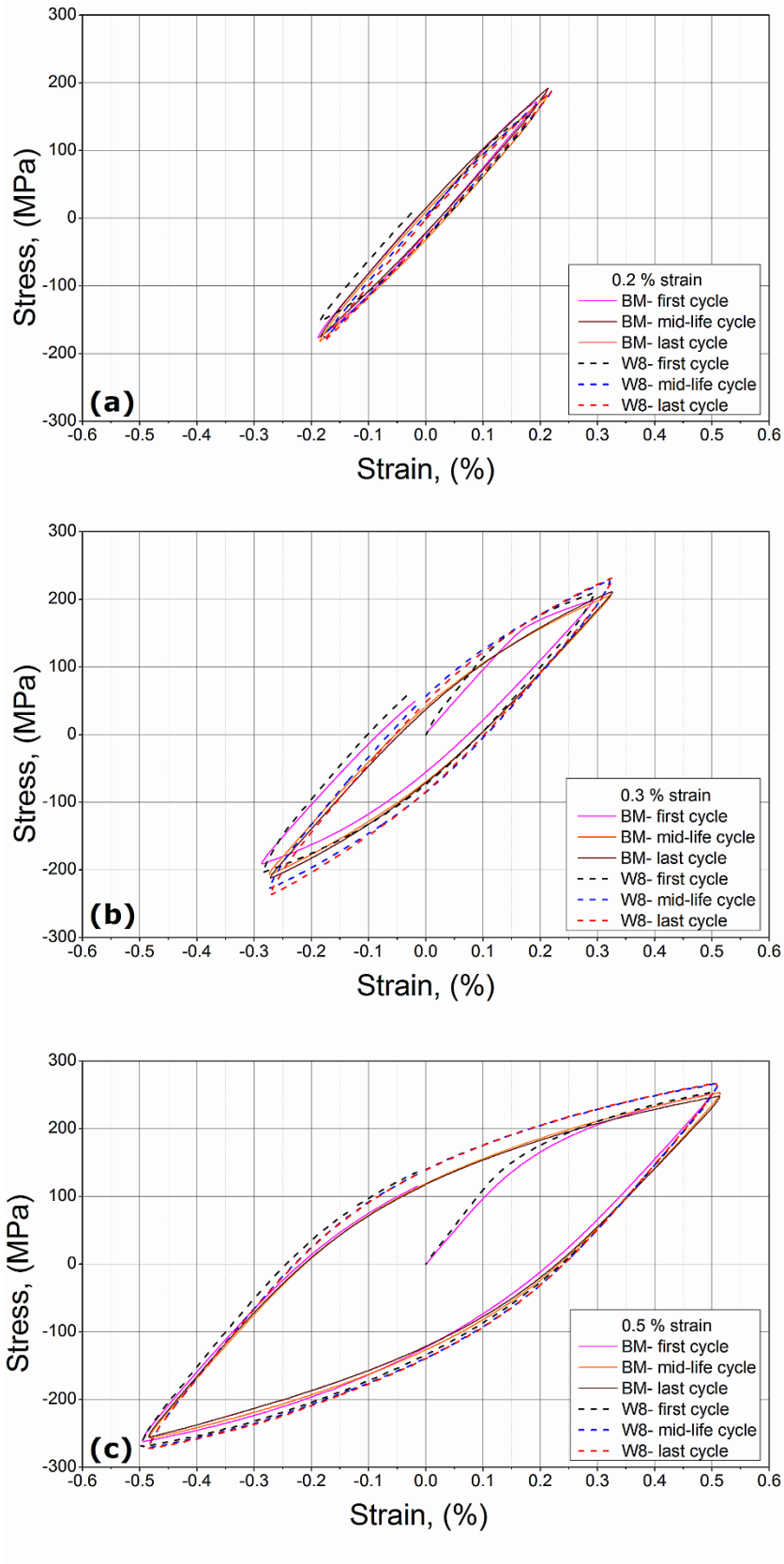


Figure 5-16 Hysteresis loops of the as-received SAMC and typical FSW joint (W8) at different strain amplitudes; (a) 0.2%, (b) 0.3%, and (c) 0.5%

5.4.3 Cyclic stress-strain curves

When a metal or alloy is subjected to cyclic loading through a constant strain amplitude, large changes normally occur in its flow stress; depending on the metal and its processing history, softening or hardening may occur. During fatigue, the cycled metal exhibits a steady state behaviour, stress and strain amplitudes have reached their saturated value. The relation between the saturated stress and strain amplitudes is called the cyclic stress-strain curve. This curve can be determined from a set of stabilised hysteresis loops obtained by loading material at different strain levels plotted in one graph, then tracing the locus of the tips of the extremities of the stable stress-strain loops for different applied strain range [152, 155] as shown typically in Figure 5-17. The cyclic stress-strain curve is one of the most important quantitive fatigue characteristics of a material. Its importance in cyclic loading is the same as the that of the monotonic stress-strain curve in monotonic loading [156]. Two approaches for establishing cyclic stress-strain curves have been employed in this work; saturated hysteresis loops are used for generating a cyclic stress-strain curve of the BMs and SAMC FSW joints. Meanwhile, in the case of AA 6082 and AMC FSW joints as the saturation state of hardening are not exhibited, half of fatigue life cycle was used as a saturated cycle [157].

The comparison between the monotonic and cyclic stress-strain response for AA 6082, AMC, and SAMC in the as-received BM and FSW joints under different welding conditions are presented in Figure 5-18, Figure 5-19, and Figure 5-20, respectively. As can be seen in these figures, the cyclic strain hardening was much faster and stronger than the monotonic strain hardening in both BM and friction-stir-welded joints. Also, the cyclic strain hardening after FSW became much more pronounced. This corresponded well to the cyclic hardening characteristics shown in the previous section. For example,

in the as-received AA 6082 (Figure 5-18 (a)), the BM exhibit cyclic hardening; as the applied strain amplitude increases, the stabilised stress amplitude rises to around 340 MPa, which is higher than the UTS reached in monotonic tensile tests (318 MPa). Also, it is seen that the cyclic hardening behaviour of FSW joints increased with increasing traverse speed and the effect of the tool rotation speed on this behaviour was relatively small (Figure 5-18 (b-d)).

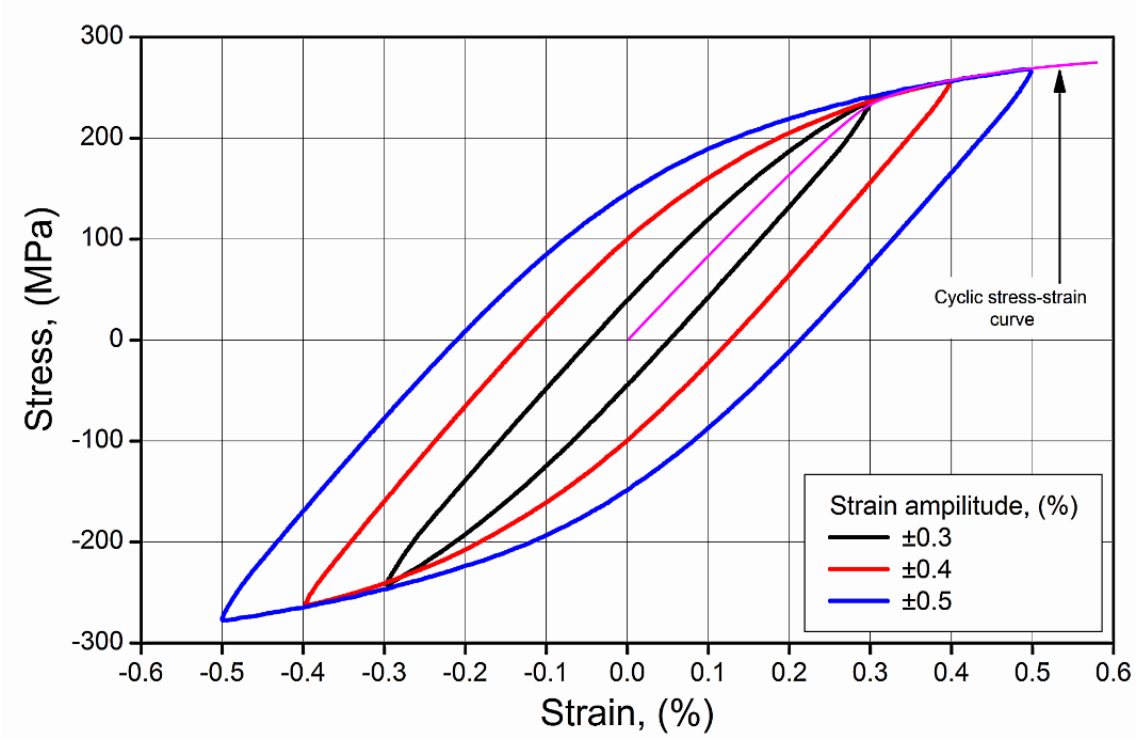


Figure 5-17 Typical saturated hysteresis loops at different total strain amplitude for AMC FSW joint fabricated at 1800 rpm and 100 mm/min (W6) joints

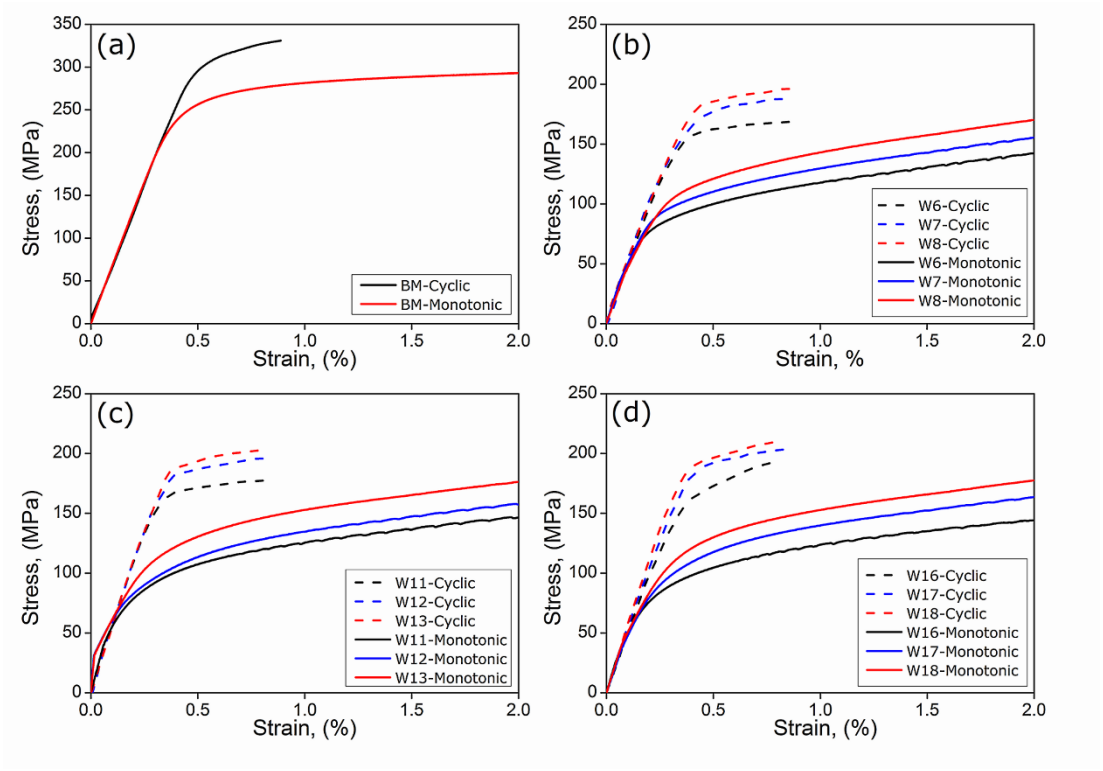


Figure 5-18 Comparison of cyclic and monotonic stress-strain curves for AA 6082; (a) As-received BM, and (c-d) FSW joints at 1100, 1500, and 1800 rpm, respectively

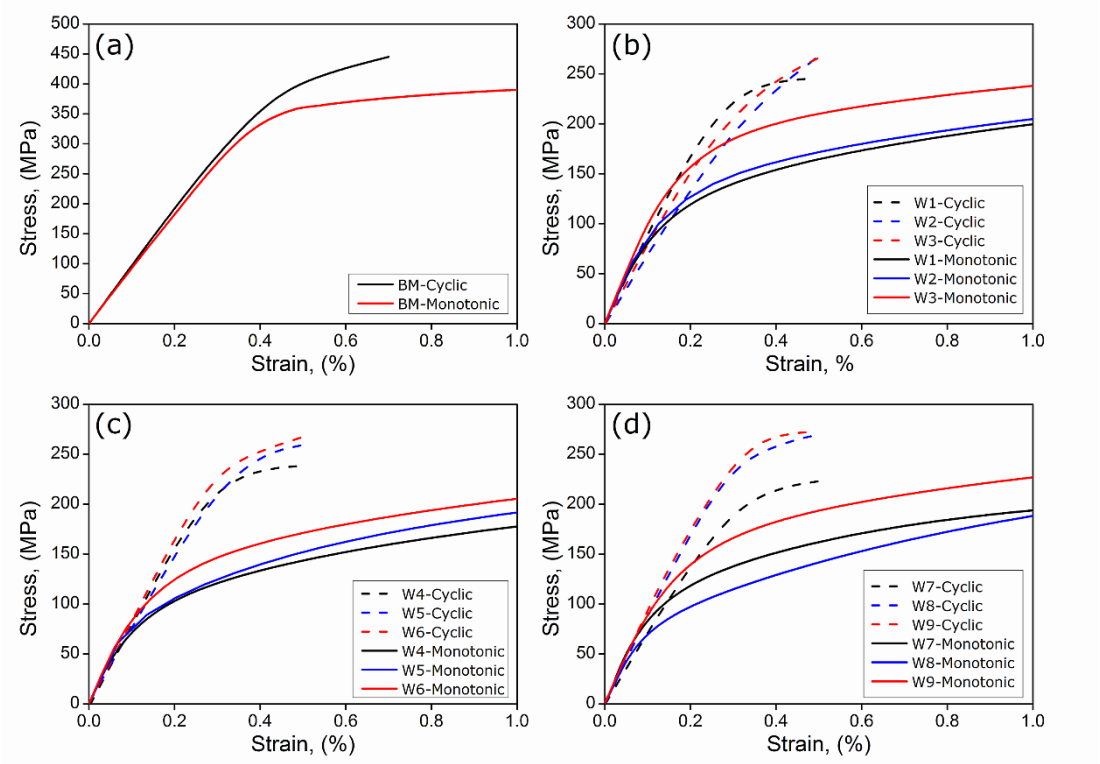


Figure 5-19 Comparison of cyclic and monotonic stress-strain curves for AMC; (a) As-received BM, and (c-d) FSW joints at 1500, 1800, and 2100 rpm, respectively

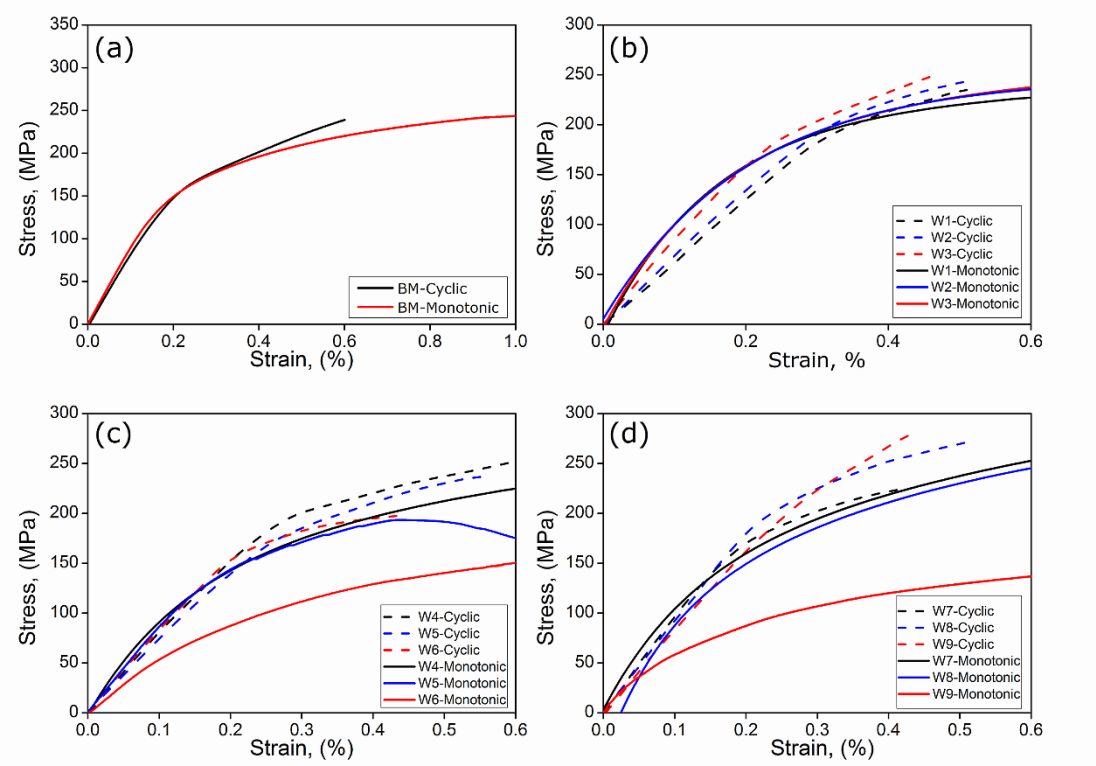


Figure 5-20 Comparison of cyclic and monotonic stress-strain curves for SAMC; (a) As-received BM, and (c-d) FSW joints at 1500, 1800, and 2100 rpm, respectively

5.5 Residual stresses

The longitudinal (L) (left) and transverse (T) (right) residual stress profiles at the mid-length of FSW joints, as obtained by neutron diffraction techniques at ISIS (ENGIN-X), for AA 6082, AMC, and SAMC FSW joints under different welding conditions are shown in Figure 5-21(a-c). The residual stress measurement indicated that compressive residual stress existed in the BM then reversing in sign to form tensile residual stress in the welding zone, i.e. NZ, TMAZ, and HAZ. Overall, the residual stresses exhibited a typical ‘‘M’’ profile, namely the HAZ showed the highest residual stress whereas the centre of the joint showed lower residual stress. This form of the profile is in agreement with the previous studies observed in FSW joints of aluminium alloys [158-164]. According to Xu et al. [161], this profile can be related to the tool action which strains and heats the material. When the cooling starts, the surrounding material without

softening does not allow the plastic material to recover the strains. Therefore, the compressive residual stress and tensile residual stress present in the base metal and welding zone, respectively. In addition, Peel et al. [165] claim the reduction in the residual stress in the centre of FSW joints around the pin position to the high temperatures associated with this region, which would limit the capacity of the material to support the generated load. Also, they demonstrated that the largest residual stresses are expected parallel to the welding direction and close to the weld zone. From the figure, it can be found that the longitudinal residual stress is higher than the transverse residual stress for all studied material. Although the residual stress maximum occurs in the retreating side (RS) for some cases, the distribution is quite symmetric. For aluminium alloy (AA 6082) FSW joint (Figure 5-21 (a)), the compressive stress (around 110 MPa) is higher than the tensile stress (about 60 MPa), which can be related to the clamping process and low amount of heat input as the joint fabricated at lowest tool rotation speed of 800 rpm. Also, it can be found that there is less difference in the residual stresses between the centre and edge of the weld, i.e. higher stress concentration. As this joint contains a volumetric defect in the centre of the weld, a higher stress concentration in the weld increases the resistance force to the dislocation motion, which weakens the stress relaxation and leads to the increase of residual stress. Therefore, the other zone makes an appropriate response to hold the whole stress equilibrium [161].

On the other hand, the AMC and SAMC (Figure 5-21 (b and c) showed an opposite trend; i.e. the tensile stress is dominated the welding joint and reached to around 110 MPa, which can be related to the higher heat input as both materials welded at a tool rotation speed of 1800 rpm. In addition, the existence of reinforcement particles (SiC) in composite aluminium leads to induce residual stresses as a result of a thermal mismatch

between the particles and base matrix due to the large difference in the coefficient of thermal expansion between them. Furthermore, the figure showed that the residual stress increases with the increase of traverse speed combined by a wider stress profile at a constant tool rotation speed in the case of AMC and SAMC. This result is consistent with other studies conducted by Lombard et al. [163], Xu et al. [161] and peel et al. [165]. This behaviour can be explained based on the concept of FSW and thermal history during the welding process. As explained in the previous chapter that the tool rotation speed controls the amount of heat input and the degree of plastic deformation in the welded joint, while the traverse speed controls the heat input per unit length of the weld joint and cooling rate. With the higher heat input per unit length, i.e. lower traverse speed, the material further away from the weld line is heated up, which is resulting in an increase in the width of the high-temperature zone around the tool and a decrease in the gradient of temperature (slow cooling rate). This leads to reducing the thermal expansion mismatch upon cooling, which results in the decreases of residual stress with the decrease of traverse speed.

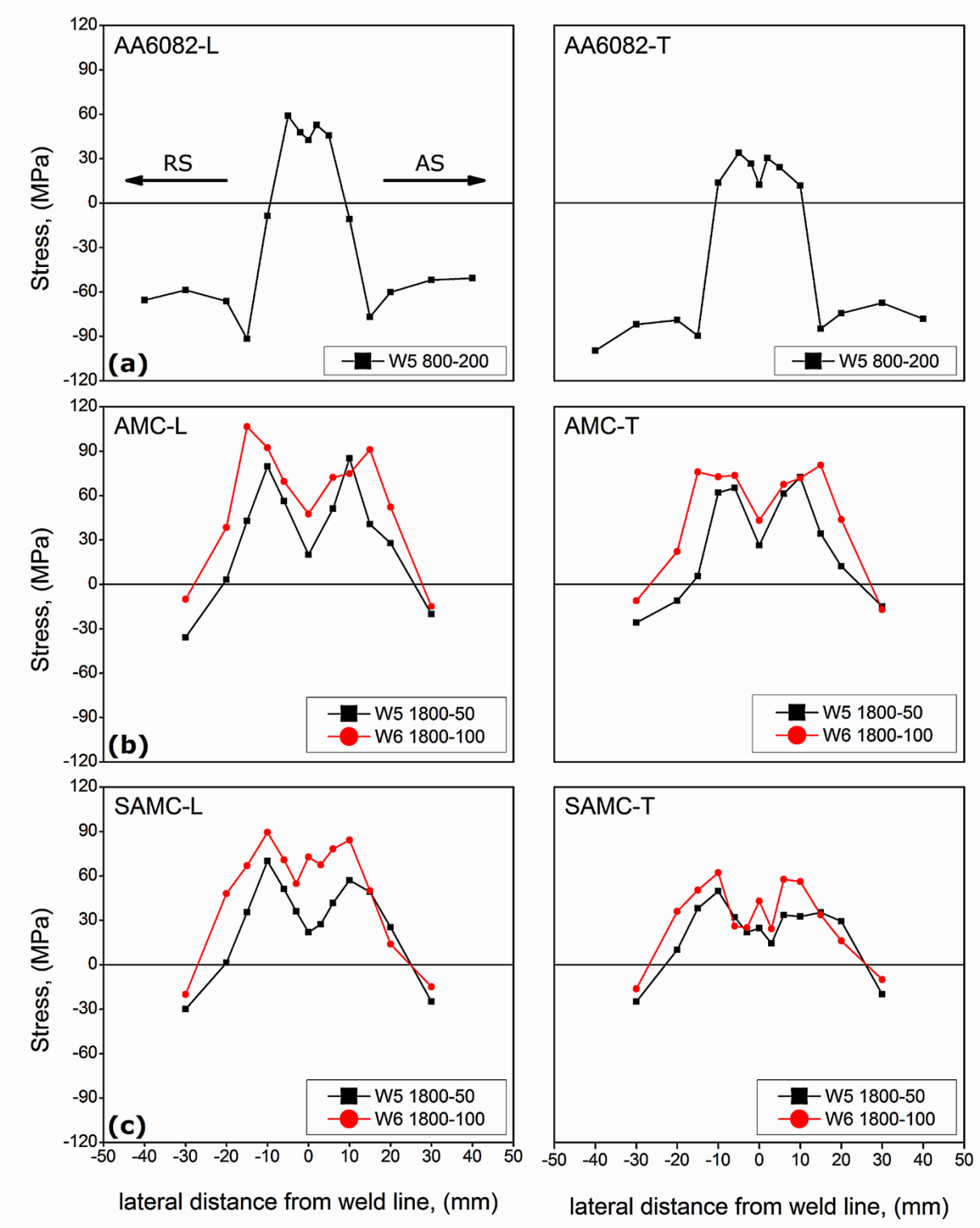


Figure 5-21 The longitudinal (left) and transverse (right) residual stress measured at the mid-length position of FSW joint as a function of distance from the weld line for; (a) AA 6082, (b) AMC, and (c) SAMC (Retreating side on the left)

5.6 Analysis and discussion of results

The strengthening mechanisms in FSW joints of aluminium alloy and composite aluminium are so complicated as there is a significant gradient in the microstructure of cross-weld from the BM through the TZ to the NZ in term of evolved grain size and strengthening precipitate, as well as the appearance of reinforcement particles.

Two main approaches are considered to study the strengthening mechanisms, which are based on continuum mechanics (direct) and micromechanics (indirect) [166, 167]. The former mechanisms depend on the reinforcement particles in AMCs, a significant amount of stress is initially borne by the higher stiffness particles when the stress transferred from the base matrix to the reinforcement particles across the matrix/particle interface. Meanwhile, the latter mechanism is based on the base matrix structure, such as grain refinement, strengthening precipitate shape, grain boundary, and thermally induced dislocations. In composite aluminium, the dislocations generated during thermomechanical processing near the matrix/particles interface from the thermal mismatch between the matrix material and reinforcement particles, as the thermal expansion coefficient of the aluminium matrix is typically much higher than that for the reinforcement particles [149, 168, 169].

Furthermore, due to the significant difference in the grain size of welded joints, strengthening due to the gradient of plastic strain with the linear gradient in grain size (which is the case in FSW joints) is considered another contributing factor, as it takes into account the size dependence and length scale on the strength. Different grain size or phase in polycrystalline materials do not deform equally as a result of the restraining effect of the surrounding grains, significant differences in the elastic modulus and thermal expansion coefficient between the matrix and the reinforcement particles. The constraint

leads to stress concentration, triaxial stress state, and steep deformation gradients [12]. According to Ashby model [170], to accommodate the gradients in deformation, gradient slip occurs on several systems and dislocations are stored in the microstructure, which is defined as geometrically necessary dislocations (GNDs), and so maintain the continuity of plastic strain and the boundaries between deforming crystals remain intact (to preserve lattice compatibility). The effect of microstructure gradient in the cross-weld sample on the formation of GNDs can be explained from a physical viewpoint. Figure 5-22(a) presents the gradient in the typical cross-weld microstructure of AMC in the AS of W1. In this figure, three significant parallel area (BM, TZ, and NZ) inclined by around 45° to the loading direction identified precisely and represented schematically in Figure 5-22 (b). This area can be considered as a slip system (SS) which consists of slip direction (SD) and a slip plane (SP). Thus the applied force (f) can be divided into two components; normal to SP (tensile (ft)), and parallel to the SP (shear (fs)). Once the shear stress on the SP in the SD reaches a threshold value called the critical resolved shear stress (τ_R), slip starting. The τ_R can be calculated based on the equation ($\tau_R = f/A \ \ cos\emptyset \ cos\lambda$), where $\emptyset$ and λ are the angles between the tensile axis normal to the SP and along the SD, respectively (see Figure 5-22 (b)). Based on this equation the maximum value of the τ_R happens when $\emptyset = \lambda = 45°$. Assuming that the sample is rigid (neglecting elastic displacements) and under non-uniform force, the displacement is achieved by a combination of plastic slip (PS) on a single SS, and lattice rotation (θ). When the applied force normal to SP (Figure 5-22 (c)) or parallel to SP (Figure 5-22 (d)), the respective sections are plastically deformed, and the plastic strain increases linearly in the SD, through the expanding of dislocation loops. The edge dislocations forced back the sections to remain together. In addition, negative edge dislocations remain at the

boundary of one cell (GNDs) as a result of incomplete cancellation by the positive dislocations at the boundary of the neighbouring cell, leading to lattice rotation as shown in Figure 5-22 (e). The strain concentration in the tensile test (see Figure 5-6 (c)), and high hardness on the edge of TZ confirm the strengthening mechanism by GNDs. Based on the above discussions a detail explanation of the effect of metallurgical properties and strengthening mechanisms on the hardness, tensile and LCF properties of FSW joints are presented below.

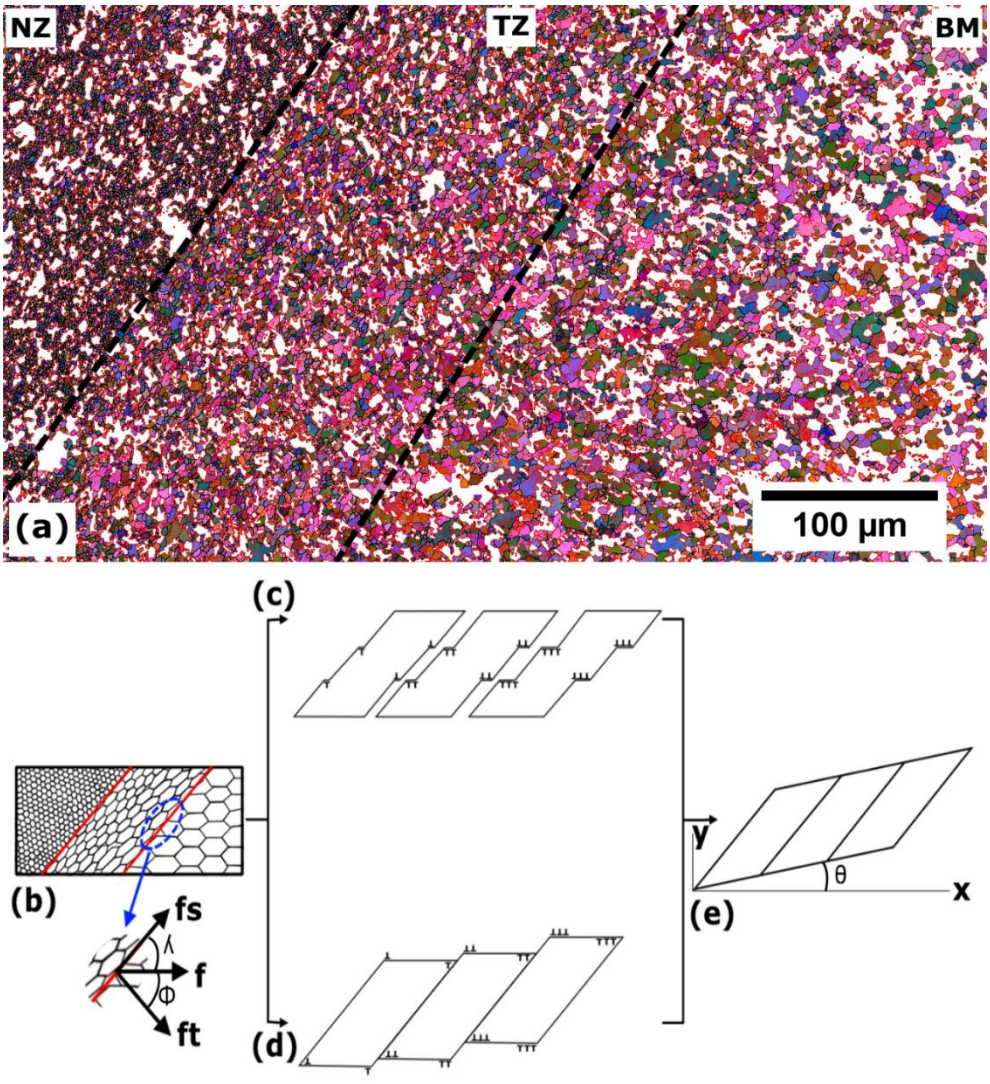


Figure 5-22 (a) Gradient in the grain size of cross-weld sample (W1), (b) Schematic illustration of the gradient in the grain size, (c) Slip due to the tensile component, (d) Slip due to the shear component, and (e) Effect of stored GNDs on the final deformation

5.6.1 Hardness profile of friction stir welded joints

The effect of FSW parameters on the hardness profile of AA 6082, AMC, and SAMC FSW joints are displayed in Figure 5-1, Figure 5-2, and Figure 5-3, respectively. According to the figures, the hardness profile of the welding zone is dependent on the process parameters, and the initial heat treatment condition of the as-received base materials. For AA 6082, and AMC (both of them in T6 condition), a significant variation in the cross-weld microhardness was achieved, and the measured hardness value is lower than the BM. As reported in the other studies, the reduction in hardness is usual in heat-treatable artificially aged aluminium alloy (6xxx-T6 series) [15, 122, 171]. Microstructural evolution due to thermomechanical effect during FSW, in term of strengthening precipitate, and grain size can be considered as two mechanisms for softening in FSW joints. Two important points are worthy of discussion. Firstly, the apparent softening and gradient in the hardness of the welding zone. This can be attributed to the decomposition of the fine needle-shaped $\acute{\beta}$ primary strengthening precipitates existent in the BM and their replacement by coarse precipitate (lathe shape $\acute{\beta}$ phase), as well as, to the difference in the grain size among the NZ , TMAZ, and BM as suggested by Moreira et al. [133]. These changes can be related to the variation in the peak temperature experienced in the different zones as a function of the location from the center of the weld, which in turn influenced the grain size and precipitate shape and density. Olea. C.A.W. et al. [172] claim the reduction in the hardness of the TMAZ to the overaging of strengthening precipitate, as transformed from needles to lath morphology. Furthermore, according to Gatea S. et al. [173], the hardness of AMC dropped when heat treated to 415°C (O-condition) as compare to T6-condition, which was nearly the same as the temperature in the HAZ and TMAZ of FSW joints. They claim

this is due to the reduction of Si concentration in the matrix/particle interface and dissolution of Al_2Cu (orthorhombic crystal structure) and reprecipitated $Al_4Cu_2Mg_8Si_7$ (hexagonal crystal structure).

Secondly, the decrease of tool traverse speed results in the decreasing of FSW joint hardness with an increase in the width of HAZ and TMAZ, and it is more evident at the highest tool rotation speed. This is related to the increase of grain size and full decomposition of strengthening precipitate in the NZ as a result of higher heat input and exposure time combined by slow cooling rate. Grain size and strengthening precipitate decisively influence the hardness of the FSW joint. At higher tool traverse speed both peak temperature and exposure time decrease combined with a higher cooling rate. Hence this leads to form finer grains and incomplete dissolution of strengthening precipitates in the welding zone, which subsequently increases the hardness. These findings agreed with the Hall–Petch equation, i.e. hardness increases as the grain size decreases, and Orowan hardening mechanism, the homogenous distribution of smaller particles of intermetallic compounds are beneficial to improve the hardness [56]. This indicated that the thermally induced cycle during FSW has a significant influence on the hardness profile. Therefore, the softening process in the HAZ and TMAZ can be attributed to the annealing or overaging of strengthening precipitate as well as to the evolved grain size.

On the other hand, the most significant recovery in hardness is observed in the NZ, which can be attributed to the refinement of both the matrix grain and SiC particles and the generation of dislocations at the matrix-SiC interface due to high differences in the thermal expansion coefficient between SiC and aluminium matrix [45, 59]. Furthermore, the NZ experiences the highest temperatures generated by the welding process (above the solvus of the initial precipitate of around 540°C), leading to the dissolution of precipitates

and the formation of a supersaturated solid solution (SSSS). The SSSS undergoes expected natural ageing and hence increases the hardness [78].

Regarding the hardness profile in SAMC, there is no apparent difference in the measured microhardness value, because there is no significant difference in the evolved grain size between the FSW joints and BM. Also, the FSW joins are exposed to thermal history looks like the initial heat treatment condition, T1, cooled from an elevated temperature shaping process and naturally aged. However, there is a drastic drop in the hardness in the TMAZ of some sample, which is resulted from the flow arm of softened aluminium alloy into the matrix composite.

5.6.2 Tensile property of FSW joints

The variation in the welding parameters results in the evolution of various microstructure in the NZ, which influences the tensile strength of FSW joints. The relationship between the tensile strength and mean size of the evolved grain in the NZ of AA 6082, AMC, and SAMC are presented in Figure 5-23 (a-c).

For AA 6082 FSW joints (Figure 5-23 (a)), two tendencies can be noticed on the effect of grain size on the tensile strength. Firstly, the tensile strength of the FSW joints increased as the tool traverse speed increases and then drops, regardless of the change in the tool rotation speed. The rise in the flow stress is related to the evolution of small grain size and incomplete dissolution or re-precipitate of fine needle-shape strengthening precipitate. This is in agreement with the Orowan and Hall-Petch strengthening mechanisms as the extremely fine strengthening precipitate, and grain refinement dominated by HAGBs hinders the motion of dislocation and pile-up at grain boundaries, which is considered to play a significant role in enhancing resistance to plastic flow [174]. Meanwhile, the drop in the strength at high tool traverse speed is related to the incomplete

penetration and void formation (as shown in Figure 4-9). Secondly, the tensile strength of weldments goes through a maximum with a higher tool rotation speed as a result of the formation of a high fraction of LAGBs, strongly aligned fibre texture, and formation joint free defects. This is in agreement with Taylor strengthening mechanism, as the moving dislocations interact with edge dislocations (LAGBs).

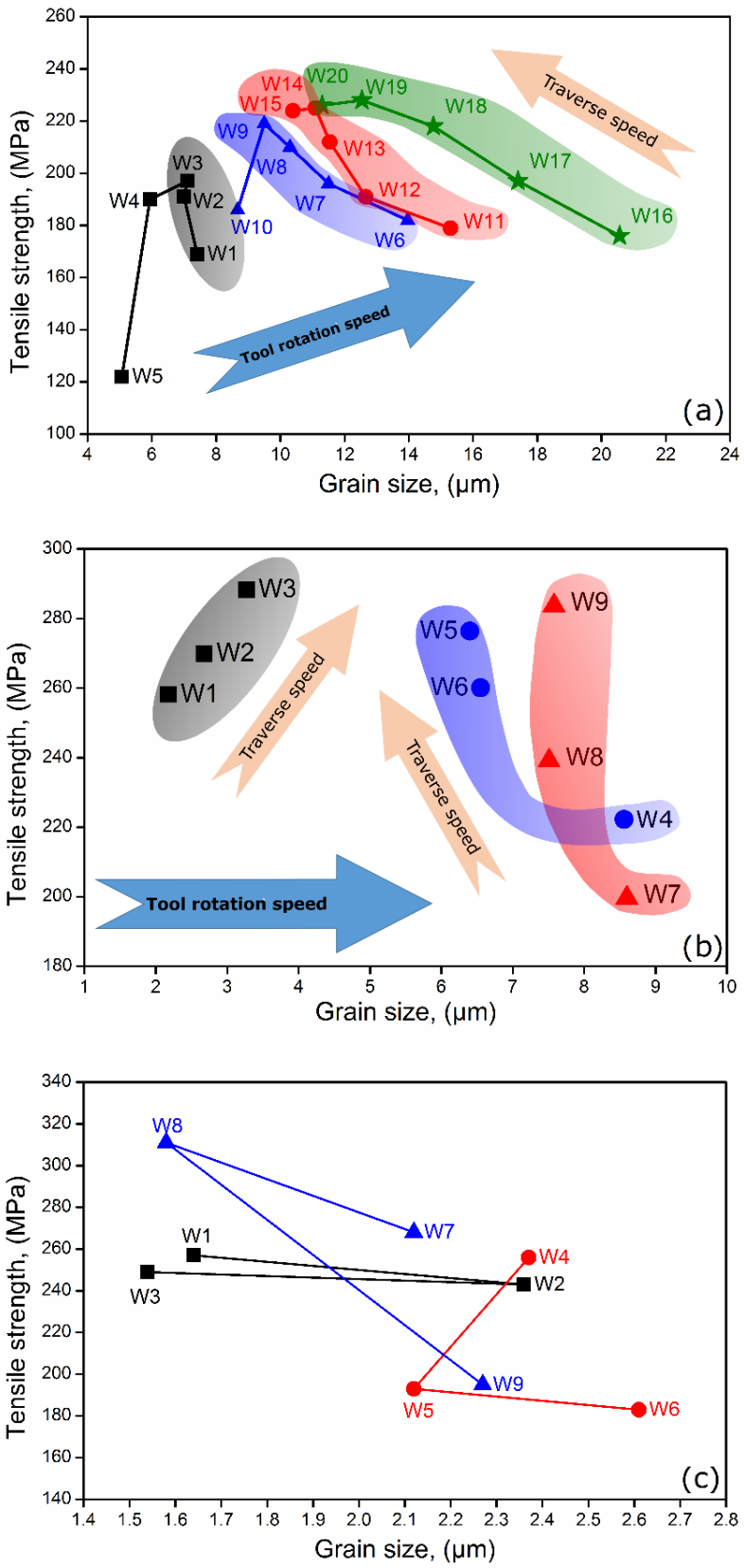


Figure 5-23 Tensile strength of FSW joints versus mean grain size in the nugget zone; (a) AA 6082, (b) AMC, and (c) SAMC

The relationship between the tensile strength, and the mean grain size of AMC FSW joints is presented in Figure 5-23 (b). According to the figure, two opposite tendencies can be observed relating the effect of grain size on the tensile strength. Firstly, at the lowest tool rotation speed of 1500 rpm, the tensile strength of FSW joints is improved with an increase of mean grain size (W3> W2> W1). The increase in monotonic strength of FSW joints can be attributed to several mechanisms. Chawla et al. [150] proved that the strengthening of AMC is significantly affected by the microstructure of the aluminium matrix and reinforcement particles. For the studied BM in T6 metallurgical conditions (strengthened by strengthening precipitates), a higher traverse speed results in partial dissolution of the strengthening precipitates and subsequent re-precipitation during natural ageing after FSW results in an increase in strength [41].

Furthermore, according to the Taylor strengthening mechanism, volumetric strain occurs in the composite when using a fast cooling rate due to the thermal mismatch between the aluminium matrix and SiC particles which leads to the generation of GNDs around the reinforcement particles. As the interaction of the mobile dislocations increases, flow stress of composite metal increase [167, 175]. This mechanism is confirmed by the formation of a high fraction of LAGBs substructure at higher traverse speed (as presented in Figure 4-35). Secondly, at a higher tool rotation speed (1800 and 2100 rpm) the tensile strength of weldments goes through a maximum with a higher traverse speed as a result of the evolution of entirely recrystallised finer grain, which is in agreement with the Hall-Petch strengthening mechanism. The effect of grain boundary on the strength of metal is also confirmed in Al–7 % Si cast alloy and SAE 1020 steel [116, 176].

Regarding the SAMC FSW joints (Figure 5-23 (c)), there is no specific trend and the relation between the strength and evolved microstructure is more complicated than the AA 6082, and AMC. Because the strength of joins depends not only on the grain size but also on the mixing process between the core composite and two aluminium surfaces. For example, the joint welded at a tool rotation speed of 1800 rpm and traverse speed of 50 mm/min (W5) showed lower strength than the joint welded at rotational speed 1800 rpm and traverse speed of 25 mm/min (W4) even with the formation of finer grain. This reduction can be related to the improper mixing between the core composite and aluminium layers and form flow arm. Meanwhile, there is no significant difference in the strength of joints welded at lowest tool rotation speed of 1500 rpm (W1, W2, W3) although there are some differences in the grain size., which can be related to the less mixing between the core and surface.

Finally, two specific tensile behaviours have been noticed in the AA 6082 and AMC FSW joints. First, the longitudinal welding samples showed excellent elongation than the cross-weld samples. It was nearly the same as the base materials in the case of AA 6082 FSW joints and higher than the base metal in the case of AMC FSW joints. The main reason for this behaviour is that the weld line specimens contain only uniform fine equiaxed grains from the NZ, while the microstructure of the cross-weld specimens is heterogeneous as it is consist of four zones, i.e., BM, HAZ, TMAZ and NZ. As the examined ductility is an average strain over the gage length that includes different zones, and these zones have different resistances to deformation owing to the differences in grain size and precipitate distribution. Second, unlike BM and longitudinal samples, the stress-strain curves of the cross-weld samples (Figure 5-4 and Figure 5-6) show a serration flow phenomenon “jerky flow”. This behaviour can be attributed to the Portevin-LeChatelier

effect as a result of inhomogeneous deformation due to the gradient in the cross-weld microstructure, and/or the deformation by the mechanical twinning mechanism. The deformation by twinning is not dominant in FCC crystals, as they have high symmetry and twelve slip systems. However, deformation by twinning instead of slipping can take place under particular conditions, i) slip system restriction; ii) increase of the critical resolved shear stress (τ_R) so that the twinning stress is lower than the stress of slip; iii) when the flow stress and dislocation density are very high the deformation mode changes from slip to a twin; iv) fine grain structure [116, 177, 178]. Therfore, it is might be that the cross-weld samples deform by a slip in the elastic region then proceed by twinning in the plastic region. In contrast, the BM and longitudinal samples showed a smooth stress-strain curves that can be related to the continouty of the microstructure.

Based on the above discussion, it is believed that the drop in the tensile strength of FSW joints is related to the strengthening precipitate and grain structure. On the other hand, elongation reduction results from the gradient in the cross-weld microstructure (grain size) and formation of an interface inclined by around 45° to the loading direction identified precisely in the AS. This interface acts as a shear plane and leads to an increase of the critical resolved shear stress. Therefore, as less gradient in the cross-weld microstructure (grain size) obtained the ductility of the welded joints increases. The results obtained in this work confirm this conclusion. The SAMC sample showed the highest gradient in the grain size, then AA 6082, and AMC (lowest gradient), which leads to a severe drop in elongation of SAMC FSW joints, and a significant improvement in the elongation of AMC.

5.6.3 Microstructure evolution induced fatigue life of FSW joints

The variation in fatigue behaviour is mainly dependent on the evolved microstructure characterisation, cyclic strain range and residual stresses [162, 179, 180]. The relationship between fatigue life at different strain amplitude and grain size of AA 6082, AMC, and SAMC FSW joints are presented in Figure 5-24 (a-c). According to Figure 5-24 (a) (AA 6082), it is evident that at a given strain amplitude, finer equiaxed grain mostly has a higher fatigue life than the coarse microstructures. Higher variations in the fatigue life were obtained with the increasing of tool rotation speed. The joints welded at a highest tool rotation speed of 1800 rpm show larger envelope (green area) with a drop in fatigue life in comparison to the joint welded at a lower tool rotation speed of 1100 rpm (blue area). This can be related to the less difference in the evolved grain size, as well as, to the lower residual stresses induced in the welded joints. As it was reported by Fratini et al. [181] that, the crack growth rate values in the softest region of HAZ (higher residual stress) is higher than the base material. Meanwhile, the propagation of a crack through the fine grain and hardest NZ has shown a decrease in crack growth rate up to values rather lower than the ones observed in HAZ. This demonstrates that the fatigue life of FSW joints is affected by the residual stresses in the HAZ and evolved microstructure and hardness in the NZ.

Figure 5-24 (b) displays the relationship between the fatigue life of AMC FSW joints and grain size at different strain amplitude. As shown in the figure, two opposite tendencies are pointed; firstly, at lowest tool rotation speed (1500 rpm), the increase of traverse speed leads to lower fatigue life (W1>W2>W3) under all strain amplitudes, this trend is opposite to that of tensile behaviour (Figure 5-23 (b)). Secondly, at high tool rotation speeds of 1800 and 2100 rpm, faster traverse speed improves the fatigue life of

FSW weldment, i.e. W9>W8>W7. For both trends, it can be seen that the fatigue life has been improved with the formation of smaller grain size combined with the high fraction of HAGBs (as presented in Figure 4-35), and high volume fraction of SiC. The formation of HAGBs almost leads to high ductility, and as the diameter of the grain is reduced more of the grain boundaries properties are reflected in the centre of the grain. Therefore, this can effectively prevent macroscopic plastic deformation, and minimise microscopic localised plastic strain under specific cyclic stress amplitude. Also, in AMC, an increase in the volume fraction of the hard ceramic reinforcing particulates (due to the particle refinement) increases dislocation density and reduces grain size. These microstructural changes tend to increase the resistance offered to the motion of mobile dislocations. Furthermore, load transfer from the matrix to the reinforcement is a significant contributor to composite strengthening [166, 167].

Regarding the SAMC (Figure 5-24 (c)), it is found that finer grain to some extent has a higher fatigue life than the coarse grain. However, there is no apparent trend between the grain size and fatigue life because the difference between the evolved grain sizes is very small. Therefore, the fatigue life is more dependent on the mixing between the core composite and aluminium layers. For example, although the grain size of W5 is less than the W4 FSW joint, the fatigue life of W4 is higher than W5. This can be related to the improper mixing, which results in the formation of flow aluminium arm.

Finally, under all strain amplitude, both the AA 6082 and AMC in the as-received and FSW joints show strain hardening behaviour (as presented in section 5.4.2 and 5.4.3) during fully reversed cyclic straining under all strain amplitude. This can be attributed to the following reasons; (i) The competing and synergistic effects of stress (load) transfer between the soft and ductile aluminium alloy matrix and the hard and brittle ceramic

reinforcement particle (SiC) [182]. (ii) Grain refinement, as the grain boundaries act as barriers to dislocations movement, thus the strain hardening in the smaller grain size is higher than the coarse grains [183]. (iii) The pre-existence of high dislocation density in the aluminium matrix produced by the presence of the SiC reinforcement due to a mismatch in the coefficients of thermal expansion [184, 185]. (iv) An increase in the storage dislocation density during cyclic plastic deformation, as they accumulate by randomly trapping each other, which is associated with plastic deformation, or they are required for compatible deformation of various parts of the crystal (GNDs) associated with plastic strain gradient [180].

Based on the above discussion, the reduction in the fatigue life of FSW joints can be related to the following factors. Firstly, the physical appearance of the inclined TZ interface by around 45° specifically in the AS. As it is known that the crack initiation (crystallographic cracks grow) stage occurred by slip generated nuclei along planes of maximum shear stress (slip planes 45° to the direction of stress axis), which is termed persistent slip bands (PSB). Thus, there is an acceleration process in the crack initiation stage leading to reduce the fatigue life of FSW joints. Secondly, non-uniform grain size in the cross weld leads to local strain concentration, which also contributes to the drop in fatigue life. Thirdly, the appearance of tensile residual stresses in the welding zone leads to the increases of fatigue crack growth rate.

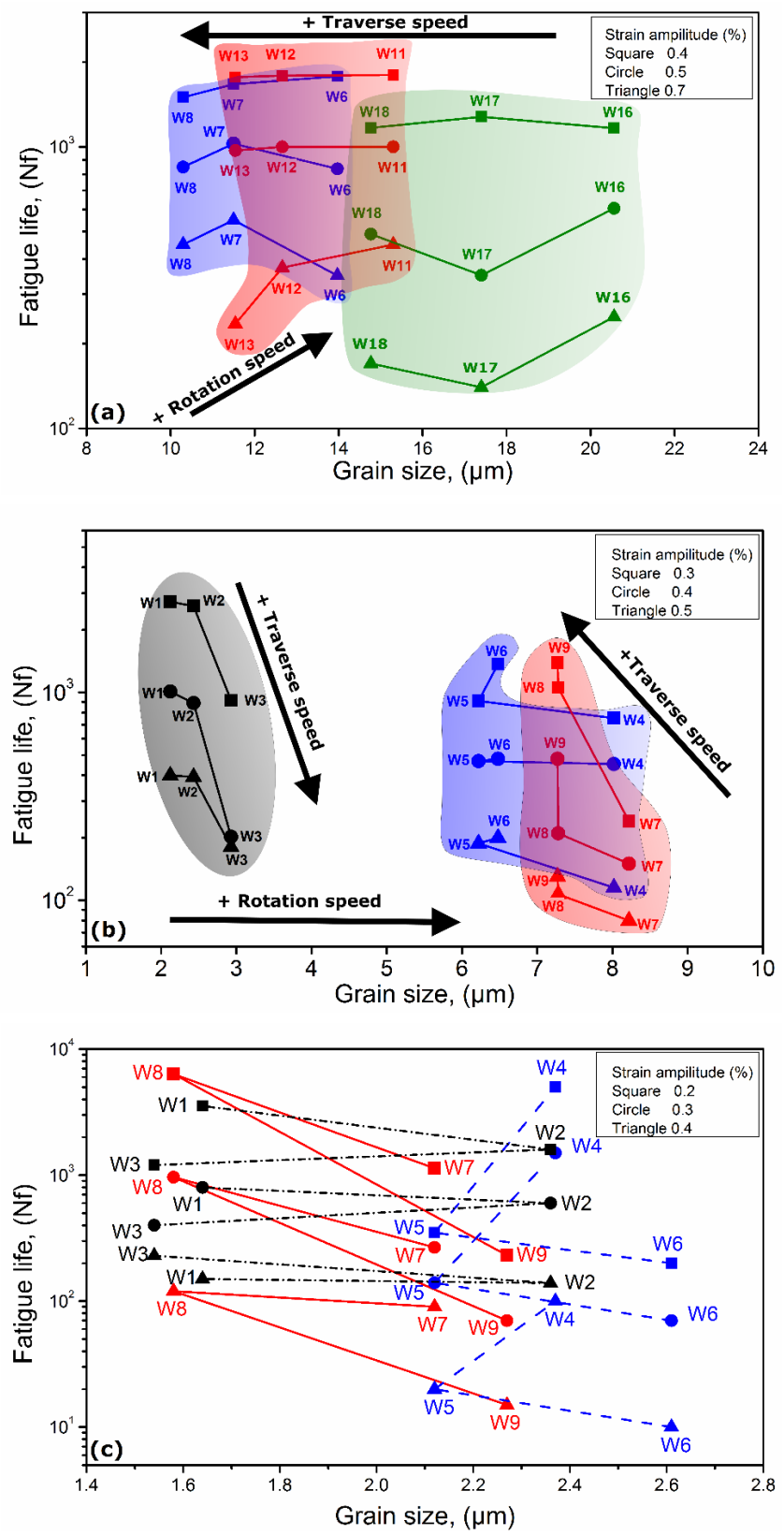


Figure 5-24 Fatigue life of FSW joints versus mean grain size in the nugget zone; (a) AA 6082, (b) AMC, and (c) SAMC

5.7 Summary

This chapter investigated the structure-property, and residual stresses in AA 6082, AMC and SAMC FSW joints in relation to the evolved microstructure under different welding conditions. Mechanical testing including hardness, tensile, and low cycle fatigue were used to assess the properties and performance (weld quality) of the weldment. It was found that grain size (Hall-Petch), reinforcement particle size (Orowan), dislocation interaction (Taylor), and strengthening precipitate are the major strengthening mechanisms in FSW joints. These mechanisms are affected by thermomechanical effect during FSW.

The main characteristic of the strengthening precipitate contributions is their localised variations within various weld regions and their dependence on the starting condition. For AA 6082 and AMC, the hardness profile showed a drop in the in the NZ due to the dissolution of strengthening precipitate. While the hardness of TMAZ and HAZ are varied between the NZ and the base materials due to the coarsening of strengthening precipitate. However, the formation of fine grain and homogenous distribution of smaller reinforcement particles lead to improved hardness based on Hall–Petch and Orowan hardening mechanism. On the other hand, the hardness profile in SAMC FSW joints showed that there is no difference in the measured hardness between the welding zone and base materials because the evolved grain size in the NZ is nearly same as the base metal. Also, welded joints are exposed to thermal history similar to the initial heat treatment condition, T1, cooled from an elevated temperature shaping process and naturally aged.

The tensile strength of AA 6082 and AMC FSW joints is lower than their base metals. While for SAMC FSW joints it is reached 108 % of that of the base metal. The drop in

the tensile strength of FSW joints is related to the strengthening precipitate, grain structure, and mixing process. On the other hand, the elongation of joints is dependent on the gradient in the cross-weld microstructure. The formation of an interface inclined by around 45° to the loading direction acts as a shear plane and leads to an increase of the critical resolved shear stress. Thus, the ductility of the welded joints increases as less gradient in the cross-weld microstructure (grain size) obtained.

The low cycle fatigue life of welded joint showed different behaviours for each studied material. However, the fatigue life of welded joints was lower than the as-received base metals. This reduction can be related to the physical appearance of the inclined TZ interface by around 45°, which accelerates the crack initiation stage and reduce the fatigue life of FSW joints. In addition to the local strain concentration from non-uniform grain size in the cross weld, as well as, the appearance of tensile residual stresses in the welding zone.

Chapter 6 Finite element simulation of friction stir welding

6.1 Overview

The quality (properties and performance) of the welded joints is dictated by the microstructure and mechanical properties which in turn are determined by the FSW process. These properties are controlled by heat generation, material flow, and residual stresses, which normally vary by changing the welding parameters, tool geometry, and characteristics of the material to be welded. Therefore, under such conditions, in-depth knowledge of the FSW process is a prerequisite for reliable prediction of the weld quality. Due to the complexity of FSW processing conditions, it is difficult to obtain all detailed information and gain insight into the joint during the actual FSW processing conditions. Thus, numerical simulation helps to overcome this problem by providing an effective way of analysing the formation of FSW joints [186].

In this work Coupled Eulerian-Lagrangian (CEL) approach is used to simulate plunge and welding step in FSW, because of its capability of solving large material deformation problems and describing the physical boundary of the material accurately. The CEL method is employed to predict the thermal history, induced residual stress, and simulate the material flow and formation of a volumetric defect during the welding process by using the commercially available finite element (FE) analysis software code ABAQUS 6.14 [187].

This chapter is structured as follows: Section 6.2 presents a brief description of the complexity of modelling FSW process with a detailed review of the previous work that has been done to simulate FSW by using different modelling approach including computational fluid dynamics (CFD), Arbitrary Lagrangian-Eulerian (ALE), and Coupled Eulerian-Lagrangian (CEL). Section 6.3 is divided into five subsections to give a detail discerption to the FE model in term of technique and model setup, geometry definition, material model, contact interaction and boundary conditions, and meshing technique and element type used in the current model. Section 6.4 is divided into three subsections to validate the experimental results (temperature distribution, material flow, and residual stresses) with FE results. Finally, the summary is given in the last section.

6.2 Introduction

The improvement of metallurgical and mechanical properties of FSW joints are dependent on the controlling the welding parameters. Thus, to investigate the mechanism of controlling welding parameters, numerical methods are necessary [188]. FE analysis is a numerical method that can be used to solve complex engineering problems which are difficult to solve analytically. Also, it is considered an essential tool for the analysis of nonlinear problems, such as geometrical and material nonlinear behaviour of solids and structures [189]. Simulation of a multi-physics problem such as FSW requiring consideration of severe plastic deformation, heat flow under varying strain rates, complex material flow, and friction conditions is highly challenging because of the complexity of the interaction of thermal and mechanical phenomena (thermomechanical process) [123, 186, 190]. A substantial effort has been done by several researchers to simulate material flow [123, 191, 192], thermal history [193, 194], and residual stresses [195, 196] in FSW by using different modelling techniques such as CFD and solid mechanics. Seidel and

Reynolds [197] developed two-dimensional (2D) FSW thermal model based on fluid mechanics. The welding process was simulated as a steady state, laminar flow of a non-Newtonian fluid past a rotating circular cylinder (assumed the FSW tool consist of pin without shoulder). They observed that the material flow was not symmetric about the welding centreline with significant vertical mixing occurred during FSW. However, the authors addressed a mismatch between the experimental and model results, owing to the absence of the tool shoulder, which has a significant effect on the mixing process. They also reported that more realistic results could be achieved by using a three-dimensional (3D) model and included the tool shoulder with a threaded pin. Colegrove et al. [198-200] systematically investigate the flow of material and temperature distribution in 2D and 3D using CFD code, FLUENT. The primary goal of their investigation was to gain a better understanding of the material flow behaviour around a standard threaded tool profile and complex tools such as Trivex, and Triflute profile. They demonstrated a novel modelling technique, which is the slip boundary condition in three dimensions. This model revealed significant differences in material flow with different tool shapes, which was not evident with the conventional stick model. They also observed that in some cases the predicted size of the deformation zone was found to be much larger than the observed experimentally, combined with a large over-prediction of the weld temperature. Ulysse [201] modelled the effects of tool rotation and traverse speeds on forces and welding temperatures during FSW of thick aluminium plates, based on a 3D viscoplastic model. The prediction of temperature was overestimated compared to the experimentally measured ones; they claim this drawback to inadequate representation of the constitutive behaviour of the metal for the wide ranges of strain-rates, temperatures and strains, which is typically found during FSW.

Another approach used to simulate FSW is based on solid mechanics. Lagrangian and Eulerian formulations are commonly used to simulate continuum deformation problems in solid mechanics. In a traditional Lagrangian formulation, the nodes are fixed within the material (mesh follows the material flow). Therefore, the highly distorted elements during FSW lead to convergence problems, loss of accuracy, and prolonged the computation time. On the other hand, in Eulerian formalism, nodes are fixed in space and mesh remains undistorted and does not move instead the material flows through elements. Therefore the large distortions in the continuum motion can be handled with relative ease, but generally at the expense of precise interface definition and the resolution of flow details [202]. As a result of the shortcomings of Lagrangian and Eulerian descriptions, a technique has been developed that succeeds, to a certain extent, in combining the best features of both the Lagrangian and the Eulerian approaches. Such a technique is known as the Arbitrary Lagrangian-Eulerian (ALE) formulation with the adaptive re-meshing technique can be used for modelling FSW with a realistic computation time as suggested by Assidi et al. [203].

Deng and Xu [204] developed a 2D FE model based on the ALE approach to simulate material flow pattern around the tool pin in FSW using ABAQUS Dynamic Explicit. Plane strain conditions were assumed, and experimentally measured temperatures were applied as body loads in the model. Modified Coulomb's frictional model and constant rate slip model were used as a contact interaction models between tool pin and workpiece. The comparison of both models showed that there is no significant difference in simulation predictions of post-weld marker positions. However, the authors stressed that several simplifications had been made in carrying out the study, and they did not provide a quantitative prediction, due to computational constraints and

the lack of experimental data. Schmidt and Hattel [205] developed a fully localised coupled thermomechanical 3D FE model using adaptive boundary conditions to determine conditions for void-free welds using finite element analysis and flow stress determined according to the Johnson-Cook law. The contact forces between tool and plate surfaces were defined based on Coulomb's law of friction. The results of their investigation showed that the cooling rate plays a significant role in defect formation with higher cooling rate leading to faulty deposition of material behind the tool pin. Later, Deng and Xu's [204] work has been extended by Zhang and Zhang [192, 206] to study the residual stresses and material flow of AA 6061-T6 FSW joints under different welding parameters in 2D and 3D model. The flow of metal during FSW was investigated using tracer particles. It was shown that with the increase of the traverse speed, the maximum longitudinal residual stress could be increased. Also, the flow of material on the advancing side and the retreating side are different. Zhang [207] carried out comparisons on various frictional model conditions (classical and modified Coulomb's). The result showed that both models predicted similar results at low tool rotational speeds. The above results proved the capability of the ALE approach to model FSW. However, The main drawback of this approach remains in the choice of the relative movement between the mesh and the welded material in order to decrease mesh distortions and the prediction of void formation [208].

Recently a Coupled Eulerian-Lagrangian (CEL) approach based on an explicit time integration formulation has been developed and implemented in the FE code ABAQUS to capture the advantages of both of the Lagrangian and the Eulerian method and deal with problems involving large deformations [187]. In CEL method the Eulerian material is tracked as it flows through the Eulerian mesh by computing its Eulerian volume

fraction (EVF). The EVF is defined as the percentage of an Eulerian element which is filled with material. An EVF of one means that the element is completely filled with material, while an EVF of zero means there is no material within the element. The Contact between Lagrangian materials and Eulerian materials is enforced using a general contact that is based on a penalty contact method. A general contact algorithm does not enforce contact between the Lagrangian elements and the Eulerian elements. The Lagrangian elements can move through the Eulerian mesh without resistance until they encounter an Eulerian element filled with a material (EVF $\neq$ 0). Based on the CEL approach, recently Al-Badour et al. [209] developed a 3D localised model with adiabatic heat effect to predict volumetric defects and material flow during FSW of AA 6061-T6 and to estimate tool reaction loads. Johnson-Cook law and Coulomb's frictional contact models were adopted to define the flow stress and tool-workpiece interaction, respectively. The results described accurately the shape of the plasticised zone as well as the presence of a void in the weld. However, there is deviation (mismatch) between the FE and experimental results of force and torque in the welding step. More recently, Tongnea et al. [208] have predicted the formation of banded structures and kissing bonds using CEL approach in the 2D model. Based on their experimental and numerical analyses, they reported that the banded structures are mainly related to the geometry of the pin whereas the friction conditions have a much smaller effect.

However, the CEL method has never been used to study the heat generation and residual stress in FSW joints. In the present work, a 3D fully coupled thermal-stress analysis model based on CEL approach is developed based on Al-Badour et al. [209] model to predict the heat generation, material flow, and residual stresses during FSW of

4 mm thick AA 6082-T6 sheet using a threaded cylindrical shape pin. The model is validated by comparing the predicted FE results with those obtained experimentally.

6.3 Finite element (FE) modelling

6.3.1 FE analysis

In the FSW process, the tool rotation leads to the large mesh deformation near the tool–plate interface. Therefore, a CEL approach with an explicit time integration, a powerful feature of ABAQUS 6.14 [187], is used to avoid mesh distortions. 3D coupled thermo-mechanical FE model of the FSW process is developed in the current study to predict thermal histories, material flow, and residual stresses during FSW. Plunge and welding steps during FSW are simulated in this model, as this approach allows plunging a Lagrangian rigid body (FSW tool) inside the Eulerian media where the base material flows. In the plunge step, a constant volume approach is used; i.e. there is no movement in the material. Meanwhile, in the welding step, the longitudinal motion of the FSW tool was considered zero. Instead, a control volume approach is performed, and the welding speed is defined as a longitudinal velocity of inflow and outflow of material over Eulerian domain boundaries.

6.3.2 Geometrical definition

The geometry of the Eulerian domain (plate) was defined as a local square cuboid shape consisting of two regions namely the full domain and void domain as shown in Figure 6-1 (a). As noticed in the experimental work that has been done in this study, the change in the welding temperature is less pronounced after 20 mm in the lateral distance from the weld centre. Thus a local domain having dimensions of 50 mm length, 50 mm width has been used as a trade-off between the model accuracy and computational expenses. The thickness of the full domain is equal to the plate thickness used in the

experimental work (4 mm), and the thickness of the void domain is taken as 2 mm. The full domain is assigned with the base metal (AA 6082-T6), and the void domain is left empty with no material to visualise the formation of flash on the surface during the welding process.

The FSW tool consists of two parts: the shoulder and the pin similar to the used tool in the experimental work. The diameter of the shoulder is 16 mm with a concavity of 6˚ angle. The tooling pin is an M6 threaded cylindrical pin having a length of 3.3 mm as shown in Figure 6-1 (b). The tool is constructed from a CAD system and then transferred into the geometry model as parts using ABAQUS built-in interface code. In the same manner, as in the experiment, the tool is tilted by 2˚ (Figure 6-1 (a)) and the plunge depth of 0.2 mm is applied during the plunge step.

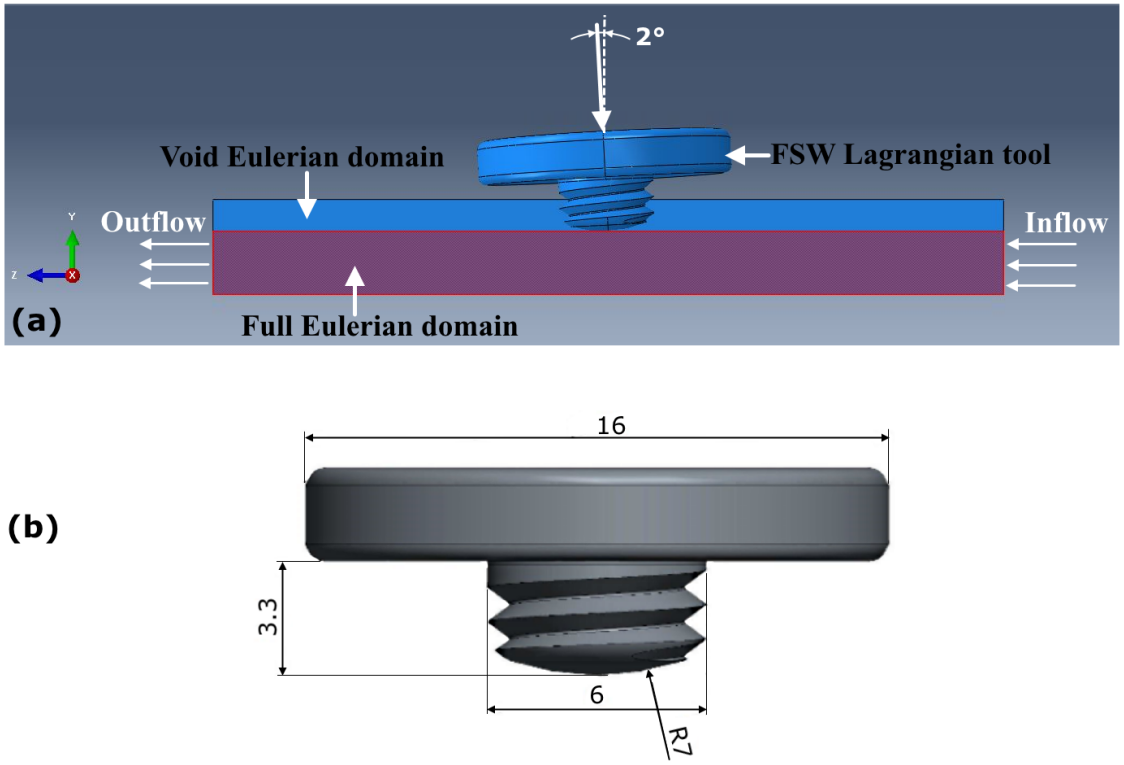


Figure 6-1 FSW geometry definition; (a) Eulerian domain (plate), and (b) FSW tool profile

6.3.3 Material properties

The AISI H13 steel and aluminium alloy AA 6082-T6 are used as the FSW tool and base metal in the FSW modelling. The FSW tool is considered as a rigid body having no thermal degree of freedom constrained to a reference point (RP). Regarding the base metal, during FSW the material is subjected to complex strain, strain rate, and temperature histories. It is known that the material properties are functions of temperature as described by Zhang et al. [192]. Thus the elastic and thermal properties used in the modelling are considered as temperature dependent as shown in Table 6-1 which are obtained from the references by Al-Badour et al. [209], Toric et al. [210], Payandeh et al. [211], Wilson [212], and Powell et al. [213]. Meanwhile, plastic flow stress is considered as strain rate and temperature dependent. ABAQUS supports the Johnson-Cook (J-C) plasticity constitutive model, which is an empirical viscoplastic constitutive model and a particular type of Mises plasticity model used to depict the work hardening, strain rate hardening and the thermal softening effect of metal. It is suitable for high-strain-rate deformation and temperature as suggested by Al-Badour et al. [209], and Tongne et al. [208]. The von Mises flow stress σ_o, according to the J-C constitutive relation is shown in equation (1).

$$\sigma_o = [A + B\varepsilon^n][1 + C \ln \dot{\varepsilon}^*][1 - (T^*)^m] \quad (\mathbf{1})$$

where ε is the equivalent plastic strain; $\dot{\varepsilon}^*$ is the dimensionless plastic strain rate given by the equation of $\dot{\varepsilon}^* = \dot{\varepsilon}/\dot{\varepsilon}_o$ in which $\dot{\varepsilon}_o$ is the reference strain rate ($1.0\ s^{-1}$); and $A, B, n, C, and\ m$, are material constants. $T^*$is dimensionless temperature expressed as shown in equation (2) in which $T, T_o, and\ T_m$ are the environment, reference and material

melting temperatures, respectively. The J-C parameters used in this model were also obtained from the literature done by Jaspers and Dautzenberg [214] based on split Hopkinson pressure bar (SHPB) method for AA 6082-T6 and it is given in Table 6-2.

$$T^* = (T - T_o)/(T_m - T_o) \qquad (\mathbf{2})$$

Table 6-1 Mechanical and thermal properties

T (°C)	E (GPa) [210]	Density (ρ) (kg/m^3) [209]	Specific heat (C_p) (J/Kg .K) [211]	Thermal coefficient of expansion (α) (µm/ m.K) *10^5 [212]	Thermal conductivity (W/cm.K) [211, 213]
25	71	2700	910	-	150
50	-	-	930	-	157
100	70	2690	940	2.54	164
150	65	2670	970	-	171
200	65	2660	990	2.65	181
250	63.5	-	1000	-	185
260	-	2660	-	-	-
300	48	-	1010	2.78	185
316	-	2630	-	-	-
350	24	-	1060	-	192
371	-	2630	-	-	-
400	-	-	-	2.99	180
427	-	2600	-	-	-
482	-	-	-	-	-
500	-	-	1110	3.25	-
527	-	-	-	-	220
600	-	-	-	3.55	-
627	-	-	-	-	213
650	-	-	-	3.72	-

Table 6-2 Johnson–Cook plasticity model parameters of AA 6082-T6 [214]

A (MPa)	B (MPa)	C	n	m	T_{ref} (°K)	T_{melt} (°K)
428.5	327.7	0.00747	1.008	1.31	298	855

6.3.4 Contact interaction and boundary conditions

The contact condition is considered a critical part of the numerical model, especially when modelling the FSW process [215]. Eulerian-Lagrangian contact allows the Eulerian materials to be combined with traditional nonlinear Lagrangian analyses. General contact algorithm that enables a fully coupled multi-physics simulation such as fluid-structure interaction is used to define tool-workpiece contact and thermal and mechanical interaction properties. The normal contact forces are obtained by using the penalty contact formulations. Also, the tangent motion is considered as part of the solution for the contact definition on the tool–plate interface. Coulomb's friction law is applied to describe the shear forces between the tool surface and the workpiece. This law predicts the mutual motion between the two segments whether they stick or slip. If the friction shear stress exceeds the yield shear stress of the base metal, the material surface stick to the moving tool surface (heat is generated by plastic deformation).

On the other hand, if the contact shear stress is smaller than the material yield shear, there is no relative motion between the contact surfaces (slipping), and heat is generated by friction. Therefore, the accurate value of the friction coefficient is the major point in the calculations of heat generation during FSW. However, this value cannot be determined from fundamental principles or experiments that are relevant to the FSW conditions [216]. Thus a different value of the friction coefficient ranging from 0.4 to 0.8 has been used in the previous study [217, 218]. Also, the numerical results showed that the friction coefficient has a significant effect on the void formation. A larger void size results from lower friction coefficient [186, 209]. Therefore, in the present study, a friction coefficient of 0.8 has been used, as it is showed by Al-Badour F. et al. [209] that this value gives the nearly accurate size of the formed defect.

The boundary conditions can have a significant effect on the model results. Therefore, the thermal and velocity boundary conditions need to be defined correctly for the domain to represent the physical situation accurately. Heat radiation for the top surface and heat convection models for the bottom surface are used to dissipate the heat through the boundaries, which were defined by creating surface radiation and film interaction.

Tool displacement and rotation are constraints to RP, to control the position of the tool, and applying the rotational tool speed. Meanwhile, the velocity boundary conditions of the model were defined in Table 6-3, to avoid the loss of flow material from sides and bottom of the Eulerian domain and to control the welding speed in plunge and welding steeps. The plunge step time has been considered as two seconds, and velocity constraints at the boundaries were defined as shown in Figure 6-2. In the welding step the velocity constraints at the boundaries are defined in Figure 6-3. Where *Vx*, *Vy*, and *Vz* are velocity magnitudes in the x, y, and z directions respectively as shown in Figure 6-3, *Vz* is the welding speed as inflow and outflow velocity.

Table 6-3 Finite element model boundary conditions

		Boundary conditions			
		Vx	Vy	Vz (mm/min)	Tool rotation speed (rpm)
Step	Plunge	0	0	0	800 or 1100
	Weld	0	0	200	800 or 1100

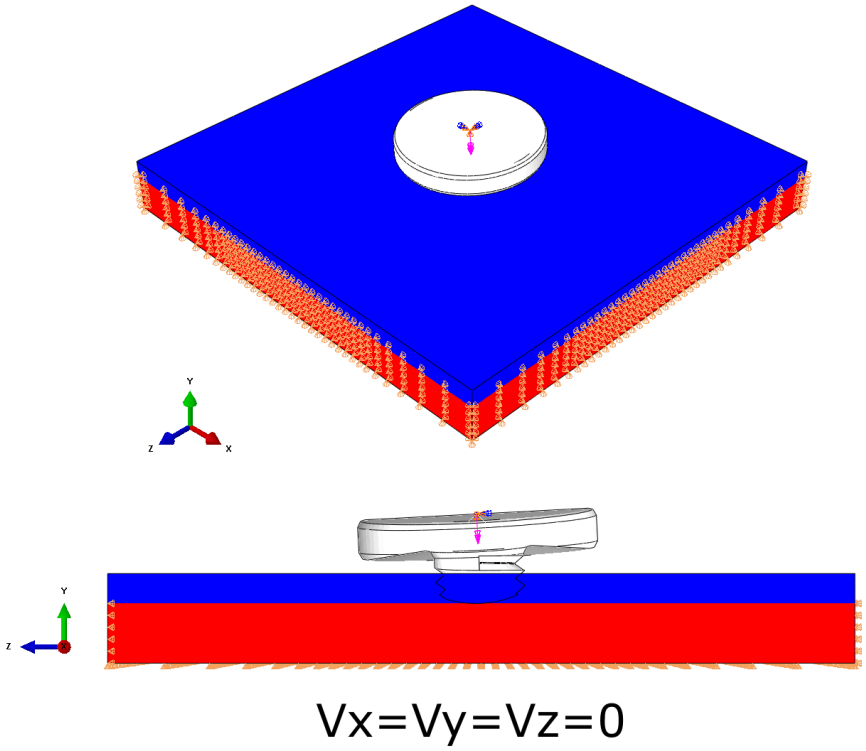


Figure 6-2 Velocity boundary conditions in the plunge steep

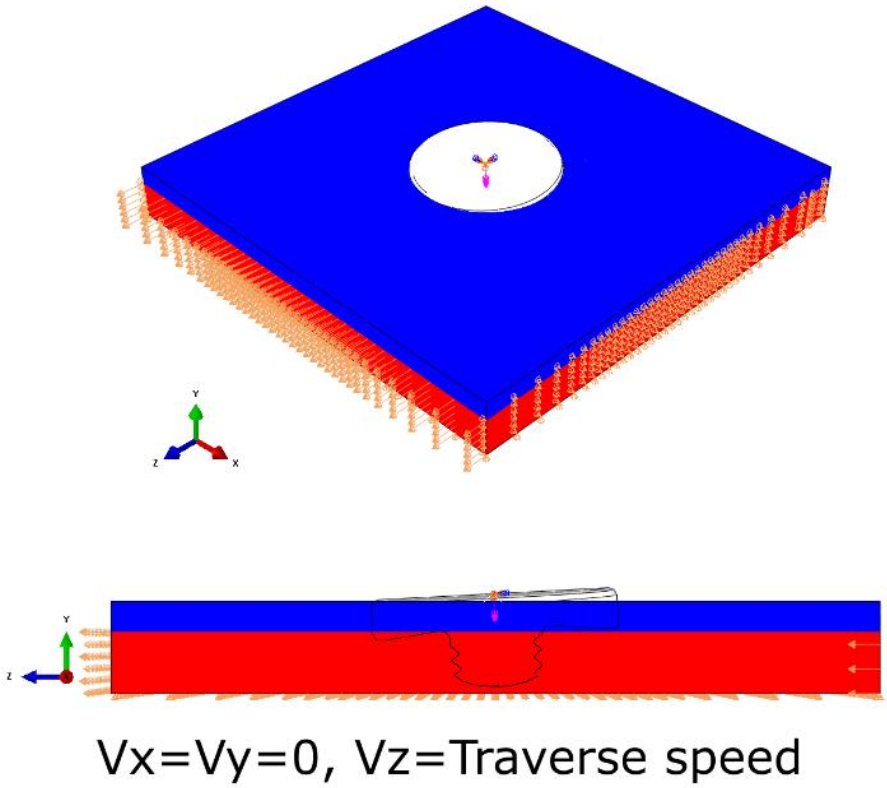


Figure 6-3 Velocity boundary conditions in the welding steep

6.3.5 Meshing and element type

In Eulerian analyses, the boundaries of each Eulerian material are reconstructed based on the computed volume fraction data for each Eulerian material in an element in each time increment. The material boundaries within an element are approximated as simple planar facets by the interface reconstruction algorithm. This assumption produces a simple, approximate material surface that may be discontinuous between neighbouring elements. Thus, fine mesh resolution is required to determine the location of material within an element accurately and to avoid the Eulerian material flowing through the Lagrangian mesh [187]. Based on the above reasons and the need for the reduction of computational time, the Eulerian domain is meshed steeply in this work; i.e. fine mesh has been generated in the tool-workpiece interaction zone, and coarse mesh at the sides by using the bias meshing technique as shown in Figure 6-4. EC3D8RT 8-node thermally coupled linear brick, multi-material, reduced integration with hourglass control and four degrees of freedom elements is used in Eulerian domain. The FSW tool is meshed by using R3D3 element (3-node 3D rigid triangular facet).

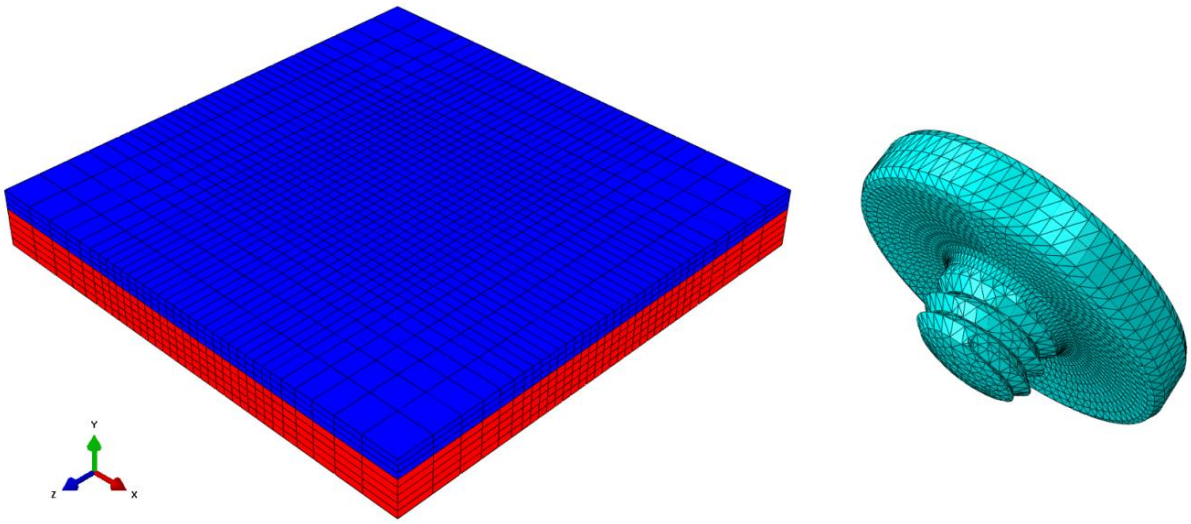


Figure 6-4 Mesh of Eulerian domain and FSW tool

6.4 Results and discussion

The predictions of FE model developed in this work were validated and confirmed by comparing to the corresponding experimental results in term of thermal history, residual stresses as well as by matching the estimated processed zone shape and void size. As mentioned earlier this model is based on aluminium alloy studied in the current study (AA 6082-T6) under welding conditions of 800 and 1100 rpm tool rotation speed and 200 mm/min tool traverse speed (W5 and W10) for the purpose of validation. The required CPU time to simulate one case with a double precision and six parallel domains is around 456 hours by using a computer with 3.7 GH processor and 64 RAM.

6.4.1 Temperature distribution

In FSW, the mixing of material to achieve a good weld needs a certain amount of heat to plasticise the material. Heat is generated in FSW due to frictional heat action between tool and base metal, as well as, from plastic deformation of the welded material. The typical cross-weld temperature distribution during the plunge and welding step with a tool rotation speed of 800 rpm and traverse speed of 200 mm/min (W5) is shown in Figure 6-5 (a-f). During the plunge step, the rotating tool pin penetrates the workpiece, until the tool shoulder contacts the workpiece, and then as in the experimental work, 0.2 mm is used as shoulder plunge depth. It can be seen that the temperature increases as the plunge depth increases due to the larger contact area between the FSW tool and workpiece, which contributes towards a large proportion of heat generation. The high-temperature region is located under the tool shoulder, where the energy density and plastic deformation is extremely high. In the welding step, the model assumes that the material traverses in the welding direction. There is a little drop and stabilising in the

high temperature as a result of less heat concentration due to high traverse speed and balance thermal distribution.

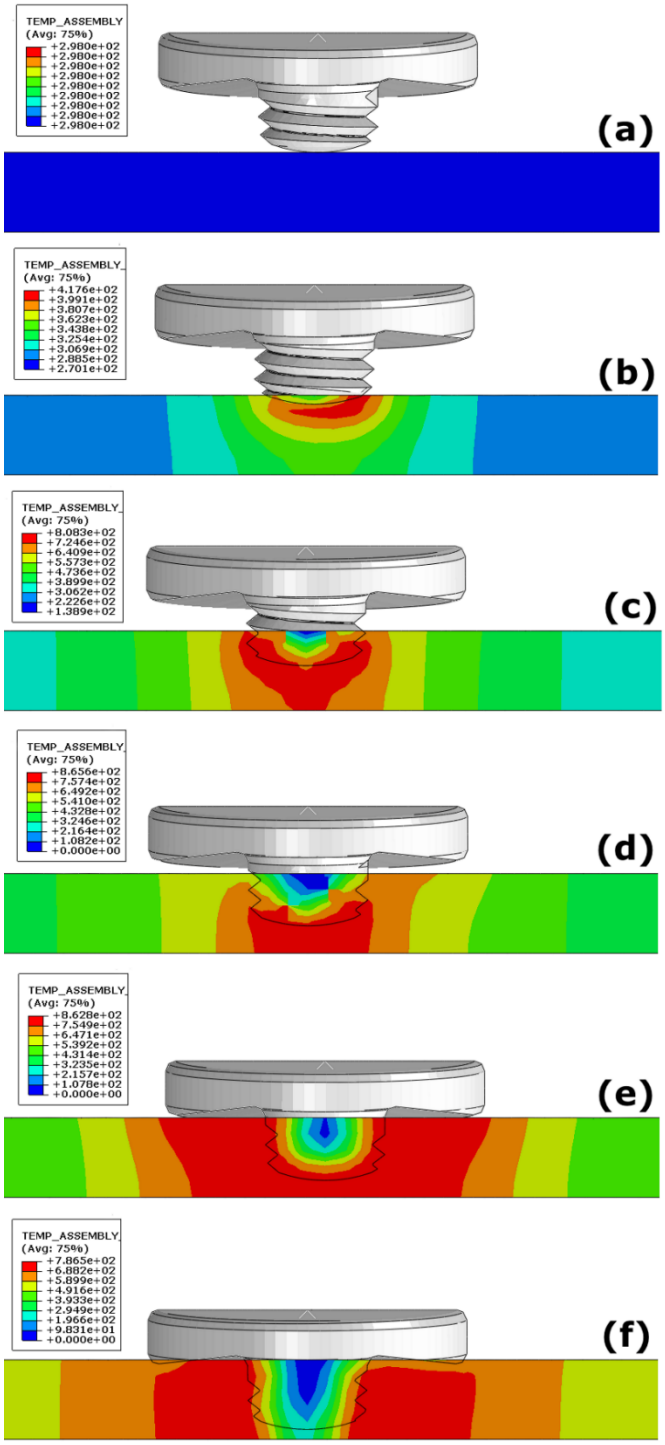


Figure 6-5 Typical cross-weld temperature distributions of W5 FSW joint at different time (sec) during plunge step; (a) 0, (b) 0.25, (c) 1, (d) 1.5, (e) 1.8, and weld steep (f), 9.4 (AS on the right, Temperature in °K)

Figure 6-6 and Figure 6-7 show the experimental validation of the model with the cross-weld temperatures results that are measured experimentally for W5 (800 rpm - 200 mm/min), and W10 (1100 rpm – 200 mm/min) FSW joints, respectively. The comparisons are made in the mid-length of the plate below the top surface by 1.6 mm. Figure 6-6 (a) shows the experimental cross-weld thermal history graphically in the FSW joint. As explained in the experimental section, nine thermocouples (TC) in specific locations have been used to measure the thermal history, eight of them to measure the cross-weld temperature in RS (TC1-4) and AS (TC5-8), as well as one thermocouple in the centre of weld to measure the peak temperature. To get temperature distribution based on the distance from welding centre to be comparable with FE model, the peak temperature of each thermocouple is used based on it is distance from the welding line to get the overall trend as shown in Figure 6-6 (b). Based on this figure, it can be seen that the simulated thermal distribution is higher than the experimental ones. However, there is good agreement between the measured and simulated peak temperature in the centre of the welding line. Also, there is no big difference between the advancing and retreating sides temperature, which is comparable to the experimentally measured temperature. A similar procedure has been used for the joint welded at a tool rotation speed of 1100 rpm and traverse speed 200 mm/min (W10) as shown in Figure 6-7 (a and b). Compared with the temperature distributions of the W5 FSW joint, the maximum temperature is increased from around 740 to 850 °K. This indicates that the peak temperature in the FSW process can be increased with the increase of tool rotation speed. Moreover, it can be seen that the generated temperature in the retreating side is higher than the advancing side, which is the same as the experimental trend. For both studied conditions, the maximum temperature obtained during the welding process is to some extent comparable

with the FE results. However, there is an overestimation to the temperature on both sides, and it increases with the increase of the distance from the weld centreline. This difference may result from the mesh size, material parameters used in the numerical simulation, the difference between actual plate size and domain size, thermal boundary conditions, backing and fixture plate, and tool rigid body assumption.

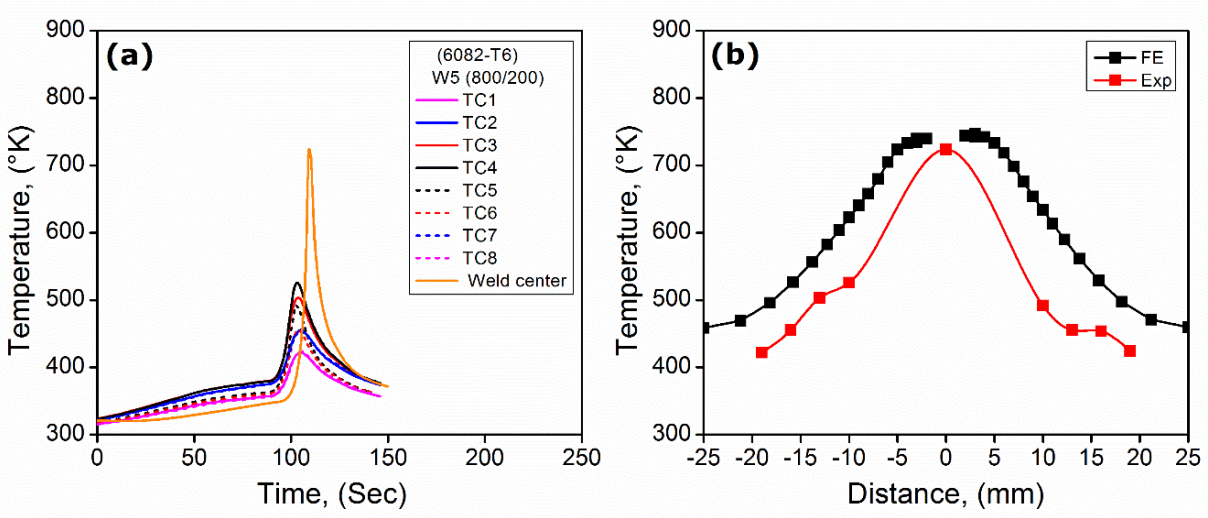


Figure 6-6 Cross-weld thermal history of W5; (a) Experimentally measured temperature, (b) Comparison between experimental and FE model solution

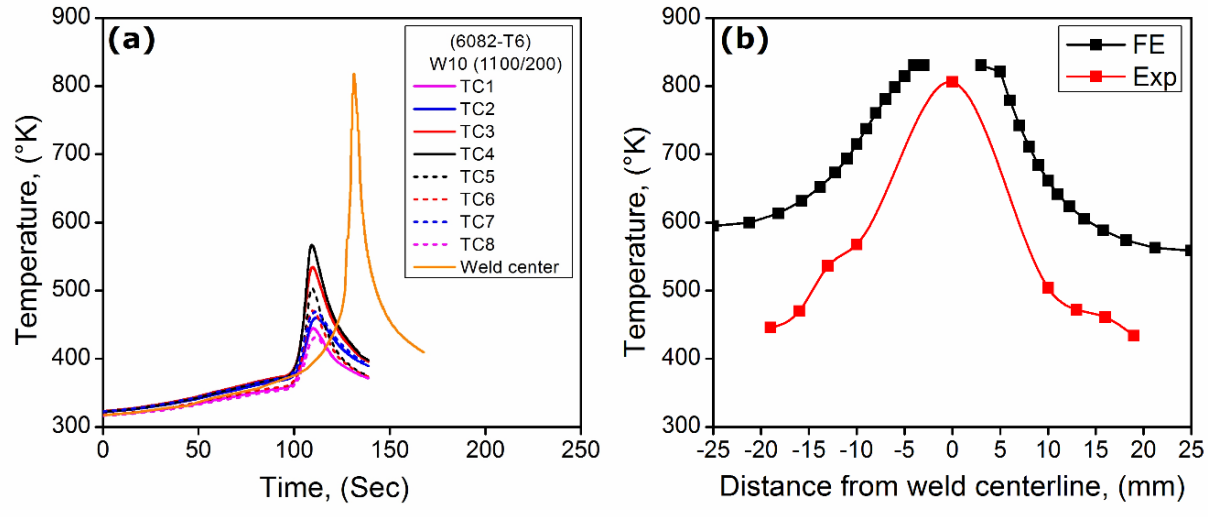


Figure 6-7 Cross-weld thermal history of W10; (a) Experimentally measured temperature, (b) Comparison between experimental and FE model solution

6.4.2 Material flow

Plastic deformation of materials plays a significant role in the flow of material and hence in the formation of a sound weld. It also affects the microstructure of the weld zone along with thermal history. During the welding process the plasticised material swept from the AS to RS to form the FSW joint. The flow of softened material around the tool during welding processes is very complicated and depends on the geometry of the FSW tool, welding parameters and the base metal. Therefore, it is vital to study the strain distribution to understand the material flow characteristics for optimum combinations of FSW parameters [127, 219-223]. Figure 6-8 shows the typical equivalent plastic strain distribution in cross-weld during plunge and welding steps of W5 FSW joint. The results showed that the equivalent plastic strain is increased as the tool plunge depth increases and reaches the maximum during the welding step. It is also seen that the maximum equivalent plastic strain in the plunge step is around the tool pin. Meanwhile, in the welding step, it occurs under the shoulder on the top surface, which means the shoulder rotation can accelerate the material deformations near the top surface. This behaviour is also confirmed in the longitudinal weld cross section as shown in Figure 6-9. This finding is consistent with the physical behaviour of FSW, as the maximum velocity is attained near the edge of the shoulder at the top surface of the workpiece followed by a rapid decrease away from this region [92, 216], and it is consistent with other studies done by Zhang and Zhang [188], and Jain et al. [224]. Furthermore, it is noted that the deformation of material at the AS and the RS is asymmetric, which can be related to the different material flows in the FSW process on both sides and the positive impact of rotational and traverse speeds of the tool [188, 224].

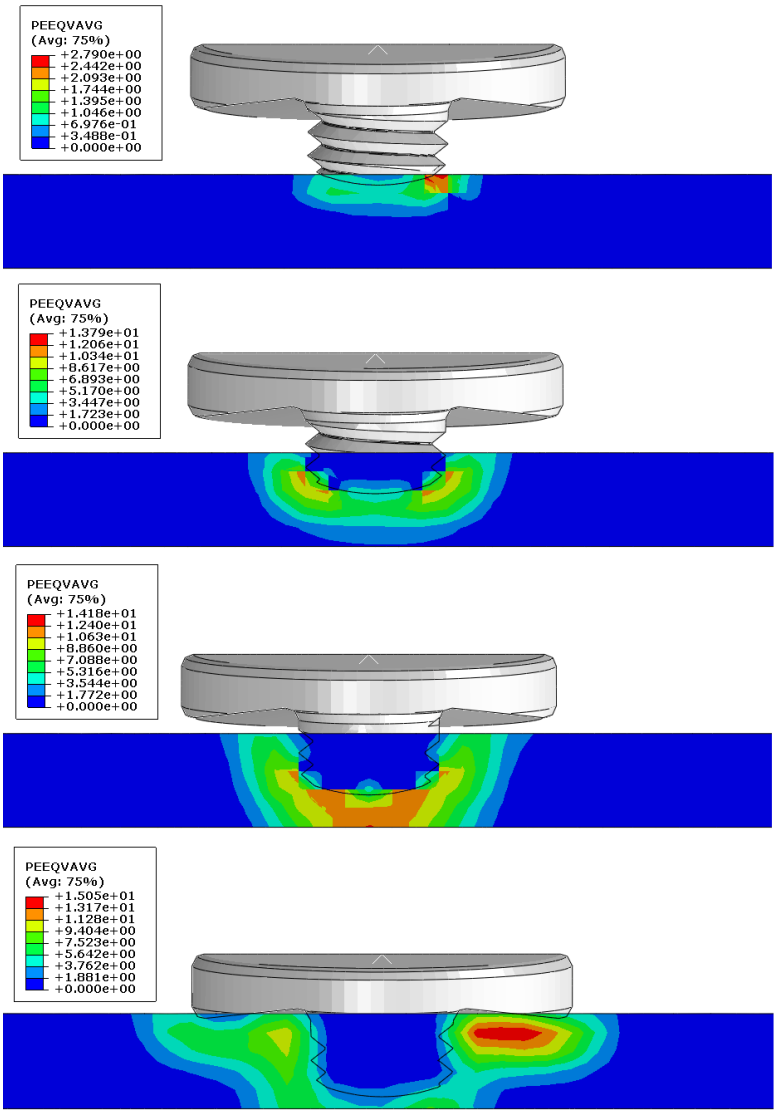


Figure 6-8 Cross-weld equivalent plastic strain distributions of W5 FSW joint at plunge step at a different time (sec); (a) 0.25, (b) 1, (c) 1.5, and welding steeps (d) 9.4 (AS on the right)

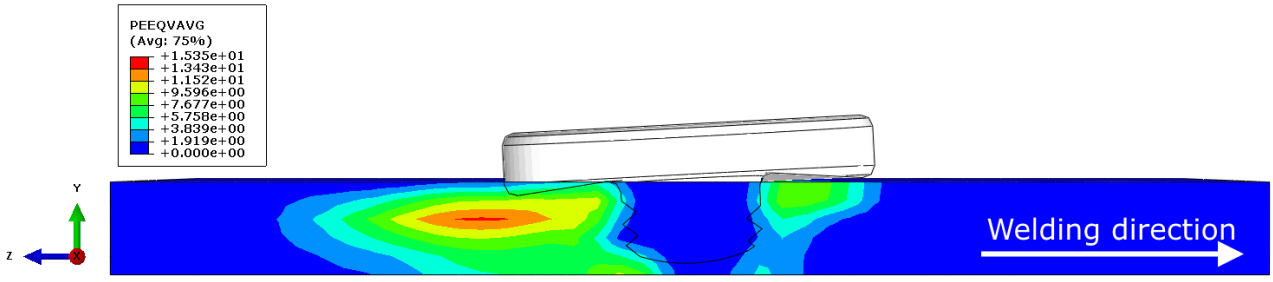


Figure 6-9 Longitudinal weld cross section of W5 FSW joint

The distributions of cross-weld plastic strain in the welding step for W5 and W10 are plotted in Figure 6-10. It is evident that the plastic strain in the AS is higher than the RS, and it increases with the increase of rotation speed. This is due to the fact that with an increase in the tool rotation speed, the rotation of the tool per minute increases, which in turn increases the plastic strain deformation and hence increases the flow of material. The results also reveal that the main deformation occurs near the top surface due to the larger contact area of tool shoulder in comparison to the tool pin as well as highest tool rotation speed near the surface. Furthermore, it can be seen that more homogenous plastic deformation is achieved when the tool rotation speed increases.

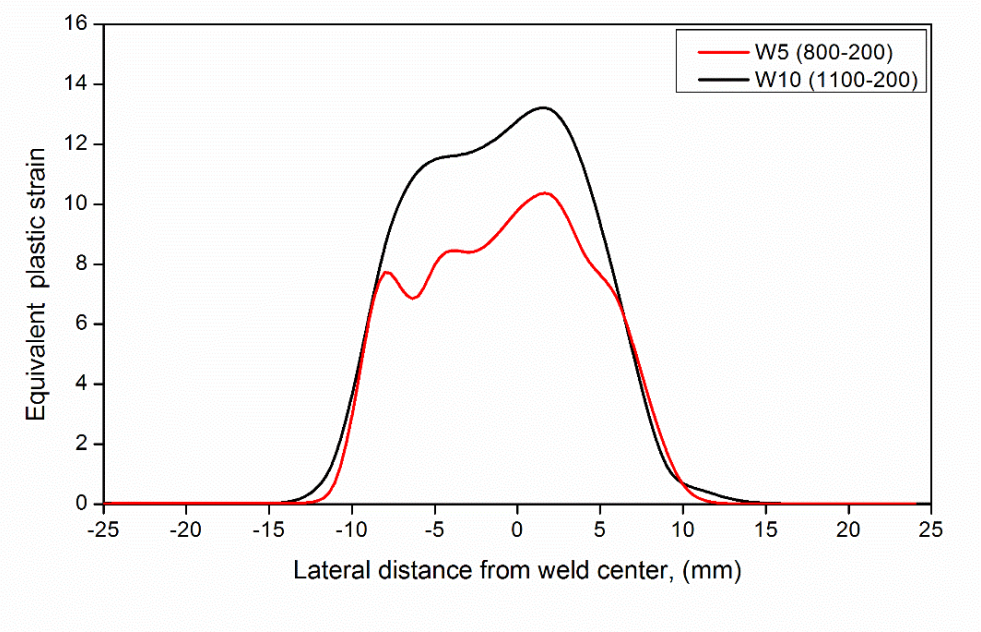


Figure 6-10 Plastic strain distribution during the welding step

The combined effect of plastic strain and thermal history (discussed in the previous section) has a significant effect on the formation of the sound joint. Figure 6-11 shows the effect of welding parameters on the joint soundness. The results revealed that, at lower tool rotation speed of 800 rpm, less heat and plastic deformation generated during the welding process, which leads to the occurrence of void defect behind the welding tool

and subsequently the welding plate fails to be friction stir welded efficiently as shown in Figure 6-11 (a). When the tool rotation speed increased to 1100 rpm, both plastic strain and heat increases in the welding zone, which leads to improve the flow of plasticised material and reduce the void size as shown in Figure 6-11 (b). This can be related to the increasing of stirring effect of the welding tool with the increasing of the rotating speed.

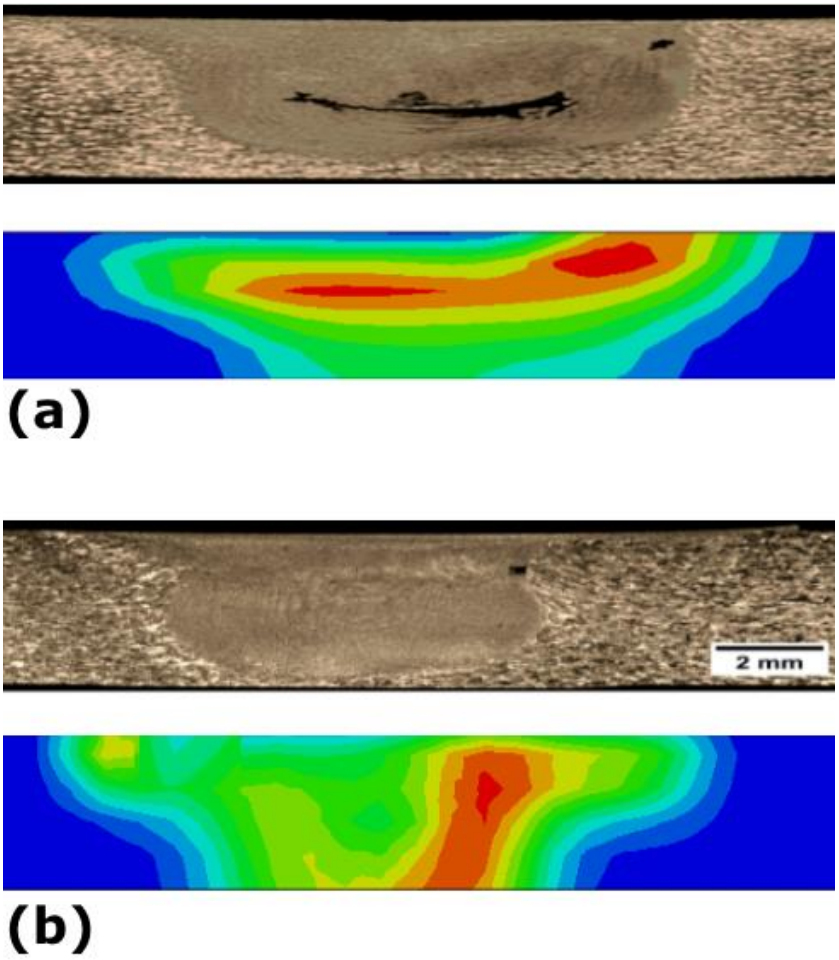


Figure 6-11 Comparison between the experimental an FE formed void, (a) W5, and (b) W10

Figure 6-12 compares the surface morphology of the experimental joint (W5) and numerical model. It can be noticed that there is an initial formation of flash at the start point of joint, which happened in the plunge step. This can be related to heat

concentration as most of the heat generation occurs at the interface between the tool shoulder and the work-piece. Significant heterogeneity in heat generation at that interface can lead to defect formation in the form of excess flash due to surface overheating [216]. Meanwhile, joint free of flash is formed during the welding step as a result of less heat concentration and exposure time at high temperature.

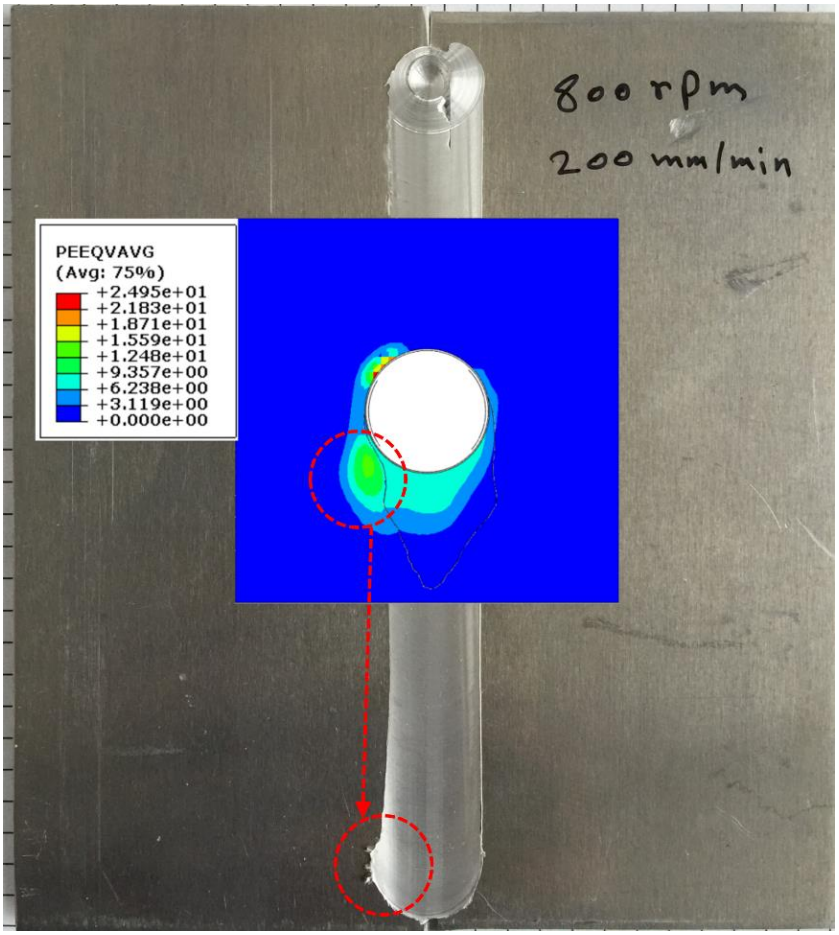


Figure 6-12 Surface morphology of W5 FSW joint

6.4.3 Residual stresses

The distortion behaviour of the welded plate and its ability to sustain applied loads while maintaining structural integrity is affected by the presence of residual stress [225-227]. In FSW thermal and mechanical residual stresses develop because of the expansion and contraction during heating and cooling, as well as from the rotation and traverse of

the FSW tool [228]. However, the induced residual stress levels in FSW joint is less than in conventional welding, but they have a significant effect on near-threshold crack propagation rates [162, 229]. Compressive residual stress dominates the fatigue crack propagation in the transition zone. Meanwhile, tensile residual stress, microstructure and intergranular failure mechanism dominate crack growth in the nugget zone [230-232]. The appearance of tensile stress components in the welding plate can cause crack initiation and increase crack growth rate, which leads to excessive failure, while compressive stresses component can be beneficial in inhibiting crack propagation [233]. Comparisons between the neutron diffraction measurements results, which were obtained experimentally and presented in Section 5.5, are compared with the predicted residual stresses of W5 FSW join and presented in Figure 6-13. The comparisons are made at around the mid-thickness of the plate. Consistent with the neutron diffraction measurement results, the numerical results reveal that both tensile and compressive residual stress component appears in the longitudinal and transverse direction of FSW joints. However, the tensile stress is higher in the longitudinal direction than the transverse direction by around 30 MPa; similar behaviour has been reported previously by Peel et al. [165]. It can be seen that the double-peak tensile stresses are located outside the stirring zone, before dropping slightly at the weld centre. This reduction of the tensile residual stress in the weld centre region is quite noticeable and has been observed previously in friction stir welding of aluminium alloys and can be related to the softening of the weld region, which would limit the capacity of the material to support the generated load [162, 181, 233, 234]. In comparison with tensile behaviour, it can be seen that the peak tensile residual stresses (around 80 MPa) are very close to the yield strength of the

same FSW joint (about 100 MPa). Therefore, the structural integrity of the welded structure is strongly affected by induced residual stress.

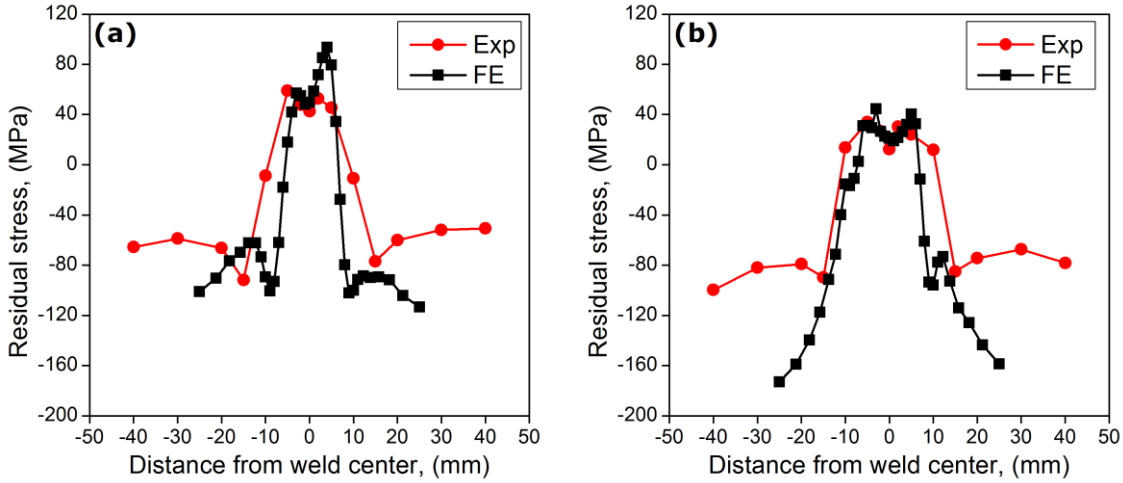


Figure 6-13 Residual stresses of W5 FSW joint as functions of position relative to the weld centreline; (a) Longitudinal, and (b) Transverse

6.5 Summary

In this chapter, a 3D fully coupled thermo-mechanical finite element model has been developed based on Coupled Eulerian-Lagrangian technique. The model is used to qualitatively analysis the effect of tool rotation speed on the weld quality through the discussions on thermal history, material flow, and residual stress for aluminium alloy AA 6082-T6. The model has been solved by ABAQUS explicit by considering temperature dependent thermal and mechanical properties and Johnson cook plasticity model. Plunge and welding steps are simulated by controlling the displacement of the tool and flow of material over the Eulerian mesh. A validation evaluation was carried out in this study as compared with the experimental work. It is found that the peak temperature in the FSW joint increased with the increase of the tool rotation speed, and it is higher on the RS. Also, plastic deformation increases with the increase of rotational tool speed, and it is observed that higher strain is found on the top surface of the workpiece as compared to

the bottom surface. The distribution of strain in FSW joint is non-uniform which indicates the asymmetrical nature of the FSW process. The increase of temperature and plastic strain leads to improve the flowability of the welded metal and reduce the size of volumetric defects. The longitudinal residual stress is higher than the transverse one. Overall, the numerical results showed a good agreement with the experimental results. However, there is an overestimate in the heat distribution and residual stress, which can be related to the meshing technique and size, the assumptions of friction coefficient and rigid tool. The contribution of this chapter is evident as the resulting outcomes can be capitalised as guidelines to assess the weld quality under different welding parameters.

Chapter 7 Conclusions and future works

7.1 Introduction

In this work, extensive and systematic experimentation have been carried out to develop a necessary understanding of the effects of two most important FSW parameters, i.e. the tool rotation and traverse speeds on the heat generation and microstructure evolution of AA 6082, AMC (AA 6092/SiC/17.5p-T6), and SAMC (AA 6061B/SiC/20p) FSW joints, and their impact on the weld quality of FSW joints. The quality of weldment is assessed based on the properties and performance of FSW joints under mechanical testing, which includes microhardness, tensile and low cycle fatigue. Also, the presented work has demonstrated the development of a 3D FE model for predicting the thermal field, residual stresses, and material flow during the FSW process. Based on the results presented, conclusions and recommendation for future work are drawn in the following sections.

7.2 Conclusions

7.2.1 Thermal history and metallurgical characterisations

The presented work has attempted to provide a detailed evaluation and fundamental understanding of the effects of FSW parameters and their interaction on the thermal histories and metallurgical characterisations of the welded joints. In addition, the differences in the welding microstructure among the investigated alloys are highlighted. From the experimental results, it can be concluded that:

1. The tool rotation speed has a more significant effect on the generated peak temperature, while the tool traverse speed controls the exposure time and subsequent cooling rate.

2. The combination of FSW parameters influences the soundness of FSW joints as they have a significant effect on the stirring process and the flow of softened material in the NZ.
3. The tendency of formation tunnel defects, cavity, and incomplete penetration in the FSW joints increases when using higher weld pitch, as a result of insufficient plastic flow and mixing time and improper heat input.
4. The initial BMs microstructure showed inhomogeneous grain structure with a mixture of HAGBs and LAGBs. On the other hand, the different zones of the weld exhibit very different microstructure, which is significantly affected by frictional heat and plastic flow.
5. The microstructure of NZ exhibits an elliptical shape, and fine equiaxed grains resulted from the CDR process with an increase in the fraction of HAGBs.
6. Grain growth in the NZ occurs as a result of incomplete CDR or in particular when exposure time at high temperature is very long.
7. The NZ microstructure showed the formation of the onion ring structure. In AA 6082 and AMC this structure consists of alternating layers of different grain size. Meanwhile, in SAMC, it consists of alternating layers of aluminium alloy and composite metal.
8. The TMAZ consists of rotated elongated grains inclined by around 45°, which is resulted from severe plastic deformation.
9. A homogeneous distribution of reinforcement particles (SiC) is obtained in the NZ of AMC and SAMC with an increase in the volume fraction because of particles refinement.

7.2.2 Mechanical characterisation and residual stresses

The influence of the microstructural characteristics governing the structure-property of FSW joints was studied, to provide a quantitative representation for the mechanical properties including hardness, tensile, and low cycle fatigue behaviours of the FSW joints. Also, neutron diffraction was used to measure residual stresses in the welded joints. Based on the experimental results, it can be concluded that:

1. Grain size (Hall-Petch), reinforcement particle size (Orowan), dislocation interaction (Taylor), and solid solution (strengthening precipitate) are the major strengthening mechanisms in FSW joints, which are affected by thermomechanical effect during FSW.
2. The main characteristic of the strengthening precipitate contributions is their localised variations within various weld regions and their dependence on the starting condition.
3. The microhardness distribution of AA 6082 exhibited both ‘‘V” and “W’’ shape features based on the welding parameters. The hardness profile showed a drop in the NZ due to the dissolution of strengthening precipitate, while in the TMAZ and HAZ the hardness varies between the NZ and base materials due to the coarsening of strengthening precipitate.
4. The microhardness profile of AMC FSW joints exhibited a typical ‘‘W’’ shape features under all welding conditions. The width of the minimum hardness zone varied with the induced temperature and corresponded accordingly with the range of the HAZ and TMAZ. The formation of fine grain and homogenous distribution of smaller reinforcement particles leads to improved hardness based on Hall–Petch and Orowan hardening mechanisms.

5. The hardness profile in SAMC FSW joints showed that there is no difference in the measured hardness between the welding zone and base materials. This can be related to the exposition of welded joints to thermal history similar to the initial heat treatment condition, T1, cooled from an elevated temperature shaping process and naturally aged.
6. The tensile strength of AA 6082 and AMC cross-weld FSW joints is lower than their base metals. The drop in the tensile strength of FSW joints is related to the strengthening precipitate, grain structure and mixing process. Meanwhile, the tensile strength of SAMC FSW joints is nearly the same as the base metal.
7. The elongation of welded joints is dependent on the gradient in the grain size of the cross-weld microstructure. The formation of an interface inclined by around 45° to the loading direction acts as a shear plane and leads to an increase of the critical resolved shear stress. Thus, the ductility of the welded joints increases as a result of less gradient in grain size obtained.
8. The fatigue life of welded joints was lower than the as-received base metals, which can be related to the physical appearance of the inclined TZ interface by around 45°. This interface accelerates the crack initiation stage and reduces the fatigue life of FSW joints.
9. The cyclic stress-strain curves of the AA 6082 and AMC FSW joints showed evidence of progressive isotropic hardening to failure for all cyclic strain amplitudes, while the BM showed less hardening ability.
10. The evolution of the stress in the as-received SAMC remains almost constant, while a very slight cyclic hardening happens in the FSW joints.

11. The neutron diffraction measurements mapped entire residual stress fields in the welded materials. The results showed that the residual stresses exhibited a typical ‘‘M’’ profile, namely the HAZ showed the highest residual stress, while the centre of the joint showed lower residual stress. The profile of residual stresses is quite symmetric, and the longitudinal residual stress is higher than the transverse residual stress.

7.2.3 Finite element simulation

In the presented work, a 3D fully coupled thermo-mechanical finite element model is developed based on Coupled Eulerian-Lagrangian technique using commercial finite element software ABAQUS/Explicit. The model is used to simulate the plunge and welding steps in FSW process and to predict the thermal history, material flow, and residual stresses in aluminium alloy AA 6082-T6 FSW joints under different tool rotation speeds. Experimental verification was performed through in-situ thermocouple measurements, evolved macrostructure, and measured residual stress. From the finite element simulation, it can be concluded that:

1. The FE results showed that the peak temperature in the FSW joint increased with the increase of the tool rotation speed, and it is higher on the RS, which is in agreement with the experimental outcome. The comparison between the experimentally measured temperature and FE results highlighted the accuracy of the predicting peak temperature in the NZ. However, there is an overestimate in the heat distribution on the AS and RS and its increase by increasing the distance from weld centre.
2. The plastic deformation increases with the increase of tool rotation speed, and it is observed that higher strain is found on the top surface of the workpiece as compared to the bottom surface. The distribution of strain in FSW joint is non-uniform which indicates the asymmetrical nature of the FSW process.

3. The numerical results reveal that both tensile and compressive residual stress components appear in the longitudinal and transverse direction of FSW joints, which is consistent with the neutron diffraction measurement results.

7.3 Future works

This thesis aimed to investigate the applicability of FSW for three different aluminium based alloys namely AA 6082, AMC, and SAMC and to provide a fundamental understanding of the microstructure evolution and structure-property development. Complementary to FSW experimental testing and evaluation, FE simulations were also conducted to provide insight into the thermal history, material deformation and residual stress distributions. On the basis of this work, some potential work can be conducted in the future as highlighted below.

1. In this study, as FSW joints under different welding conditions were subjected to detailed microstructural examination and property evaluation. There is a scope for looking into using post weld heat treatment (PWHT) (T6) to improve the mechanical properties of welded joints.
2. PWHT plays an essential role in residual stress relief for the welded structures. Therefore, the evaluation of residual stress after PWHT is another area of work that is of interest to the manufacturing industry.
3. After investigation of the feasibility of using FSW to join AMC and SAMC sheets for the first time, the results show that these alloys can be satisfactorily welded by using threaded cylindrical FSW tool. This work can be extended to study the effect of tool profile on the mechanical properties.
4. In this study, the results of SAMC FSW joints showed a significant reduction in the elongation of the welded joins, which was related to the improper mixing between the

core composite and top and bottom aluminium layers and formation flow arm. Therefore, using a stationary shoulder may lead to reducing this harmful effect. An initial trial had been done at TWI and the results were very promising. Homogeneous surface morphology, less mixing with a higher improvement in the elongation, was obtained.

5. Conducting high cycle fatigue for FSW joints will be beneficial since such data are required in industry to estimate the life of structural components and to guarantee the structural integrity, reliability, and longevity of the FSW joints.
6. In this study, the FE model was developed to simulate FSW of AA 6082. There is a need to carry out a parametric study and considering a deformable tool. Also, this model may be extended to simulate FSW of AMC and SAMC as till now there has no work carried out on these materials. Therefore, it is believed that such a model would be beneficial to simulate and analyze the welding process of the metal matrix composites, which could be used to optimize the process parameters in order to improve the quality of weldment.

References

[1] A.P. Mouritz, Introduction to aerospace materials, Elsevier2012.

[2] T. Prater, Friction Stir Welding of Metal Matrix Composites for use in aerospace structures, Acta Astronautica 93 (2014) 366-373.

[3] G. Çam, M. Koçak, Progress in joining of advanced materials, International Materials Reviews 43(1) (1998) 1-44.

[4] A.M. Hassan, M. Almomani, T. Qasim, A. Ghaithan, Effect of Processing Parameters on Friction Stir Welded Aluminum Matrix Composites Wear Behavior, Materials and Manufacturing Processes 27(12) (2012) 1419-1423.

[5] K. Suryanarayanan, R. Praveen, S. Raghuraman, Silicon Carbide Reinforced Aluminium Metal Matrix Composites for Aerospace Applications: A Literature Review, International Journal of Innovative Research in Science Engineering and Technology 2(11) (2013).

[6] J.M. Kunze, C.C. Bampton, Challenges to Developing and Producing MMCs for Space Applications, JOM (2001).

[7] P.L. Threadgill, A.J. Leonard, H.R. Shercliff, P.J. Withers, Friction stir welding of aluminium alloys, International Materials Reviews 54(2) (2009) 49-93.

[8] O.S. Salih, H. Ou, W. Sun, D. McCartney, A review of friction stir welding of aluminium matrix composites, Materials & Design 86 (2015) 61-71.

[9] <6 friction stir welding of dissimilar materials.pdf>.

[10] <16 Dissimilar friction stir welding between 5052 aluminum alloy and.pdf>.

[11] S.P. Rawal, Metal-matrix composites for space applications, JOM 53(4) (2001) 14-17.

[12] S. Suresh, Fundamentals of metal-matrix composites, Elsevier2013.

[13] Global Friction Stir Welding Market – Industry Analysis and Forecast (2016-2024) _ by welding zones, equipment type, material, application, and Region. https://www.maximizemarketresearch.com/market-report/global-friction-stir-welding-market/10856/, (accessed 22/10/2018.).

[14] T. Clyne, P. Withers, An introduction to metal matrix composites, Cambridge university press1995.

[15] R.S. Mishra, Z.Y. Ma, Friction stir welding and processing, Materials Science and Engineering: R: Reports 50(1-2) (2005) 1-78.

[16] S. Kallee, Application of friction stir welding in the shipbuilding industry. https://www.twi-global.com/technical-knowledge/published-papers/application-of-friction-stir-welding-in-the-shipbuilding-industry-february-2000/, (accessed 29/10.2018).

[17] S. Kallee, Industrial applications of friction stir welding, Friction stir welding, Elsevier2010, pp. 118-163.

[18] M. Surappa, Aluminium matrix composites: Challenges and opportunities, Sadhana 28(1-2) (2003) 319-334.

[19] M. Rosso, Ceramic and metal matrix composites: Routes and properties, Journal of Materials Processing Technology 175(1-3) (2006) 364-375.

[20] W. Thomas, E. Nicholas, J. Needham, M. Murch, P. Temple-Smith, C. Dawes, Friction Stir Butt Welding, International Patent No. PCT/GB92/02203, GB Patent No. 9125978.8, 1991, U.S. Patent No. 5,460,317, 1995, 1991.

[21] J.F. Lancaster, metallurgy of welding, Sixth ed., Abington Publishing, Cambridge/England, 1999.

[22] P. Threadgill, A. Leonard, H. Shercliff, P. Withers, Friction stir welding of aluminium alloys, International Materials Reviews 54(2) (2009) 49-93.

[23] Y.N. Zhang, X. Cao, S. Larose, P. Wanjara, Review of tools for friction stir welding and processing, Canadian Metallurgical Quarterly 51(3) (2012) 250-261.

[24] W.J. Arbegast, Friction Stir Welding After a Decade of Development It's not just welding anymore, Welding Journal 85(3) (2006).

[25] C.B. Fuller, Friction Stir Tooling: Tool Materials and Designs, in: R.S. Mishra, M.W. Mahoney (Eds.) Friction Stir Welding and Processing, ASM International, USA, 2007.

[26] R. Rai, A. De, H.K.D.H. Bhadeshia, T. DebRoy, Review: friction stir welding tools, Science and Technology of Welding and Joining 16(4) (2011) 325-342.

[27] A. Meilinger, I. Török, THE IMPORTANCE OF FRICTION STIR WELDING TOOL, Production Processes and Systems 6(1) (2013) 25-34.

[28] W.M. Thomas, D.G. Staines, I.M. Norris, R. de Frias, FRICTION STIR WELDING TOOLS AND DEVELOPMENTS, Welding in the World 47 (2003) 10-17.

[29] Metal Matrix Composites (MMC) Market for Ground Transportation, Electronics/Thermal Management, Aerospace and Other End-users - Global Industry Analysis, Size, Share, Growth, Trends and Forecast, 2013 - 2019. https://www.linkedin.com/pulse/20140605070839-173774513-metal-matrix-composites-market-review, 2014 2015).

[30] J. Kaczmar, K. Pietrzak, W. Włosiński, The production and application of metal matrix composite materials, Journal of Materials Processing Technology 106(1) (2000) 58-67.

[31] J. Pakkanen, A. Huetter, C. Poletti, N. Enzinger, C. Sommitsch, J.T. Niu, Friction Stir Welding of Aluminum Metal Matrix Composite Containers for Electric Components, Key Engineering Materials 611-612 (2014) 1445-1451.

[32] J.J. Rino, D. Chandramohan, K. Sucitharan, An Overview On Development Of Aluminium Metal Matrix Composites With Hybrid Reinforcement, International Journal of Science and Research 1(3) (2012) 2319-7064.

[33] S. Rawal, Metal-Matrix Composite for Space Application, JOM (2001).

[34] G. Mathers, The welding of aluminium and its alloys, Woodhead Publishing Limited, Cambridge , England, 2002.

[35] Aluminum and Aluminum Alloys, in: J.R. Davis (Ed.) ASM International, 1993.

[36] S. Kou, WELDING METALLURGY, Second ed., John Wiley & Sons, New Jersey, 2003.

[37] D. Storjohann, O.M. Barabash, S.S. Babu, S.A. David, P.S. Sklad, E.E. Bloom, Fusion and Friction Stir Welding of Aluminum Metal-Matrix Composites, Metallurgical and Materials Transactions A 36A (2005) 3237-3247.

[38] D.R. Ni, D.L. Chen, D. Wang, B.L. Xiao, Z.Y. Ma, Influence of microstructural evolution on tensile properties of friction stir welded joint of rolled SiCp/AA2009-T351 sheet, Materials & Design 51 (2013) 199-205.

[39] K. Kalaiselvan, I. Dinaharan, N. Murugan, Characterization of friction stir welded boron carbide particulate reinforced AA6061 aluminum alloy stir cast composite, Materials & Design 55 (2014) 176-182.

[40] L. Ceschini, I. Boromei, G. Minak, A. Morrri, F. Tarterini, Effect of friction stir welding on microstructure, tensile and fatigue properties of the AA7005/10 vol.%Al2O3p composite, Composites Science and Technology 67(3-4) (2007) 605-615.

[41] A. Feng, B. Xiao, Z. Ma, Effect of microstructural evolution on mechanical properties of friction stir welded AA2009/SiCp composite, Composites Science and Technology 68(9) (2008) 2141-2148.

[42] D. Wang, B.L. Xiao, Q.Z. Wang, Z.Y. Ma, Evolution of the Microstructure and Strength in the Nugget Zone of Friction Stir Welded SiCp/Al–Cu–Mg Composite, Journal of Materials Science & Technology 30(1) (2014) 54-60.

[43] P. CAVALIERE, E. Cerri, L. Marzoli, J. Dos Santos, Friction Stir Welding of Ceramic Particle Reinforced Aluminium Based Metal Matrix Composites, Applied Composite Materials 11 (2004) 247-258.

[44] L. Ceschini, I. Boromei, G. Minak, A. Morri, F. Tarterini, Microstructure, tensile and fatigue properties of AA6061/20vol.%Al2O3p friction stir welded joints, Composites Part A: Applied Science and Manufacturing 38(4) (2007) 1200-1210.

[45] Y. Bozkurt, H. Uzun, S. Salman, Microstructure and mechanical properties of friction stir welded particulate reinforced AA2124/SiC/25p-T4 composite, Journal of Composite Materials 45(21) (2011) 2237-2245.

[46] H. Nami, H. Adgi, M. Sharifitabar, H. Shamabadi, Microstructure and mechanical properties of friction stir welded Al/Mg2Si metal matrix cast composite, Materials & Design 32(2) (2011) 976-983.

[47] X.G. Chen, M. da Silva, P. Gougeon, L. St-Georges, Microstructure and mechanical properties of friction stir welded AA6063–B4C metal matrix composites, Materials Science and Engineering: A 518(1-2) (2009) 174-184.

[48] L.M. Marzoli, A.v. Strombeck, J.F. Dos Santos, C. Gambaro, L.M. Volpone, Friction stir welding of an AA6061/Al2O3/20p reinforced alloy, Composites Science and Technology 66(2) (2006) 363-371.

[49] F. Cioffi, R. Fernández, D. Gesto, P. Rey, D. Verdera, G. González-Doncel, Friction stir welding of thick plates of aluminum alloy matrix composite with a high volume fraction of ceramic reinforcement, Composites Part A: Applied Science and Manufacturing 54 (2013) 117-123.

[50] N. Murugan, B. Ashok Kumar, Prediction of tensile strength of friction stir welded stir cast AA6061-T6/AlNp composite, Materials & Design 51 (2013) 998-1007.

[51] P. Periyasamy, B. Mohan, V. Balasubramanian, Effect of Heat Input on Mechanical and Metallurgical Properties of Friction Stir Welded AA6061-10% SiCp MMCs, Journal of Materials Engineering and Performance 21(11) (2012) 2417-2428.

[52] R.D. Fu, R.C. Sun, F.C. Zhang, H.J. Liu, Improvement of Formation Quality for Friction Stir Welded Joints, WELDING JOURNAL 91 (2012) 169-s -173-s.

[53] B.L. Xiao, D. Wang, J. Bi, Z. Zhang, Z.Y. Ma, Friction Stir Welding of SiCp/Al Composite and 2024 Al Alloy, Materials Science Forum 638-642 (2010) 1500-1505.

[54] G. Minak, L. Ceschini, I. Boromei, M. Ponte, Fatigue properties of friction stir welded particulate reinforced aluminium matrix composites, International Journal of Fatigue 32(1) (2010) 218-226.

[55] I. Dinaharan, N. Murugan, Effect of friction stir welding on microstructure, mechanical and wear properties of AA6061/ZrB2 in situ cast composites, Materials Science and Engineering: A 543 (2012) 257-266.

[56] P. Periyasamy, B. Mohan, V. Balasubramanian, S. Rajakumar, S. Venugopal, Multi-objective optimization of friction stir welding parameters using desirability approach to join Al/SiCp metal matrix composites, Transactions of Nonferrous Metals Society of China 23(4) (2013) 942-955.

[57] A. Kumar, M.M. Mahapatra, P.K. Jha, N.R. Mandal, V. Devuri, Influence of tool geometries and process variables on friction stir butt welding of Al–4.5%Cu/TiC in situ metal matrix composites, Materials & Design 59 (2014) 406-414.

[58] D. Wang, Q.Z. Wang, B.L. Xiao, Z.Y. Ma, Achieving friction stir welded SiCp/Al–Cu–Mg composite joint of nearly equal strength to base material at high welding speed, Materials Science and Engineering: A 589 (2014) 271-274.

[59] I. Dinaharan, N. Murugan, Optimization of friction stir welding process to maximize tensile strength of AA6061/ZrB2 in-situ composite butt joints, Metals and Materials International 18(1) (2012) 135-142.

[60] K. Kalaiselvan, N. Murugan, Role of friction stir welding parameters on tensile strength of AA6061–B4C composite joints, Transactions of Nonferrous Metals Society of China 23(3) (2013) 616-624.

[61] B. Ashok Kumar, N. Murugan, Optimization of friction stir welding process parameters to maximize tensile strength of stir cast AA6061-T6/AlNp composite, Materials & Design 57 (2014) 383-393.

[62] Y. Bozkurt, A. Kentlİ, H. Uzun, S. Salman, Experimental Investigation and Prediction of Mechanical Properties of Friction Stir Welded Aluminium Metal Matrix Composite Plates, Materials Science 18(4) (2012).

[63] S.J. Vijay, N. Murugan, Influence of tool pin profile on the metallurgical and mechanical properties of friction stir welded Al–10wt.% TiB2 metal matrix composite, Materials & Design 31(7) (2010) 3585-3589.

[64] A.M. Hassan, T. Qasim, A. Ghaithan, Effect of Pin Profile on Friction Stir Welded Aluminum Matrix Composites, Materials and Manufacturing Processes 27(12) (2012) 1397-1401.

[65] B.S. Yigezu, D. Venkateswarlu, M.M. Mahapatra, P.K. Jha, N.R. Mandal, On friction stir butt welding of Al+12Si/10wt%TiC in situ composite, Materials & Design 54 (2014) 1019-1027.

[66] D. Wang, B.L. Xiao, Q.Z. Wang, Z.Y. Ma, Friction stir welding of SiCp/2009Al composite plate, Materials & Design 47 (2013) 243-247.

[67] D.R. Ni, D.L. Chen, D. Wang, B.L. Xiao, Z.Y. Ma, Tensile properties and strain-hardening behaviour of friction stir welded SiCp/AA2009 composite joints, Materials Science and Engineering: A 608 (2014) 1-10.

[68] A. Pirondi, L. Collini, D. Fersini, Fracture and fatigue crack growth behaviour of PMMC friction stir welded butt joints, Engineering Fracture Mechanics 75(15) (2008) 4333-4342.

[69] A. Pirondi, L. Collini, Analysis of crack propagation resistance of Al–Al2O3 particulate-reinforced composite friction stir welded butt joints, International Journal of Fatigue 31(1) (2009) 111-121.

[70] D.R. Ni, D.L. Chen, B.L. Xiao, D. Wang, Z.Y. Ma, Residual stresses and high cycle fatigue properties of friction stir welded SiCp/AA2009 composites, International Journal of Fatigue 55 (2013) 64-73.

[71] R.A. Prado, L.E. Murr, D.J. Shindo, K.F. Soto, Tool wear in the friction-stir welding of aluminum alloy 6061+20% Al2O3: a preliminary study, Scripta Materialia 45 (2001) 75-80.

[72] R.A. Prado, L.E. Murr, K.F. Soto, J.C. McClure, Self-optimization in tool wear for friction-stir welding of Al 6061+20% Al2O3 MMC, Materials Science and Engineering: A 349(1-2) (2003) 156-165.

[73] D.J. Shindo, A.R. Rivera, L.E. Murr, Shape optimization for tool wear in the friction-stir welding of cast AI359-20% SiC MMC, MATERIALS SCIENCE 37 (2002) 4999-5005.

[74] G.J. Fernandez, L.E. Murr, Characterization of tool wear and weld optimization in the friction-stir welding of cast aluminum 359+20% SiC metal-matrix composite, Materials Characterization 52(1) (2004) 65-75.

[75] T. Prater, A. Strauss, G. Cook, B. Gibson, C. Cox, A Comparative Evaluation of the Wear Resistance of Various Tool Materials in Friction Stir Welding of Metal Matrix Composites, Journal of Materials Engineering and Performance 22(6) (2013) 1807-1813.

[76] D. Contorno, M.G. Faga, L. Fratini, L. Settineri, G. Gautier di Confiengo, Wear Analysis during Friction Stir Processing of A359+20%SiC MMC, Key Engineering Materials 410-411 (2009) 235-244.

[77] E. Romhanji, M. Popović, Problems and prospect of Al-Mg alloys application in marine constructions, Metalurgija 12(4) (2006) 297-307.

[78] C. Marioara, S. Andersen, J. Jansen, H. Zandbergen, The influence of temperature and storage time at RT on nucleation of the β ″phase in a 6082 Al–Mg–Si alloy, Acta Materialia 51(3) (2003) 789-796.

[79] Y. Ruan, X. Qiu, W. Gong, D. Sun, Y. Li, Mechanical properties and microstructures of 6082-T6 joint welded by twin wire metal inert gas arc welding with the SiO2 flux, Materials & Design 35 (2012) 20-24.

[80] W. Bo, S.-b. Xue, Y.-l. HAN, Z.-q. LIN, Effect of combinative addition of Ti and Sr on modification of AA4043 welding wire and mechanical properties of AA6082 welded by TIG welding, Transactions of Nonferrous Metals Society of China 27(2) (2017) 272-281.

[81] N. Woodward, I. Richardson, A. Thomas, Variable polarity plasma arc welding of 6· 35 mm aluminium alloys: parameter development and preliminary analysis, Science and Technology of Welding and Joining 5(1) (2000) 21-1718.

[82] J. Adamiec, J. Rykała, Effect of MIG Welding Method Choice on Hot Cracking Occurrence in EN AW 6082 Aluminium Alloys, Solid State Phenomena, Trans Tech Publ, 2015, pp. 25-34.

[83] J. Adamiec, J. Rykała, Low Energy versus Pulse in MIG Welding of "Thin" Sheets of Aluminium Alloy EN AW 6082, Solid State Phenomena, Trans Tech Publ, 2015, pp. 35-44.

[84] Y. RUAN, L.-q. SUN, Y. WANG, S. YUAN, Study of weld cracks in double-wire MIG welded joints of 6082-T6 Al-alloy, Welding Technology 10 (2015) 026.

[85] V. Walter, K. Weidenmann, V. Schulze, A Comparison of FSW, BHLW and TIG Joints for Al-Si-Mg Alloy (EN AW-6082 T6), Procedia CIRP 18 (2014) 120-125.

[86] D. Lohwasser, Z. Chen, Friction stir welding: From basics to applications, Elsevier2009.

[87] P. Cavaliere, G. Campanile, F. Panella, A. Squillace, Effect of welding parameters on mechanical and microstructural properties of AA6056 joints produced by Friction Stir Welding, Journal of Materials Processing Technology 180(1) (2006) 263-270.

[88] K. Deplus, A. Simar, W. Van Haver, B. de Meester, Residual stresses in aluminium alloy friction stir welds, The International Journal of Advanced Manufacturing Technology 56(5-8) (2011) 493-504.

[89] S. Rajakumar, C. Muralidharan, V. Balasubramanian, Influence of friction stir welding process and tool parameters on strength properties of AA7075-T 6 aluminium alloy joints, Materials & Design 32(2) (2011) 535-549.

[90] S. Mironov, T. Onuma, Y. Sato, H. Kokawa, Microstructure evolution during friction-stir welding of AZ31 magnesium alloy, Acta Materialia 100 (2015) 301-312.

[91] H.J. Aval, Microstructure and residual stress distributions in friction stir welding of dissimilar aluminium alloys, Materials & Design 87 (2015) 405-413.

[92] A. Hasan, C. Bennett, P. Shipway, A numerical comparison of the flow behaviour in Friction Stir Welding (FSW) using unworn and worn tool geometries, Materials & Design 87 (2015) 1037-1046.

[93] P. Cavaliere, A. Squillace, F. Panella, Effect of welding parameters on mechanical and microstructural properties of AA6082 joints produced by friction stir welding, Journal of materials processing technology 200(1) (2008) 364-372.

[94] E.A. El-Danaf, M.M. El-Rayes, Microstructure and mechanical properties of friction stir welded 6082 AA in as welded and post weld heat treated conditions, Materials & Design 46 (2013) 561-572.

[95] M. Ericsson, R. Sandström, Influence of welding speed on the fatigue of friction stir welds, and comparison with MIG and TIG, International Journal of Fatigue 25(12) (2003) 1379-1387.

[96] W.B. Gong, S.J. Wang, Y.J. Wang, J.J. Wang, Microstructures and properties of thick plate butt joints of Al alloy 6082 prepared with FSW, Advanced Materials Research, Trans Tech Publ, 2011, pp. 3400-3404.

[97] P. Moreira, A. De Jesus, A. Ribeiro, P. De Castro, Fatigue crack growth in friction stir welds of 6082-T6 and 6061-T6 aluminium alloys: a comparison, Theoretical and Applied Fracture Mechanics 50(2) (2008) 81-91.

[98] Z. Ma, A. Feng, D. Chen, J. Shen, Recent advances in friction stir welding/processing of aluminum alloys: microstructural evolution and mechanical properties, Critical Reviews in Solid State and Materials Sciences 43(4) (2018) 269-333.

[99] J. Polak, Cyclic plasticity and low cycle fatigue life of metals, Elsevier Science Publishers Amsterdam, The Netherlands,, 1991.

[100] M. De Giorgi, A. Scialpi, F. Panella, L. De Filippis, Effect of shoulder geometry on residual stress and fatigue properties of AA6082 fsw joints, Journal of Mechanical Science and Technology 23(1) (2009) 26-35.

[101] T. Wang, O. Hopperstad, O.-G. Lademo, P. Larsen, Finite element analysis of welded beam-to-column joints in aluminium alloy EN AW 6082 T6, Finite elements in analysis and design 44(1) (2007) 1-16.

[102] D.A. COMPOSITES, https://www.dwa-usa.com/6092-sic-17.5p.html, 2018).

[103] MATERION, https://materion.com/-/media/files/aerospace-metal-composites/supremex/supremex-620xf-data-sheet.pdf?la=en&hash=9A70ACA2061D5B5E5AA11C936555C5EAB39AD3ED, 2108).

[104] F. Humphreys, Review grain and subgrain characterisation by electron backscatter diffraction, Journal of materials science 36(16) (2001) 3833-3854.

[105] A. Standard, ASTM E8/E8M-13a, Standard test methods for tension testing of metallic materials (2013).

[106] Standard ISO 12106, Metallic materials -- Fatigue testing -- Axial-strain-controlled method, 2017.

[107] M.E. Fitzpatrick, A. Lodini, Analysis of residual stress by diffraction using neutron and synchrotron radiation, CRC Press2003.

[108] J. Santisteban, M. Daymond, J. James, L. Edwards, ENGIN-X: a third-generation neutron strain scanner, Journal of Applied Crystallography 39(6) (2006) 812-825.

[109] H. Zandbergen, S. Andersen, J. Jansen, Structure determination of Mg5Si6 particles in Al by dynamic electron diffraction studies, Science 277(5330) (1997) 1221-1225.

[110] A. Scialpi, L. De Filippis, P. Cavaliere, Influence of shoulder geometry on microstructure and mechanical properties of friction stir welded 6082 aluminium alloy, Materials & design 28(4) (2007) 1124-1129.

[111] M. De Giorgi, A. Scialpi, F.W. Panella, L.A.C. De Filippis, Effect of shoulder geometry on residual stress and fatigue properties of AA6082 fsw joints, Journal of Mechanical Science and Technology 23(1) (2009) 26-35.

[112] R.S. Mishra, P.S. De, N. Kumar, Friction Stir Welding and Processing Science and Engineering, Springer Cham Heidelberg, New York Dordrecht London, 2014.

[113] Y.S. Sato, H. Kokawa, K. Ikeda, M. Enomoto, T. Hashimoto, S. Jogan, Microtexture in the friction-stir weld of an aluminum alloy, Metallurgical and Materials Transactions A 32(4) (2001) 941-948.

[114] S.-J. Lee, Y. Sun, H. Fujii, Stacking-fault energy, mechanical twinning and strain hardening of Fe-18Mn-0.6 C-(0, 1.5) Al twinning-induced plasticity steels during friction stir welding, Acta Materialia 148 (2018) 235-248.

[115] L.-E. Svensson, L. Karlsson, H. Larsson, B. Karlsson, M. Fazzini, J. Karlsson, Microstructure and mechanical properties of friction stir welded aluminium alloys with special reference to AA 5083 and AA 6082, Science and technology of welding and joining 5(5) (2000) 285-296.

[116] G. Dieter, Mechanical Metallurgy" McGraw-Hill Book Company (UK) Limited, ISBN-0-07-084187-x1988.

[117] P. Cavaliere, G. Rossi, R. Di Sante, M. Moretti, Thermoelasticity for the evaluation of fatigue behavior of 7005/Al2O3/10p metal matrix composite sheets joined by FSW, International Journal of Fatigue 30(1) (2008) 198-206.

[118] K. Krishnan, On the formation of onion rings in friction stir welds, Materials science and engineering: A 327(2) (2002) 246-251.

[119] S.-J. Hong, H.-M. Kim, D. Huh, C. Suryanarayana, B.S. Chun, Effect of clustering on the mechanical properties of SiC particulate-reinforced aluminum alloy 2024 metal matrix composites, Materials Science and Engineering: A 347(1-2) (2003) 198-204.

[120] K. Nie, X. Wang, L. Xu, K. Wu, X. Hu, M. Zheng, Effect of hot extrusion on microstructures and mechanical properties of SiC nanoparticles reinforced magnesium matrix composite, Journal of Alloys and Compounds 512(1) (2012) 355-360.

[121] R.-d. Fu, J.-f. Zhang, Y.-j. Li, J. Kang, H.-j. Liu, F.-c. Zhang, Effect of welding heat input and post-welding natural aging on hardness of stir zone for friction stir-welded 2024-T3 aluminum alloy thin-sheet, Materials Science and Engineering: A 559 (2013) 319-324.

[122] P.L. Threadgill, A.J. Leonard, H.R. Shercliff, P.J. Withers, Friction stir welding of aluminium alloys, International Materials Reviews 54(2) (2013) 49-93.

[123] R. Nandan, G. Roy, T. Lienert, T. Debroy, Three-dimensional heat and material flow during friction stir welding of mild steel, Acta Materialia 55(3) (2007) 883-895.

[124] Y.-M. Hwang, Z.-W. Kang, Y.-C. Chiou, H.-H. Hsu, Experimental study on temperature distributions within the workpiece during friction stir welding of aluminum alloys, International Journal of Machine Tools and Manufacture 48(7-8) (2008) 778-787.

[125] P. Dong, H. Li, D. Sun, W. Gong, J. Liu, Effects of welding speed on the microstructure and hardness in friction stir welding joints of 6005A-T6 aluminum alloy, Materials & Design 45 (2013) 524-531.

[126] Y.S. Sato, M. Urata, H. Kokawa, Parameters controlling microstructure and hardness during friction-stir welding of precipitation-hardenable aluminum alloy 6063, Metallurgical and Materials Transactions A 33(3) (2002) 625-635.

[127] T. Seidel, A.P. Reynolds, Visualization of the material flow in AA2195 friction-stir welds using a marker insert technique, Metallurgical and materials transactions A 32(11) (2001) 2879-2884.

[128] J.A. Schneider, Temperature Distribution and Resulting Metal Flow, in: R.S. Mishra, M.W. Mahoney (Eds.), Friction Stir Welding and Processing, ASM International2007.

[129] F. Rui-Dong, S. Zeng-Qiang, S. Rui-Cheng, L. Ying, L. Hui-jie, L. Lei, Improvement of weld temperature distribution and mechanical properties of 7050

aluminum alloy butt joints by submerged friction stir welding, Materials & Design 32(10) (2011) 4825-4831.

[130] M. Song, R. Kovacevic, Numerical and experimental study of the heat transfer process in friction stir welding, Proceedings of the Institution of Mechanical Engineers, Part B: Journal of Engineering Manufacture 217(1) (2003) 73-85.

[131] W. Guo, D. Crowther, J.A. Francis, A. Thompson, Z. Liu, L. Li, Microstructure and mechanical properties of laser welded S960 high strength steel, Materials & Design 85 (2015) 534-548.

[132] Z. Ma, S. Sharma, R. Mishra, Effect of friction stir processing on the microstructure of cast A356 aluminum, Materials Science and Engineering: A 433(1) (2006) 269-278.

[133] P. Moreira, T. Santos, S. Tavares, V. Richter-Trummer, P. Vilaça, P. De Castro, Mechanical and metallurgical characterization of friction stir welding joints of AA6061-T6 with AA6082-T6, Materials & design 30(1) (2009) 180-187.

[134] Y.S. Sato, H. Kokawa, M. Enomoto, S. Jogan, Microstructural evolution of 6063 aluminum during friction-stir welding, Metallurgical and Materials Transactions A 30(9) (1999) 2429-2437.

[135] A. Heidarzadeh, K. Kazemi-Choobi, H.H. an, P. Asadi, Microstructural evolution, in: M.K.B. Givi, P. Asadi (Eds.), Advances in Friction Stir Welding and Processing, Woodhead Publishing, UK, 2014.

[136] A. Rollett, F. Humphreys, G.S. Rohrer, M. Hatherly, Recrystallization and related annealing phenomena, Elsevier2004.

[137] K. Jata, S. Semiatin, Continuous dynamic recrystallization during friction stir welding of high strength aluminum alloys, AIR FORCE RESEARCH LAB WRIGHT-PATTERSON AFB OH MATERIALS AND MANUFACTURING DIRECTORATE, 2000.

[138] E.A. El-Danaf, M. Baig, High temperature deformation characteristics of equal channel angular pressed AA6082-T6, Materials Science and Engineering: A 565 (2013) 301-307.

[139] A. Feng, D. Chen, Z. Ma, Microstructure and low-cycle fatigue of a friction-stir-welded 6061 aluminum alloy, Metallurgical and Materials Transactions A 41(10) (2010) 2626-2641.

[140] A.G. Frøseth, R. Høier, P.M. Derlet, S.J. Andersen, C.D. Marioara, Bonding in mgsi and Al-Mg-Si compounds relevant to Al-Mg-Si alloys, Physical Review B 67(22) (2003) 224106.

[141] W. Lee, Y. Yeon, S. Jung, Joint properties of friction stir welded AZ31B–H24 magnesium alloy, Materials Science and Technology 19(6) (2003) 785-790.

[142] N. Öztoprak, Ç.E. Yeni, B.G. Kıral, Fatigue and monotonic tensile behaviors of friction stir welded AA6061/SiC/20p-T1 composite joints at various tool rotation speeds, Materials Research Express 5(6) (2018) 066547.

[143] M. Mahmoudiniya, A.H. Kokabi, S. Kheirandish, L.A. Kestens, Microstructure and mechanical properties of friction stir welded ferrite-martensite DP700 steel, Materials Science and Engineering: A (2018).

[144] N. Pathak, K. Bandyopadhyay, M. Sarangi, S.K. Panda, Microstructure and mechanical performance of friction stir spot-welded aluminum-5754 sheets, Journal of Materials Engineering and Performance 22(1) (2013) 131-144.

[145] P.M.G.P. Moreira, A.M.P. de Jesus, A.S. Ribeiro, P.M.S.T. de Castro, Fatigue crack growth in friction stir welds of 6082-T6 and 6061-T6 aluminium alloys: A comparison, Theoretical and Applied Fracture Mechanics 50(2) (2008) 81-91.

[146] Y. Sano, K. Masaki, T. Gushi, T. Sano, Improvement in fatigue performance of friction stir welded A6061-T6 aluminum alloy by laser peening without coating, Materials & Design (1980-2015) 36 (2012) 809-814.

[147] C. Zhou, X. Yang, G. Luan, Investigation of microstructures and fatigue properties of friction stir welded Al–Mg alloy, Materials Chemistry and Physics 98(2-3) (2006) 285-290.

[148] M. Levin, B. Karlsson, Crack initiation and growth during low-cycle fatigue of discontinuously reinforced metal-matrix composites, International journal of fatigue 15(5) (1993) 377-387.

[149] J.E. ALLISON, J.W. JONES, Fatigue Behavior of Discontinuously Reinforced Metal-Matrix Composites, in: S. Suresh, A. Mortensen, A. Needleman (Eds.), Fundamentals of Metal-Matrix Composites, Elsevier2013.

[150] N. Chawla, U. Habel, Y.-L. Shen, C. Andres, J. Jones, J. Allison, The effect of matrix microstructure on the tensile and fatigue behavior of SiC particle-reinforced 2080 Al matrix composites, Metallurgical and Materials Transactions A 31(2) (2000) 531-540.

[151] J.N. Hall, J.W. Jones, A.K. Sachdev, Particle size, volume fraction and matrix strength effects on fatigue behavior and particle fracture in 2124 aluminum-SiCp composites, Materials Science and Engineering: A 183(1-2) (1994) 69-80.

[152] R. Rodriguez, J. Jordon, P. Allison, T. Rushing, L. Garcia, Low-cycle fatigue of dissimilar friction stir welded aluminum alloys, Materials Science and Engineering: A 654 (2016) 236-248.

[153] P. Cavaliere, E. Cerri, A. Squillace, Mechanical response of 2024-7075 aluminium alloys joined by Friction Stir Welding, Journal of Materials Science 40(14) (2005) 3669-3676.

[154] A. Hamada, A. Järvenpää, M. Ahmed, M. Jaskari, B. Wynne, D. Porter, L. Karjalainen, The microstructural evolution of friction stir welded AA6082-T6 aluminum alloy during cyclic deformation, Materials Science and Engineering: A 642 (2015) 366-376.

[155] C. Feltner, C. Laird, Cyclic stress-strain response of FCC metals and alloys—I Phenomenological experiments, Acta metallurgica 15(10) (1967) 1621-1632.

[156] M. Klesnil, P. Lukas, P. Lukáš, Fatigue of metallic materials, Elsevier1992.

[157] S.K. Paul, N. Stanford, A. Taylor, T. Hilditch, The effect of low cycle fatigue, ratcheting and mean stress relaxation on stress–strain response and microstructural development in a dual phase steel, International Journal of Fatigue 80 (2015) 341-348.

[158] W. Woo, H. Choo, D.W. Brown, Z. Feng, P.K. Liaw, Angular distortion and through-thickness residual stress distribution in the friction-stir processed 6061-T6 aluminum alloy, Materials Science and Engineering: A 437(1) (2006) 64-69.

[159] M.B. Prime, T. Gnäupel-Herold, J.A. Baumann, R.J. Lederich, D.M. Bowden, R.J. Sebring, Residual stress measurements in a thick, dissimilar aluminum alloy friction stir weld, Acta materialia 54(15) (2006) 4013-4021.

[160] O. Hatamleh, I.V. Rivero, S.E. Swain, An investigation of the residual stress characterization and relaxation in peened friction stir welded aluminum–lithium alloy joints, Materials & Design 30(9) (2009) 3367-3373.

[161] W. Xu, J. Liu, H. Zhu, Analysis of residual stresses in thick aluminum friction stir welded butt joints, Materials & Design 32(4) (2011) 2000-2005.

[162] G. Pouget, A.P. Reynolds, Residual stress and microstructure effects on fatigue crack growth in AA2050 friction stir welds, International Journal of Fatigue 30(3) (2008) 463-472.

[163] H. Lombard, D. Hattingh, A. Steuwer, M. James, Effect of process parameters on the residual stresses in AA5083-H321 friction stir welds, Materials Science and Engineering: A 501(1-2) (2009) 119-124.

[164] D. Richards, P. Prangnell, S. Williams, P. Withers, Global mechanical tensioning for the management of residual stresses in welds, Materials Science and Engineering: A 489(1-2) (2008) 351-362.

[165] M. Peel, A. Steuwer, M. Preuss, P. Withers, Microstructure, mechanical properties and residual stresses as a function of welding speed in aluminium AA5083 friction stir welds, Acta materialia 51(16) (2003) 4791-4801.

[166] N. Chawla, Y.-L. Shen, Mechanical behavior of particle reinforced metal matrix composites, Advanced engineering materials 3(6) (2001) 357-370.

[167] R. Gupta, G. Chaudhari, B. Daniel, Strengthening mechanisms in ultrasonically processed aluminium matrix composite with in-situ Al 3 Ti by salt addition, Composites Part B: Engineering 140 (2018) 27-34.

[168] N. Chawla, J. Jones, C. Andres, J. Allison, Effect of SiC volume fraction and particle size on the fatigue resistance of a 2080 Al/SiC p composite, Metallurgical and Materials Transactions A 29(11) (1998) 2843-2854.

[169] C. Ramesh, R. Keshavamurthy, B. Channabasappa, A. Ahmed, Microstructure and mechanical properties of Ni–P coated Si3N4 reinforced Al6061 composites, Materials Science and Engineering: A 502(1-2) (2009) 99-106.

[170] M. Ashby, The deformation of plastically non-homogeneous materials, Philosophical Magazine 21(170) (1970) 399-424.

[171] C. Olea, L. Roldo, T. Strohaecker, J. Dos Santos, Friction stir welding of precipitate hardenable aluminium alloys: a review, Welding in the World 50(11-12) (2006) 78-87.

[172] C. Olea, L. Roldo, J. Dos Santos, T. Strohaecker, A sub-structural analysis of friction stir welded joints in an AA6056 Al-alloy in T4 and T6 temper conditions, Materials Science and Engineering: A 454 (2007) 52-62.

[173] S. Gatea, H. Ou, G. McCartney, Deformation and fracture characteristics of Al6092/SiC/17.5 p metal matrix composite sheets due to heat treatments, Materials Characterization 142 (2018) 365-376.

[174] K. Kumar, H. Van Swygenhoven, S. Suresh, Mechanical behavior of nanocrystalline metals and alloys1, Acta Materialia 51(19) (2003) 5743-5774.

[175] C.-S. Kim, I. Sohn, M. Nezafati, J.B. Ferguson, B.F. Schultz, Z. Bajestani-Gohari, P.K. Rohatgi, K. Cho, Prediction models for the yield strength of particle-reinforced unimodal pure magnesium (Mg) metal matrix nanocomposites (MMNCs), Journal of Materials Science 48(12) (2013) 4191-4204.

[176] T. Mungole, P. Kumar, M. Kawasaki, T.G. Langdon, The contribution of grain boundary sliding in tensile deformation of an ultrafine-grained aluminum alloy having high strength and high ductility, Journal of Materials Science 50(10) (2015) 3549-3561.

[177] Z. Basinski, M. Szczerba, M. Niewczas, J. Embury, S. Basinski, The transformation of slip dislocations during twinning of copper-aluminum alloy crystals, Revue de mEtallurgie 94(9) (1997) 1037-1044.

[178] M. Chen, E. Ma, K.J. Hemker, H. Sheng, Y. Wang, X. Cheng, Deformation twinning in nanocrystalline aluminum, Science 300(5623) (2003) 1275-1277.

[179] T. Srivatsan, A. Prakash, Effect of particulate silicon carbide on cyclic strain resistance and fracture behavior of X2080 aluminum alloy metal matrix composites, Engineering fracture mechanics 49(5) (1994) 751-772.

[180] T. Srivatsan, The low-cycle fatigue behaviour of an aluminium-alloy-ceramic-particle composite, International journal of fatigue 14(3) (1992) 173-182.

[181] L. Fratini, S. Pasta, A.P. Reynolds, Fatigue crack growth in 2024-T351 friction stir welded joints: Longitudinal residual stress and microstructural effects, International Journal of Fatigue 31(3) (2009) 495-500.

[182] V. Nardone, K. Prewo, On the strength of discontinuous silicon carbide reinforced aluminum composites, Scripta Metallurgica 20(1) (1986) 43-48.

[183] Z. Zhang, Z. Wang, Grain boundary effects on cyclic deformation and fatigue damage, Progress in Materials Science 53(7) (2008) 1025-1099.

[184] R. Arsenault, L. Wang, C. Feng, Strengthening of composites due to microstructural changes in the matrix, Acta metallurgica et materialia 39(1) (1991) 47-57.

[185] Z. Zhang, D. Chen, Consideration of Orowan strengthening effect in particulate-reinforced metal matrix nanocomposites: A model for predicting their yield strength, Scripta Materialia 54(7) (2006) 1321-1326.

[186] X. He, F. Gu, A. Ball, A review of numerical analysis of friction stir welding, Progress in Materials Science 65 (2014) 1-66.

[187] ABAQUS, Version "2016 Documentation.", Dassault Systemes Simulia, Providence, RI, USA, 2016.

[188] Z. Zhang, H. Zhang, Numerical studies on controlling of process parameters in friction stir welding, Journal of materials processing technology 209(1) (2009) 241-270.

[189] S. Krenk, Non-linear modeling and analysis of solids and structures, Cambridge University Press2009.

[190] M. Mijajlović, D. Milčić, M. Milčić, Numerical simulation of friction stir welding, Thermal Science 18(3) (2014) 967-978.

[191] M. Grujicic, G. Arakere, B. Pandurangan, J.M. Ochterbeck, C. Yen, B. Cheeseman, A.P. Reynolds, M.A. Sutton, Computational analysis of material flow during friction stir welding of AA5059 aluminum alloys, Journal of materials engineering and performance 21(9) (2012) 1824-1840.

[192] H. Zhang, Z. Zhang, J. Chen, 3D modeling of material flow in friction stir welding under different process parameters, Journal of Materials Processing Technology 183(1) (2007) 62-70.

[193] P.A. Colegrove, H.R. Shercliff, R. Zettler, Model for predicting heat generation and temperature in friction stir welding from the material properties, Science and Technology of Welding & Joining 12(4) (2007) 284-297.

[194] A. Mishra, A. Kumar Sharma, Analysis of Heat Generation During Friction Stir Processing of Aluminium Similar Joints, (2017).

[195] S. Rajesh, H.S. Bang, W.S. Chang, H.J. Kim, H.S. Bang, C.I. Oh, J.S. Chu, Numerical determination of residual stress in friction stir weld using 3D-analytical model of stir zone, Journal of materials processing technology 187 (2007) 224-226.

[196] X. Zhu, Y. Chao, Numerical simulation of transient temperature and residual stresses in friction stir welding of 304L stainless steel, Journal of materials processing technology 146(2) (2004) 263-272.

[197] T. Seidel, A.P. Reynolds, Two-dimensional friction stir welding process model based on fluid mechanics, Science and technology of welding and joining 8(3) (2003) 175-183.

[198] P. Colegrove, H. Shercliff, Two-dimensional CFD modelling of flow round profiled FSW tooling, Science and technology of welding and joining 9(6) (2004) 483-492.

[199] P.A. Colegrove, H. Shercliff, Development of Trivex friction stir welding tool Part 2–three-dimensional flow modelling, Science and Technology of Welding and Joining 9(4) (2004) 352-361.

[200] P.A. Colegrove, H.R. Shercliff, 3-Dimensional CFD modelling of flow round a threaded friction stir welding tool profile, Journal of Materials Processing Technology 169(2) (2005) 320-327.

[201] P. Ulysse, Three-dimensional modeling of the friction stir-welding process, Int J Mach Tool Manu 42(14) (2002) 1549-1557.

[202] J. Donea, A. Huerta, J.-P. Ponthot, A. Rodriguez-Ferran, Encyclopedia of Computational Mechanics Vol. 1: Fundamentals., Chapter 14: Arbitrary Lagrangian-Eulerian Methods, Wiley & Sons, 2004.

[203] M. Assidi, L. Fourment, S. Guerdoux, T. Nelson, Friction model for friction stir welding process simulation: Calibrations from welding experiments, International Journal of Machine Tools and Manufacture 50(2) (2010) 143-155.

[204] X. Deng, S. Xu, Two-dimensional finite element simulation of material flow in the friction stir welding process, Journal of manufacturing processes 6(2) (2004) 125.

[205] H. Schmidt, J. Hattel, A local model for the thermomechanical conditions in friction stir welding, Modelling and simulation in materials science and engineering 13(1) (2004) 77.

[206] H. Zhang, Z. Zhang, J. Chen, The finite element simulation of the friction stir welding process, Materials Science and Engineering: A 403(1) (2005) 340-348.

[207] Z. Zhang, Comparison of two contact models in the simulation of friction stir welding process, Journal of Materials Science 43(17) (2008) 5867-5877.

[208] A. Tongne, C. Desrayaud, M. Jahazi, E. Feulvarch, On material flow in friction stir welded Al alloys, Journal of Materials Processing Technology 239 (2017) 284-296.

[209] F. Al-Badour, N. Merah, A. Shuaib, A. Bazoune, Coupled Eulerian Lagrangian finite element modeling of friction stir welding processes, Journal of Materials Processing Technology 213(8) (2013) 1433-1439.

[210] N. Torić, J. Brnić, I. Boko, M. Brčić, I.W. Burgess, I. Uzelac, Experimental analysis of the behaviour of aluminium alloy EN 6082AW T6 at high temperature, Metals 7(4) (2017) 126.

[211] M. Payandeh, E. Sjölander, A.E. Jarfors, M. Wessen, Mechanical and Thermal Properties of Rheocast Telecom Component Using Low Silicon Aluminium Alloy in As-Cast and Heat-Treated Conditions, Light Metals 2015, Springer2015, pp. 209-214.

[212] A. Wilson, The thermal expansion of aluminium from 0 to 650 C, Proceedings of the Physical Society 53(3) (1941) 235.

[213] R. Powell, C.Y. Ho, P.E. Liley, Thermal conductivity of selected materials, US Government Printing Office Washington, D. C1966.

[214] S. Jaspers, J. Dautzenberg, Material behaviour in conditions similar to metal cutting: flow stress in the primary shear zone, Journal of Materials Processing Technology 122(2-3) (2002) 322-330.

[215] H. Schmidt, J. Hattel, J. Wert, An analytical model for the heat generation in friction stir welding, Modelling and Simulation in Materials Science and Engineering 12(1) (2003) 143.

[216] R. Nandan, T. DebRoy, H. Bhadeshia, Recent advances in friction-stir welding–process, weldment structure and properties, Progress in Materials Science 53(6) (2008) 980-1023.

[217] S. Tutunchilar, M. Haghpanahi, M.B. Givi, P. Asadi, P. Bahemmat, Simulation of material flow in friction stir processing of a cast Al–Si alloy, Materials & Design 40 (2012) 415-426.

[218] G. Buffa, G. Campanile, L. Fratini, A. Prisco, Friction stir welding of lap joints: Influence of process parameters on the metallurgical and mechanical properties, Materials Science and Engineering: A 519(1-2) (2009) 19-26.

[219] R. Nandan, B. Prabu, A. De, T. Debroy, Improving reliability of heat transfer and materials flow calculations during friction stir welding of dissimilar aluminum alloys, WELDING JOURNAL-NEW YORK- 86(10) (2007) 313.

[220] X.C. He, Thermo-mechanical modelling of friction stir welding process, Advanced Materials Research, Trans Tech Publ, 2013, pp. 1155-1159.

[221] M. Guerra, C. Schmidt, J. McClure, L. Murr, A. Nunes, Flow patterns during friction stir welding, Materials characterization 49(2) (2002) 95-101.

[222] L. Ke, L. Xing, J. Indacochea, Material flow patterns and cavity model in friction-stir welding of aluminum alloys, Metallurgical and Materials Transactions B 35(1) (2004) 153-160.

[223] D.M. Neto, P. Neto, Numerical modeling of friction stir welding process: a literature review, The International Journal of Advanced Manufacturing Technology 65(1-4) (2013) 115-126.

[224] R. Jain, S.K. Pal, S.B. Singh, Finite element simulation of temperature and strain distribution during friction stir welding of AA2024 aluminum alloy, Journal of The Institution of Engineers (India): Series C 98(1) (2017) 37-43.

[225] P.J. Withers, H. Bhadeshia, Residual stress. Part 2–Nature and origins, Materials science and technology 17(4) (2001) 366-375.

[226] P.J. Withers, H. Bhadeshia, Residual stress. Part 1–measurement techniques, Materials science and Technology 17(4) (2001) 355-365.

[227] J. Francis, H. Stone, S. Kundu, R. Rogge, H. Bhadeshia, P. Withers, L. Karlsson, Transformation temperatures and welding residual stresses in ferritic steels, ASME 2007 Pressure Vessels and Piping Conference, American Society of Mechanical Engineers, 2007, pp. 949-956.

[228] C. Chen, R. Kovacevic, Parametric finite element analysis of stress evolution during friction stir welding, Proceedings of the Institution of Mechanical Engineers, Part B: Journal of Engineering Manufacture 220(8) (2006) 1359-1371.

[229] G. Biallas, Effect of welding residual stresses on fatigue crack growth thresholds, International Journal of fatigue 50 (2013) 10-17.

[230] K. Jata, K. Sankaran, J. Ruschau, Friction-stir welding effects on microstructure and fatigue of aluminum alloy 7050-T7451, Metallurgical and materials transactions A 31(9) (2000) 2181-2192.

[231] G. Bussu, P. Irving, The role of residual stress and heat affected zone properties on fatigue crack propagation in friction stir welded 2024-T351 aluminium joints, International Journal of Fatigue 25(1) (2003) 77-88.

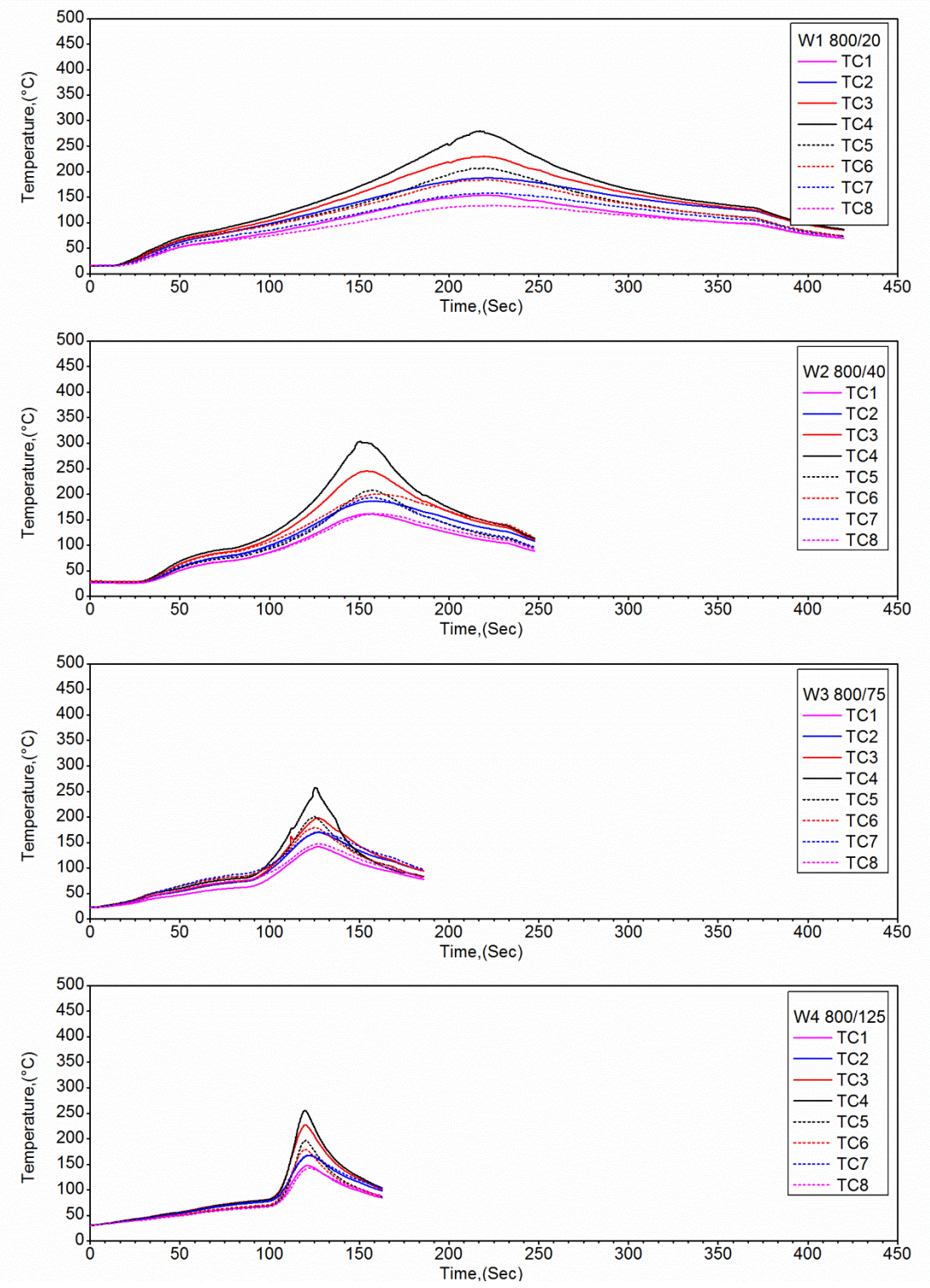
[232] R. John, K. Jata, K. Sadananda, Residual stress effects on near-threshold fatigue crack growth in friction stir welds in aerospace alloys, International Journal of fatigue 25(9-11) (2003) 939-948.

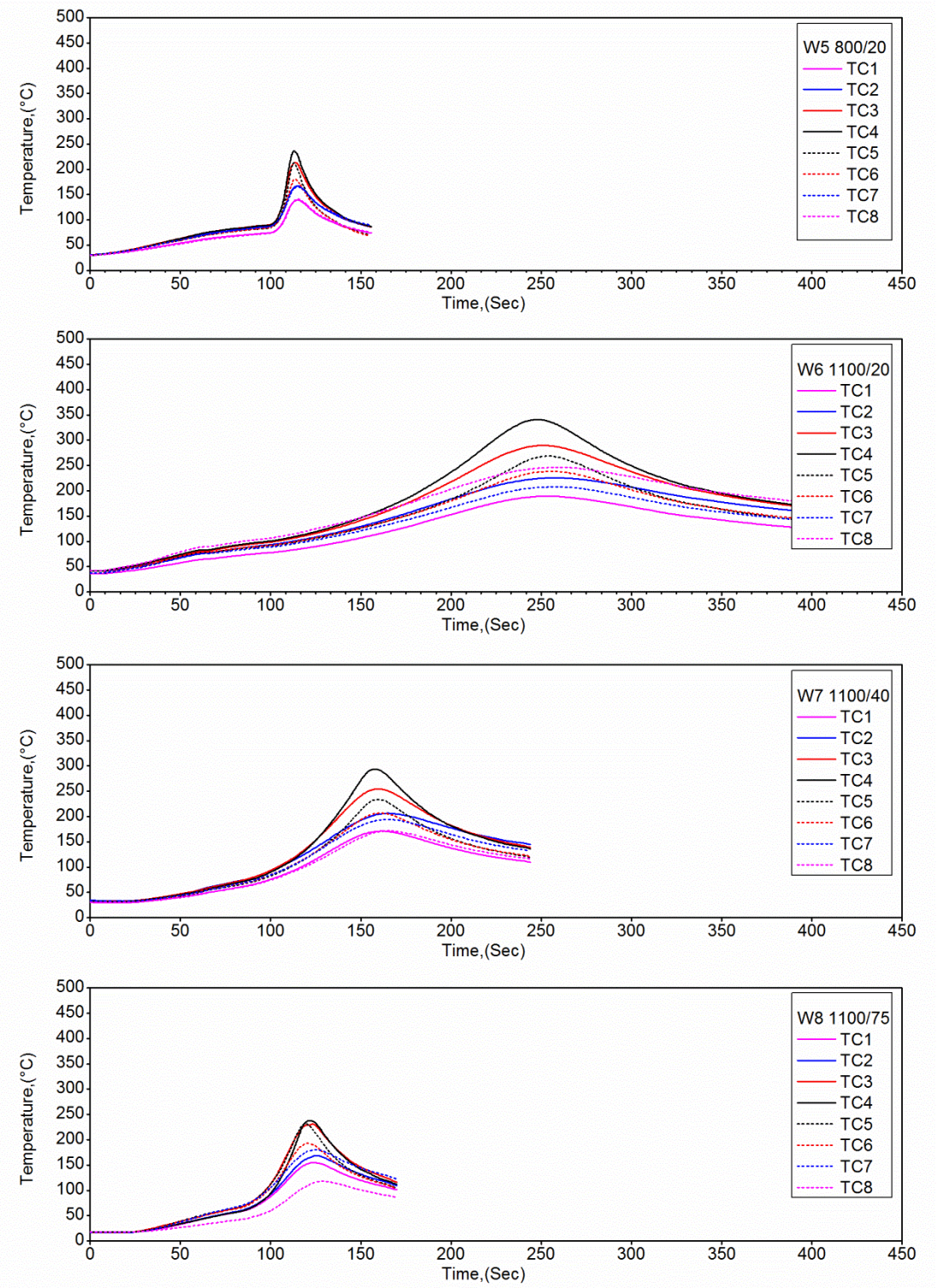
[233] P. Staron, M. Kocak, S. Williams, A. Wescott, Residual stress in friction stir-welded Al sheets, Physica B: Condensed Matter 350(1-3) (2004) E491-E493.

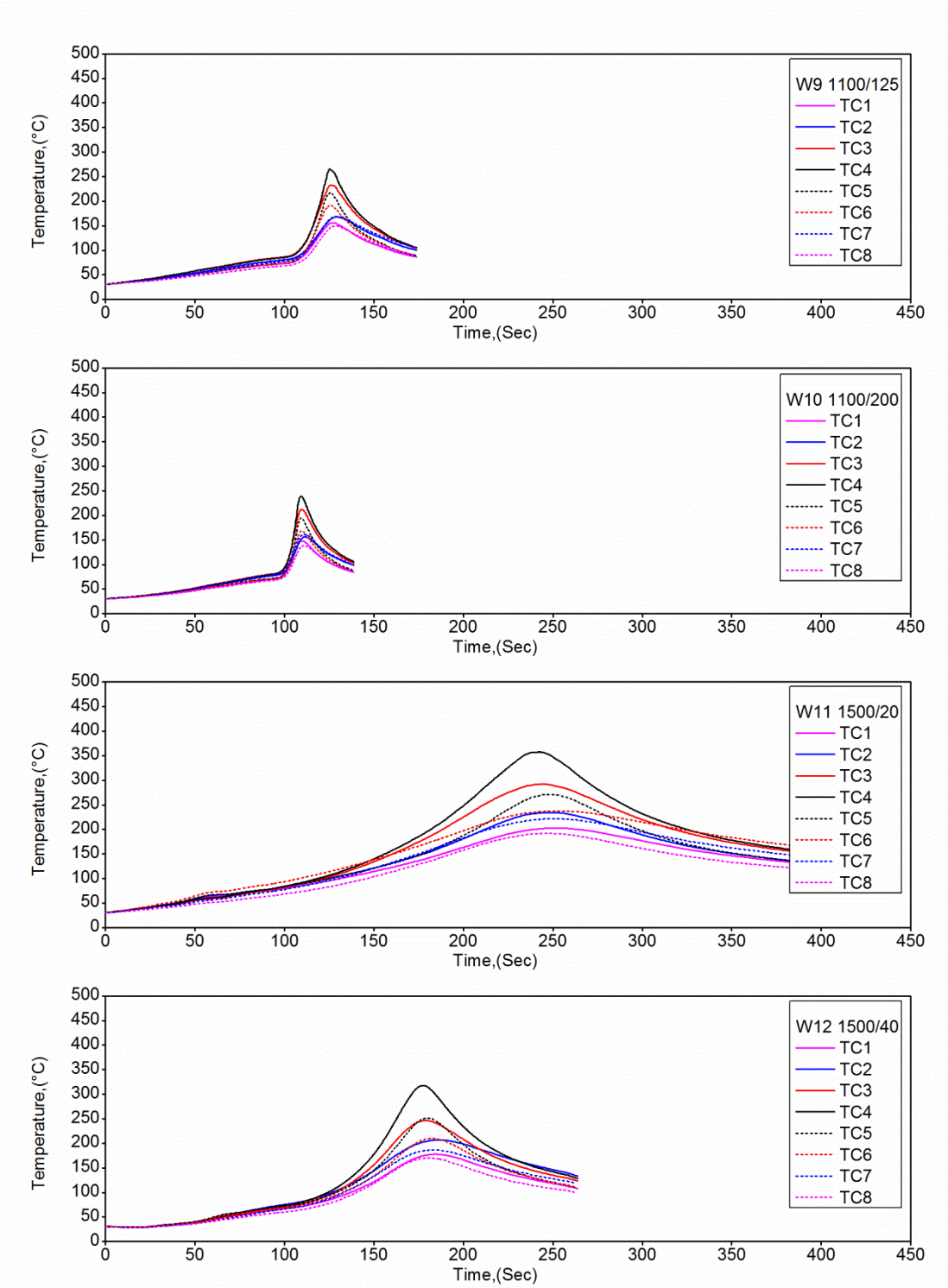
[234] Z. Feng, X.-L. Wang, S.A. David, P.S. Sklad, Modelling of residual stresses and property distributions in friction stir welds of aluminium alloy 6061-T6, Science and Technology of Welding and Joining 12(4) (2007) 348-356.

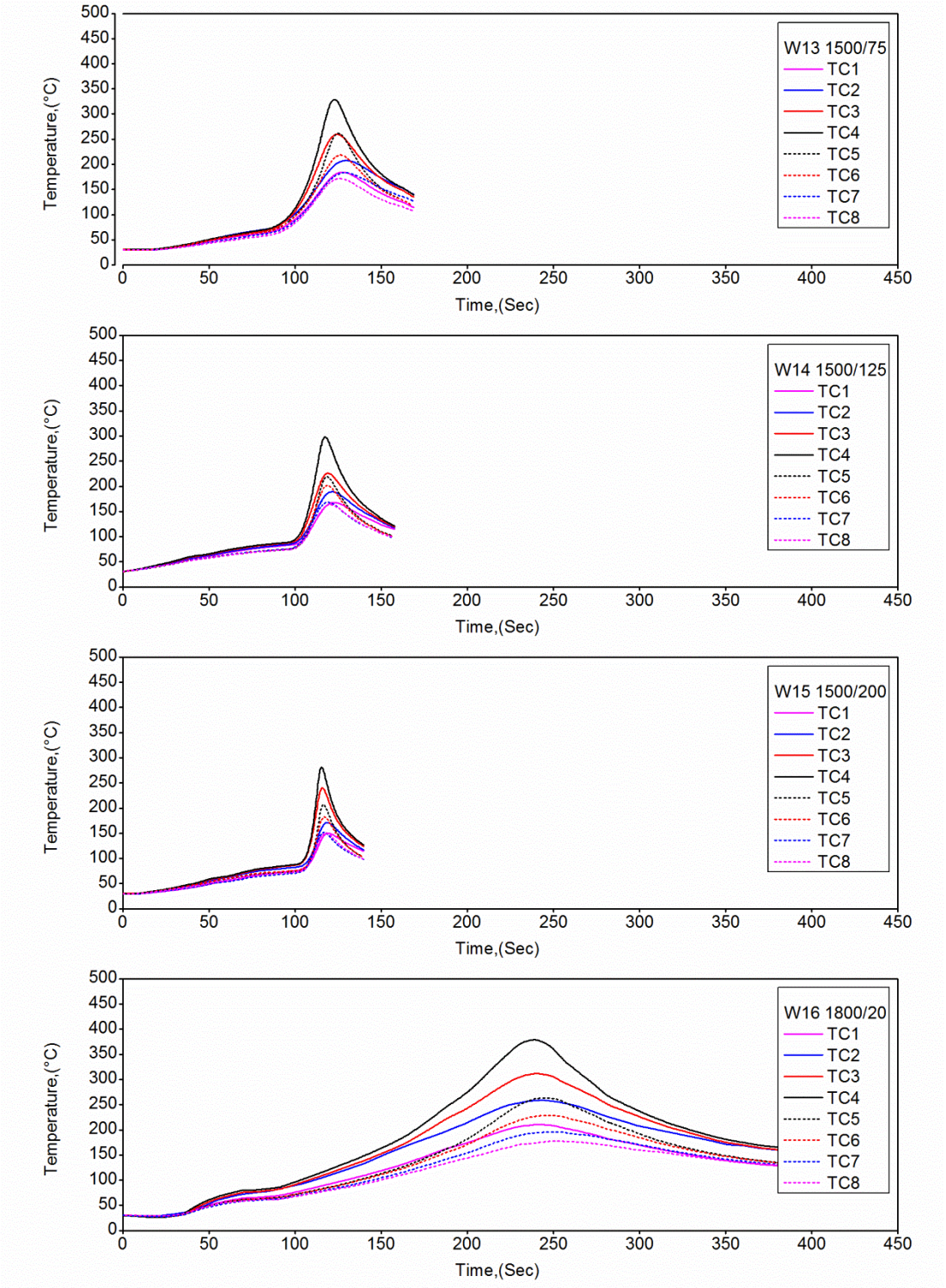
Appendices

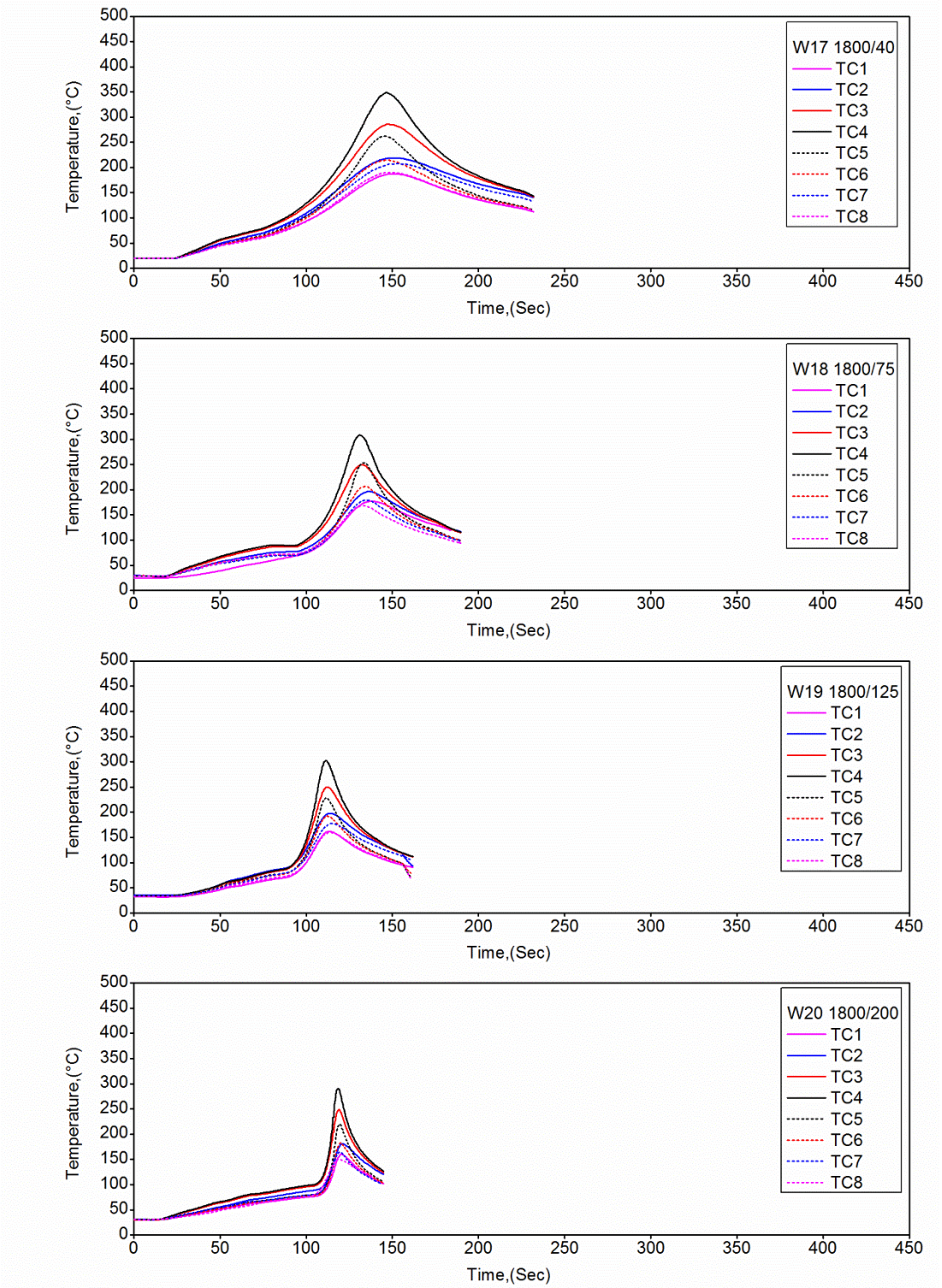
A. Thermal histories of AA 6082 FSW joints



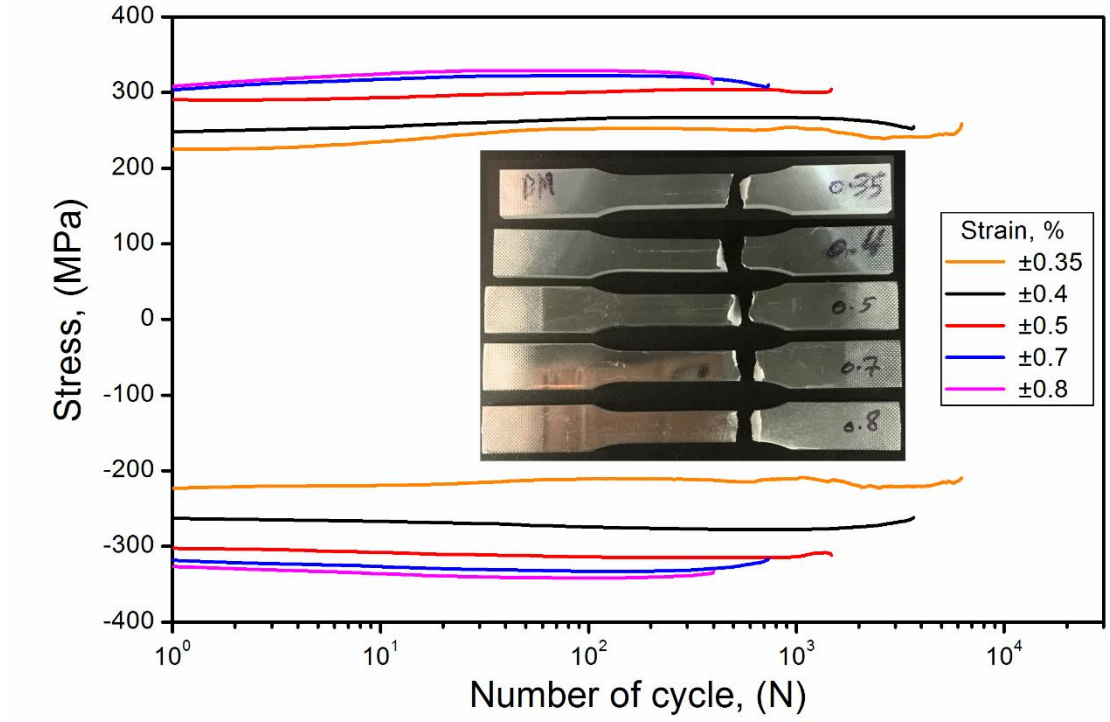

W5 800/20
TC1
TC2
TC3
TC4
TC5
TC6
TC7
TC8
Temperature,(°C)
Time,(Sec)
W6 1100/20
W7 1100/40
W8 1100/75

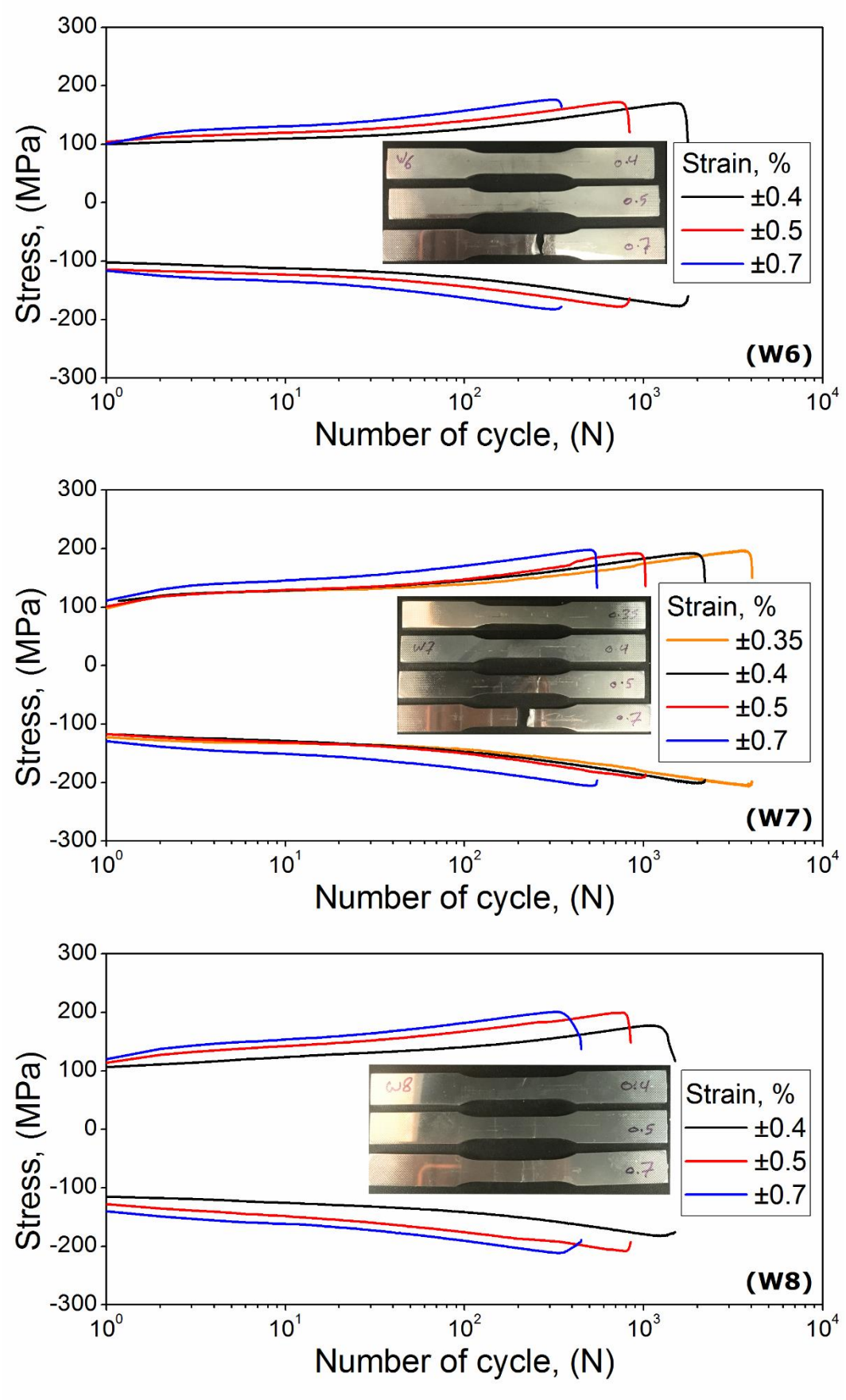

W9 1100/125
TC1
TC2
TC3
TC4
TC5
TC6
TC7
TC8
Temperature,(°C)
Time,(Sec)
W10 1100/200
TC1
TC2
TC3
TC4
TC5
TC6
TC7
TC8
Temperature,(°C)
Time,(Sec)
W11 1500/20
TC1
TC2
TC3
TC4
TC5
TC6
TC7
TC8
Temperature,(°C)
Time,(Sec)
W12 1500/40
TC1
TC2
TC3
TC4
TC5
TC6
TC7
TC8
Temperature,(°C)
Time,(Sec)

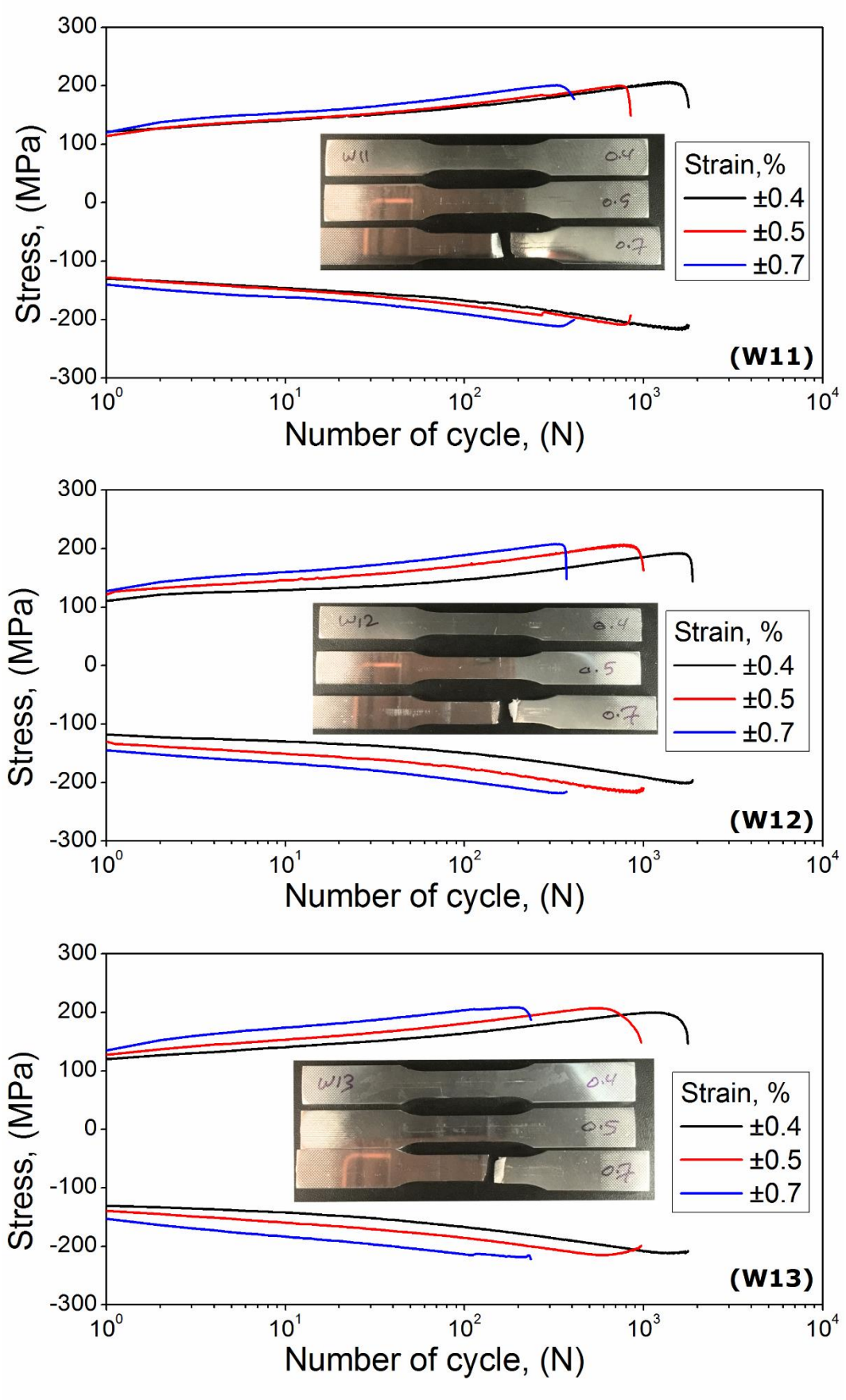

W13 1500/75
TC1
TC2
TC3
TC4
TC5
TC6
TC7
TC8
Temperature,(°C)
Time,(Sec)
W14 1500/125
W15 1500/200
W16 1800/20

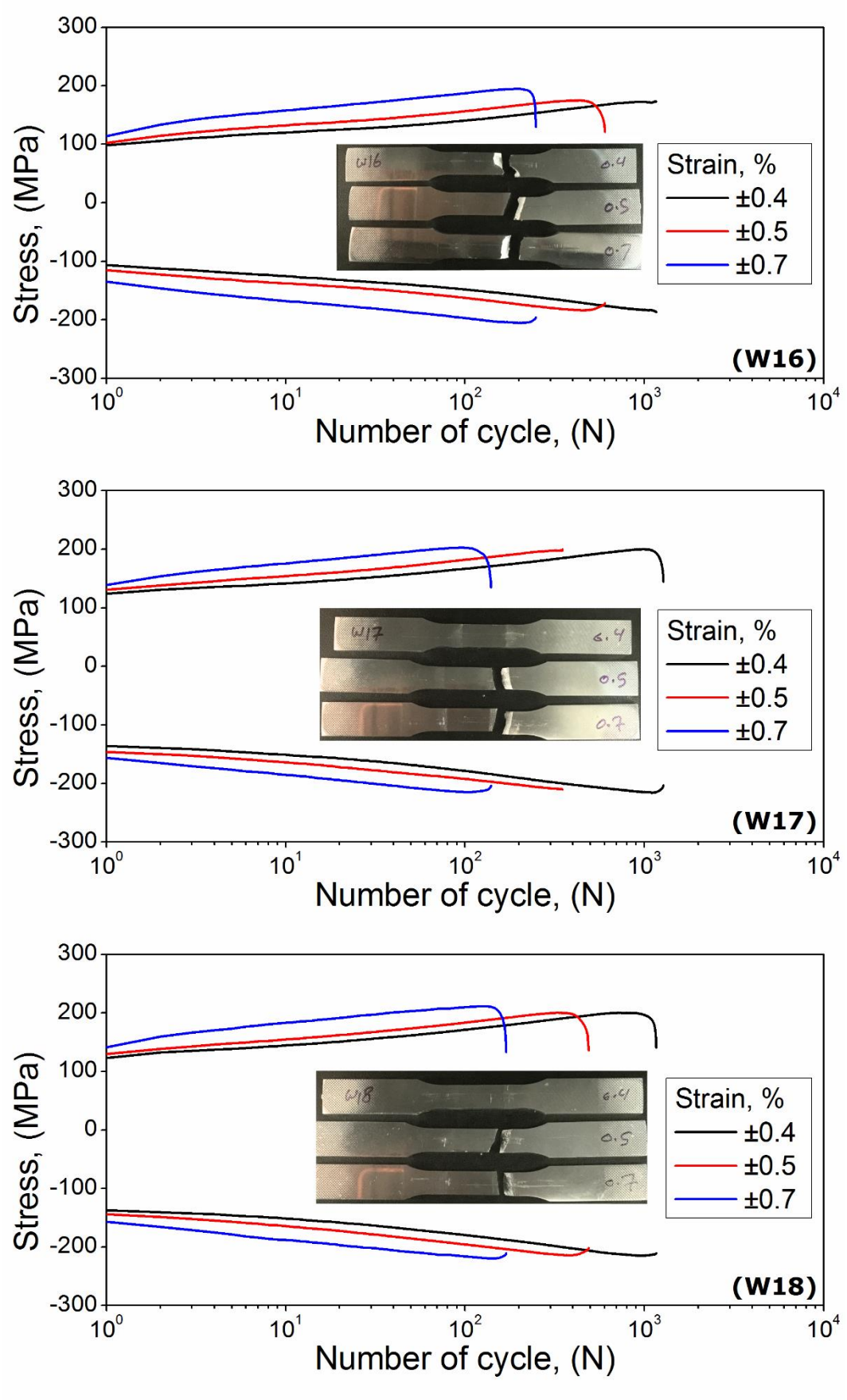

W17 1800/40
TC1
TC2
TC3
TC4
TC5
TC6
TC7
TC8
Temperature,(°C)
Time,(Sec)
W18 1800/75
TC1
TC2
TC3
TC4
TC5
TC6
TC7
TC8
Temperature,(°C)
Time,(Sec)
W19 1800/125
TC1
TC2
TC3
TC4
TC5
TC6
TC7
TC8
Temperature,(°C)
Time,(Sec)
W20 1800/200
TC1
TC2
TC3
TC4
TC5
TC6
TC7
TC8
Temperature,(°C)
Time,(Sec)

B. Cyclic deformation response of AA 6082 and FSW joints

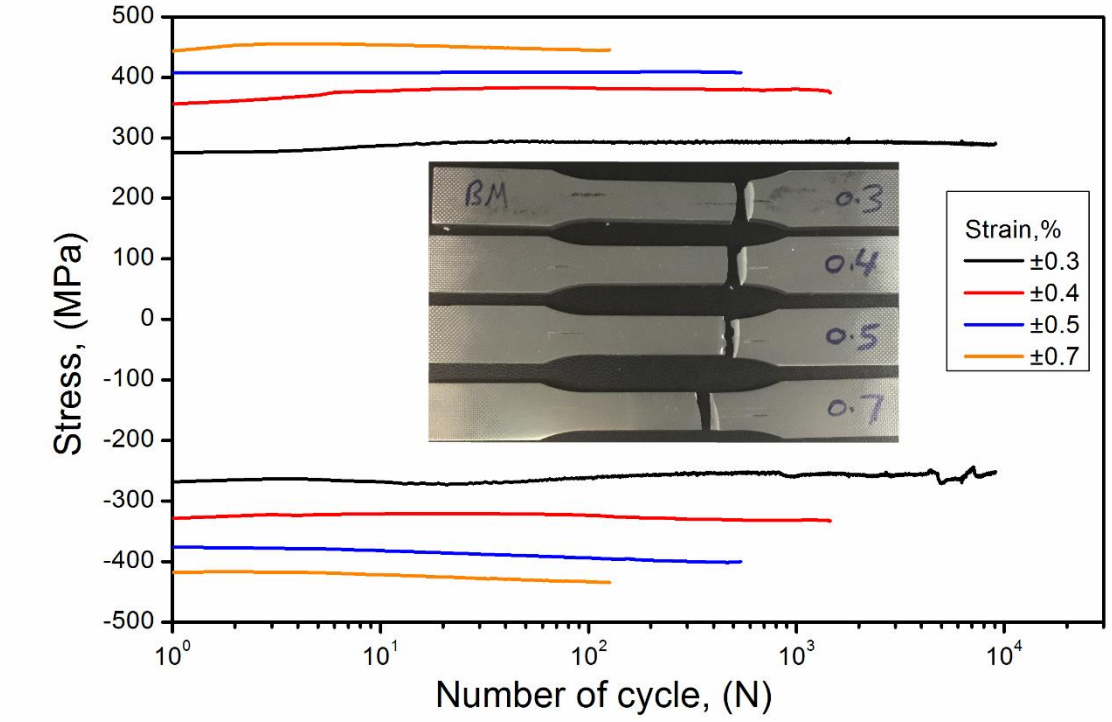


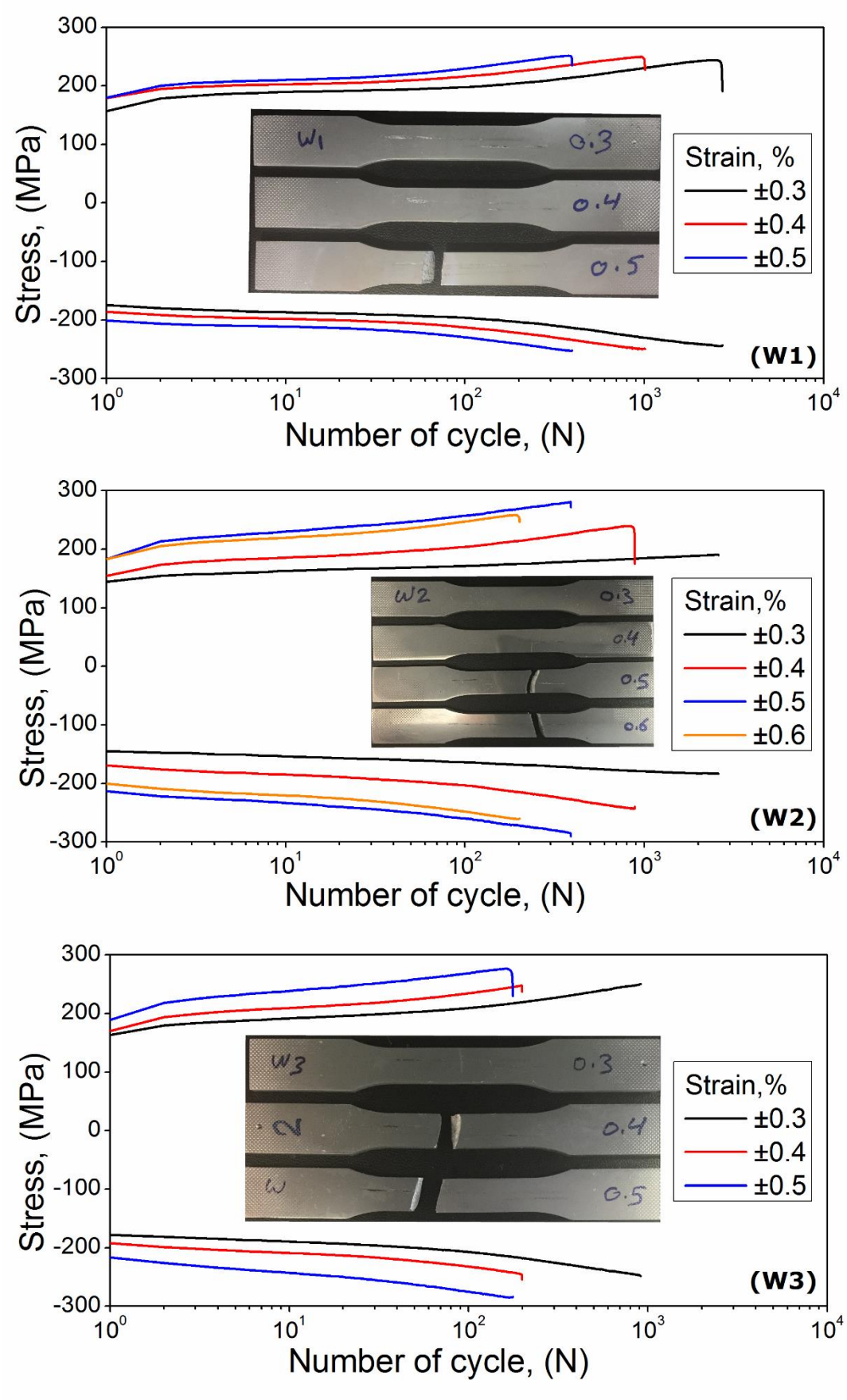

Stress, (MPa)
Number of cycle, (N)
Strain, %
±0.4
±0.5
±0.7
(W6)
Strain, %
±0.35
±0.4
±0.5
±0.7
(W7)
Strain, %
±0.4
±0.5
±0.7
(W8)

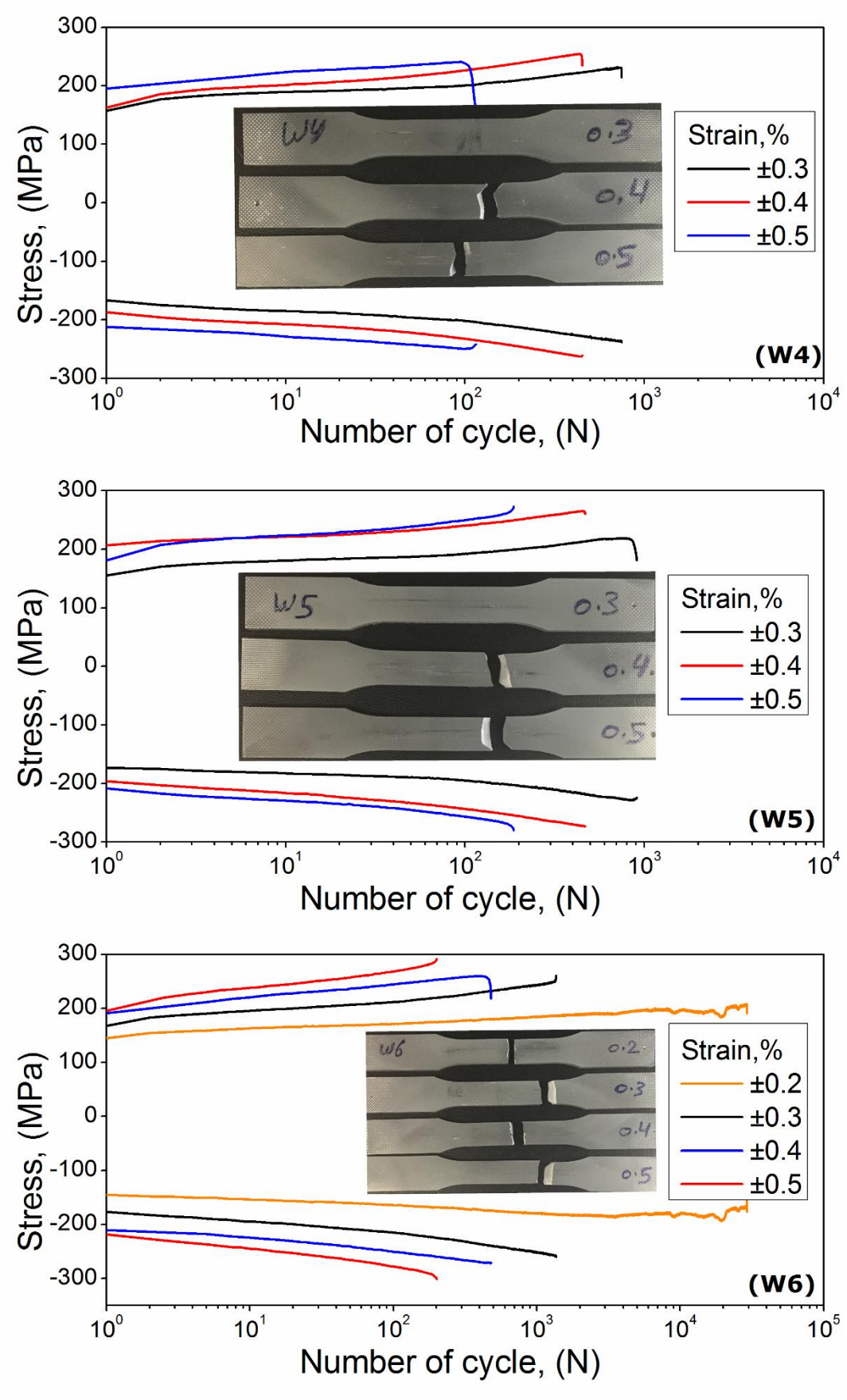

Stress, (MPa)
Number of cycle, (N)
Strain,%
±0.4
±0.5
±0.7
(W11)
W11
0.4
0.5
0.7
Stress, (MPa)
Number of cycle, (N)
Strain, %
±0.4
±0.5
±0.7
(W12)
W12
0.4
0.5
0.7
Stress, (MPa)
Number of cycle, (N)
Strain, %
±0.4
±0.5
±0.7
(W13)
W13
0.4
0.5
0.7

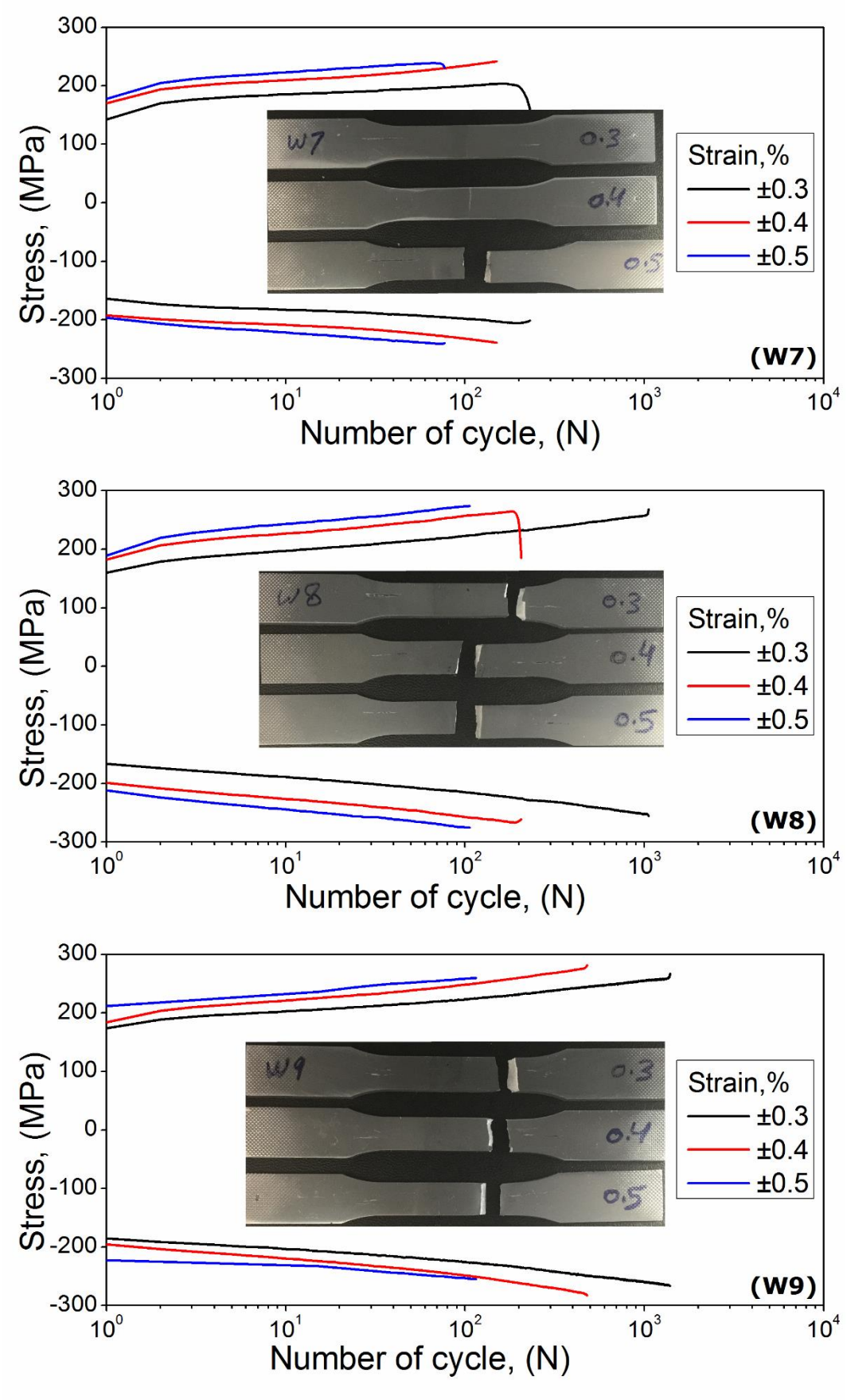

Stress, (MPa)
Number of cycle, (N)
Strain, %
±0.4
±0.5
±0.7
(W16)
(W17)
(W18)

C. Cyclic deformation response of AMC and FSW joints

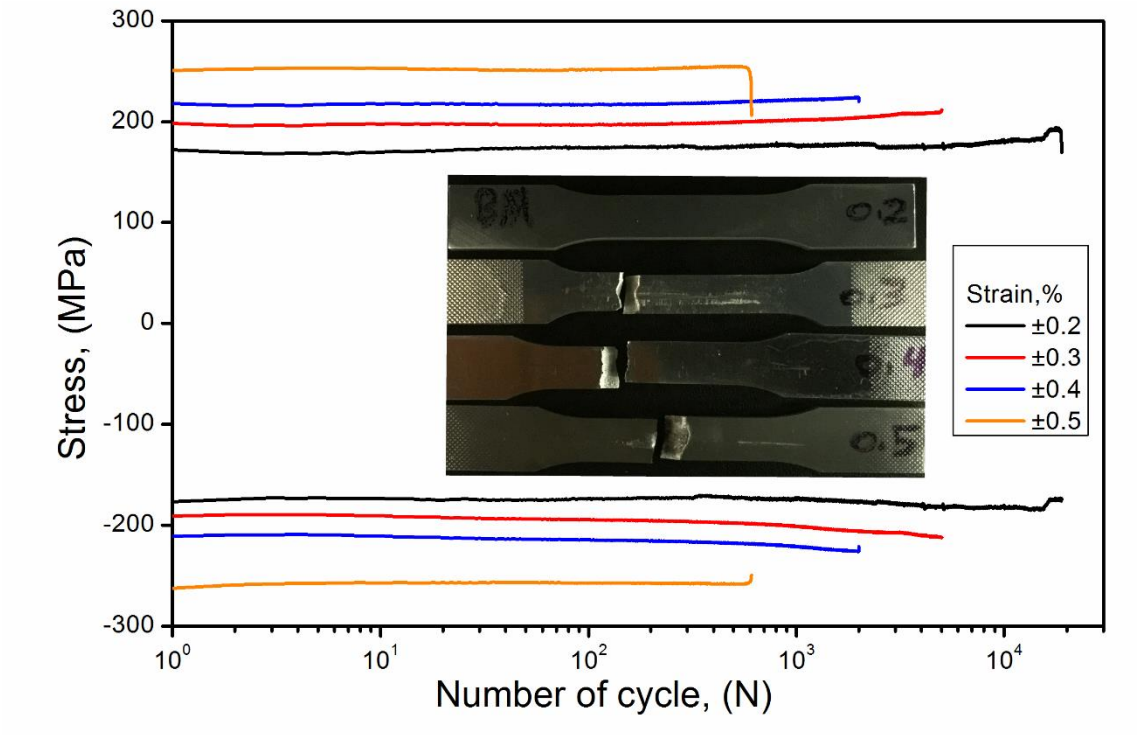


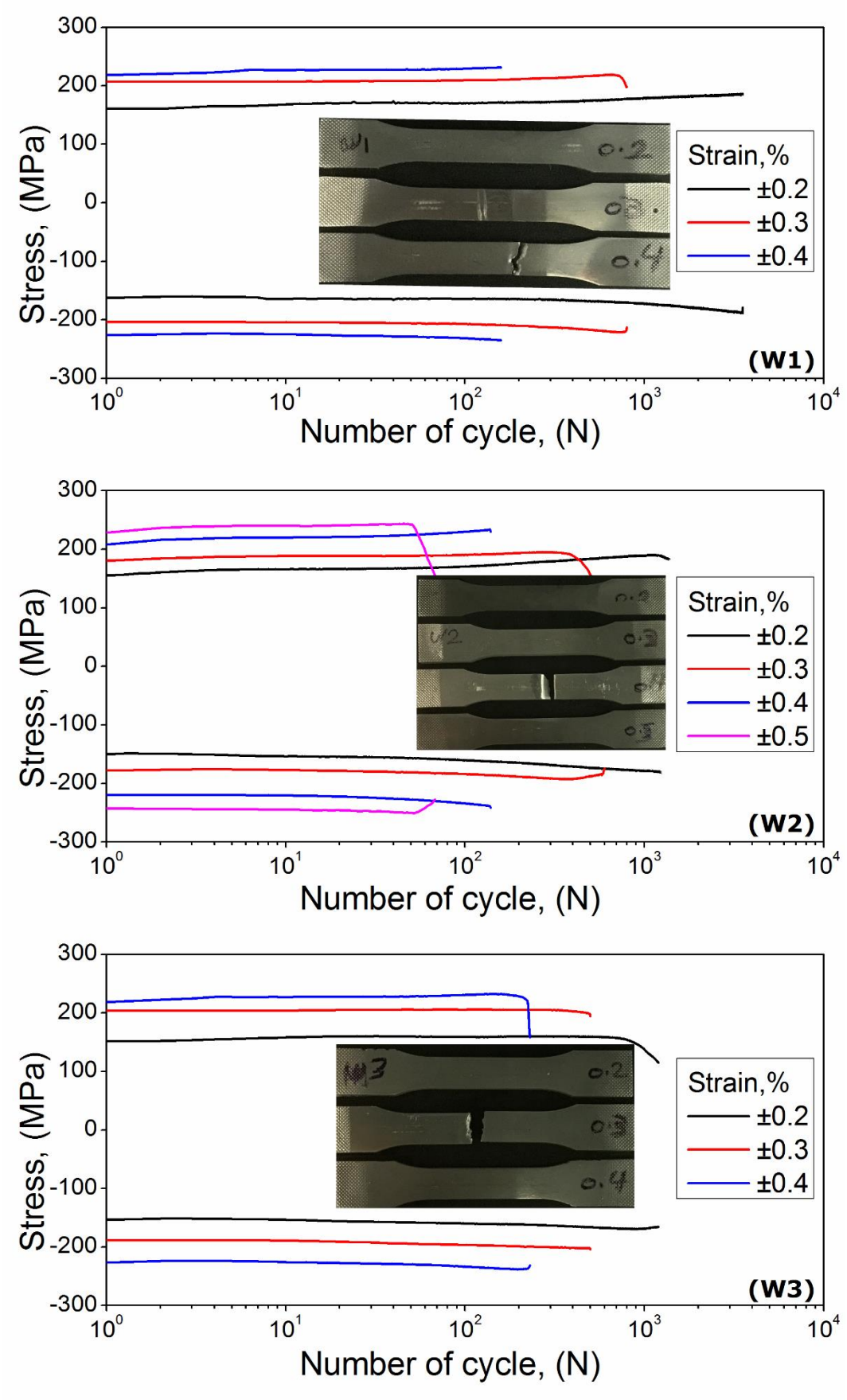

Stress, (MPa)
Number of cycle, (N)
Strain, %
±0.3
±0.4
±0.5
(W1)
W1
0.3
0.4
0.5
Strain,%
±0.6
(W2)
W2
0.6
(W3)
W3

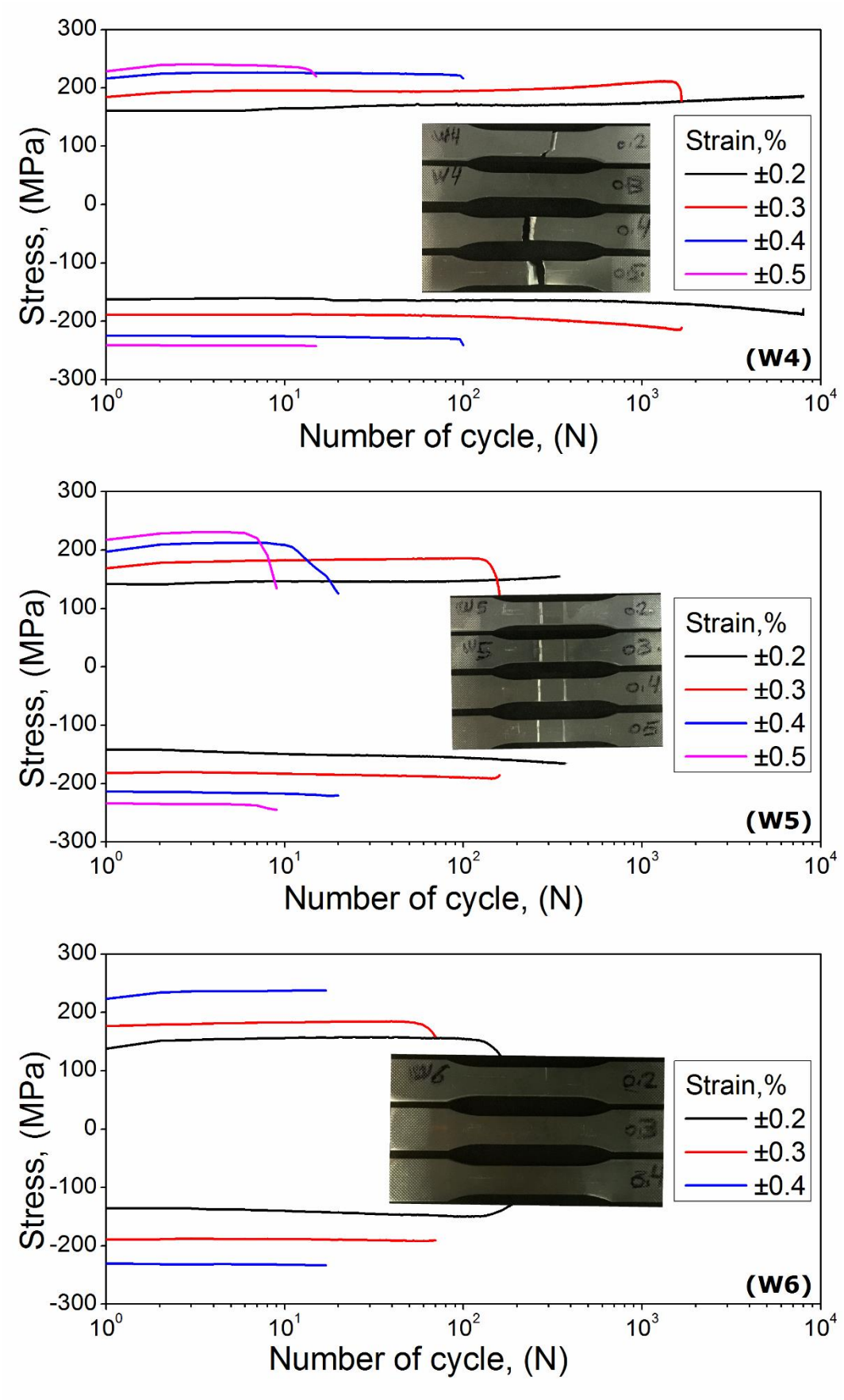

Stress, (MPa)
Number of cycle, (N)
Strain,%
±0.3
±0.4
±0.5
(W4)
W4
0.3
0.4
0.5
(W5)
W5
(W6)
W6
±0.2

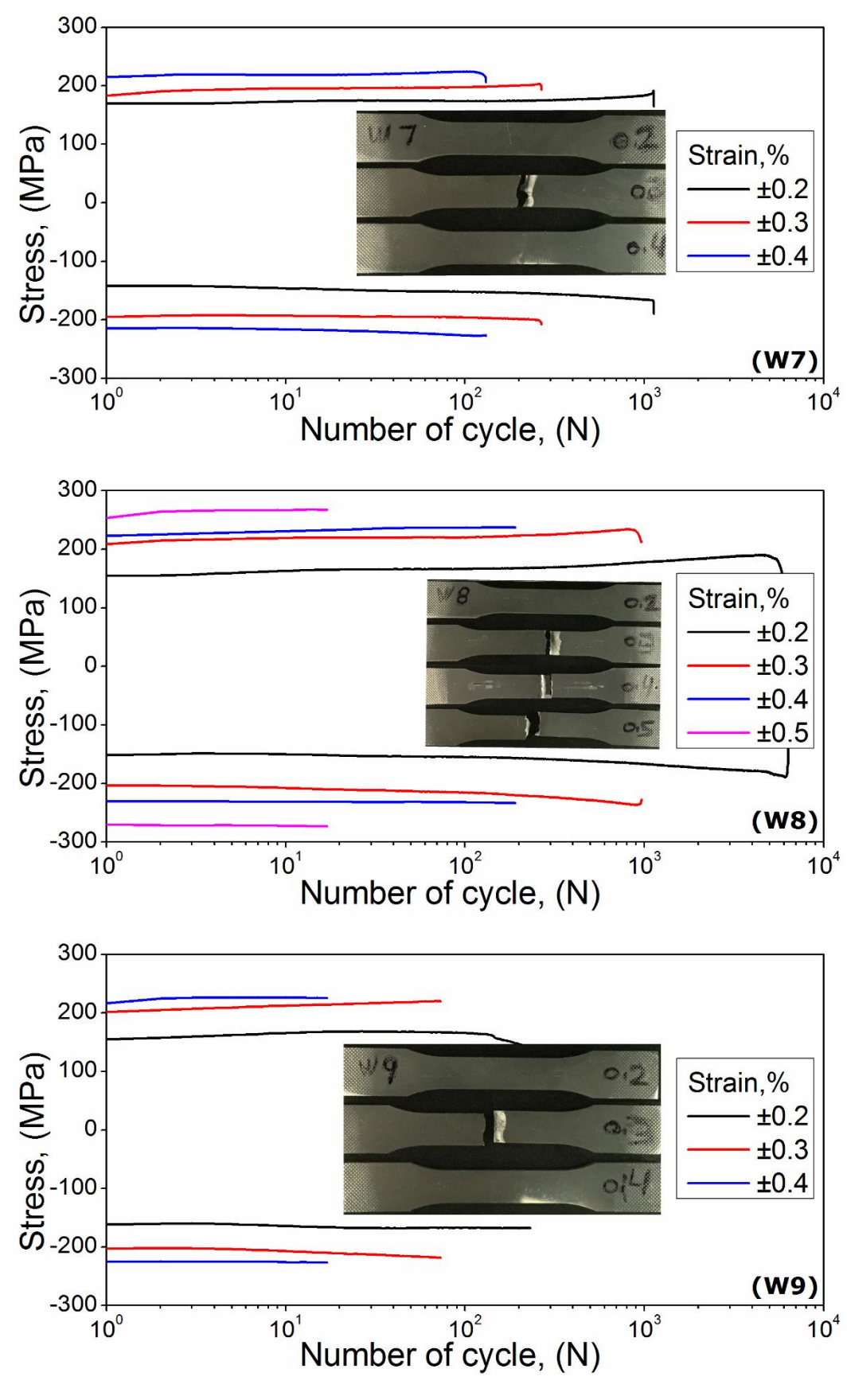

300
200
100
0
-100
-200
-300
Stress, (MPa)
10^0
10^1
10^2
10^3
10^4
Number of cycle, (N)
W7
0.3
0.4
0.5
Strain,%
±0.3
±0.4
±0.5
(W7)
W8
(W8)
W9
(W9)

D. Cyclic deformation response of SAMC and FSW joints




Stress, (MPa)
Number of cycle, (N)
Strain,%
±0.2
±0.3
±0.4
(W1)
Stress, (MPa)
Number of cycle, (N)
Strain,%
±0.2
±0.3
±0.4
±0.5
(W2)
Stress, (MPa)
Number of cycle, (N)
Strain,%
±0.2
±0.3
±0.4
(W3)


Stress, (MPa)
Number of cycle, (N)
Strain,%
±0.2
±0.3
±0.4
±0.5
(W4)
(W5)
(W6)


Stress, (MPa)
Number of cycle, (N)
Strain,%
±0.2
±0.3
±0.4
(W7)
Strain,%
±0.2
±0.3
±0.4
±0.5
(W8)
Strain,%
±0.2
±0.3
±0.4
(W9)